The Role of Thermal Boundary Conditions in Rotating Rayleigh–Bénard Convection

Janet Peifer

The University of Leeds

School of Mathematics

Submitted in accordance with the requirements for the degree of

Doctor of Philosophy

September 2022

Declaration

The candidate confirms that the work submitted is her own and that appropriate credit has been given where reference has been made to the work of others. This copy has been supplied on the understanding that it is copyright material and that no quotation from the thesis may be published without proper acknowledgement.

For my dad.

Thank you for teaching me the audacity and grit to pursue something so bold.

Acknowledgements

My thanks first and foremost go to my supervision team: Steven Tobias and Onno Bokhove. Thank you for giving me the chance to pursue this project and supporting my development as a researcher over the last four years. Your advice and insights have been invaluable.

I acknowledge the School of Mathematics for my studentship funding as well as funding for conference fees and travel. This work was undertaken on ARC3, part of the High Performance Computing facilities at the University of Leeds, UK.

My success in this endeavour is in no small part due to the constant companionship of my colleagues. Special gratitude is due to Erily, who gave me the much needed courage to persevere through the difficulties of a PhD. My thanks as well to Joseph, Patrick and Christina along with my peers in AGFD – to have been your friend and peer these last few years has been a privilege. A special thanks to Sophie & Sappho, Mikey & Hobbes and Lydia for many reassuring walks, chats, and giggles. I am very grateful to my Philosophy-adjacent friends for welcoming me to Leeds and to your wonderful selves. To all my old friends, especially Thalia and Amanda, thank you for all of the love and support.

Vishnu, it's impossible to express how grateful I am for your support, guidance, and love throughout this process. Thank you for all the amazing food, votes of confidence, and comforting hugs. I couldn't have done this without you.

I owe any and all accomplishments to the unconditional love and support from my family. To Mom and Emma, thank you for supporting me even when my pursuits took me 3000 miles away. Thank you for always answering the phone, playing online games, and believing in me.

Abstract

Rotating Rayleigh–Bénard convection (RRBC) is ubiquitous in nature. RRBC is present in the dynamics of planetary cores and atmospheres. Numerical models of RRBC are limited in their ability to represent geophysical convective flows. In addition, while thermal boundary conditions which are physically appropriate for geophysical flows are available, many numerical models chose to simplify the boundaries to be fixed temperature and all thermal conditions to be homogeneous. We are motivated to explore the significance of these simplified conditions by exploring the effects of physically-appropriate thermal boundary conditions on RRBC.

We study RRBC in a cylindrical domain, which is appropriate both for comparison to experimental models and for understanding dynamics in the polar regions of planetary flows.

On the horizontal boundaries, the fixed temperature condition is compared to the astrophysically appropriate fixed flux, mixed (fixed temperature on the lower boundary and fixed flux on the upper boundary) conditions, and the Robin condition which straddles the fixed flux and fixed temperature conditions. We show that at rapid rotation, convection onset is independent of thermal boundary condition, extending the theory presented in Calkins et al. (2015). We also define a novel parameter for comparing systems with Robin boundary conditions to those fixed temperature boundaries. We show that, while the fixed temperature thermal boundary condition is sufficient for modelling the bulk flow of experimental RRBC systems, natural systems may require use of the Robin condition.

Subsequently, we investigate the effect of inhomogeneous insulation on lateral walls, motivated by the irregular heat flux which the Earth's mantle applies to the outer core. The inhomogeneity is sinusoidal along the azimuthal axis with azimuthal mode m_θ which is varied relative to the dominant length-scale of convection in three scenarios: larger length-scale than convection; the same length-scale as convection; and a secondary convective length-scale. The first instance is appropriate for molten planetary cores, while the latter two are of interest for experimental studies. The main results are: large-length scale m_θ causes a convection roll rotation about the domain to slow, and matching m_θ to the convective length-scale- or a multiple of it- causes convection rolls to be pinned.

Finally, an experimental set-up is proposed based on the simplified precipitation model in Hernadez-Duenas et al. (2012). The specifications for the set-up are determined using the results of numerically modelled RRBC with the Robin condition. The experiment would have applications in Numerical Weather Prediction.

Contents

List of Figures

List of Tables

Chapter 1

Introduction

1.1 Motivation

Thermal convection is a heat transportation phenomenon in fluids – liquids, gases, and plasmas – driven by a temperature gradient. Given a fluid with a density that decreases with increased temperature, an increase in temperature will cause the fluid to expand. Consequently, the density decreases. Moreover, when cool fluid is layered over warm fluid, buoyancy causes the warmer fluid to rise as its density decreases and the cooler, more dense, fluid to descend.

Rayleigh–Bénard convection (RBC) is the quintessential process by which this thermally-driven motion continues due to a maintained difference in the temperature below and above the fluid. This proves an efficient method of heat transport through fluids. While seemingly quite simple in its basic state, RBC is a basis for modelling increasingly complex flows.

In the simplest instance, RBC takes the form of a fluid layer heated from below and cooled from above. Figure 1.1 visualises a classic RBC scenario: a layer of fluid, represented as the white space, contained by two boundaries: a lower boundary which is heated (red) and upper boundary which is cooled (blue). Cellular flow patterns, as shown by the arrows, develop when the temperature difference is gradually increased, due to the fluid rising as it is heated and descending as it cools. Each set of arrows comprises what is known as a convection roll wherein fluid is equally rising and falling. By studying this basic process we gain insight into more complex astrophysical and geophysical flows.

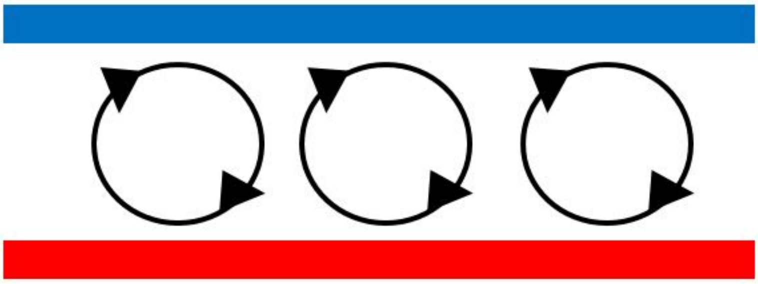

Figure 1.1: A diagram of RBC. A layer of fluid is heated from below (red) and cooled from above (blue). The fluid moves, as shown by the arrows, upward when heated and downward when cooled, forming cellular patterns of flow.

RBC is ubiquitous in astrophysical and geophysical systems. For example, planetary cores undergo convection, wherein molten metal is driven away from the planet's centre due to heating and flows back down as it cools. Human life is greatly affected by the convective process in both the oceans and the atmosphere. The air and water vapour in the atmosphere wrap around the earth, being heated and cooled in layers as the atmosphere extends away from the Earth. These essential instances of convection cause the study of convection to become necessary for both day-to-day life – in the form of weather forecasting – and for a deeper understanding of our universe – investigating the motion of fluids on planets.

1.1.1 Planetary cores

One example of an astrophysical system that is explored with RBC is a planetary core. A typical core structure is illustrated in Figure 1.2 by the Earth's core. Below a planet's surface, known as the crust, is the mantle, a layer of rock or ice. The mantle insulates the outer core, which is a layer of molten metal heated from below by the solid inner core due variation in the composition of the inner core. The scales of these layers are immense. The Earth's diameter is nearly 6500km, of which a mere 100km is the crust on which we live. The two thickest layers – the mantle and the outer core – both undergo convection. The mantle moves very slowly causing shifts in tectonic plates under the Earth's crust. While the study of plate tectonics is of interest to many geophysical processes, this thesis is primarily

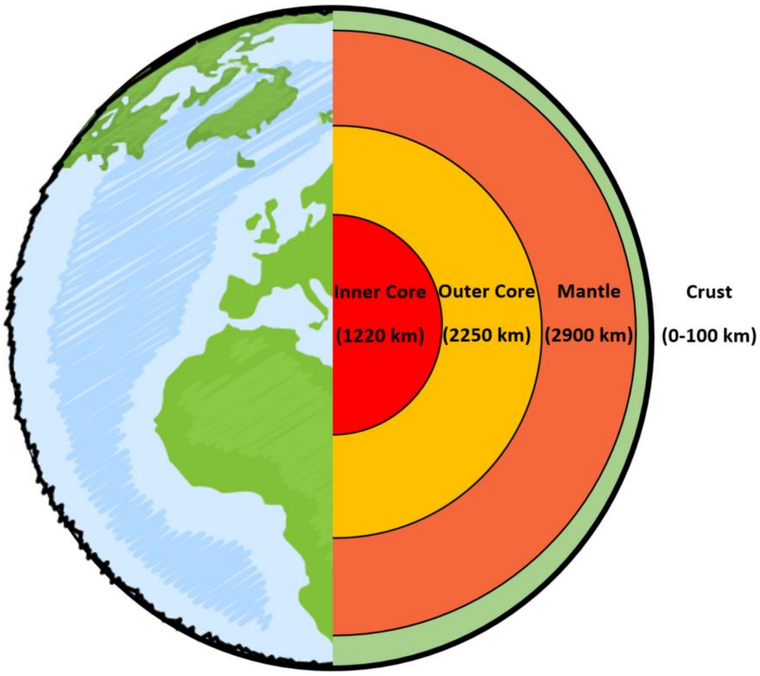

Figure 1.2: A schematic of the structure of the Earth's core.

concerned with the flow of molten metals in planetary cores. Further information on mantle convection is available in G. F. Davies and Richards (1992) and Schubert et al. (2001).

Planetary cores introduce several layers of complexity to the simple convection process described previously. One of which is the constraint of the molten metals not by simple Cartesian parallel boundaries, as shown in Figure 1.1, but within a spherical-shell – bounded on the interior by the solid core and on the exterior by the mantle. In the study of RBC, the fluid dynamics within a spherical geometry are difficult to solve analytically (F. H. Busse, 1975; F. H. Busse & Cuong, 1977) and experimental studies of fluid dynamics are often conducted in cylindrical domains due to practicality (Sahoo & Sreenivasan, 2020). However, experimental studies in spherical and hemispherical-shells are possible (e.g. Cardin & Olson, 1994; Sumita & Olson, 2002; Aujogue et al., 2018). Due to the analytical and experimental difficulties (i.e. inappropriate direction of gravity), numerical studies are the preferred method of investigation for planetary cores (e.g., T. Nakagawa & Tackley, 2008; Gastine et al., 2016; R. Long et al., 2020; Clarté et al., 2021).

Both numerical and experimental models are constrained in their ability to capture the scale at which planetary cores flow. The ratio of buoyant driving forces to diffusive forces is described by the Rayleigh number (Ra), and the ratio between the Coriolis force to viscous force is parameterised by the Ekman number (Ek), which is inversely related to the speed of rotation. For instance, the Earth's outer core is estimated to have $Ek = 10^{-15}$ (Yadav et al., 2016) and $Ra = 10^{25}$ (R. S. Long, 2020). Each of these parameters are respectively too small and too large to currently be numerically modelled. To enable predictions of large-scale behaviours from models, scaling laws have been developed which relate heat transport in numerically and experimentally achievable systems to parameters Ra and Ek. However, this topic is subject to great debate (see e.g. Plumley & Julien, 2019).

The rotation of planets greatly affects convective flow. The primary effect of rotation in fluids is explained by the Taylor–Proudman Theorem. This theorem was developed from experimental studies in Taylor (1923, 1936) and analytic efforts in Proudman (1916), both of which reported that the velocity of a rapidly rotating fluid tends to be approximately uniform in the direction parallel to the axis of rotation. Consequently, rapid rotation leads to columnar structures, often termed Taylor-columns. Figure 1.3 illustrates such columnar behaviour in a numerical model of rapidly rotating convection in a spherical-shell.

Rotation also contributes to the generation of magnetic fields in a process known as dynamo action. Dynamos are caused by a complex process involving electrically conducting metals undergoing convection. Though dynamos are of great interest in astrophysical and geophysical contexts, this thesis is concerned primarily with thermal convection. More information on dynamo theory is available in Dormy and Soward (2007) and Tobias (2021).

Additional complications to RBC in the Earth's core arise from the non-uniform conditions at the interface between the outer core and the mantle – known as the core-mantle boundary (CMB). Researchers predict, due to analysis of magnetic field maps, that there are variations in the heat flux at the CMB (Cox & Doell, 1964; Bloxham & Gubbins, 1987). Such variations are also indicated by seismic tomography (Masters et al., 1996). In analytical and numerical models, this boundary tends to be idealised. However, idealisations lead to deviations in behaviour

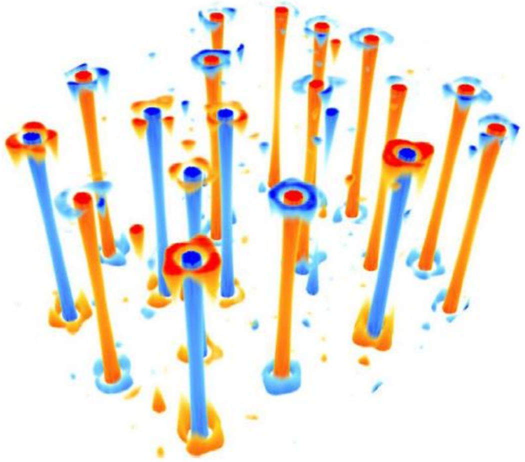

Figure 1.3: A representative example of columnar flow structure in numerically modelled rapidly rotating convection. The columns visualise temperature perturbations such that orange indicates warmer fluid and blue indicates cooler fluid. Taken from Grooms et al. (2010).

between models and physical systems. Such deviations have motivated a number of numerical studies with inhomogeneous thermal boundary conditions in both spherical-shells (C. J. Davies et al., 2009; Mound & Davies, 2017) and cylindrical domains (Reiter et al., 2022) as well as experimental studies in cylindrical domains (Chung et al., 2000; Sahoo & Sreenivasan, 2020).

The composition of the outer core is also subject to heterogeneity. The Earth's core is believed to be composed of molten iron along with oxygen and sulphur (Gubbins & Herrero-Bervera, 2007). The interactions of these components of varying densities and thermal properties is relevant to the understanding of the Earth's dynamo. Another way to study the effects of various materials in a convective flow is with multi-phase convection. While several numerical models have isolated aspects of multi-phase convection in planetary cores (Wong et al., 2018; Tremblin et al., 2019), multi-phase convection is better understood in the geophysical context of atmospheric convection.

1.1.2 Atmospheric convection

It is widely agreed by scientists that the ongoing rapid climate change will directly affect existing agriculture practices, wildlife populations, and water resources

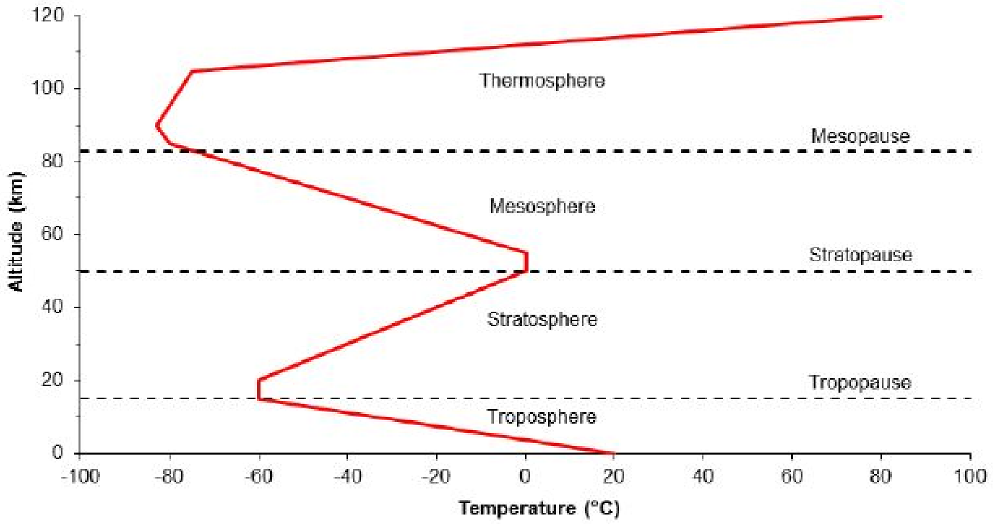

Figure 1.4: The averaged temperature profile of the Earth's atmosphere as a function of altitude. Taken from Manning (2013).

(Pachauri & Meyer, 2014). Thus, it is imperative that substantial efforts be made to describe and predict the changing weather trends and events. Numerical Weather Prediction (NWP) is an important tool in weather forecasting (Bauer et al., 2015). NWP combines computational fluid dynamics and data assimilation, using real-time observations to inform the evolution of numerical models which provide predictions. One area of NWP which needs considerable improvement is atmospheric convection because the interaction between convecting air and moisture in the atmosphere is directly related to the development of storms and precipitation (Trapp, 2018). Therefore, modified forms of RBC are usefully applied to understanding atmospheres and consequently weather and climate patterns.

The Earth's atmosphere has a mean temperature profile, as visualised in Figure 1.4, which extends upward from the surface in specifically recognised layers. Furthest from the Earth's surface is the Thermosphere, which absorbs X- and UV-rays from the Sun, heating the fluid. Below is the Mesosphere, containing the coldest temperatures in the atmosphere due to decreasing air density. This layer is cooler above than below, and consequently, undergoes thermal convection (Lehmacher & Lübken, 1995). The following layer is the Stratosphere, containing the Ozone layer. The Troposphere is where humans live and most weather occurs. As seen in the lowest layer of Figure 1.4, the average temperature decreases upward in the Troposphere, which drives thermal convection.

While both the Troposphere and Mesosphere have the necessary conditions for thermal convection, this thesis focuses on the Troposphere in order to better understand weather patterns. Weather phenomena such as El Niño, and squall lines are each related to local convective processes as well as global air circulation. Predicting such weather patterns is difficult due to the complexity in modelling interactions between the atmosphere and the Earth's surface and the interactions between the air, water, and particles which compose the atmosphere.

Hence, the mixed composition of the Earth's atmosphere complicates the RBC process. The interaction of air, water, and particulate components, each influenced by heat and density gradients, causes water to undergo phase changes resulting in cloud formations and precipitation. Figure 1.5 illustrates the different transition processes and phases of water in the atmosphere. Water vapour condenses into cloud water, which undergoes autoconversion and collects into rain water. Rain water then precipitates or evaporates back into water vapour. Each of these processes impacts the convective flow of air in the atmosphere. To study the essential dynamics of process, RBC can be modified to include a moisture component.

Within moist convection, there are two primary aspects: precipitation and phase change. During phase change, when water condenses from gas to liquid, a significant amount of latent heat is released, affecting the local thermal conditions. Such perturbations to temperature have effects on RBC (Pauluis & Schumacher, 2010). The modelling of moist RBC generally employs a piece-wise constant or Heaviside function controlled by water saturation levels to determine what dynamics are locally dominant. However, simplified models differ in their treatment of the fluid after phase change, further affecting RBC dynamics. For instance, in Pauluis and Schumacher (2010) condensation retention leads to cloud formation, while the model presented in Vallis et al. (2019) immediately removes water vapour from the system. Generally, for fixed Ra and Pr values, moist convection is more unstable than dry convection, becoming more turbulent with the presence of a precipitant (Oresta et al., 2009; L. E. Schmidt et al., 2011; Vallis et al., 2019).

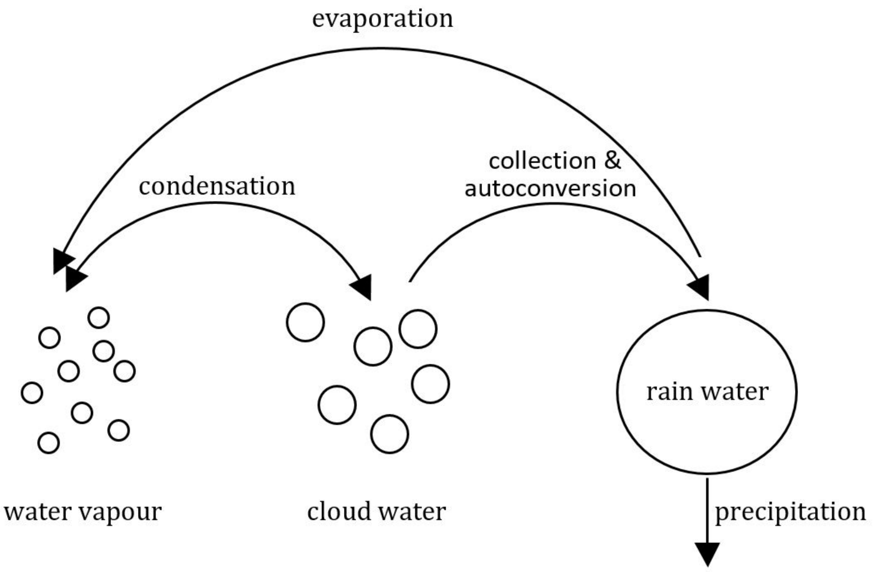

Figure 1.5: Diagram of the phases of water in the atmosphere. Liquid rain water either precipitates or is evaporated into water vapour. Cloud water is formed from the condensation of water vapour. Then, cloud water undergoes autoconversion and collection to become rain water. A simplification of Figure 2 in Hernadez-Duenas et al. (2012).

The other facet of moist convection is precipitation, wherein the more dense phase falls through the system. The addition of a free-fall velocity, as illustrated by V_T in Figure 1.5, requires the consideration of an additional timescale. While condensation takes only seconds, evaporation and the transition from cloud water to rain water (autoconversion) take minutes. In order to unify these time scales in a simple RBC system, the Fast Autoconversion and Rain Evaporation (FARE) model was derived (Hernadez-Duenas et al., 2012; Hernandez-Duenas et al., 2015). Similarly to Pauluis and Schumacher (2010), the FARE model considers a simplified atmosphere of air and water which is dependent on the local saturation level of the system. The FARE model incorporates precipitation by introducing a falling velocity for rain water. Fast autoconversion and rain evaporation are two of the essential assumptions made in the derivation of the FARE model, allowing for the timescales of autoconversion and evaporation to unify with the timescale of condensation. However, this modification eliminates the cloud water phase. Despite this simplification, the FARE model is still capable of capturing weather events such as squall lines.

One shortcoming of the FARE model in capturing atmospheric RBC is the lack of rotation. As we previously discussed in the context of planetary cores, the Earth's rotation plays an important role in large-scale fluid flows. However, the interaction between precipitation, phase change, and rotation is not well understood. By investigating rotating moist convection in parts, it was shown that the faster rain falls, the more dominant large-scale flow becomes in rotating RBC (RRBC) (Smith & Stechmann, 2017; T. K. Edwards et al., 2019). With the addition of phase change, an asymptotically derived model has captured the jets of air in the atmosphere which move toward the north and south poles (Hu et al., 2021).

The development of different weather events differ over land and water. One example is the large cellular pattern of clouds observed over the ocean which rarely occur over land. The reason for this difference is that the thermal properties of ocean water differ from that of land. Land is highly thermally conductive, which practically fixes the temperature at the surface, whereas the ocean is less conductive, resulting in a variable temperature at the surface but a near-constant heat flux. Early studies such as Sasaki (1970) and Fiedler (1989) investigated these differences between land-bound and ocean-bound convection by creating a boundary condition which has fixed temperature and fixed flux properties in proportion to the thermal conductivity of the land and ocean with respect to that of the atmosphere. However, many simplified models currently use periodic boundary conditions (Hernandez-Duenas et al., 2015) or simple fixed temperature or fixed flux conditions (Ishiwatari et al., 1994). It has not yet been fully investigated how the changes in this thermal conductivity over land and water affects our understanding of atmospheric convection, especially with rotation and precipitation.

1.2 History and progress

Though simple in its conception, RBC offers many avenues for the investigation of complexities which arise in astrophysical and geophysical flows. The study of RBC began when Henri Bénard observed a cellular pattern in a layer of heated oil (Bénard, 1900, 1901). When the fluid was sufficiently heated, he observed that it

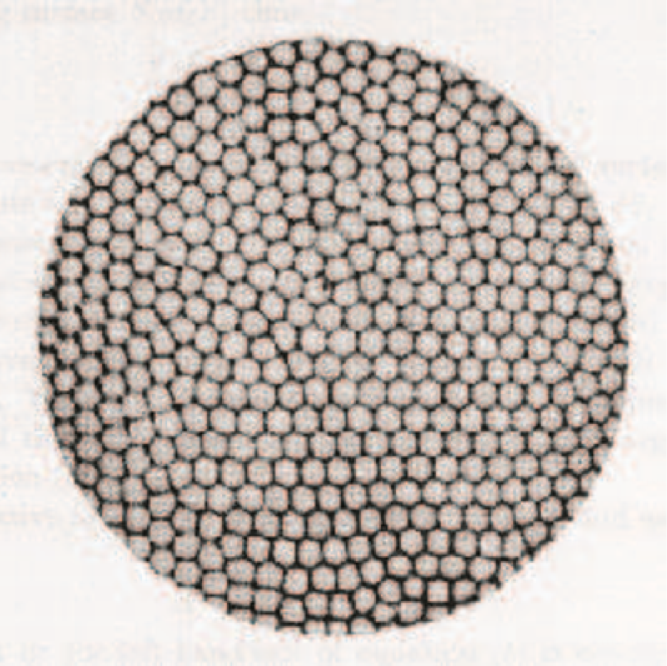

Figure 1.6: A re-creation of the Bénard (1900) study of a thin layer of oil heated from below. The hexagonal cell pattern is what originally interested Bénard in the convection phenomenon. Taken from Chandrasekhar (1961).

developed a hexagonal pattern. Figure 1.6 is a re-creation of the original experiment which Bénard performed (Chandrasekhar, 1961). The formation of convection rolls into cellular patterns, as observed by Bénard, motivated Lord Rayleigh to develop a mathematical model of RBC (Rayleigh, 1916).

Lord Rayleigh's original theory was a linear model of RBC which predicts the thermal conditions that cause convection to onset for a chosen horizontal wavenumber a. Such conditions are parameterised by the critical Rayleigh number Ra_c. The Ra_c value observed by Bénard differed from Lord Rayleigh's calculations due to a discrepancy between the experimental and analytic boundary conditions which did not take surface tension into consideration. This discrepancy inspired further linear models to be developed by Jeffreys (1926, 1928) and Pellow and Southwell (1940) to allow for robust boundary conditions such as no-slip and stress-free velocity. Additional experimental studies by R. J. Schmidt and Milverton (1935) were able to reproduce Bénard's results and confirm an adapted version of Lord Rayleigh's theory. The development of linear theory culminated in the canonical treatise on

RBC in Chandrasekhar (1961), which considered all aspects of convection in a plane-layer including boundary conditions, rotation, and magnetic fields.

While linear theory provides insight into the conditions and behaviours of fluids near convection onset, consideration of nonlinear terms enables investigation of time-dependent and turbulent instabilities. Early weakly nonlinear analyses by W. V. Malkus (1954b) and W. Malkus and Veronis (1958) found that the alignment of convection rolls depends on the viscosity of the fluid. The ratio between viscosity and thermal diffusion is parameterised by the Prandtl number (Pr), which is defined such that liquid metals have $Pr \ll 1$, oils have $Pr \gg 1$, and air has $Pr = 0.7$. An important result calculated from nonlinear studies is the ratio between total and conductive heat flux: the Nusselt number (Nu). This metric of heat transport allowed results from experimental data to be compared with analytical theories (W. V. Malkus, 1954a; Veronis, 1959). The relationship between Ra, Pr and heat transport was first developed in Kraichnan (1962) and continues to drive research today (see Plumley and Julien (2019)).

However, as the study of nonlinear RBC advanced, researchers sought increasingly complex solutions which became difficult, even impossible, to solve analytically. This complexity led to the development of numerical models which use algorithms to closely approximate analytic results for systems which have complex solutions, or no analytic solution at all. An early numerical model was developed by Veronis (1966) to solve nonlinear RBC in a 2D plane-layer. Despite being unable to reach a turbulent state, the Nu calculations from the numerical model agreed with experimental results. The addition of rotation to numerical models in Veronis (1968) enabled comparison with some of the extensive rotational experiments conducted in Rossby (1969).

The experiments of Rossby (1969) were among the first to incorporate rotation with convection. The images he was able to capture provide insight into the different patterns that convection cells form. An example is shown in Figure 1.7, wherein we see convective flow in a spiral form without rotation and a cellular pattern with weak rotation. Though there was some agreement between these experiments and the numerical model in Veronis (1968), there were key differences between the systems, which were attributed to the restrictions of the numerical model's 2D domain

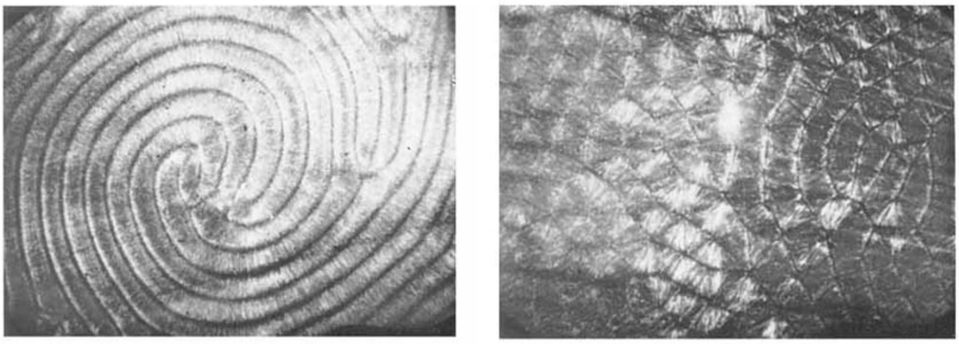

Figure 1.7: Examples of convection roll patterns in a thin layer of rotating fluid. On the left, the fluid is not rotating and on the right the fluid is weakly rotating. Taken from Rossby (1969).

in comparison to the 3D experimental setup. This conclusion illustrates two aspects of modern day convection research: the relationship between numerical and experimental results and the implications of geometry on RBC. Along with aspects of convection previously mentioned, such as boundary conditions and rotation, the geometry of convecting systems and the ability to relate numerical models to physical systems remain of interest to this day.

1.2.1 Geometry

The simplicity of a plane-layer geometry enabled the initial studies of RBC. As proven in Behringer et al. (1980), thin-layer experiments, such as those conducted by Bénard, saw some agreement with analytical and numerical solutions because a fluid layer that has a sufficiently greater width than depth will develop the same flow structures as fluid in a plane-layer. The ratio between fluid depth and width is referred to as the aspect ratio Γ, where a large aspect ratio system approaches a plane-layer and small aspect ratio domains are tall and narrow.

Despite some early agreement between numerical and experimental results, the 3D nature of astrophysical and geophysical flows motivated the consideration of alternative domain geometries. Figure 1.8 illustrates three common geometries used to study RBC. From left to right, plane-layer, cylinder, and spherical-shell geometries are shown. Note that in the spherical-shell domain, gravity acts along the radial axis, not the vertical axis as in the plane-layer and cylindrical domains.

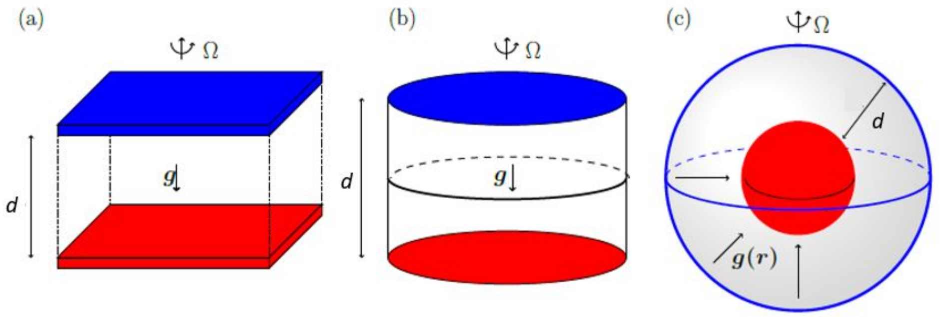

Figure 1.8: Diagrams of three common configurations used to study convection: (a) plane-layer, (b) cylindrical, and (c) spherical-shell. The red(blue) boundaries are hot(cold). The vertical length-scale of each system is d and $\boldsymbol{g}$ is the acceleration due to gravity. Rotating systems move about the vertical axis with constant angular velocity, Ω. Modified from R. S. Long (2020).

As previously mentioned in section 1.1.1, astrophysical and geophysical systems are most appropriately modelled in spherical-shell geometries. However, spherical geometries are not practical for many experimental studies due to the inherit direction of gravity on the Earth's surface. Consequently, the majority of laboratory experiments have been carried out in cylindrical cells.

The choice to model astrophysical and geophysical flows in plane-layer and cylindrical domains is often rationalised as modelling the polar regions of a planetary fluid layer. Figure 1.9 illustrates this idea, showing how a cylindrical cell may capture the dynamics of the polar region of a planetary core. Note that this region may be modelled with a cylinder because it maintains the heating from below by the inner core. This thermal condition would not necessarily be met at other regions within the spherical-shell. Furthermore, gravity and rotation act in the appropriate directions. An alternative domain which straddles experimental feasibility and application to large-scale systems is the cylindrical annulus, wherein a layer of fluid is contained between a cylinder and a narrower, nested cylinder. This geometry can be used to relate an experimental model with cylindrical annulus domain to numerical models with spherical-shell domains (Sahoo & Sreenivasan, 2017, 2020). Indeed, a common approach in the study of RBC, is to develop complementary experimental and numerical studies (Friedrich et al., 1999; Stellmach

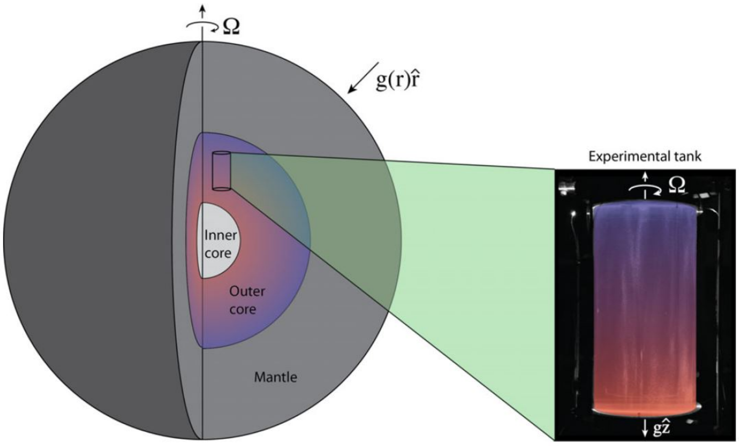

Figure 1.9: An illustration of the relationship between the spherical-shell geometry of a planetary core and the cylindrical geometry of many experimental and numerical models. Taken from J. Cheng et al. (2015).

et al., 2014; J. Cheng et al., 2015; Horn & Aurnou, 2017). For this reason, many numerical models are constrained by cylindrical domains.

The choice of domain shape and size strongly effects convection onset, transition to turbulence, and solution forms. In Koshmeider (1966) and Daya and Ecke (2001), it was shown through experimentation, that domain shape has a significant effect on the onset of convection and pattern formation. This effect is shown in Figure 1.10, which visualises the difference in flow patterns between box geometries with argon gas (Croquette, 1989) and cylindrical geometries with silicon oil (Hoard et al., 1970). Due to interactions between the fluid and domain walls, within the box geometry, convection rolls arrange themselves in parallel lines, while fluid in cylindrical geometries flow in axisymmetric convection rolls. Furthermore, the spherical-shell geometry can generate complex patterns with icosahedral symmetry (Matthews, 2003).

The aspect ratio Γ of the domain also affects the onset of convection and subsequent behaviour. Behringer et al. (1980) established that in non-rotating cylindrical geometry, behaviour after onset becomes independent of Γ when the system is 10 times wider than it is tall. As a non-rotating domain narrows, the Ra_c value increases, for any geometry, which suggests that lateral walls have a stabilising effect. However, cylindrical domains with small Γ drive stronger heat transport, quantified

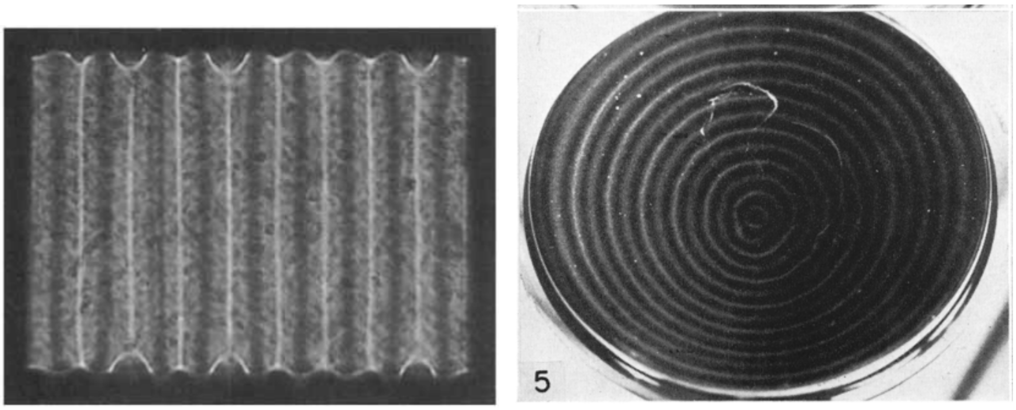

Figure 1.10: Two patterns of convection common to (left) plane-layer and (right) cylindrical geometries. Taken from Croquette (1989) and Hoard et al. (1970), respectively.

by a larger Nu, than cuboid domains of the same Γ and Ra/Ra_c (Daya & Ecke, 2001; S.-D. Huang et al., 2013; Chong & Xia, 2016; Hartmann et al., 2021). Additionally, in sufficiently narrow, cylindrical domains, convection is time-dependent at onset (Ahlers & Behringer, 1978; Behringer & Ahlers, 1982; Gao & Behringer, 1984). Moreover, the addition of rotation to RBC caused additional effects on fluid behaviours (e.g. Chandrasekhar, 1961; Buell & Catton, 1983a; Ecke et al., 2022), rotation has additional effects on RBC.

1.2.2 Rotation

Prior to the rotating convection experiments reported in Rossby (1969), G. I. Taylor paved the way for the experimental study of rotating fluids (Taylor, 1923, 1936). While Taylor did not consider convection directly, his observations of the considerable effects of rotation on fluids led, in combination with the theoretical efforts of Proudman (1916), to the development of the Taylor-Proudman Theorem. This theorem describes a rapidly rotating fluid's tendency to vary only weakly or not at all in the direction parallel to the axis of rotation. The Coriolis force is the inertial force acting on an object in a rotating frame. We often refer to the Coriolis force in reference to the effect of the Earth's rotation on geophysical flows. See Figure 1.3 which visualises the Taylor-column structure in rotating convection.

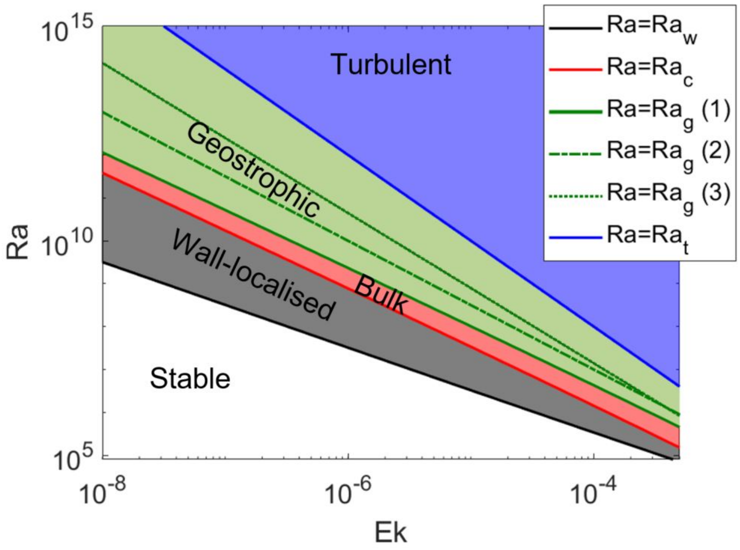

Figure 1.11: Diagram of the regimes of convection as a function of the Rayleigh number and Ekman number. As Ek decreases, rotation becomes more rapid. The transition from stable to wall-localised convection occurs at $Ra = Ra_c^w$ (black), then at $Ra = Ra_c^b$ (red) convection onsets in the bulk of the domain. At $Ra = Ra_c^g$, the geostrophic regime begins. There are conflicting predictions for the precise value of Ra_g. Three predictions are: (1) from Ecke and Niemela (2014), (2) from E. King et al. (2009), and (3) from E. King et al. (2012). Finally, for $Ra \geq Ra_t$ (blue), the flow becomes turbulent. See text for further explanation.

The effects of rotation on RBC were originally explored analytically in Chandrasekhar (1953) and experimentally in Fultz et al. (1954), the latter of which reports an initial experiment using mercury in a cylindrical container. Subsequent studies verified that for rotating fluids of $Pr < 1$ convection onset is over-stable (Y. Nakagawa & Frenzen, 1954; Fultz & Nakagawa, 1955). This inspired the study in Rossby (1969), which investigated relationships between rotation and Ra. Several metrics are used to parameterise rotation including the Ekman number– which is the ratio between viscous forces and rotational forces– and the Taylor number – which is the inverse square of the Ekman number. In this thesis, systematic variations of the Ekman number Ek are considered.

To understand the regimes of rotating convection, consider the diagram in Figure 1.11. The white space at the bottom illustrates the parameter range wherein fluids are stable and conducting with $Ra < Ra_c$. In rotating convection, where

$Ek < 10^{-3}$, convection first onsets in convection rolls localised at the lateral boundaries, often referred to as wall modes (H. F. Goldstein et al., 1993; Herrmann & Busse, 1993; H. Goldstein et al., 1994). As indicated by the black line demarcating the grey region in Figure 1.11, wall-localised convection can be approximated to onset at $Ra_c^w = \pi^2(6\sqrt{3})^{1/2}Ek^{-1}$ (Herrmann & Busse, 1993). Wall-localised convection is the subject of great interest in the study of RRBC and causes effects such as boundary-zonal flow (Ecke et al., 2022) – where the wall modes convect independently of the turbulent bulk– and robust wall states (Favier & Knobloch, 2020)– which are wall modes that persist despite irregularities in domain geometry.

Such effects are observed as Ra increases past a critical threshold for bulk convection Ra_b^c at which convective heat transport begins to affect the bulk of the fluid. It is well documented that as the rotation rate increases (a decrease in Ek), the Ra_c value increases. In Figure 1.11, the red region indicates bulk convection and begins at an estimate of $Ra_c^b = 3(\pi^2/2)^{2/3}Ek^{-4/3}$ for plane-layer RRBC (Chandrasekhar, 1961). However, as previously mentioned, this transition is greatly affected by the domain shape and size (Buell & Catton, 1983a). The form of convection in this regime is often strongly dominated by the columnar structure indicted by the Taylor–Proudman Theorem, i.e. tall thin convection rolls.

Geostrophic flow onsets as the flow structure transitions away from vertical uniformity. The precise Ra_g value at which geostrophic flow onsets is unclear. In Figure 1.11, we mark the geostrophic regime (green) from the lowest transition boundary $Ra_g = 3Ra_c^b$, shown as a solid line (Ecke & Niemela, 2014). Alternative predictions from E. King et al. (2012) (dot-dashed line) and E. King et al. (2009) (dotted line) suggest $Ra_g = 10Ek^{-3/2}$ and $Ra_g = 1.7Ek^{-7/4}$, respectively. The discrepancies between predictions for Ra_g values may be due to differences in Pr and geometry of the fluid domain. In the simplest terms, the geostrophic regime occurs when rotational and buoyant forces are balanced. This is qualitatively exhibited as a deviation from the columnar patterns dictated by the Taylor-Proudman Theorem, favouring 3D flow though maintaining small horizontal scales (Sprague et al., 2006).

The geostrophic regime is of particular interest in the geophysical and astrophysical context for which estimates of Ra and Ek values suggest a balance between buoyant and rotational forces (Aurnou et al., 2015; J. Cheng et al., 2015). Theories and models often simplify the full geostrophic theory into the quasi-geostrophic regime, wherein the force balance that characterises geostrophic flow is also affected by inertia (Charney, 1948). This regime is highly studied in the field of rotating convection (Julien et al., 2006; Kunnen et al., 2010; Smith & Stechmann, 2017; T. K. Edwards et al., 2019).

The final regime of rotating, and non-rotating, convection is turbulence, which may take different forms. Generally, the transition to turbulence can be estimated as $Ra_t = Ek^{-2}$ (Ecke et al., 2022). In this regime, flow is fully 3D and independent of rotation and consequently is often referred to as rotation-unaffected turbulence (Kunnen et al., 2016). The transition away from rotation-affected flow is indicated by a change in heat flux behaviour such that the scale between heat transport and buoyancy unifies to that of a non-rotating system (Plumley & Julien, 2019).

The study of heat transport scaling laws allow insight into convection regimes in large-scale systems. Geophysical and astrophysical systems tend to have very low Ek and high Ra which are difficult to achieve either experimentally or numerically (Kunnen et al., 2010; de Wit et al., 2020). In order to attempt to understand the behaviour of such large-scale flows, scaling laws are developed for smaller parameter ranges and used to predict behaviour of planetary-scale systems.

A common scaling metric used to measure heat transport, in rotating and non-rotating systems, is the Nusselt number Nu which is defined as the ratio between the total heat transfer and the conductive heat transfer such that a non-convecting system has $Nu = 1$. The relationship between Ra and Nu is often described by a power law such that $Nu \propto Ra^{\gamma}$, where γ is unique for each value of Ek. There is debate around the precise values of γ for any given Ek, and how the behaviour observed at modelled Ek can be used to understand systems with more extreme parameter ranges (Plumley & Julien, 2019).

For the non-rotating case, a theory of heat transport is defined in Grossmann and Lohse (2000) and Grossmann and Lohse (2002). This theory accounts for changes in Nu scaling across regimes of Ra and Pr. Despite many studies which calculate Nu in RRBC, there is no unified theory of rotating convection heat transfer (E. King et al., 2009). A compilation of notable Nu results for varying Ra and

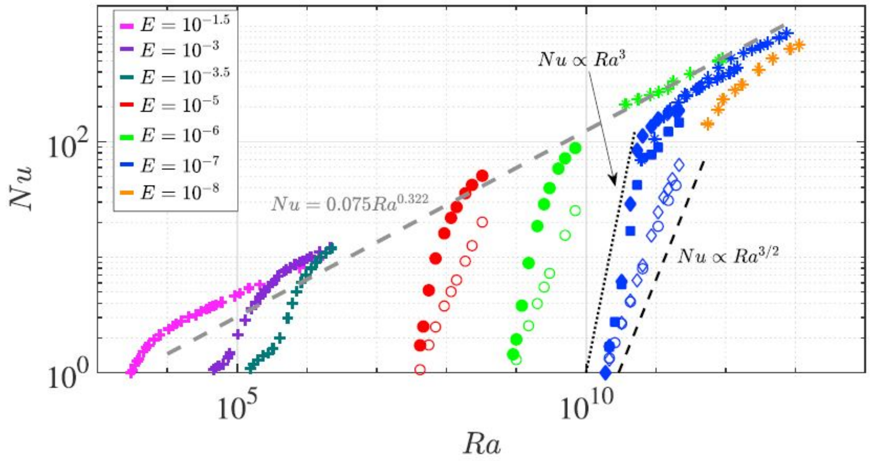

Figure 1.12: The Nusselt number results from laboratory and numerical experiments. Results are shown from Rossby (1969) (plus), J. Cheng et al. (2015) (asterisk), Plumley et al. (2016) (diamonds), and Stellmach et al. (2014) (circles). The grey line shows the non-rotating scaling while the black lines show scaling for $Ek = 10^{-7}$. Taken from Plumley and Julien (2019).

Ek is shown in Figure 1.12 for fixed $Pr = 7$ (Plumley & Julien, 2019). As shown by the grey dashed line, without rotation, it is generally reported that for $Ra \gg Ra_c$, $Nu \propto Ra^{0.322}$ (Funfschilling et al., 2005; Sun et al., 2005; J. Cheng et al., 2015). Rotating systems are observed to approach this scaling as Ra increases, as demonstrated by each coloured set of markers approaching the grey dashed line in Figure 1.12 for greater Ra values (Plumley & Julien, 2019). This corresponds with the transition to the rotating-unaffected tubulent regime.

Note in Figure 1.12, the γ values shown by filled (open) markers and dotted (dashed) black line correspond to rigid (stress-free) boundary conditions applied to the velocity. The deviation of these two power laws when only the boundary condition is varied illustrates an example of the effect that different boundary conditions have on RRBC.

1.2.3 Boundary conditions

Boundary conditions are the constraints which define the local behaviour of fluids at domain surfaces. Boundary conditions play an important role in relating RBC theory to physical fluids. In his original study, Bénard noted the necessity of a large aspect ratio domain with an open top to observe the patterns shown in Figure 1.6 (Bénard, 1900; Fauve, 2017). Moreover, it is because Rayleigh's original mathematical formulation of RBC considered free boundaries without consideration of surface tension that his results did not agree with Bénard's experiments (Rayleigh, 1916; Jeffreys, 1928). The search for sufficiently physically-appropriate boundary conditions for both experimental models and astrophysical and geophysical flows continues to inspire research (Verzicco & Sreenivasan, 2008; Calkins et al., 2015; Mound & Davies, 2017).

Boundary conditions are commonly applied on the velocity $\boldsymbol{u}$ and temperature T. Pressure p may also be constrained at the edge of the domain (Brangeon et al., 2015). In this section, common velocity boundary conditions are described followed by a discussion of thermal boundary conditions in two parts: on horizontal boundaries and on lateral boundaries.

1.2.3.1 Velocity boundary conditions

The most common velocity boundary conditions are impermeable as well as either stress-free or no-slip (Pellow & Southwell, 1940; Chandrasekhar, 1961). In a Cartesian domain, designating velocity in 3D space as $\boldsymbol{u}(x, y, z) = (u, v, w)$, impermeability forces normal flow to stop as the surface such that

$$\boldsymbol{u} \cdot \boldsymbol{n} = 0, \tag{1.1}$$

where $\boldsymbol{n}$ is a normal vector. On a horizontal boundary, Eq (1.1) requires that $w = 0$.

Stress-free conditions, also called free conditions, eliminate tangential stress at boundaries by enforcing that there is no velocity gradient parallel to the wall. Applying the impermeability condition, and again considering a horizontal boundary, the stress-free condition is defined such that

$$\frac{\partial u}{\partial z} = 0, \qquad \frac{\partial v}{\partial z} = 0. \tag{1.2}$$

If the fluid is also incompressible such that $\nabla \cdot \boldsymbol{u} = 0$, then Eq(1.2) becomes,

$$\frac{\partial^2 w}{\partial z^2} = 0 \tag{1.3}$$

at the domain walls.

However, free conditions are difficult to achieve in experimental setups which generally have walled domains. On wall or wall-like boundaries, the no-slip condition is often considered to be the more physically appropriate boundary condition (Clever & Busse, 1979; Kunnen et al., 2010). The no-slip condition, also known as the rigid condition, disallows fluid movement at the bounding surfaces by requiring that $u = v = 0$, which, with the consideration of Eq (1.1), becomes,

$$\boldsymbol{u} = 0 \tag{1.4}$$

at the horizontal boundaries.

Lord Rayleigh originally applied stress-free conditions on the upper and lower boundaries, a setup which is difficult to physically realise, but allows for easily obtained analytical solutions (Rayleigh, 1916). In an entirely stress-free bounded plane-layer, convection onsets at $Ra_c = 675.115$ with a critical wavenumber of $a_c = \pi/\sqrt{2}$ (Chandrasekhar, 1961). Alternatively, applying no-slip conditions on both boundaries necessitates either numerical solutions or asymptotic solutions (Pellow & Southwell, 1940; Prosperetti, 2012). Estimates of the onset parameters in no-slip configuration is $Ra_c = 1707.76$ and $a_c = 3.11$ (Chandrasekhar, 1961). From these linear arguments, it is clear that convection onsets at a lower thermal threshold with stress-free boundaries than with no-slip boundaries. However, with the introduction of rapid rotation to plane-layer convection, these roles reverse and stress-free boundaries have a marginally higher Ra_c than no-slip boundaries (Chandrasekhar, 1961).

Away from convection onset, velocity boundary conditions are of interest due to their effect on the development of boundary layers, which are regions of fluid flow that are strongly influenced by the boundary conditions. In Kunnen et al. (2016), a comparison of boundary layer thickness in rapidly rotating plane-layer RBC with either stress-free or no-slip boundaries revealed that stress-free boundary layers become thicker than no-slip boundary layers as Ek decreases. However, the boundary layer did not affect the transition to geostrophic flow. Because the transition to the geostrophic regime is thermally driven, the effect of velocity boundary conditions is overshadowed by thermal conditions in rotating RBC.

1.2.3.2 Thermal conditions on horizontal boundaries

As RBC is driven by a vertical temperature gradient, the thermal boundary conditions applied at the horizontal surfaces are of great interest. The most common thermal boundary conditions are known as fixed temperature (also referred to as Dirichlet or perfectly conducting) and fixed flux (also known as Neumann). The fixed temperature condition requires that the temperature be constant at each surface. Referring to the upper boundary as z_1 and lower boundary as z_0, the fixed temperature condition is defined as such,

$$T(z = z_0) = T_0, \quad T(z = z_1) = T_1 = T_0 - \Delta T, \tag{1.5}$$

where $T_{0,1}$ are constants and $\Delta T > 0$ is the temperature difference across the system. Alternatively, the fixed flux condition requires a constant heat flux at each boundary such that,

$$-\kappa \frac{\partial T}{\partial z} = q \quad \text{at} \quad z = z_0, z_1, \tag{1.6}$$

where κ is the coefficient of thermal diffusivity and q is a constant imposed heat flux. For the insulating condition, $q = 0$, i.e. no heat flux. Figure 1.13a visualises the fixed temperature condition on the left and the fixed flux condition on the right.

The fixed temperature condition was favoured in the canonical RBC text: Chandrasekhar (1961). This condition is well studied with and without rotation in cuboidal (Kunnen et al., 2016; Guzmán et al., 2021), cylindrical (Verzicco & Camussi, 2003; Kunnen, Clercx, & Geurts, 2008), and spherical-shell (Khodadadi & Zhang, 2001; Hernlund & Tackley, 2008) domains.

However, it is evident that in many instances the Dirichlet condition is not physically realistic. Particularly for astrophysical and geophysical systems where the boundaries are poorly conducting and the planet produces a relatively fixed amount of heat. In such scenarios, the fixed flux condition is more appropriate. The fixed flux condition is popular in spherical-shell geometries (e.g. Glatzmaier & Gilman, 1982; R. Long et al., 2020) for astrophysical systems and has been investigated thoroughly in infinite layers (e.g. Dowling, 1988; Ishiwatari et al., 1994; Otero et al., 2002).

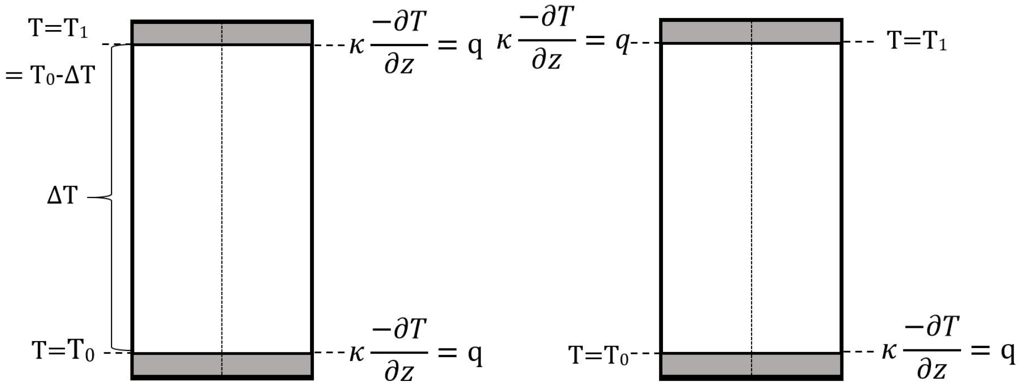

(a) Fixed temperature (left) and fixed flux (right)

(b) Two configurations of the mixed condition

Figure 1.13: Diagrams of thermal boundary conditions(from left to right): fixed temperature, fixed flux, and mixed thermal boundary conditions. Heat flux q, the coefficient of thermal diffusivity κ, T_0 and T_1 are constants and ΔT is the temperature difference across the system. The mixed condition diagram shows the two possible configurations of the mixed boundary condition.

An alternative boundary condition used in astrophysical and geophysical fluid dynamics is the mixed condition where the Dirichlet condition is applied on one boundary and Neumann condition on the other. This boundary condition has been studied in plane-layers (e.g. Ishiwatari et al., 1994; Brummell et al., 2002; Currie et al., 2020), spherical-shell (e.g. Glatzmaier & Gilman, 1982), and in cylindrical geometries (e.g. S. Huang et al., 2015; Anders et al., 2020). The mixed condition is visualised in two forms in Figure 1.13b. On the left, the bottom is fixed temperature an the top is fixed flux and on the right these roles are reversed. In astrophysical context, the latter case is more commonly used to fix the flux on the inner core of a spherical-shell and fixed the temperature on the outer boundary (e.g. Anders et al., 2020; Currie et al., 2020).

Without rotation, thermal boundary conditions affect convection onset behaviour. The fixed temperature condition onsets at higher Ra_c than the fixed flux condition, and the mixed condition has a Ra_c value between the fixed temperature and fixed flux values because fixed flux boundaries deviate from the stable linear temperature profile of conducting systems more readily than fixed temperature boundaries (Sparrow et al., 1964; Hurle et al., 1967). Further, the fixed flux boundary condition onsets to a time-dependent flow while the fixed temperature condition onsets to a time-independent state (Chapman & Proctor, 1980). Introducing rapid rotation causes the onset parameters of the fixed temperature and fixed flux configurations to converge as Ek approaches 0. However, the mixed condition has not been investigated in this limit (Calkins et al., 2015).

Away from onset, both theoretical and experimental studies have suggested that – without rotation – mixed and fixed flux systems behave similarly to fixed temperature systems when $Ra < 10^9$ because fixed flux boundaries do not strongly emit enough heat in such time-independent flows to differ from a fixed temperature boundary in a plane-layer (Otero et al., 2002) or a cylinder (Verzicco & Sreenivasan, 2008). Indeed, near onset and without rotation, solution forms of mixed configurations closely resemble fixed temperature solutions in a plane-layer (Ishiwatari et al., 1994). In a box with Ra on the order of 10^9, the fixed temperature and mixed cases behave the same in the bulk of non-rotating systems and in a limited study of rotating systems (Anders et al., 2020). In a rapidly rotating Cartesian domain– with misaligned gravity and rotation vectors– observed that with mixed boundary conditions, the aspect ratio of the domain is observed to be important in the development of zonal flows which impacts the temperature gradient (Currie et al., 2020). However, results were not compared with a complementary fixed temperature system.

Few other studies have investigated the differences between thermal boundary conditions in rapidly rotating systems. Calkins et al. (2015) used an asymptotic expansion in a plane-layer to show that in the geostrophic regime (Ra on the order of $Ek^{1/3}$) there may only be differences between fixed temperature and fixed flux configurations in the flow dynamics due to the different effects on boundary layers. In spherical-shells, fixed flux boundaries cause larger-scale convection than equivalent fixed temperature systems (Gibbons et al., 2007; Sakuraba & Roberts, 2009). While it is not clear whether fixed flux, mixed, and fixed temperature boundary conditions cause different flow forms in a rotating cylinder, papers such as Verzicco and Sreenivasan (2008) bring to our attention an additional issue: how well do these boundary conditions imitate the situation in experimental domains?

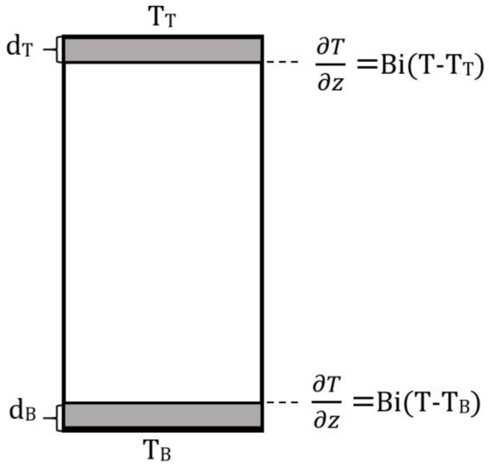

Figure 1.14: Schematic of Robin boundary conditions on horizontal boundaries. The temperature T is regulated on the boundaries by the Biot number Bi and the temperature outside of the domain at the top(bottom) T_T (T_B). The Biot number is a ratio between the thermal conductivity and height of the boundary $d_{B,T}$ and those of the fluid.

Indeed, physical systems, both experimental and natural, rarely attain either perfect conduction or insulation. Therefore it is of interest to investigate a boundary condition that straddles fixed temperature and fixed flux conditions. Early comparisons of linear RBC with fixed temperature and fixed flux considered the transition between the two as the thermal conductivity k of the boundary varied (Sparrow et al., 1964; Hurle et al., 1967; Dowling, 1988). This theory known under several names: the thin-lid approximation, Newton's cooling, or the Robin condition (Buell & Catton, 1983b; Gringé et al., 2007; Clarté et al., 2021). Herein, this condition is referred to as the Robin condition.

There are three different cases which are modelled with the Robin condition: (i) weakly conductive boundaries (Riahi, 1982), (ii) radiative-conductive boundaries (O'Sullivan, 1990; Clarté et al., 2021), and (iii) boundaries of finite thickness (Gringé et al., 2007). Case (ii) is most applicable to atmospheric systems whereas case (iii) is most useful for relating numerical models to experimental set-ups where the conductivity and thickness of the boundaries and fluids can be measured.

Considering an experimental domain, it is intuitive that a boundary which is very thin and highly conductive transfers heat from outside to the fluid very efficiently, behaving like a fixed temperature boundary. Alternatively, a boundary which is very thick or poorly conducting loses heat through the boundary, causing a more fixed flux-like effect. To determine how similarly a boundary acts to fixed temperature or fixed flux, a we consider the Biot number Bi, which is a ratio between the thermal conductivity and depth of the fluid and that of the boundary. Using $\cdot_M$ to denote boundary properties, the Biot number is defined,

$$Bi = \frac{dk_M}{d_M k}. \tag{1.7}$$

For context, an experiment described in Kunnen, Clercx, and Geurts (2008) used a layer of copper with $k_M = 400\text{W/mK}$ and $d_M = 0.03\text{m}$ to contain a layer of water with $k = 0.6\text{W/mK}$ and $d = 0.23\text{m}$. This copper boundary has a $Bi = 5 \times 10^3$.

The theoretical limits of the Robin condition are such that as Bi approaches 0, the condition becomes fixed flux and as Bi approached ∞, the condition becomes fixed temperature. Considering an experimental system such as shown in Figure 1.14, where the fluid is contained from above by a boundary of depth d_T. The temperature is constant T_T outside the domain. The Robin condition is applied at the interface of the upper boundary and the fluid such that

$$\frac{\partial T}{\partial z} = Bi\,(T - T_T)\,. \tag{1.8}$$

From this formulation, it is clear that when $Bi = 0$, the thermal flux becomes fixed. When Bi approaches ∞, the temperature of the boundary becomes the controlling term, fixing the temperature.

However, it is not necessary for Bi to reach either extreme value for a boundary to behave sufficiently similarly to the fixed flux or fixed temperature condition. In a spherical-shell, Clarté et al. (2021) reported achieving sufficiently fixed temperature-like boundary conditions with $Bi = 30$ and fixed flux-like conditions with $Bi = 0.03$, suggesting that the copper boundary we described earlier would act very closely to a fixed temperature boundary. However, we lack understanding of RRBC dynamics bounded by moderate materials with moderate Bi values.

1.2.3.3 Thermal conditions on lateral boundaries

In 3D constrained domains, conditions on the sidewalls may differ from those applied at the top and the bottom. The forms of these thermal conditions are often

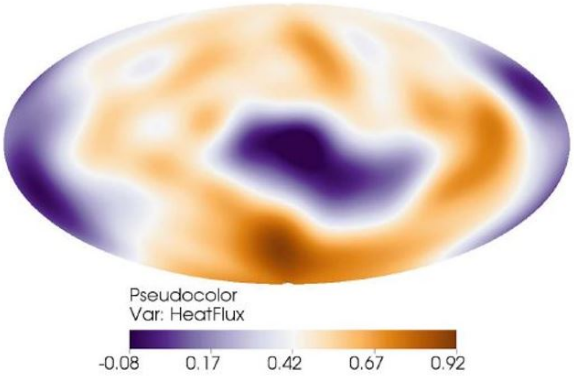

Figure 1.15: A pattern of heat flux developed from tomographic results projected on the outer boundary of a spherical-shell. Purple(orange) indicates low(high) heat flux. Taken from Mound and Davies (2017).

the same as applied on the vertical boundaries. However, the fixed temperature and fixed flux conditions are often referred to as the conducting and insulating cases, respectively, when applied to lateral boundaries.

In Charlson and Sani (1970), crucial differences between insulating and conducting sidewall boundary conditions are identified in cylindrical domains. With and without rotation, the systems with conducting sidewalls have higher Ra_c values due to the retention of linear temperature profiles to higher Ra when temperatures are fixed than when heat flux is fixed. The difference between Ra_c with conducting and insulating boundaries increases as the domain narrows (Buell & Catton, 1983b).

However, as previously discussed, heterogeneous conduction or insulation is not generally appropriate to model astrophysical and geophysical systems, such as the Earth's core. Figure 1.15 illustrates the tomographic measurements of heat flux at the Earth's CMB. Other instances of laterally varying heat flux in astrophysics include Mars (Zhong, 2009; Šrámek & Zhong, 2010), the moon (Takahashi & Tsunakawa, 2009; Oliveira & Wieczorek, 2017), and oceans (Terra-Nova et al., 2022). In the context of these astrophysical systems, numerical models have been studied with inhomogeneous insulation of spherical-shells with and without magnetic fields (Bloxham, 2000; Gibbons et al., 2007; C. J. Davies et al., 2008; Mound & Davies, 2017).

In Chung et al. (2000) and Chung and Hyun (2001), a non-rotating cylindrical domain is considered where the sidewall temperature is fixed but not uniform. The temperature is varied along both the vertical and azimuthal axes. They concluded that the heterogeneity is limited to the boundary layer of high Ra systems while the fluid on the interior of the domain was influenced only by the average of the azimuthal temperature. In agreement, in Laube et al. (2022) it was determined that, with relatively low Ra values, Nu measurements were not affected in a pipe with inhomogeneous and homogeneous insulation.

Sahoo and Sreenivasan (2020) reported an experimental investigation of lateral variation in heat flux in the azimuthal direction about a cylindrical annulus. Results for large wavelength variations in heat flux agreed with C. J. Davies et al. (2009)'s spherical-shell studies of the same variation, that small-scale convection is trapped by the heat flux variations. Larger variations in the lateral wall heat flux caused convection to onset at significantly lower Ra_c values than for homogeneous boundary conditions. In Reiter et al. (2022), a numerical model compares RBC dynamics with perfect conducting sidewalls and a varied temperature sidewall condition in a cylindrical domain. They concluded that sidewall variations had limited effect on high Ra systems and, in agreement with Sahoo and Sreenivasan (2020), found that the mean temperature was more important than the variations. At lower Ra, changes in flow structure were identified in non-rotating systems (Reiter et al., 2022).

There has been some connection suggested between inhomogeneous boundary conditions and irregular topography. In Parsons and Daly (1983), it was found that sinusoidal boundary topography with a large wavelength caused fluid behaviour to be more dependent on boundary conditions. Additionally, a transition in convective flow from large length-scale to short length-scale flow structures occurred when the wavelength of the boundary deformation was equivalent to that of the convective scale. As Ra increases, the topography of the boundary becomes unimportant (Krettenauer & Schumann, 1989). A numerical study of rapidly rotating convection by Favier and Knobloch (2020) found that a change in the domain shape did not disturb the wall-localised convection inherent to RRBC. However, it remains unclear whether or not irregular boundary shapes may have the same effect as inhomogeneous thermal boundary conditions. Overall, the role irregularities in heat flux at the core-mantle boundary play in convection is unclear and simplified numerical and experimental models can be useful to understanding these effects.

1.3 Thesis outline

This thesis is concerned with understanding the role of thermal boundary conditions in RRBC in order to improve the interpretation of numerical models in the context of physical systems. As previously discussed, a cylindrical geometry is appropriate both for experimental studies and for offering insight into the dynamics in the polar regions of astrophysical and geophysical systems (i.e. Figure 1.9). While the no-slip velocity condition is ubiquitously considered physically appropriate for rigid boundaries, it is unclear what thermal boundary condition is most appropriate. The uniformly fixed temperature boundary condition is often assumed in numerical models, but with more physically appropriate boundary conditions available, is the fixed temperature condition sufficient?

We will consider a numerical model in a cylindrical domain with thermal boundary conditions which are experimentally feasible simplifications of thermal conditions affecting astrophysical and geophysical flows. Cylindrical domains have two sets of boundaries to consider: horizontal and lateral. Therefore, it is natural to approach numerical modelling as a two-part investigation, first considering horizontal boundaries in Chapter 3 and 4 and then lateral boundaries in Chapter 5. Additionally, the motivation to relate numerical models to physical flows is reflected in an application of the numerical results to the design of an experimental model of simplified precipitation in Chapter 6. A more detailed outline is as follows.

First, the governing equations of RRBC are established in Chapter 2. The equations are made dimensionless and the appropriate parameters are defined. Next, the numerical methods for solving the system of equations are described. We use the open- source frameworks Dedalus (Burns et al., 2016) and Nek5000 (Nek5000, 2019) to solve 2D linear systems in a plane layer and a 3D nonlinear systems in a cylinder, respectively. The method of testing the nonlinear numerical setup is discussed.

In Chapter 3, we investigate common thermal boundary conditions for horizontal boundaries: fixed temperature, fixed flux, and the mixed conditions. A linear stability analysis provides insight regarding convection onset for each condition and reveals the validity of the theory established in Calkins et al. (2015): that the thermal boundary condition does not affect convection onset at low Ek. Aspects of convective flows are quantified and categorised using various metrics such as a novel approach to quantifying vertical structure which is used to indicate the transition to geostrophic flow. These metrics are applied to an array of numerical results, enabling an analysis regarding the impact of the choice of each thermal boundary condition, focusing on the rapidly rotating regime. The results provide insight into the importance of boundary condition choice for numerical models of RRBC at moderate Ra values.

In Chapter 4, we derive the Robin condition and present a numerical linear stability analysis to determine onset behaviour. A novel definition of the Rayleigh number is developed to relate Robin configurations to fixed temperature systems. The comparisons between flow properties when the model has Robin conditions rather than fixed temperature or fixed flux conditions illuminates the ability of rapidly rotating numerical models to capture physical results. The results fill an important gap in the research to better understand the influence that boundary conditions have in experimental and natural systems.

In Chapter 5, we define inhomogeneous thermal boundary conditions on the sidewalls of a rotating numerical model in two ways: Positive/Negative and Positive/Zero. In the former instance, the heat flux oscillates from positive to negative. The latter is always positive and hence more appropriate for the Earth's core and experiments. A solid steady state solution which is derived for the Positive/Negative configuration and a global heat flux accounting of the Positive/Zero configuration each provide analytical results to test the accuracy of the numerical setups. The results illustrate significant changes in wall-localised convection of rapidly rotating systems with the introduction of inhomogeneous boundary conditions, with implications on our understanding of core convection.

The results from Chapter 3 and Chapter 4 are applied in Chapter 6 to an experimental design. Recent numerical developments in simplified precipitation–

i.e. Hernadez-Duenas et al. (2012) and T. K. Edwards et al. (2019) – motivate a rapidly rotating experiment in a cylindrical domain with two-phase precipitation. Each experimental specification is determined to ensure a practical and observable experiment. Finally, Chapter 7 provides a summary of the thesis and discusses future directions for this work.

Chapter 2

Technical Introduction

In the previous chapter, we discussed the ubiquity of Rayleigh–Bénard convection (RBC) in nature and the advancements that have been made toward understanding this thermal phenomenon. After describing the important role thermal boundary conditions play in the relationship between numerical models and physical systems, we outlined a set of aims to further explore thermal boundary conditions in rotating RBC (RRBC).

This thesis is motivated to improve the understanding of astrophysical and geophysical flows by investigating the role of physically realisable boundary conditions via numerical rotating RBC. Though large-scale systems are appropriately modelled in a spherical-shell, experimental setups most commonly have cylindrical geometry. Additionally, previous studies have established the application of cylindrical domains in modelling dynamics in the polar regions of spherical-shells (see Figure 1.9). Hence, we consider a cylindrical layer of air-like fluid with $Pr = 0.7$ to be both experimentally feasible and to model an atmospheric system. The domain is illustrated in Figure 2.1. A Cartesian coordinate system is used with horizontal axes $\hat{\boldsymbol{x}}$ and $\hat{\boldsymbol{y}}$, though we also employ cylindrical coordinate system with radial axis $\hat{\boldsymbol{r}}$, azimuthal axis $\hat{\boldsymbol{\theta}}$. The vertical axis is always $\hat{\boldsymbol{z}}$. The aspect ratio of the domain is $\Gamma = R/d = 0.7$ which relates the radius R to the height $d = z_1 - z_0$ and is chosen to maximise Ra_t, the Rayleigh number at which a system transitions to turbulence unaffected by rotation. Gravity $\boldsymbol{g} = -g\hat{\boldsymbol{z}}$ acts downward and the domain rotates with angular velocity $\boldsymbol{\Omega}$. The temperature is T_0 at the lower domain and decreases by ΔT across the system to T_1 at the upper boundary.

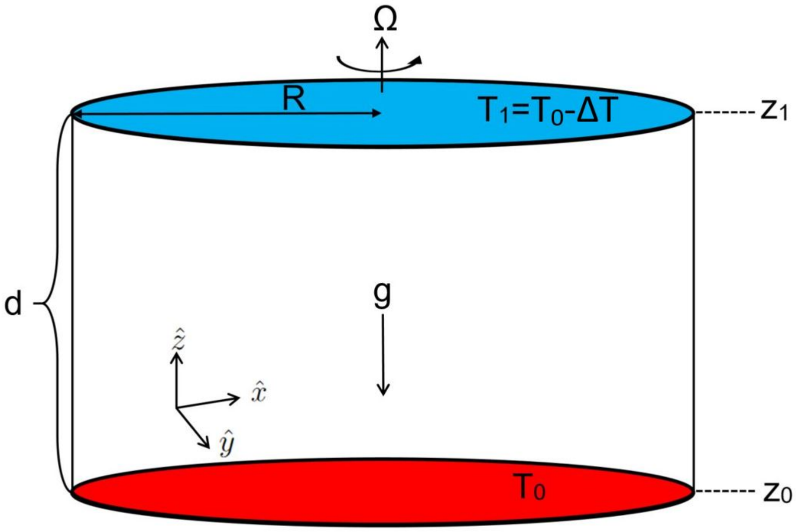

Figure 2.1: Schematic of the cylindrical domain with Cartesian coordinates (x, y, z) and aspect ratio $\Gamma = R/d = 0.7$ where R is the radius and $d = z_1 - z_0$ is the height of the domain. The gravitational acceleration $\boldsymbol{g}$ acts downward and the domain rotates with angular velocity $\boldsymbol{\Omega}$ about $\hat{z}$. The lower boundary has temperature T_0 and upper boundary has temperature $T_1 = T_0 - \Delta T$ where $\Delta T > 0$ is the temperature difference across the system.

In this chapter, the methods of modelling this RRBC system are described. First, the equations of motion and parameter ranges used in this thesis are presented. Then, the numerical methods of solving the governing equations are discussed. Finally, the nonlinear numerical setup is tested for accuracy.

2.1 Governing equations

The equations of motion governing RBC have been thoroughly described in a number of canonical texts including Chandrasekhar (1961) and Batchelor (2000). RBC is mathematically defined by a system comprised of momentum, continuity, and temperature equations.

We first consider the momentum equation which is derived from the Navier-Stokes equations. As in Chandrasekhar (1961), the equation is written such that

$$\rho \frac{D\boldsymbol{u}}{Dt} = \rho \boldsymbol{F} - \nabla p + \mu \nabla^2 \boldsymbol{u}, \tag{2.1}$$

where

$$\frac{D}{Dt} = \frac{\partial}{\partial t} + \boldsymbol{u} \cdot \nabla \tag{2.2}$$

is the Lagrangian derivative with respect to time t. The fluid has a dynamic viscosity μ, taken here to be constant, and variables: velocity $\boldsymbol{u}$, density ρ, and pressure p. All external accelerations acting on the fluid, which, in RRBC, are the buoyant and rotation-caused forces, are contained in $\boldsymbol{F}$. In convection, the buoyant force $\boldsymbol{F_b}$ is the interaction between density and gravity such that

$$\boldsymbol{F_b} = \boldsymbol{g} \tag{2.3}$$

where $\boldsymbol{g}$ is the gravity vector. The rotational term has two parts: the Coriolis acceleration and centrifugal force which act, respectively, perpendicular to and away from the axis of rotation. Combining these terms, and considering a rotating frame, the force due to rotation can be written as

$$\boldsymbol{F_r} = -2\boldsymbol{\Omega} \times \boldsymbol{u} - \frac{1}{2}\nabla|\boldsymbol{\Omega} \times \boldsymbol{X}|^2, \tag{2.4}$$

where $\boldsymbol{\Omega}$ is angular velocity and $\boldsymbol{X}$ is the position vector.

An essential element of the common RBC model is the Boussinesq approximation which affects the treatment of density. The Boussinesq approximation assumes that the fluid velocity is sufficiently slower than the speed of sound, and that the fluid depth is sufficiently smaller than the hydrostatic scale heights of pressure, density, and temperature (Spiegel & Veronis, 1960). Further, in the Boussinesq approximation, it is assumed that variations in density are not driven by pressure. Consequently, the equation of state is approximated as

$$\rho = \rho_0(1 - \alpha(T - T_0)), \tag{2.5}$$

where ρ_0 is the reference density and α is the coefficient of thermal expansion. The temperature is T with reference temperature T_0 which is taken to be the temperature at the lower boundary. Under these assumptions, the density is taken as constant for inertial terms, hence excluding buoyancy wherein density variation allows for the rise and fall of fluids with heating and cooling.

Applying the Boussinesq approximation and substituting Eqs (2.3) and (2.4) into Eq (2.1), we write the momentum equation for RRBC as such

$$\frac{D\boldsymbol{u}}{Dt} + 2\boldsymbol{\Omega} \times \boldsymbol{u} = \frac{\rho}{\rho_0}\boldsymbol{g} - \frac{1}{\rho_0}\nabla P^* + \nu\nabla^2\boldsymbol{u}, \tag{2.6}$$

where $\nu = \mu/\rho$ is the kinematic viscosity and P^* is a reduced pressure that includes the centrifugal force term. Applying Eq (2.5) to Eq (2.6), the momentum equation becomes

$$\frac{D\boldsymbol{u}}{Dt} + 2\boldsymbol{\Omega} \times \boldsymbol{u} = \alpha\left(T - T_0\right) g\hat{z} - \frac{1}{\rho_0}\nabla P + \nu\nabla^2\boldsymbol{u}. \tag{2.7}$$

Note that pressure P is a modified pressure which has absorbed both the centrifugal force and the pressure basic state from the Boussinesq approximation such that

$$P = p - \frac{\rho_0}{2}|\boldsymbol{\Omega} \times \boldsymbol{X}|^2 + \rho_0 g z. \tag{2.8}$$

We next consider the continuity of mass and by applying the Boussinesq approximation (i.e. assuming a fluid of constant density), obtain the incompressibility condition

$$\nabla \cdot \boldsymbol{u} = 0. \tag{2.9}$$

Finally, an equation of temperature is necessary. Assuming a simple energy conservation law with no internal heating the expression is

$$\frac{DT}{Dt} = \kappa\nabla^2 T, \tag{2.10}$$

where κ is the coefficient of thermal diffusivity (Chandrasekhar, 1961). Note $\kappa = k/\rho_0 c_p$, taken as constant, is a function of thermal conductivity k and specific heat c_p.

Thus, Eqs (2.7), (2.9), and (2.10) comprise the governing equations for RRBC. Table 2.1 summarises the fluid properties and corresponding SI units introduced in the governing equations. Dimensional analysis is performed to simplify the comparison between physical and dimensionless systems.

2.1.1 Dimensional analysis

Non-dimensionalisation allows for comparisons between different fluid systems and simplifies calculations. In order to make the governing equations dimensionless,

Property	Symbol	SI Units
Position	$\boldsymbol{X} = (x, y, z)$	m
Height	d	m
Radius	R	m
Time	t	s
Velocity	$\boldsymbol{u} = (u, v, w)$	$\frac{\mathrm{m}}{\mathrm{s}}$
Density	ρ	$\frac{\mathrm{kg}}{\mathrm{m}^3}$
Pressure	p	$\frac{\mathrm{kg}}{\mathrm{ms}^2}$
Temperature	T	K
Angular velocity	$\boldsymbol{\Omega}$	Hz
Gravity	g	$\frac{\mathrm{m}}{\mathrm{s}^2}$
Coefficient of thermal expansion	α	$\frac{1}{\mathrm{K}}$
Dynamic viscosity	μ	$\frac{\mathrm{kg}}{\mathrm{ms}}$
Kinematic viscosity	ν	$\frac{\mathrm{m}^2}{\mathrm{s}}$
Coefficient of thermal diffusivity	κ	$\frac{\mathrm{m}^2}{\mathrm{s}}$
Thermal conductivity	k	$\frac{\mathrm{W}}{\mathrm{mK}}$
Specific heat	c_p	$\frac{\mathrm{J}}{\mathrm{kgK}}$

Table 2.1: List of fluid properties relevant to rotating RBC and the appropriate SI units. Note Cartesian coordinates are indicated in this table, though cylindrical coordinates $\boldsymbol{X} = (\theta, r, z)$ are also used where θ is the azimuthal angle and r is the radius. Hence velocity may also be considered to be $\boldsymbol{u} = (u_\theta, u_r, w)$.

scaling terms for each variable are applied. Generally, in convective systems, where vertical motion is of interest, the vertical characteristic length is used that $\tilde{\boldsymbol{x}} = d\boldsymbol{x}$, where d is the height of the system. Note that herein we designate variables with tildes as dimensional and therefore dimensionless variables do not have tildes. Constants are generally dimensional, but for the sake of readability do not have tildes. The appropriate temperature scaling is related to the thermal behaviour at the boundaries of the system. We discuss thermal scaling factors in more depth in Chapter 3. For simplicity, in this chapter, we apply the temperature difference timescale such that $\tilde{T} = \Delta\tilde{T}T + T_0$. Table 2.2 lists the common temporal scales for RBC, their dimensional definitions, and the corresponding velocity, and pressure scaling factors (Kunnen, Clercx, & Geurts, 2008; Calkins et al., 2015; Mound & Davies, 2017; Clarté et al., 2021).

timescale	$\tilde{t}$	$\tilde{\boldsymbol{x}}$	$\tilde{\boldsymbol{u}}$	$\tilde{P}$
thermal diffusion	$\frac{d^2}{\kappa}t$	$d\boldsymbol{x}$	$\frac{\kappa}{d}\boldsymbol{u}$	$\rho_0\frac{\kappa^2}{d^2}P$
viscous diffusion	$\frac{d^2}{\nu}t$	$d\boldsymbol{x}$	$\frac{\nu}{d}\boldsymbol{u}$	$\rho_0\frac{\nu^2}{d^2}P$
rotation	$\frac{1}{2\Omega}t$	$d\boldsymbol{x}$	$2d\Omega\boldsymbol{u}$	$4\rho_0\Omega^2 d^2 P$
free-fall velocity	$\sqrt{\frac{d}{g\alpha\Delta\tilde{T}}}t$	$d\boldsymbol{x}$	$\sqrt{g\alpha\Delta\tilde{T}d}\boldsymbol{u}$	$\rho_0 g\alpha\Delta\tilde{T}dP$

Table 2.2: List of characteristic time scales and their related length $\boldsymbol{x}$, velocity $\boldsymbol{u}$, and modified pressure P, scales. The tilded variables are dimensional. d is the system height, $\Delta\tilde{T}$ is the temperature difference between the top and bottom of the domain, and ρ_0 is the reference density. The temperature is here scaled appropriately for fixed temperature boundaries such that $\tilde{T} = \Delta\tilde{T}T + T_0$.

As this thesis considers both rotating and non-rotating systems and a system of air, which is not highly viscous, the thermal diffusion time scale is considered (J. Cheng et al., 2015). We define the non-dimensional measurements of our domain such that at the lower (upper) boundary, $z = -0.5$ ($z = 0.5$) and the radius is 0.7 to satisfy $\Gamma = 0.7$. We apply the thermal diffusion time scale, vertical height length scale, and temperature difference thermal scale to Eqs (2.7), (2.9), and (2.10), obtaining

$$\frac{D\boldsymbol{u}}{Dt} + \frac{Pr}{Ek}\hat{\boldsymbol{z}} \times \boldsymbol{u} = RaPrT\hat{\boldsymbol{z}} - \nabla P + Pr\nabla^2\boldsymbol{u}, \tag{2.11a}$$

$$\nabla \cdot \boldsymbol{u} = 0, \tag{2.11b}$$

$$\frac{DT}{Dt} = \nabla^2 T. \tag{2.11c}$$

Several non-dimensional parameters are introduced into the governing equations: the Prandtl number Pr, the Ekman number Ek, and the Rayleigh number Ra.

The Prandtl number is a ratio between the viscous and thermal diffusion time scales such that,

$$Pr = \frac{\nu}{\kappa}. \tag{2.12}$$

Liquid metals, such as those in the Earth's core, tend to have $Pr \ll 1$, while silicon oils have $Pr \gg 1$ (Schmalzl et al., 2002). The value of Pr can inform the choice of temporal scale. When $Pr > 1$, viscous diffusion is more important in convection, whereas when $Pr < 1$ thermal diffusion is dominant. Consequently, the viscous diffusion timescale is preferred for high-Pr models while the thermal diffusion time scale is preferred for low-Pr models. This thesis considers air as the working fluid for which $Pr = 0.7 < 1$, and therefore the thermal diffusion timescale is appropriate.

The Ekman number, Ek, is a parameter relevant to rotating systems. Defined as,

$$Ek = \frac{\nu}{2\Omega d^2}, \tag{2.13}$$

the Ekman number is the ratio between vicious and Coriolis forces. Without rotation, $Ek = \infty$ and a rotation increases Ek decreases. The Ek values of planets tend to be low. For example, the Earth is estimated to have $Ek = 10^{-15}$ (Schubert & Soderlund, 2011) due to a kinematic viscosity on the order of $10^{-7}\mathrm{m}^2/\mathrm{s}$, thickness on the order of $10^6\mathrm{m}$, and angular velocity on the order of $10^{-5}\mathrm{Hz}$ (Jones & Schubert, 2015). However, $Ek = 10^{-15}$ is not currently able to be modelled either numerically or experimentally.

The Rayleigh number, Ra, is the ratio of the destabilising effects of buoyancy to the stabilising effects of the diffusion of momentum and heat (Jeffreys, 1928; R. J. Schmidt & Milverton, 1935). We defined the Rayleigh number such that,

$$Ra = \frac{\alpha g \Delta\tilde{T} d^3}{\nu\kappa}, \tag{2.14}$$

where $\Delta\tilde{T}$ is related to the characteristic temperature scaling. The thermal scale is dependent on thermal boundary conditions, and as such will be modified throughout this thesis to accommodate the different conditions. Ra is used to parameterise the strength of convective (buoyant) forcing relative to dissipation.

Rotating convection is often considered in two regimes: weakly rotating and rapidly rotating. To determine these two categories, it is useful to consider the convective Rossby number $Ro = \sqrt{Ek^2 Ra/Pr}$, which is the ratio inertial forces to Coriolis forces. Rapidly rotating systems have $Ro << 1$. Here, we define rapidly rotating as $Ro \leq 0.3$. Due to the range of Ra values and fixed Pr value considered in this thesis, we are able to approximate the weakly and rapidly rotating regimes with Ek values such that $\infty > Ek > 10^{-4}$ is weakly rotating and $Ek \leq 10^{-4}$ is rapidly rotating.

2.1.2 Boundary conditions

In order to solve the governing equations described in Eqs (2.11a)-(2.11c), a set of boundary conditions must be developed to constrain fluid behaviour at the edges of the domain. As discussed in section 1.2.3, boundary conditions are most commonly applied to fluid velocity and temperature. The most physically appropriate velocity boundary condition for rigid walls, as in an experiment, is the no-slip condition. Therefore, we choose to apply the no-slip condition on all surfaces. By modifying Eq (1.4), the no-slip condition requires,

$$\boldsymbol{u} = 0 \qquad \text{at} \qquad z = -0.5 \quad \text{and} \quad 0.5 \qquad \text{and} \quad \text{at} \qquad r = 0.7, \tag{2.15}$$

where r is the radial direction in cylindrical coordinates defined as $r = \sqrt{x^2 + y^2}$.

As the focus of this thesis is on the role of thermal boundary conditions in RBC, the relevant conditions in each chapter are defined separately. However, for the sake of completeness in this chapter, we consider the fixed temperature boundary condition on the horizontal surfaces and an uniformly insulating sidewall. The fixed temperature condition is non-dimensionalised from Eq (1.5) and as such is defined as

$$T = 1 \qquad \text{at} \quad z = -0.5 \qquad \text{and} \qquad T = 0 \qquad \text{at} \quad z = 0.5, \tag{2.16}$$

such that the dimensionless temperature difference across the system is $\Delta T = 1$.

On the sidewalls, an insulating condition is defined such that the heat flux is fixed at zero. Therefore, we require that

$$\frac{\partial T}{\partial r} = 0 \qquad \text{at} \quad r = 0.7. \tag{2.17}$$

2.1.3 Linear analysis

To begin our linear analysis, we consider the full, nondimensional governing equations Eqs (2.11a)-(2.11c) and perturb them about a steady, static basic state such that each variable is defined as a sum of the basic state $\cdot_B$ and the perturbation $\cdot_p$ in the form $\boldsymbol{u} = \boldsymbol{u_p} + \boldsymbol{u_B}$. See Appendix A for the full derivation. The resulting equations are

$$\frac{D\boldsymbol{u}_p}{Dt} + \frac{Pr}{Ek}\hat{\boldsymbol{z}} \times \boldsymbol{u}_p = -\nabla P_p + RaPrT_p\hat{\boldsymbol{z}} + Pr\nabla^2\boldsymbol{u}_p, \tag{2.18a}$$

$$\nabla \cdot \boldsymbol{u}_p = 0, \tag{2.18b}$$

$$\frac{DT_p}{Dt} - w = \nabla^2 T_p. \tag{2.18c}$$

We remove the nonlinear terms, obtaining the linear governing equations:

$$\frac{\partial\boldsymbol{u}_p}{\partial t} + \frac{Pr}{Ek}\hat{\boldsymbol{z}} \times \boldsymbol{u}_p = -\nabla P_p + RaPrT_p\hat{\boldsymbol{z}} + Pr\nabla^2\boldsymbol{u}_p, \tag{2.19a}$$

$$\nabla \cdot \boldsymbol{u}_p = 0, \tag{2.19b}$$

$$\frac{\partial T_p}{\partial t} - w = \nabla^2 T_p. \tag{2.19c}$$

To derive a solution, we begin by twice taking the curl of Eq (2.19a). We find

$$\frac{\partial \nabla^2 \boldsymbol{u_p}}{\partial t} + \frac{Pr}{Ek}\nabla \times (\hat{z} \cdot \nabla \boldsymbol{u}_p) = RaPr\left(\nabla^2 T_p \hat{z} - \frac{\partial \nabla T_p}{\partial z}\right) + Pr\nabla^4 \boldsymbol{u}_p. \tag{2.20}$$

The vertical components of Eq (2.20) and Eq (2.19c) are

$$\left(\frac{\partial}{\partial t} - Pr\nabla^2\right)\nabla^2 w_p = RaPr\nabla_H^2 T_p - \frac{Pr}{EK}\frac{\partial \omega_z}{\partial z}, \tag{2.21}$$

and

$$\left(\frac{\partial}{\partial t} - Pr\nabla^2\right)\omega_z = \frac{Pr}{Ek}\frac{\partial w}{\partial z}, \tag{2.22}$$

where $\boldsymbol{\omega} = \nabla \times \boldsymbol{u_p}$ is the vorticity.

Using these equations and the linear temperature equation Eq (2.19c), the vertical velocity is isolated such that

$$\left(\frac{\partial}{\partial t} - Pr\nabla^2\right)^2 \left(\frac{\partial}{\partial t} - \nabla^2\right) \nabla^2 w_p = RaPr\left(\frac{\partial}{\partial t} - Pr\nabla^2\right)\nabla_H^2 w - \frac{Pr^2}{Ek^2}\left(\frac{\partial}{\partial t} - \nabla^2\right)\frac{\partial^2 w}{\partial z^2}. \quad (2.23)$$

At this stage, boundary conditions are applied to determine an ansatz solution against which to solve. However, we wish to retain generality such that each of the proposed vertical boundary conditions – fixed temperature, fixed flux, mixed, and Robin – may be applied. Thus, we suggest an ansatz solution for normal modes of the form

$$w = \hat{w}(z) f(x, y) e^{i\omega t}, \quad (2.24)$$

where $\hat{w}(z)$ satisfies the conditions on boundaries in the vertical and $f(x, y)$, – or in cylindrical coordinate $f(r, \theta)$– a function of horizontal position, satisfies lateral conditions. Hence, we may solve the linear governing equations numerically as an eigenvalue problem where ω is our eigenvalue.

2.2 Numerical methods

Solving the RRBC equations of motion, Eqs (2.11a-2.11c), often necessitates numerical methods of integration. There are many numerical methods including finite-volume, finite-difference, finite-element, spectral-element, and spectral. These methods vary in speed, computational expense and ability to solve RRBC dynamics within diverse domain shapes. We chose to apply the spectral method for solving linear systems and the spectral-element method for solving nonlinear systems, respectively employing the open source frameworks Dedalus (Burns et al., 2016) and Nek5000 (Nek5000, 2019).

2.2.1 Dedalus

Dedalus is a spectral method solver developed for and by researchers studying fluid dynamics (Burns et al., 2016). The spectral method represents a solution across the domain as a sum of basis functions. Due to the global nature of the method, the boundary conditions and domain shape constrain the choice of basis function. The spectral method is regarded as having greater accuracy than the finite element method for the same computational expense.

We chose to employ Dedalus due to its optimised performance and ability to run in parallel processes. Dedalus is used to perform linear stability analysis by solving Eqs (2.19a)- (2.19c) as an eigenvalue problem. Note because Dedalus is limited in the number of dimensions which can be solved with Chebyshev basis functions, it does not support cylindrical domains. Due to this limitation, along with the complexity of solving the linear problem in a cylindrical domain (K. Zhang & Liao, 2009), we solve linear RRBC systems in a 1D plane-layer with 64 Chebyshev nodes in the vertical domain. The maximum growth rate of eigenvalue ω is determined assuming an ansatz solution as in Eq (2.24). The results presented in Chapter 3 provide validation of the numerical model by comparison of Ra_c values with previous asymptotic results for fixed temperature and fixed flux boundary systems from Calkins et al. (2015). In order to overcome the geometric limitations of Dedalus, we choose to use a spectral-element solver to study nonlinear RRBC systems.

2.2.2 Nek5000

For nonlinear 3D numerical models, a spectral-element method solver is more appropriate to accommodate a cylindrical domain. The spectral-element method is an extension of the finite element method where piece-wise high-order polynomials serve as basis functions. Such basis functions are often either Chebyshev or Lagrange polynomials. An advantage of the spectral-element method is ease in mesh generation and ability to solve in irregular geometries. Additionally, by increasing the polynomial order, spatial refinement is possible without generating a new mesh. Furthermore, it is easy to implement different boundary conditions with the spectral-element method. However, the spectral-element method is computationally expensive to run and therefore limits the parameter range of RRBC which we are able to model.

Nek5000 is a spectral-element method solver which uses Legendre polynomials as basis functions for velocity and pressure solutions (Nek5000, 2019). The so-

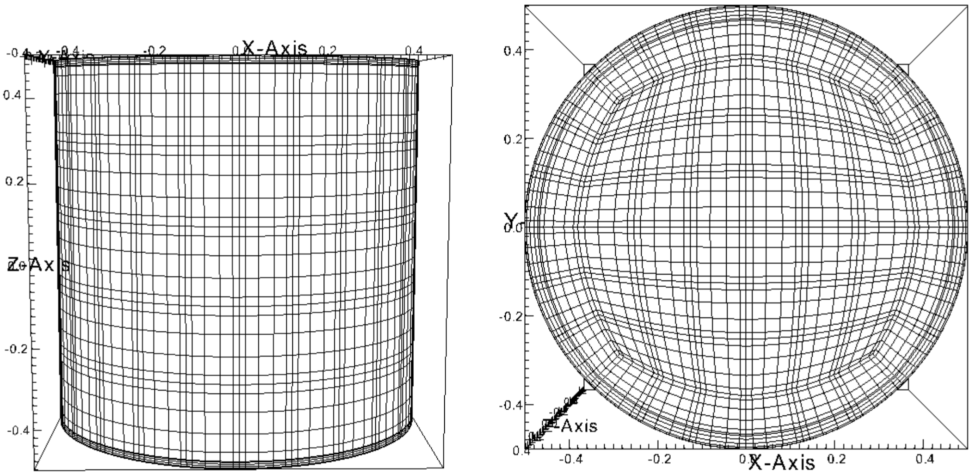

(a) Side view

(b) Top view

Figure 2.2: Side and top views of the 588-element mesh. There is a denser arrangement of elements near the walls.

lutions are found using the PnPn-2 method where pressure is solved without the boundary points. This is capable of solving on has high-order curved domains, suitable for cylindrical geometries, as well as optimised parallel processing. We employ Nek5000 to solve the nonlinear model defined in Eq (2.11a-2.11c) in a cylindrical domain with a third-order Adams-Bashforth multi-step scheme. We use two resolutions: 588 elements and 4704 elements. The smaller mesh is sufficient for simple flows at moderate Ra values while the larger mesh is necessary for rapidly rotating and time-dependent systems. The smaller mesh is shown in Figure 2.2 from the side and the top. The meshes have refined spatial distribution near the walls to ensure wall-localised convection can evolve in rotating systems. A minimum polynomial order of six is used, increasing as systems become more temporally chaotic. In this thesis, the time-step is $\Delta t = 2 \times 10^{-4}$ for non-rotating systems and decreased to $\Delta t = 5 \times 10^{-6}$ to accommodate a minimum Ekman number of $Ek = 10^{-5}$. We consider $Ra < 10^{9}$. The initial conditions of the model are a linear, conductive background temperature gradient with small, random perturbations to a zero velocity state.

2.2.2.1 Test of convergence

It is necessary to ensure the convergence of numerical models to confirm that the spatial and temporal domains are sufficiently refined (Stevens et al., 2010).

Due to the chaotic nature of convection at high Ra, time-averaging is necessary for the measurement of convergence criteria. Averaged quantities are identified by an overbar $\bar{\cdot}$ and defined such that

$$\overline{f} = \frac{1}{\Delta t} \int_{t_0}^{t_0+\Delta t} f \mathrm{d}t, \tag{2.25}$$

where t_0 is some time after a statistically steady state has been established.

The mean kinetic energy balance is used as a criteria of convergence. Following Hepworth (2014), the kinetic energy balance is derived in Appendix B. Hence, the conservation of energy requires that

$$\int_V Ra\overline{Tw} + \overline{(\nabla \times \boldsymbol{u})^2}\mathrm{d}V = 0, \tag{2.26}$$

where V is the volume of the domain. The first term of Eq (2.26) is the buoyant energy and the second term is the viscous dissipation. A relative error percentage between the two quantities is calculated as such

$$err = 100\% \frac{< Ra\overline{Tw} >_V - < \overline{(\nabla \times \boldsymbol{u})^2} >_V}{< Ra\overline{Tw} >_V}, \tag{2.27}$$

where $< \cdot >_V$ is a volume average. As in E. King et al. (2012), we consider an $err \leq 1\%$ to indicate sufficient resolution of the model.

Figure 2.3 illustrates an example of the mean kinetic energy balance for the fixed temperature model with uniformly insulated sidewalls. The err percentage is plotted against the supercriticality $Ra_{sc} = Ra/Ra_c$ which indicates how far from convection onset a system is. Simulations with Ek values ∞ (non-rotating), 10^{-2}, 10^{-3}, 10^{-4}, and 10^{-5} are respectively indicated by marker shapes. Note that the simulations represented in Figure 2.3 have varying resolutions in both time and space, spanning the range of resolutions used in this thesis. It is clear that as Ra_{sc} increases, err approaches 1%, but remain below 1% for the parameter range considered in this thesis. The mean kinetic energy balance is performed for each boundary condition considered in this thesis to ensure sufficient resolution.

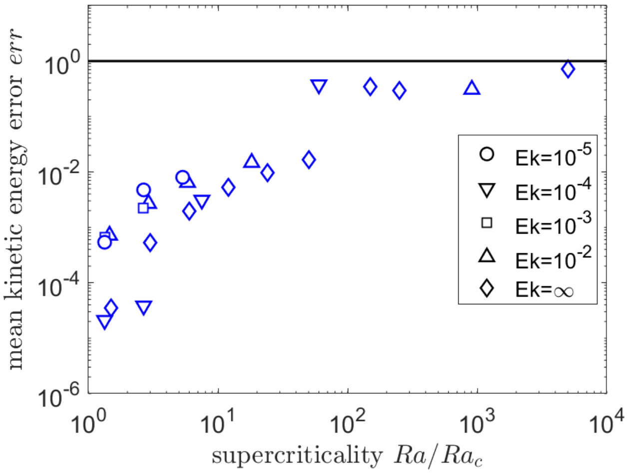

Figure 2.3: An example of the mean kinetic energy error err vs. the supercriticality $Ra_{sc} = Ra/Ra_c$. The fixed temperature condition is applied on the vertical boundaries and there is uniform insulation on the sidewalls. Each marker indicates results with a different Ek values.

2.3 Summary

In this chapter, the technical aspects of our investigation of RRBC have been discussed. The proposed cylindrical domain and corresponding properties were visualised in Figure 2.1. The aspect ratio is $\Gamma = 0.7$ and, in order to represent an air-like fluid, $Pr = 0.7$ is used– both values are constant throughout this thesis.

The governing equations of RRBC were defined and nondimensionalised in Eq (2.11a)-(2.11c). Relevant non-dimensional parameters Pr, Ek, and Ra were defined in Eqs (2.12), (2.13) and (2.14), respectively. In this thesis, rotation is varied from $Ek = \infty$ to $Ek \geq 10^{-5}$ with $Ra \leq 10^9$. With fixed $Pr = 0.7$, these ranges span from non-rotating with $Ro = \infty$ to rapidly rotating with $Ro \leq 0.3$. In order to consider convection onset behaviour where $Ra = Ra_c$, the governing equations were linearised in Eqs (2.19a)- (2.19c).

The linear and nonlinear equations are solved using open-source frameworks Dedalus (Burns et al., 2016) and Nek5000 (Nek5000, 2019), respectively. The resolution of the nonlinear model was tested using a mean kinetic energy balance error err, as defined in Eq (2.27). When $err \leq 1\%$, we consider the system sufficiently resolved (E. King et al., 2012). Figure 2.3 illustrates an example of the

err measurements for a fixed temperature model. For each boundary condition, the unique numerical setup is confirmed to be adequately resolved with the same method.

The governing equations are paired with a set of boundary conditions described specifically in each chapter and solved using the methods we have discussed. The fixed temperature, fixed flux, and mixed vertical thermal boundary conditions are applied in Chapter 3 for both the linear and nonlinear systems.

Chapter 3

Fixed Temperature and Fixed Flux Thermal Boundary Conditions

Chapter 2 provided a mathematical and numerical framework for the exploration of rotating Rayleigh-Bénard convection (RRBC). The Boussinesq approximation was applied to the Navier–Stokes momentum equation with an incompressibility condition and all equations were nondimensionalised with thermal diffusion time, the system height d as the length scale, and the temperature drop across the system $\Delta\tilde{T}$ for thermal scaling, resulting in Eqs (2.11a-2.11c). Numerical solvers Dedalus (Burns et al., 2016) and Nek5000 (Nek5000, 2019) were introduced for solving linear and non-linear systems, respectively. In this chapter, the consequences of applying different thermal boundary conditions to the top and bottom of an RRBC system are investigated.

3.1 Introduction

The boundaries of a domain impose behavioural conditions on the fluid, dependent on either material characteristics of the physical domain or mathematical conditions imposed on a numerical domain. Numerical boundary conditions are often chosen to best imitate physical conditions. It is well-agreed that no-slip velocity conditions are experimentally and physically appropriate (Chandrasekhar, 1961). However, physically appropriate thermal boundary conditions are less easily defined. There are limited methods for controlling the boundary conditions of experiments (e.g. choice of wall material, wall thickness, or external heating/cooling) whereas numerical studies allow for the prescription of mathematical boundary conditions. Therefore, numerical studies are better suited than experiments to exploring the differences in fluid behaviour between thermal boundary conditions.

In traditional RRBC, the heat difference between the top and the bottom of the system drives a flow (Chandrasekhar, 1961). Therefore, it is apparent that the thermal conditions applied at the top and bottom of the domain are of importance to the overall understanding of RRBC. In geophysically and astrophysically motivated numerical RRBC models, commonly applied thermal boundary conditions include fixed temperature, fixed flux and a mixed condition, where a fixed temperature is applied at the bottom and fixed flux at the top of the domain.

The investigation begins by defining the three most common thermal boundary conditions applied in numerical RBC and RRBC. It is common to fix the temperature at the upper and lower boundaries . While the fixed temperature condition can be realistic in experimental studies, where temperature is precisely controlled (Ouertatani et al., 2008; Verzicco & Sreenivasan, 2008; Kunnen et al., 2010), it often does not approximate large-scale systems well. Therefore, many astrophysical systems are numerically modelled with either mixed or fixed temperature conditions (e.g. Glatzmaier & Gilman, 1982; Anders et al., 2020). Additionally, some studies have found that mixed and fixed flux thermal boundary conditions can be usefully applied to better represent experimental studies (Verzicco & Sreenivasan, 2008).

Beyond the study of fixed temperature, mixed, and fixed flux thermal conditions individually, it is necessary to compare results across boundary conditions. In order to compare each condition, the systems must be equivalently parameterised. Due to the presence of the thermal scaling term in the definition of the Rayleigh number, it is necessary to consider different Rayleigh number definitions for different thermal boundary conditions (Calkins et al., 2015).

From the literature reviewed in Chapter 1, it is clear that there is not full understanding of the differences in solution form as well as a lack of data for Nusselt number Nu scaling near to onset of convection when comparing fixed temperature, mixed and fixed flux boundary conditions. This chapter aims to fill this research gap by applying each thermal boundary condition to a cylindrical RBC and RRBC system. First, each boundary condition is defined along with the appropriate non-dimensional parameters to understand each condition. Then, a linear stability analysis is performed to provide insight into the fluid behaviour at the onset of convection. Then, we describe the tools used to analyse the full non-linear results resulting from the numerical system previously described in Chapter 2. The temporal behaviour of each configuration is analysed using Nu time series and plots of attractors. The time averaged Nusselt number $\overline{Nu}$ is used to determine the relationship between heat transport and Rayleigh number Ra for each thermal condition. The spatial behaviour of the fluid for each thermal boundary condition is analysed along the horizontal, vertical, and azimuthal axes. We develop a novel factor which quantifies the deviation of vertical velocity in the vertical axis to identify the transition from 2D to 3D flow. Finally, the results are presented and described such that the conclusion adds to the discussion of physically appropriate thermal boundary conditions for numerical models.

3.2 Boundary conditions

Recalling the dimensionless equations of motion from Chapter 2, Eqs (2.11a-2.11c), we now define appropriate thermal boundary conditions. Note that dimensional variables are designated with a tilde. The velocity is no-slip on all surfaces and the sidewalls are thermally insulated as defined in Eq (2.15) and Eq (2.17), respectively. The thermal boundary conditions at the top and bottom of the cylinder are either fixed temperature, fixed flux, or mixed.

3.2.1 Fixed temperature

Fixed temperature boundary conditions require constant temperatures at the top and bottom surfaces, such that $\Delta\tilde{T}$, the temperature drop across the system, is constant. The dimensionless temperatures at the boundaries are fixed such that

$$T = 0 \qquad \text{at} \qquad z = 0.5 \qquad \text{and} \qquad T = 1 \qquad \text{at} \qquad z = -0.5. \tag{3.1}$$

Consequently, the appropriate thermal scaling is $\tilde{T} = T\Delta\tilde{T} + T_0$, where T_0 is the reference temperature, and the appropriate Rayleigh number definition is

$$Ra_{FT} = \frac{\alpha g \Delta\tilde{T} d^3}{\nu\kappa}. \tag{3.2}$$

3.2.2 Fixed flux

The fixed flux thermal boundary condition requires the vertical temperature gradient, $\tilde{\beta} = \partial\tilde{T}/\partial\tilde{z}$, to be constant at the boundaries. Hence, the nondimensional fixed flux boundary condition is defined such that

$$\nabla T \cdot \boldsymbol{n} = \beta = -1 \qquad \text{at} \qquad z = 0.5, \quad 0.5, \tag{3.3}$$

where β is the nondimensional vertical temperature gradient and $\boldsymbol{n}$ is the outward facing normal vector. Fixing $\beta = -1$ ensures that the conductive state will have the same linear profile as the fixed temperature case.

For a system with fixed flux boundary conditions, the most appropriate thermal scaling is $\tilde{T} = T\tilde{\beta}d + T_0$ and consequently, we define the fixed flux Rayleigh number as

$$Ra_{FF} = \frac{\alpha g \tilde{\beta} d^4}{\nu\kappa}. \tag{3.4}$$

3.2.3 Mixed

Applying the fixed flux condition to the top boundary and the fixed temperature condition to the bottom boundary creates the mixed boundary condition. The nondimensional mixed boundary condition is defined as

$$\nabla T \cdot \boldsymbol{n} = \beta = -1 \qquad \text{at} \qquad z = 0.5 \qquad \text{and} \qquad T = 1 \qquad \text{at} \qquad z = -0.5. \tag{3.5}$$

Unlike the fixed temperature condition, $\Delta\tilde{T}$ is not fixed, instead, like the fixed flux condition, $\tilde{\beta}$ is fixed at the upper boundary. Therefore, it is appropriate to use the same thermal scaling and Rayleigh number definition as for the fixed flux condition. Note that for consistency, whenever β is used, it is the vertical temperature gradient taken at the upper boundary, $\beta = \partial T/\partial z|_{z=0.5}$.

3.2.4 Rayleigh number relationship

In order to compare results between systems with different boundary conditions, we must define a relationship between Rayleigh number definitions. Following Calkins et al. (2015), defining the Nusselt number as,

$$Nu = \frac{\tilde{\beta} d}{\Delta \tilde{T}}, \tag{3.6}$$

we may define a relationship between Ra_{FF} and Ra_{FT} such that,

$$Ra_{FF} = Nu Ra_{FT}. \tag{3.7}$$

Note, in the fixed temperature systems, Nu is proportional to the heat flux crossing the upper boundary and in the fixed flux systems, Nu is proportional to the inverse of the temperature difference across the domain. Further, when the system is conductive and sufficiently close to convection onset, $Nu = 1$, and therefore $Ra_{FF} = Ra_{FT}$.

3.3 Linear stability analysis

Considering convection onset, it is appropriate to perform a linear stability analysis to determine the behaviour of RRBC with each thermal boundary condition. Therefore, in this section, we follow the linear analysis described in Chapter 2. Using the numerical solver Dedalus (Burns et al., 2016), the linear governing equations Eq (2.19a)-(2.19c) are solved in a 2D plane-layer geometry. The results reveal the critical Rayleigh number, Ra_c, at which convection onsets, and the critical wavenumber, a_c, which informs the solution form at onset.

Note that at onset Nu is sufficiently close to 1 that we consider $Ra_{FF} = Ra_{FT}$. Therefore, in this section, we ubiquitously refer to the Rayleigh number as Ra. Additionally, a_c is a useful value to predict the pattern formation near the onset of convection. We define the critical wavenumber as

$$a_c = \frac{m\pi}{2\Gamma}, \tag{3.8}$$

where m is the mode number, in other words, the number of convection rolls (Gao & Behringer, 1984). Note that this approximation was defined for cylindrical domains.

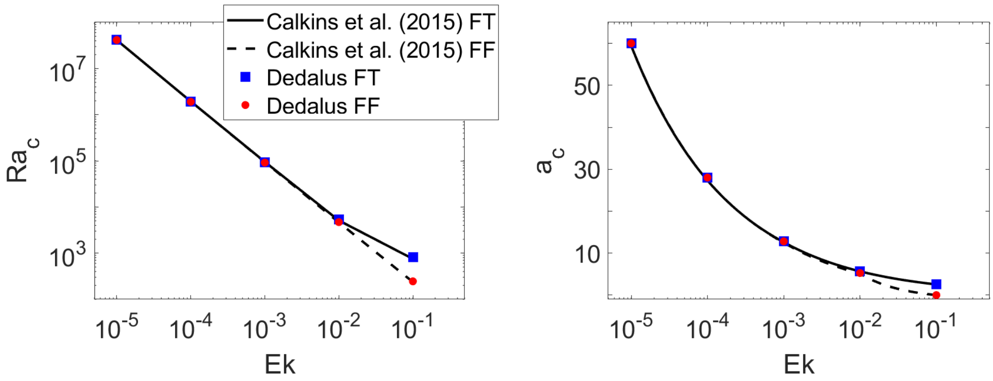

(a) Ek vs. Ra_c. (b) Ek vs. a_c.

Figure 3.1: Graphs of Ra_c and a_c as functions of Ek in a plane layer with stress-free velocity conditions, $Pr = 1$, and either fixed temperature (FT) or fixed flux (FF) thermal boundary conditions. The results derived from a Dedalus-based eigenvalue problem for fixed temperature (blue) and fixed flux (red) agree with results from Calkins et al. (2015), which are shown as solid (dashed) lines for fixed temperature (fixed flux) conditions.

However, the linear stability analysis is conducted in a plane layer. Consequently, Ra_c and a_c are approximations of the same parameters in the cylindrical domain. In later sections, these onset values are used to determine the minimum Ra value to solve for in the cylindrical, non-linear system.

Previously, it has been found that as Ek approaches 0, the Ra_c and a_c values converged independent of thermal boundary conditions. This result has proven accurate in both a plane-layer with stress-free velocity conditions and fixed temperature and fixed flux conditions and a spherical shell with stress-free velocity conditions for fixed temperature and mixed conditions (Calkins et al., 2015; Clarté et al., 2021). We seek to extend this result for no-slip velocity conditions within a plane-layer across fixed temperature, fixed flux, and mixed conditions.

3.3.1 Numerical testing

Before beginning our investigation of thermal boundary conditions, we first compare results from the Dedalus solver with previous literature. In Calkins et al. (2015), an asymptotic solution is presented for linear RRBC equations in a plane layer with $Pr = 1$ and stress-free velocity boundary conditions and either fixed temperature or fixed flux thermal boundary conditions. They found that as Ek approaches 0, Ra_c and a_c converge regardless of thermal boundary conditions.

In order to replicate these results with the numerical methods described in Chapter 2, stress-free velocity conditions are applied at the horizontal boundaries such that

$$\frac{\partial u}{\partial z} = 0, \quad \frac{\partial v}{\partial z} = 0, \quad \text{and} \quad w = 0 \qquad \text{at} \quad z = -0.5, \quad 0.5. \tag{3.9}$$

Further, we set $Pr = 1$ and model $10^{-1} \geq Ek \geq 10^{-5}$ which corresponds to $10^-2 \leq Ro \leq 10$.

Figure 3.1 shows the linear stability analysis results in two graphs: Figure 3.1a which shows Ra_c vs. Ek and Figure 3.1b which shows a_c vs. Ek. In both plots, the asymptotically derived results from Calkins et al. (2015) for the fixed temperature (fixed flux) thermal boundary condition are plotted as a solid (dashed) black line. The results from the Dedalus solver are indicated by blue squares (red circles) for fixed temperature (fixed flux) boundary conditions. Note that, as Ek decreases, it becomes difficult to distinguish the black dashed and solid line and the blue squares are difficult to see because they are covered by the red circles.

Figures 3.1a and 3.1b show that the Ra_c and a_c values found with our numerical method are similar to that of Calkins et al. (2015). Additionally, in both plots of Figure 3.1, the red circles and blue squares collapse to the same values of Ra_c and a_c as Ek decreases, showing agreement with Calkins et al. (2015)'s prediction that onset parameters converge in rapidly rotating systems independent of thermal boundary conditions. Thus, we suggest that the Dedalus-based numerical solver is appropriate to conduct further linear stability analysis.

3.3.2 Convergence of linear stability parameters with no-slip boundary conditions

We apply the parameters and conditions appropriate to the non-linear system to the linear setup. Hence, an air-like fluid with $Pr = 0.7$ is considered with no-slip velocity conditions and $10^0 \geq Ek \geq 10^{-6}$. The thermal boundary conditions are applied respectively as fixed temperature, fixed flux, or mixed, following Eqs (3.1),

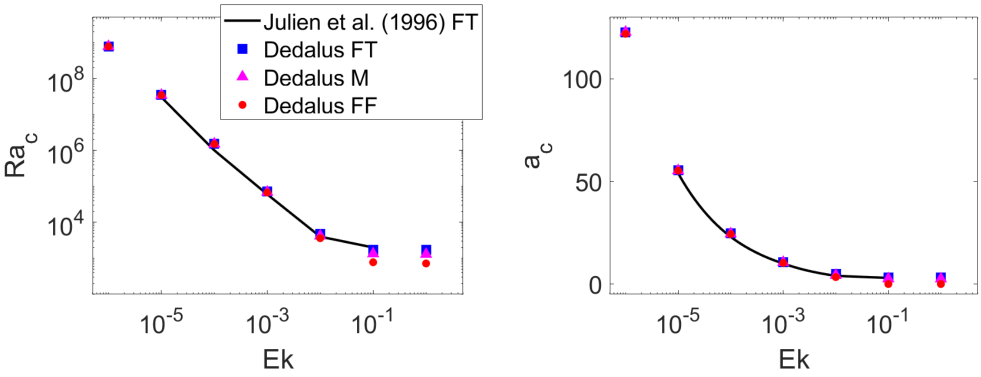

(a) Ra_c vs. Ek.

(b) a_c vs. Ek.

Figure 3.2: Graphs of Ra_c and a_c as functions of Ek, calculated for a fluid with $Pr = 0.7$ in a plane layer with no-slip velocity conditions and fixed temperature (FT, blue square), mixed (M, magenta triangle), or fixed flux (FF, red circle) thermal boundary conditions. Results from Julien et al. (1996) for $Pr = 1$ (solid black line) are presented for comparison.

(3.3), and (3.5). Results from similar study – reported in Julien et al. (1996) with $Pr = 1$ and fixed temperature thermal boundaries – are presented for comparison.

Figure 3.2 is composed of two plots which respectively show the Ra_c and a_c values as functions of Ek. Results produced using the Dedalus solver are indicated with the addition of magenta upward pointing triangles for the mixed boundary condition. The solid black line indicates Ra_c and a_c calculations from Julien et al. (1996).

Figure 3.2 indicates that the no-slip Dedalus solver solutions for fixed temperature and $Pr = 0.7$ closely match the results given in Julien et al. (1996) for the same system with $Pr = 1$, which is expected because Pr value does not affect the Ra_c value of steady modes. Additionally, it is clear that Ra_c and a_c become independent of thermal boundary condition for $Ek \leq 10^{-3}$, confirming Calkins et al. (2015)'s assertion that, when rapidly rotating, convection onset is independent of thermal boundary condition with the no-slip velocity boundary condition. This is a novel result both with no-slip and the mixed boundary conditions. The implication of this result is that in the rapidly rotating astrophysical and geophysical systems (on the order of $Ek = 10^{-15}$), convection onset behaviour is not likely influenced by boundary conditions.

However, the linear stability analysis is conducted in a plane-layer geometry. While these results provide a foundation of convection-onset behaviour for each thermal boundary condition, the Ra_c and a_c values will differ in the cylindrical geometry used in this thesis for non-linear investigations. In K. Zhang and Liao (2009) it was found that, in cylindrical geometry for $Pr \leq 0.1$ and $Ek \ll 1$ with fixed temperature conditions, the Ra_c value was generally greater than in a system of same parameters in a plane layer. Hence, we anticipate greater Ra_c values in the non-linear model described in Chapter 2.

3.4 Diagnostic tools

Before obtaining non-linear numerical results, we describe the analysis methods used to categorise and compare results between thermal boundary conditions. First, we discuss the definition and use of the Nusselt number Nu, followed by metrics of time-dependence. Finally, the methods of analysing spatial behaviour are defined along the horizontal, vertical, and zonal directions.

3.4.1 Nusselt number

Nu values measure heat transport by comparing the total heat transfer to the heat transfer due to convection. Thus, as Nu increases, the movement of heat due to convection increases and is related to an increase in fluid motion within a system. Recall from Eq (3.6) that $Nu = \tilde{\beta} d / \Delta \tilde{T}$ where $\tilde{\beta}$ is calculated by averaging the vertical heat flux at the upper boundary while $\Delta \tilde{T}$ is measured by the difference between the average temperature at the bottom and top boundaries. In order to measure Nu with dimensionless quantities, we apply the appropriate thermal scaling to Eq (3.6). With either the fixed flux or fixed temperature system arrive at

$$Nu = \frac{\beta}{\Delta T} \tag{3.10}$$

where $\beta = \partial T / \partial z|_{z=0.5}$ and $\Delta T = T|_{z=-0.5} - T|_{z=0.5}$. The Nu value is calculated at each time-step, establishing $Nu(t)$ as a function of time.

A time average of $Nu(t)$ is taken once the system has reached a statistically steady state. The $\overline{Nu}$ value has a standard deviation σ_{Nu} which measures the

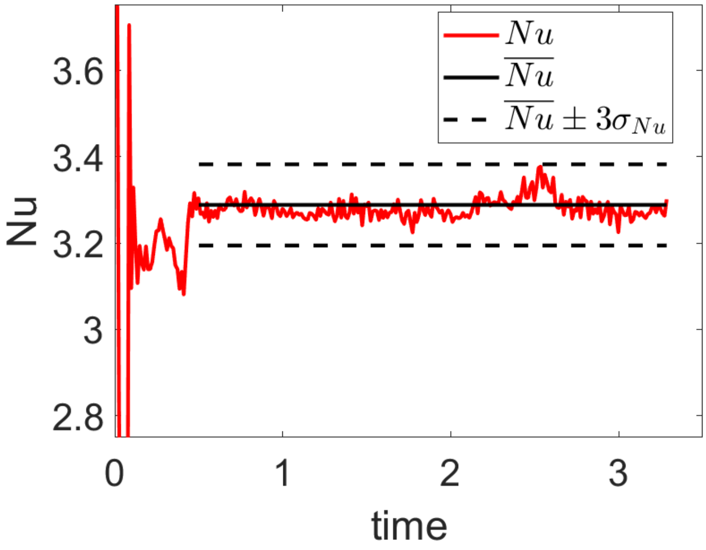

Figure 3.3: An example $Nu(t)$ for a fixed flux simulation with $Ek = 10^{-4}$ and $Ra_{FF} = 3.6 \times 10^6$ (red). The average value $\overline{Nu}$ calculated from the time average is indicated by the black line and the 99% confidence interval of $\pm 3\sigma_{Nu}$ is outlined by the dotted black lines.

variation of $Nu(t)$ from $\overline{Nu}$. We also consider 99% confidence intervals (CI) about the mean which is defined as $\overline{Nu} \pm 3\sigma_{Nu}$.

For example, in Figure 3.3, the time series $Nu\,(t)$ is plotted in red for a system with fixed flux conditions and $Ek = 10^{-4}$ and $Ra_{FF} = 3.6 \times 10^6$. The $\overline{Nu}$ value (black line) is determined by the average Nu after time $t = 0.5$, where a statistically steady state has been achieved. The standard deviation of the $Nu\,(t \geq 0.5)$ is used to show a 99% confidence interval of $3\sigma_{Nu}$ (dashed lines).

From Figure 3.3, it is clear that the confidence interval contains the majority of the data points once the series has settled into a dominant state. This demonstrates the ability of the $\overline{Nu}$ and σ_{Nu} to summarise the behaviour of the Nu time series.

The $\overline{Nu}$ and σ_{Nu} values for a range of Ek and Ra_{FT} values are compiled for each thermal boundary condition. The $\overline{Nu}$ value of each simulation is used within the $Ra_{FF} = NuRa_{FT}$ relationship to determine a Ra_{FT}. Additionally, the $\overline{Nu}$ and σ_{Nu} results are used to fit a weighted-least-squares logarithmic-scaled line of the form $\overline{Nu} \propto Ra^{\gamma}$. Using a propagation of error, we also measure the standard deviation σ_{γ} that corresponds with each γ value.

Paper	Ek	Ra_{FT}	Pr	Γ	γ	σ_γ
E. King et al. (2012)	∞	$< 10^{10}$	7	$0.5 - 2$	0.284	0.002
J. Cheng et al. (2015)	∞	$> 10^8$	$4 - 7$	≤ 0.125	0.322	0.003
E. King et al. (2009)	10^{-3}	5×10^5	7, 10	$0.5 - 3.12$	1.2	
E. King et al. (2012)	10^{-4}	$< 10^7$	7	$0.5 - 2$	0.8	-
Stellmach et al. (2014)	10^{-5}	$< 10^8$	1, 7	-	$1.5 - 3$	-

Table 3.1: Previous literature results for $Nu \propto Ra_{FT}^{\gamma \pm 3\sigma_\gamma}$ along with parameter regimes used for the measurements.

As discussed in section 1.2.2, the scaling between $\overline{Nu}$ and Ra is of interest for extrapolating behaviour of large-scale flows from the heat transport measurements of numerical and experimental models. Thus, the results here can be compared to previous literature. Table 3.1 lists several previous results for predicted γ values and the corresponding parameter values. Note each of these studies used fixed temperature thermal boundary conditions.

Though the Pr, geometry, and Γ from the previous studies differs from the system considered here, which has $Pr = 0.7$ in a cylindrical domain of $\Gamma = 0.7$, Plumley and Julien (2019) showed that without rotation, shows agreement between γ values in systems with $0.1 \lesssim \Gamma < 3$ and Pr on the order of 1. Additionally, a similar γ value for non-rotating convection was measured in an RBC system with $Pr = 0.7$ and $\Gamma = 0.5$ in Emran and Schumacher (2008) and in Johnston and Doering (2009) for a plane-layer of fluid with $Pr = 1$ and fixed flux boundaries. Therefore, we consider the γ values listed in Table 3.1 to be appropriate for comparison against the RRBC systems modelled in this thesis.

Thus, we have described the implementation of Nu in our analysis of RRBC in a cylindrical domain with different thermal boundary conditions. For each time-step of the numerical solution, a Nu value is calculated using Eq (3.10). The time-averaged value $\overline{Nu}$ is measured with standard deviation σ_{Nu}. For a fixed Ek, we use a regression to find a line of the form $Nu \propto Ra^\gamma$. The results for γ are usefully compared against previous studies listed in Table 3.1. The $Nu(t)$ time series is further useful to determine the temporal behaviour of a system.

3.4.2 Time-dependence

As described in section 1.2.2, there are several regimes of rotating convection including wall-localised, bulk, geostrophic, and turbulent flow. Investigating time-dependence of flows helps to determine which regime a system exhibits after the mode has saturated. The temporal behaviour of each system is categorised into one of the following: conducting, time-independent, oscillatory, quasi-oscillatory, or temporally chaotic. Chaotic flows often indicate geostrophic or turbulent regimes while oscillatory and quasi-oscillatory behaviour suggests wall-localised or bulk flow in rotating systems and time-independence is expected for non-rotating systems near onset. In this section, we describe the methods for categorising temporal behaviour.

The determination for conducting systems is simply that $\overline{Nu} = 1 \pm 10^{-4}$ such that the variations in $Nu(t)$ over time are negligible. Time-independent solutions are determined by a sufficiently small standard deviation such that $\sigma_{Nu} < 10^{-4}$, indicating that Nu does not vary significantly from $\overline{Nu}$ after the behaviour of the system has converged. However, rotating systems often have oscillatory behaviour with small amplitudes resulting in $\sigma_{Nu} < 10^{-4}$ for an oscillatory system. To identify such instances, time-dependent systems are categorised visually using Nu time series and attractor plots.

3.4.2.1 Nusselt number time series

By observing $Nu(t)$, we visually identify the different categories of time-dependence. Figure 3.4 demonstrates the three time-dependent forms of $Nu\,(t)$. In each panel of Figure 3.4, a $Nu(t)$ time series is plotted for some Ra_{FF} with mixed thermal boundary conditions and $Ek = 10^{-5}$. The upper panel shows the Nu time series for an oscillatory system with $Ra_{FF} = 3.6 \times 10^{6}$. The time series appears as a single mode sine wave which oscillates in time with a fixed frequency. In the middle panel, the $Ra_{FF} = 2.88 \times 10^{7}$ system demonstrates a quasi-oscillatory Nu time series, which is a superposition of several sine modes, i.e. a sine wave in an envelope. Finally, the bottom panel shows the time series for a $Ra_{FF} = 4.8 \times 10^{8}$ system, which is temporally chaotic. In temporally chaotic flows the Nu time se-

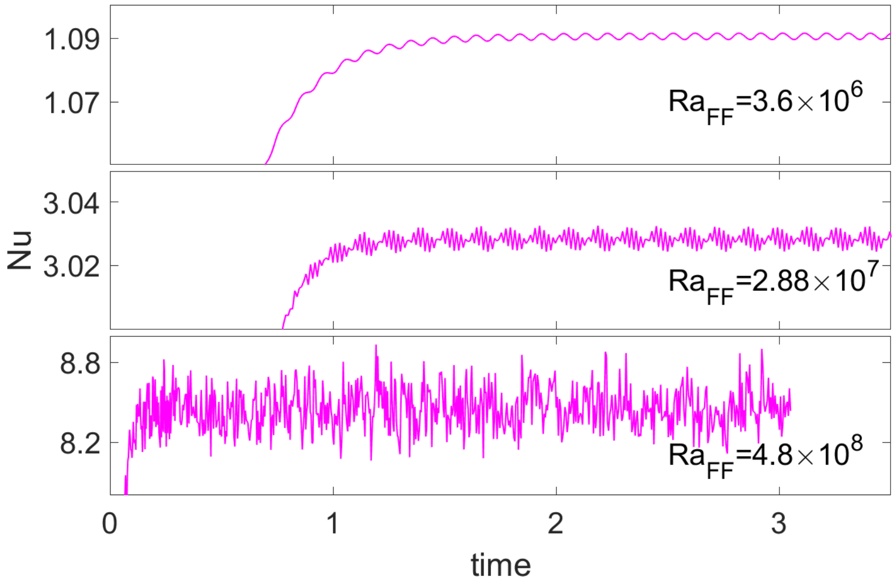

Figure 3.4: $Nu(t)$ for three different cases of mixed configurations with $Ek = 10^{-5}$: (top) an oscillatory time series with $Ra_{FF} = 2.6 \times 10^6$, (middle) a quasi-oscillatory time series with $Ra_{FF} = 2.88 \times 10^7$, and (bottom) a temporally chaotic time series for $Ra_{FF} = 4.8 \times 10^8$.

ries changes value irregularly. Sometimes these series are not sufficient to make a determination, so it is necessary to make an attractor plot.

3.4.2.2 Attractor plots

An attractor plot is made by plotting the values of three variables at three suitably distinct locations over time. Here, T, w, and u are considered at points $P_T = (-0.08, 0.38, -0.38)$, $P_w = (0.58, -1.9, 0.29)$, and $P_u = (-0.26, 0.17, 0.13)$, respectively. The points must be sufficiently distant from one another such that the flow properties are not directly related and hence each point may represent the flow in a distinct area of the domain.

Figure 3.5 illustrates attractor diagrams for flows with mixed thermal boundary conditions and $Ek = 10^{-5}$. The colour of each data point indicates the time at which it was taken. Figure 3.5a shows an oscillatory system which is categorised based on the consistent, circular pattern of motion. A quasi-oscillatory system, exemplified in Figure 3.5b, also has a consistent pattern, but is not a strictly circular

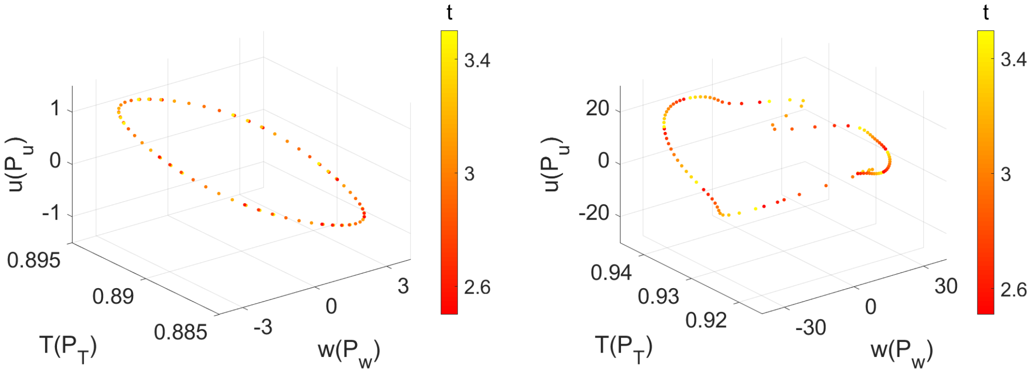

(a) Oscillatory, $Ra_{FF} = 3.6 \times 10^6$ (b) Quasi-oscillatory, $Ra_{FF} = 2.88 \times 10^7$

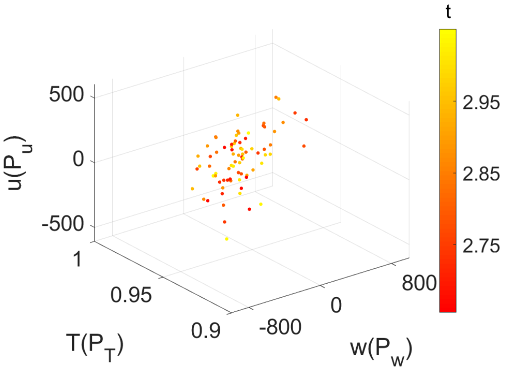

(c) Temporally chaotic, $Ra_{FF} = 4.8 \times 10^8$

Figure 3.5: Examples of attractor plots from simulations with mixed thermal boundary conditions and $Ek = 10^{-5}$ for each category of time-dependence. As indicated by the colour-bar, the points transition from red to yellow as time passes. The axes are vertical velocity w at point $P_w = (0.58, -0.19, 0.29)$, temperature T at point $P_T = (-0.08, 0.38, -0.38)$, and x velocity u at point $P_u = (-0.26, 0.17, 0.13)$.

or oblong in shape. Finally, Figure 3.5c shows an attractor which demonstrates a temporally chaotic system, characterised by random behaviour with no pattern.

3.4.3 Spatial behaviour

The formation of flow structures is also indicative of convection regimes. In RRBC, wall-localised convection is characterised by convection rolls present at the walls only while bulk convection has flow throughout the domain. These regimes, as well as the time-independent regime of non-rotating convection, tend to have columnar vertical flow structure. The breakdown of vertical uniformity is indicative of the transition to geostrophic turbulence. Further, boundary zonal flows may occur where wall-localised convection coincides with bulk flows of different structures. To identify such regimes, we investigate horizontal, vertical, and zonal flow forms.

3.4.3.1 Horizontal structure

We analyse horizontal structure by identifying the number and location of convection rolls within the domain at a fixed z. The dominant mode for each system m is determined as well as whether the convection is stronger along the wall boundary, in the bulk of the fluid, or equally strong in the bulk and along the wall.

Figure 3.6 demonstrates the process by which a zonal fast Fourier transform (FFT) is conducted with a fixed temperature system with $Ek = 10^{-4}$ and $Ra_{FF} = 3.2 \times 10^5$. First, w at $z = 0.3$ is considered, as Figure 3.6a illustrates, where red indicates upward motion and blue indicates downward motion, and white indicates no motion. The dashed lines in Figure 3.6a correspond to the two r of data considered in Figure 3.6b.

The two sets of data at $r = 0.665$ and 0.21 are chosen to capture the behaviour of the system near the wall and in the bulk. Each r of data is individually transformed with a FFT, and in time-dependent systems, the FFT is averaged over time. Figure 3.6c shows the results of the FFT for $r = 0.665$ and $r = 0.21$ in red and blue, respectively. Note that the FFT amplitude axis has a logarithmic scale. The number of convection rolls is identified by the maximum of the absolute value of the FFT amplitude from either ring. For example, Figure 3.6c shows a global maximum at mode $m = 3$ for $r = 0.665$. Thus, the system has $m = 3$ wall-localised rolls.

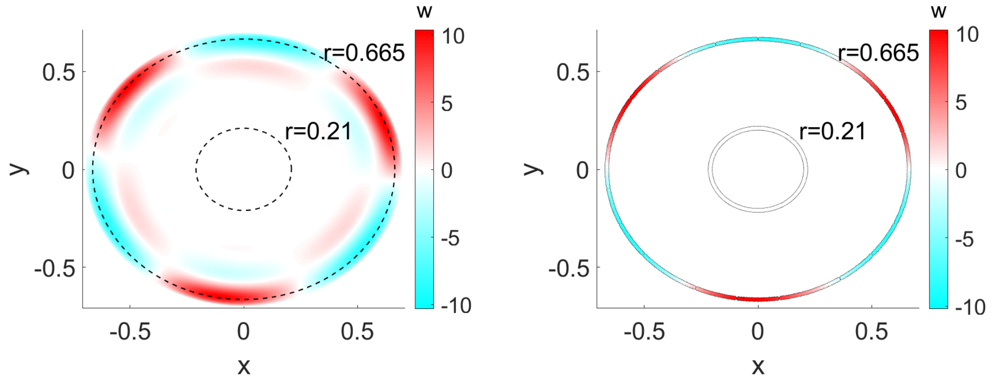

(a) w at $z = 0.3$. (b) $w\,(z = 0.3)$ at $r = 0.665$ and $r = 0.21$.

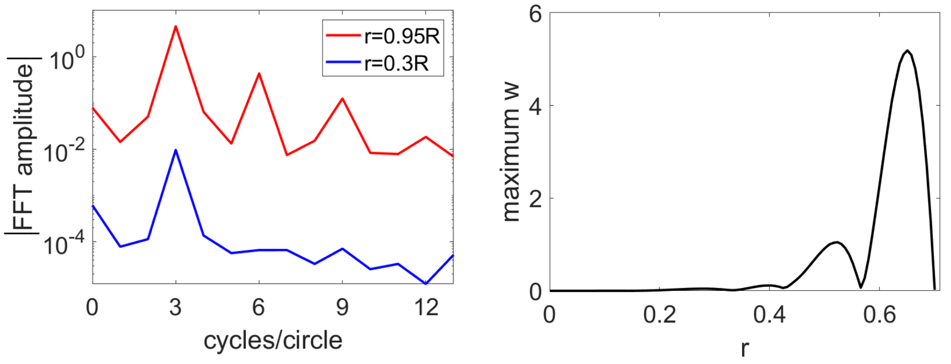

(c) FFT at inner (blue) and outer (red) r. (d) Maximum amplitude of $< w >_\theta$ vs. r

Figure 3.6: The processes for determining horizontal solution forms of a fixed temperature system with $Ek = 10^{-4}$, and $Ra_{FT} = 3.2 \times 10^5$. (a)-(c): The process of taking FFTs of w at $r = 0.665$ and $r = 0.21$ to determine the dominant mode, m. (d): The maximum w amplitude at each r used to determine the dominant radial location of convection. The example shown is and $m = 3$ wall mode.

However, further investigation is necessary to conclude on the dominant location of convection.

In order to categorise the location of the mode, at the wall, in the bulk, or both, w is again considered at $z = 0.3$. The maximum amplitude of w is found at each radius, as shown in Figure 3.6d. The derivative in r in taken, $d\max(w)/dr$, to identify maximums. If the first maximum is within $r \geq 0.6$, and there are no other maximums of similar amplitude at $r < 0.6$, then the system has a wall mode. When there are other maximums similar to that of the mode closest to the wall, then the system is categorised as having both bulk and wall modes. When the maximum of highest amplitude is at $r < 0.6$, then the system is considered to have bulk convection. For example, in Figure 3.6d, there is a maximum at $r \geq 0.6$ and another $r \approx 0.5$ but with a significantly lower amplitude. Therefore, the system is categorised as a wall mode.

3.4.3.2 Vertical uniformity

Vertical behaviour, especially in RRBC, is often considered to either be quasi-2D or 3D. Well known quasi-2D structures include convective cells, which exist for $Ra_{FT} \leq 2Ra_{FTc}$ (Chandrasekhar, 1961), Taylor columns, which typically form at low Ra_{FT} in RRBC. As Ra_{FT} increases, the flow becomes increasing irregular along the vertical axis and transitions into 3D dynamics. In rapidly rotating convection, this transition may mark the onset of geostrophic turbulence.

The deviation in fluid motion along the vertical axis is measured by a uniformity factor, Λ, which is defined as a ratio between the change in vertical velocity along the vertical axis and the total vertical velocity such that

$$\Lambda = \left(\frac{d}{\pi}\right)^2 \frac{\int_{-0.4}^{0.4} \left(\frac{\partial w}{\partial z}\right)^2 \mathrm{d}z}{\int_{-0.4}^{0.4} w^2 \mathrm{d}z} \tag{3.11}$$

Thus, a vertical velocity which has little dependence on z will have a small Λ and as a system becomes 3D, Λ increases. Convective cells and Taylor columns have small Λ values while 3D structures are indicated by large Λ. We find that the transition from 2D to 3D flow occurs at $\Lambda = 2$. Note that the integrals only consider the domain away from the vertical boundaries and for $r \leq 0.69$, which we have chosen as an arbitrary range to generally avoid interference from boundary layers. This

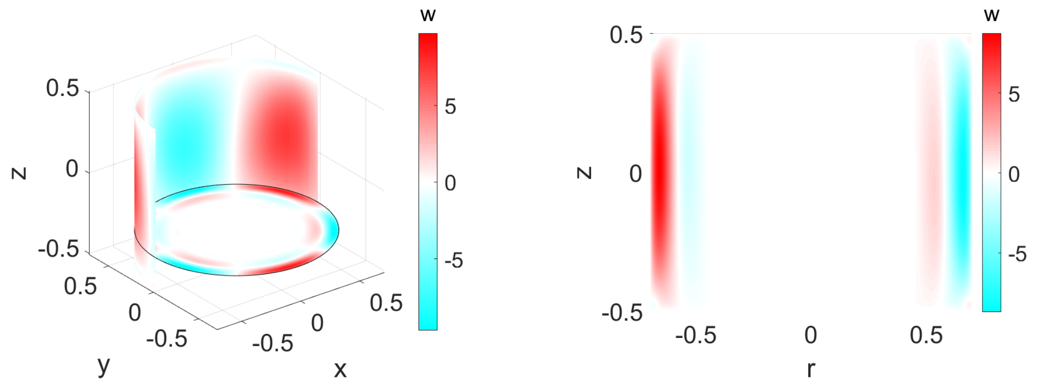

(a) A ring-slice diagram at $r = 0.685$ and $z = -0.3$.

(b) A vertical plot at $\theta = 0.44$

Figure 3.7: w visualised vertically for a fixed temperature system with $Ek = 10^{-4}$ and $Ra_{FT} = 3.2 \times 10^5$. The system has $\Lambda = 1$.

threshold could be altered based on Ra and Ek values for further accuracy (e.g. R. S. Long, 2020).

The vertical solution form is also visually investigated with 'ring-slice diagrams', which visualise vertical behaviour at some radius and horizontal behaviour at some height, as exemplified by Figure 3.7a. As well, simple vertical plots at some fixed θ are useful for visual inspection, as in Figure 3.7b.

3.4.3.3 Zonal flow

The mean zonal flow (MZF) is a measurement of the fluid velocity in the azimuthal direction and indicates the rotational flow. It is expected that for non-chaotic systems without rotation, that there is not any mean zonal flow but with rotation or in a chaotic system, the MZF indicates where the azimuthal flow is strongest.

MZF is here considered as a field such that,

$$\overline{u_{\theta t}}(r, z) = < u_\theta >_{\theta,t}, \tag{3.12}$$

where $< \cdot >$ indicates averaging over the sub-scripted variables.

To average over θ, the Cartesian data output by the Nek5000 numerical solver must be converted into cylindrical coordinates. However, to better resolve wall modes, the mesh is refined at the outer radius and is less dense on the interior. Therefore, there is a lack of data around $r = 0$. Hence, interpolation into cylindrical

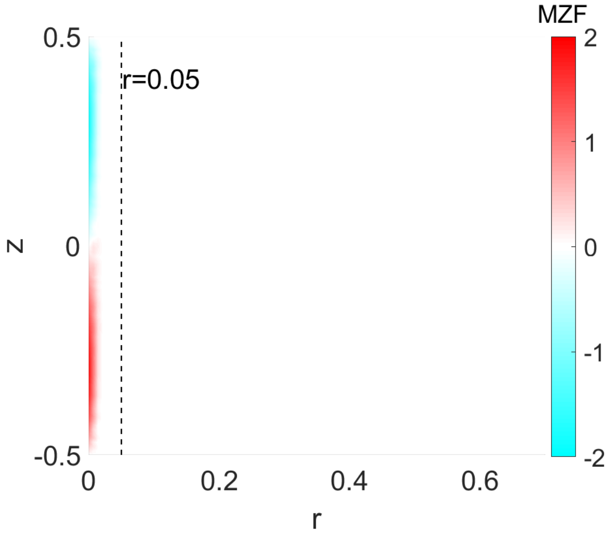

Figure 3.8: MZF for a fixed temperature system with $Ek = \infty$ and $Rak = 3 \times 10^3$, demonstrating the coordinate conversion error which occurs for $r \leq 0.05$.

coordinates causes errors to accumulate around $r = 0$. The error accumulation is significant when u_θ is low. Thus, the MZF is only considered for $r >= 0.05$.

Figure 3.8 demonstrates the error by plotting the $\overline{u_{\theta t}}$ field of a fixed temperature system with $Ek = \infty$ and $Ra_{FT} = 3 \times 10^3$. It is evident that the error has accumulated to become more significant than the value of $\overline{u_{\theta t}}$, which in this low Ra_{FT}, non-rotating case, would be expected to have an insignificant amplitude. The minimum radius at which $\overline{u_{\theta t}}$ will be considered is indicated by the dashed line. It is clear that the accumulated errors dissipate before the chosen minimum $r = 0.05$.

We also compute a volume average MZF value such that

$$MZF = \frac{1}{V} \int_V u_\theta \mathrm{d}V. \tag{3.13}$$

3.4.4 Overview

Thus, we have described our methods of analysing heat transport, temporal behaviour and spatial structure. We employ Nu as defined in Eq (3.10) for both the quantification of heat transport and categorisation of time-dependence. With time averaging, $\overline{Nu}$ is used to compare heat transport scaling γ results with previous literature. Further, attractor plots are employed to complete temporal behaviour categorisation.

The fluid motion is quantified in the horizontal, vertical and zonal directions. Horizontally, FFTs are applied to calculating the number m and location of convection rolls within the domain. We use a novel factor Λ, defined in Eq (3.11) to calculate vertical uniformity. Zonal flow is measured with the MZF as defined in Eq (3.13). Each of these metrics will allow for the comparison between flows with different thermal boundary conditions and contextualising results within previous literature.

3.5 Non-linear results

The analysis methods discussed in section 3.4 are used to interpret the results of numerically modelled RRBC governed by Eqs (2.11a)-(2.11c). The equations of motion are solved numerically with Nek5000 (Nek5000, 2019) as described in section 2.2.2. The boundary conditions from section 3.2 are applied to a cylinder of aspect ratio $\Gamma = 0.7$ and $Pr = 0.7$. The cylinder is rotating about the vertical axis using $\infty \geq Ek \geq 10^{-5}$. For each boundary condition configuration and Ek, the appropriately defined Ra – Ra_{FT} for fixed temperature systems and Ra_{FF} for mixed and fixed flux systems – are modelled from $Ra < Ra_c$ to $Ra = 10^5 Ra_c$.

Table C.1 in Appendix C summarises the ranges of Ek and Ra_{FT} simulated for each thermal boundary condition. Fewer Ra_{FT} values were considered for $Ek = 10^{-2}$ and 10^{-3} because $Ek > 10^{-4}$ is weakly rotating at the considered Ra_{FT} values and we primarily focus on the non-rotating and rapidly rotating regimes. Using methods described in Section 3.4, heat transport, time-dependence, and solution forms are compared across thermal boundary conditions.

3.5.1 Heat transport scaling

In order to compare between fixed temperature, mixed, and fixed flux thermal boundary conditions, it is necessary to calculate the Ra_{FT} for all systems with mixed and fixed flux conditions using Eq (3.6). Therefore, we first measure $\overline{Nu}$ and σ_{Nu} for each case. Figure 3.9 shows the $\overline{Nu}$-Ra relationship for each boundary

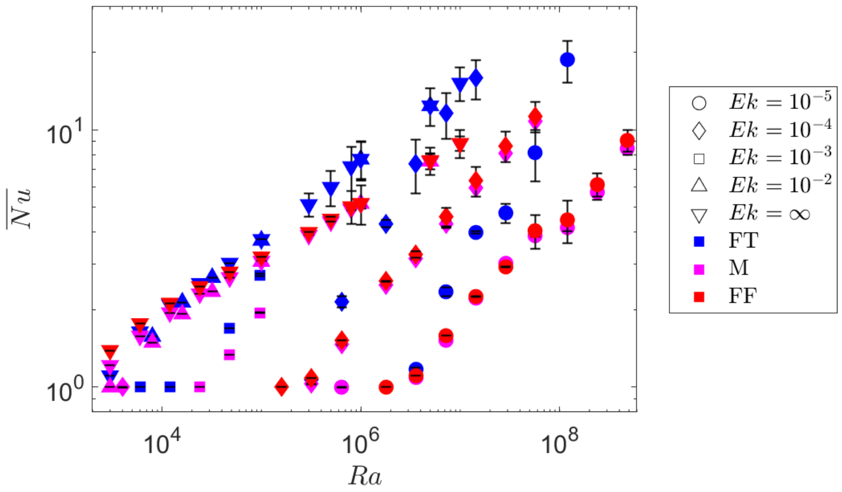

Figure 3.9: $\overline{Nu}$ vs the appropriate Ra for each simulated case where for the fixed temperature (FT, blue) $Ra = Ra_{FT}$ and for the mixed (M, magenta) and fixed flux (FF, red) conditions $Ra = Ra_{FF}$. Marker shape indicates Ek such that inverted triangles represent $Ek = \infty$, upright triangles represent $Ek = 10^{-2}$, squares represent $Ek = 10^{-3}$, diamonds represent $Ek = 10^{-4}$, and circles represent $Ek = 10^{-5}$. The error bars indicate the 99% confidence interval calculated from $3\sigma_{Nu}$.

condition. Each $\overline{Nu}$ has associated error-bars of $\pm 3\sigma_{Nu}$, illustrating a 99% CI. The Ek value of each system is indicated by a marker shape, listed in the figure legend. The fixed temperature configurations are shown in blue, the mixed in magenta, and fixed flux in red.

It is clear from Figure 3.9 that for each Ek value, the systems have similar $\overline{Nu}$ values for low Ra, though as Ra increases, the deviation in $\overline{Nu}$ value increases between the fixed temperature configuration and the mixed and fixed flux systems. Additionally, it is seen in the fixed temperature and mixed cases that for $Ek > 10^{-3}$, $\overline{Nu} - Ra$ scales similarly to $Ek = \infty$. To quantify these observations γ is calculated for each boundary condition and Ek such that $\overline{Nu} \propto Ra^{\gamma}$.

Table 3.2 shows the γ and σ_γ measurements for each thermal boundary conditions using their respective Ra. Note that no scaling was able to be calculated for $Ek = 10^{-3}$ due to a paucity of Ra values simulated. Comparing across thermal boundary conditions for $Ek = \infty$, 10^{-4} and 10^{-5}, respectively, it is clear that the mixed and fixed flux condition scale similarly while fixed temperature has significantly different γ values.

BC	Ek	γ	σ_γ	$\gamma \pm 3\sigma_\gamma$
FT	∞	0.296	0.001	0.292 – 0.300
	10^{-2}	0.311	0.006	0.292 – 0.330
	10^{-4}	0.564	0.092	0.289 – 0.8389
	10^{-5}	0.889	0.145	0.454 – 1.326
M	∞	0.235	0.001	0.232 – 0.237
	10^{-2}	0.227	0.003	0.218 – 0.236
	10^{-4}	0.435	0.008	0.411 – 0.458
	10^{-5}	0.499	0.043	0.368 – 0.629
FF	∞	0.234	0.007	0.215 – 0.254
	10^{-4}	0.426	0.030	0.336 – 0.516
	10^{-5}	0.512	0.068	0.308 – 0.716

Table 3.2: $\overline{Nu}-Ra$ scaling calculations for each Ek value and boundary condition: fixed temperature (FT), fixed flux (FF), and mixed (M). The γ value is calculated such that $Nu \propto Ra^\gamma$. The 99% CI is presented as $\gamma \pm 3\sigma_\gamma$. For fixed temperature, $Ra = Ra_{FT}$ is used and for mixed and fixed flux, $Ra = Ra_{FF}$ is used.

To compare between boundary conditions, it is necessary to compute Ra_{FT} with Eq (3.7) for the mixed and fixed flux boundary condition cases. The results are presented in Figure 3.10 where $\overline{Nu}$ is plotted against Ra_{FT} for each thermal boundary condition. Results are illustrated for fixed temperature (FT, blue), fixed flux (FF, red), and mixed (M, magenta) boundary conditions. Each Ek value is depicted by a respective marker shape: $Ek = \infty$ by inverted triangles, $Ek = 10^{-2}$ by upright triangles, $Ek = 10^{-3}$ by square, $Ek = 10^{-4}$ by diamonds, and $Ek = 10^{-5}$ by circles. The black dashed line indicates the $\overline{Nu} - Ra_{FT}$ scaling, $\gamma = 0.285$ for non-rotating systems (Johnston & Doering, 2009; E. King et al., 2012). The black dotted lines indicate $1.5 \geq \gamma \geq 3$, the range reported in Stellmach et al. (2014) for $Ek = 10^{-5}$ with $Pr = 1$ in a cuboid domain with fixed temperature boundary conditions.

The γ value is measured such that, $\overline{Nu} \propto Ra_{FT}^\gamma$. Table 3.3 reports the γ and σ_γ values for each Ek and thermal boundary condition: fixed temperature (FT), mixed (M), and fixed flux (FF). Note that γ for $Ek = 10^{-2}$ and 10^{-3} are not reported due to a paucity of data, and lack of previous literature regarding the $\overline{Nu}$

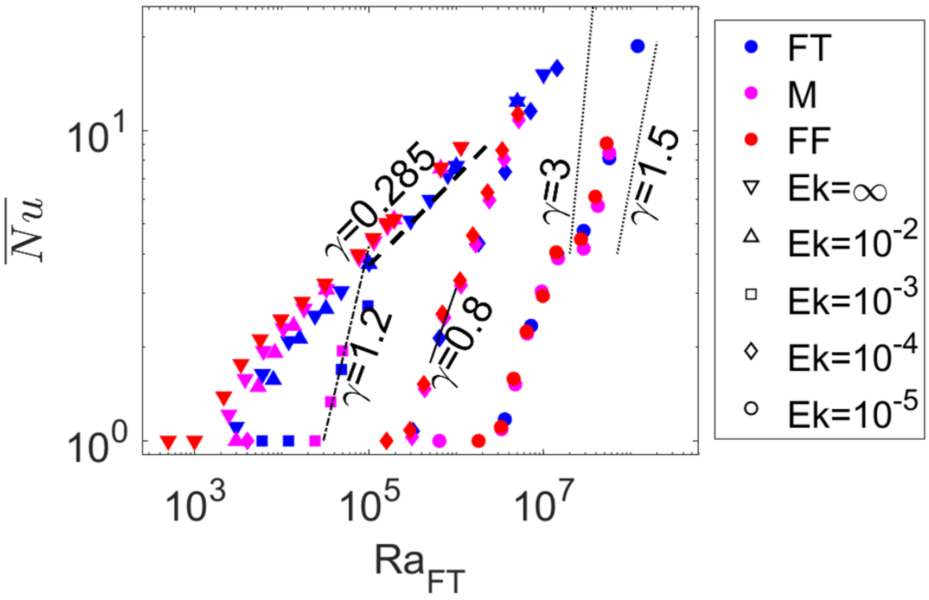

Figure 3.10: $\overline{Nu}$ vs Ra_{FT} for fixed temperature (FT, blue), mixed (M, magenta), and fixed flux (FF, red), thermal boundary conditions. The marker shape indicates Ek such that inverted triangles represent $Ek = \infty$, upright triangles represent $Ek = 10^{-2}$, squares represent $Ek = 10^{-3}$, diamonds represent $Ek = 10^{-4}$, and circles represent $Ek = 10^{-5}$. The black lines indicate γ from previous literature. The dashed line with $\gamma = 0.285$ is a result for non-rotating convection and the solid line is $\gamma = 0.8$ for $Ek = 10^{-4}$ (E. King et al., 2012). The dash-doted line is $\gamma = 1.2$ for $Ek = 10^{-3}$ (E. King et al., 2009). The dotted and lines with $\gamma = 1.5$ and 3, respectively, show the range predicted for $Ek = 10^{-5}$ (Stellmach et al., 2014).

scaling for weakly rotating systems for comparison.

BC	Ek	γ	σ_γ	$\gamma \pm 3\sigma_\gamma$
FT	∞	0.296	0.001	0.292 – 0.300
	10^{-2}	0.311	0.006	0.292 – 0.3305
	10^{-4}	0.564	0.092	0.289 – 0.839
	10^{-5}	0.889	0.145	0.454 – 1.33
M	∞	0.306	0.001	0.303 – 0.310
	10^{-2}	0.293	0.005	0.278 – 0.309
	10^{-4}	0.768	0.024	0.695 – 0.841
	10^{-5}	0.989	0.172	0.472 – 1.51
FF	∞	0.306	0.011	0.273 – 0.340
	10^{-4}	0.740	0.091	0.467 – 1.01
	10^{-5}	1.035	0.284	0.185 – 1.89

Table 3.3: γ calculations of the form $\overline{Nu} \propto Ra_{FT}$ for each Ek value and boundary condition: fixed temperature (FT), fixed flux (FF), and mixed (M). The 99% confidence interval of the scaling is presented as $\gamma \pm 3\sigma_\gamma$.

From previous literature, as listed in Table 3.1, it is expected that without rotation, $\gamma = 0.285 \pm 0.006$ in the range of Ra_{FT} which we have modelled. A visual inspection of Figure 3.10 suggest that the fixed temperature case scales quite well with $\gamma = 0.285$. In comparison, Table 3.3 shows that the non-rotating fixed flux case is the only condition which has an overlapping 99% CI with the literature, though it's γ value is steeper than that of the fixed temperature case. Each boundary condition results in $\gamma > 0.285$. The differences between the literature and current study may be due to differences in line-fitting to determine γ. Previous literature has favoured a linear regression while the present study has employed a weighted-least-squares regression, which includes the σ_{Nu} in the determination of γ and tends to increase σ_γ. Some differences may also be due to a difference in Pr values and Γ which restricts a solutions. Further, the Ra range used here is low in comparison to many of the studies listed in Table 3.1. It is worth noting that Anders et al. (2020) also reported a deviation of both fixed temperature and mixed condition non-rotating systems deviating slightly from the predicted $\gamma = 0.285$.

From Table 3.3, it is evident that the γ values of the mixed and fixed flux configurations are more similar than that of the fixed temperature case. However, the γ values are generally similar. This result generally agrees with Anders et al. (2020)'s conclusion that the mixed and fixed temperature boundary conditions have similar, though not exactly the same, γ and expands upon the conclusion to find that systems with a fixed flux thermal boundary condition will also have a similar scaling. Additionally, it is shown that fixed flux and mixed condition systems scale more closely to each other than to fixed temperature systems.

Considering RRBC, Table 3.3 shows that the fixed flux and mixed boundary conditions have a steeper γ than the fixed temperature condition. However, due to rotation, Nu varies more greatly as it oscillates, and thus σ_{Nu} is larger than in the non-rotating RBC cases. Considering $Ek = 10^{-4}$, in E. King et al. (2012) it was found that $\gamma = 0.8$ for $Ra_{FT} < 10^7$ with $Pr = 7$ in a cylindrical geometry. A visual inspection of Figure 3.10 shows that the results presented here are a close match for the range $Ra_{FT} < 10^7$. In concurrence, Table 3.3 shows that all thermal boundary conditions include $\gamma = 0.8$ in their 99% CIs, though the γ of fixed flux and mixed thermal boundary conditions are more similar to the approximation from E. M. King et al. (2010) than the fixed temperature case. The difference between boundary conditions is likely due to $Ra_{FT} > 10^7$ being included in the γ calculation for fixed temperature, and not for fixed flux or mixed. As observed in (Plumley & Julien, 2019), there is a threshold of Ra above which Nu scaling behaviour approaches that of the non-rotating systems. Hence, the inclusion of a larger Ra value in the calculation of γ for one boundary condition but not the others may skew the result.

The most rapid rotation we consider is $Ek = 10^{-5}$. Stellmach et al. (2014), found that for $Ek = 10^{-5}$, $Ra_{FT} \geq 10^8$, and $Pr = 1$, $1.5 \leq \gamma \leq 3$ with fixed temperature boundary conditions. Figure 3.10 shows that for $Ra_{FT} \geq 10^7$ all of the boundary conditions appear to scale within the range of $1.5 \leq \gamma \leq 3$. However, Table 3.3 shows that only fixed flux and, marginally, mixed boundary conditions have γ ranges which overlap with the scaling predictions. This is likely due to the inclusion of $Ra_{FT} < 10^7$ in the calculation of γ. Between boundary conditions, the fixed flux and mixed conditions scale more similarly to one another than to the fixed temperature condition, though they are all lie within each other's 99% CIs. Further, they each follow the pattern of increasing scaling steepness at $Ra_{FT} = 10^7$.

Overall, the γ measurements presented in Table 3.3 do not align with results from the previous literature summarised in Table 3.1. These differences are likely due to several factors: using weighted-least-squares regression rather than linear regression, a different Γ domain, and considering lower Ra_{FT} and different Pr values than the literature. Between thermal boundary conditions, the $\overline{Nu} - Ra_{FT}$ relationship generally collapse onto a common γ value for each Ek while Ra_{FT} is low enough that the sytem is rotationally affected. However, fixed flux and mixed conditions scale more closely than fixed temperature; these differences will be due to different solution forms. The agreement of $\overline{Nu} - Ra_{FT}$ behaviour between thermal conditions supports the use of universal scaling laws to predict $\overline{Nu}$ across experimental, numerical, and large-scale systems. Therefore, $\overline{Nu}$ scaling laws, such as those presented in Plumley and Julien (2019), which considered only fixed temperature boundary conditions, can be applied more widely to systems with boundaries more similar to fixed flux or mixed conditions. Indeed, in Currie et al. (2020) and (Barker et al., 2014), different methods of internal heating and cooling were investigated in rotating Cartesian domains and yielded similar γ measurements as those reported in Plumley and Julien (2019).

3.5.2 Time dependence

While there are important similarities in $\overline{Nu}$ between fixed temperature, mixed, and fixed flux configurations, $\overline{Nu}$ does not provide insight into the motion of the fluid. As described in section 3.4.2, Nu time series and attractors are used to categorise temporal behaviour into five categories: stable, time-independent, oscillatory, quasi-oscillatory, temporally chaotic.

Figure 3.11 summarises the time dependence results for each Ek value. The panels, from left to right, show results for $Ek = \infty$, $Ek = 10^{-4}$, and $Ek = 10^{-5}$ each as functions of Ra_{FT}. Boundary conditions are indicated from left to the right such that: fixed temperature conditions are blue, mixed conditions are magenta, and fixed flux conditions are red. The marker shape shows the designated time dependence category for each system: either conducting (circle), time-independent

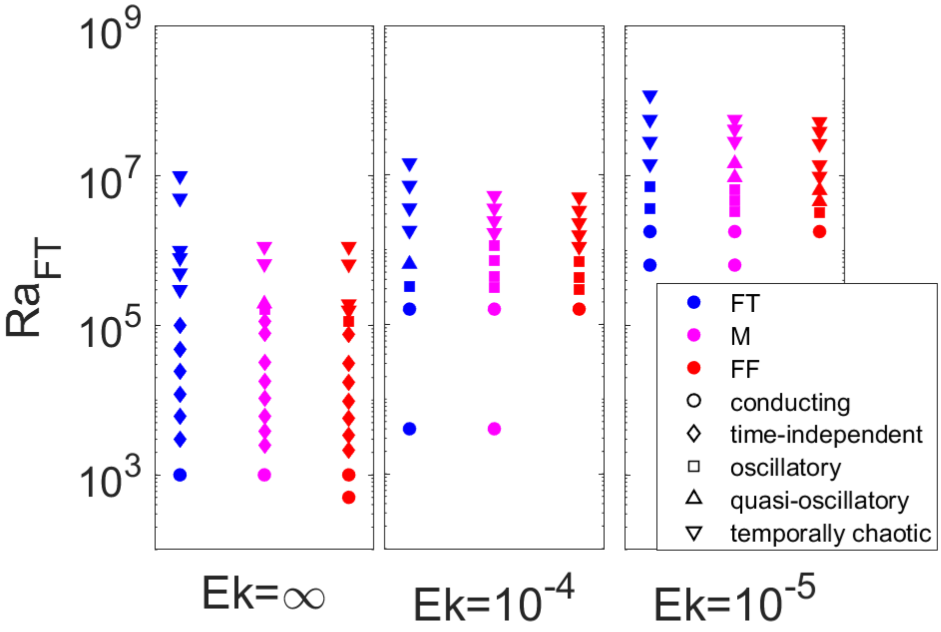

Figure 3.11: Time dependence results for RBC systems with fixed temperature (FT, blue), mixed (M, magenta), or fixed flux (FF, red) boundary conditions for all Ra_{FT} modelled with $Ek = \infty$, 10^{-4}, and 10^{-5}. Each system is categorised as either: conductive (circle), time-independent (diamond), oscillatory (square), quasi-oscillatory (upward pointing triangle), or temporally chaotic (downward pointing triangle).

(diamond), oscillatory (square), quasi-oscillatory (upward triangle), or temporally chaotic (downward triangle).

Beginning with the non-rotating results presented in Figure 3.11, the onset of convection occurred more uniformly than predicted in section 3.3. It was expected from linear stability analysis in a plane layers, convection onsets at lower Ra_{FT} for fixed flux systems than mixed and fixed temperature boundary condition systems. However, we find that Ra_{FTc} is nearly constant for each condition, decreasing only slightly in fixed flux systems. This is likely due to affects from the small aspect-ratio geometry. D. K. Edwards (1969) and Buell and Catton (1983b) found that as Γ decreases, Ra_c increases. Hence, we believe that without rotation, the effect of sidewalls is stronger than the effect of the thermal boundary condition at onset.

For $Ra_{FT} > Ra_{FTc}$, the non-rotating system retains time-independence after saturation while $Ra_{FT} < 50Ra_{FTc}$, regardless of thermal boundary condition. Figure 3.11 shows that fixed flux systems are temporally chaotic at lower Ra_{FT} than mixed boundary condition systems. Additionally, mixed boundary condition systems have oscillatory or quasi-oscillatory behaviour in the absence of rotation while fixed flux thermal boundary conditions have a smaller range of Ra_{FT} between time-independence and temporal chaos for which an only oscillatory behaviour develops. This result expands the conclusion presented in Anders et al. (2020) that systems with mixed thermal boundary conditions remain non-chaotic to higher Ra_{FT} values than fixed temperature system, to show that mixed thermal boundary condition systems also retain time-independence to higher Ra_{FT} values than fixed temperature boundary conditions.

Considering rotation, the onset behaviour shown in Figure 3.11 concurs with the conclusion section 3.3, that as Ek decreases, Ra_{FTc} converges regardless of thermal boundary condition. For $Ra_{FT} \geq Ra_{FTc}$, convection ubiquitously becomes oscillatory, due to the rotation effects. Quasi-oscillatory systems are less common and only occur in the transition to temporal chaos. Fixed flux systems becomes chaotic at the lowest Ra_{FT} values, closely followed by fixed temperature thermal boundary conditions, while mixed boundary condition systems are sub-chaotic to higher Ra_{FT} values.

Overall, the configuration with mixed thermal boundary conditions refrains from temporal chaos to the highest Ra_{FT} values, both with and without rotation, in comparison with configurations with either fixed temperature or fixed flux boundary conditions. In future studies this work could be expanded by categorising types of temporal chaos. The transitions between temporal behaviour can be better understood by investigating the form of convection taken in each system.

3.5.3 Spatial structures

Following the methods described in section 3.4.3, we analyse the horizontal, vertical and zonal spatial structures of fluid motion. From the horizontal behaviour, convection can be categorised into wall modes or bulk modes. Vertical flow is categorised as either vertically columnar, and therefore quasi-2D, or with variation in the vertical, and therefore 3D. The tendency of a flow toward 2D or 3D behaviour is an important distinction between rotationally-affected, geostrophic, and rotationally-unaffected flows. Finally, zonal behaviour illuminates the effects of wall boundaries and rotation on fluid motion.

3.5.3.1 Horizontal structures

Beginning with an investigation of horizontal behaviour, the analysis methods described in section 3.4.3.1 are applied to determine the number of convection rolls m and the location of the strongest convective motion away from the midpoint at $z = 0.3$. Each panel in Figure 3.12 contains results for each Ek value: from left to right, $Ek = \infty$, $Ek = 10^{-4}$, and $Ek = 10^{-5}$. Within each panel, the vertical axis shows the Ra_{FT} of each system and the horizontal axis designates the thermal boundary conditions: from left to right, fixed temperature (FT), mixed (M), and fixed flux (FF). The colour of each marker indicates m and the shape indicates if the flow is wall-localised (square), in the bulk (circle), or both (diamond). The dotted (dashed) line indicates where wall-localised (bulk) convection is predicted to onset (Ecke & Niemela, 2014; Favier & Knobloch, 2020).

The left-most frame of Figure 3.12 indicates that non-rotating systems are ubiquitously convecting in the bulk of the fluid with mode $m = 1$. The bulk convection behaviour when $Ek = \infty$ is expected, because wall-localised convection is primarily

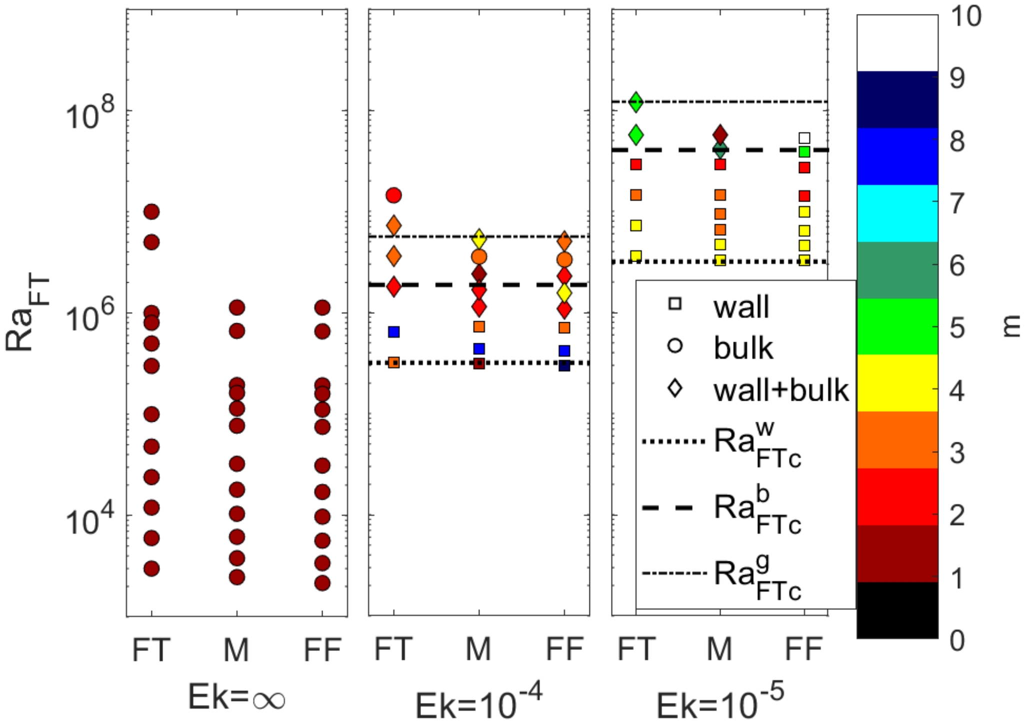

Figure 3.12: The number m of convection rolls and their location in the domain for (from left to right) $Ek = \infty$, 10^{-4}, 10^{-5}. The shapes represent the location of the convection, either at the walls (square), in the bulk (circle) or both (diamond). The colours represent the number of convection rolls m, as described by the colour bar. The dotted (dashed/ dot-dashed) line indicates where wall-localised (bulk/geostrophic) convection is predicted to onset (Favier & Knobloch, 2020).

caused by rotation (Chandrasekhar, 1961; H. Goldstein et al., 1994). Regarding the dominant mode, the linear stability analysis in section 3.3 predicted that, at onset, non-rotating convection with fixed temperature and mixed thermal boundary conditions would each have wavenumber $a = 3.1$ and 2.5, respectively. Both wavenumbers correspond to an $m = 1$ mode through Eq (3.8). The fixed flux condition caused systems to onset with $a = 0$, and therefore $m = 0$. However, these modes are only possible in a plane layer with periodic boundary conditions. Hence, the difference for the fixed flux configuration is due to the effects of geometry and aspect ratio (Charlson & Sani, 1970; Buell & Catton, 1983b).

To visualise the solution form we plot w at $z = 0.4$ and $t = 3$ for two fixed flux systems in Figure 3.13. The left plot shows a time-independent solution. On the right, a deformation from a clear $m = 1$ state is evident as the Ra_{FT} value is increased and the system becomes time-dependent. These solution forms are also representative of the non-rotating fixed temperature and fixed flux systems in the transition to time-dependence and chaotic behaviour. Comparing the horizontal solution form of w between different thermal boundary conditions, it is evident that at $Ra_{FT} = 10^5$, fixed temperature, mixed, and fixed flux configurations all have the same $m = 1$ form. However, as Ra_{FT} increases for each boundary condition, differences in w behaviour appear. As reflected in Figure 3.11, the mixed configuration maintains a less chaotic solution form in w as Ra_{FT} increases, while the fixed flux and fixed temperature boundary conditions cause systems to demonstrate chaotic behaviour for $Ra_{FT} = 2 \times 10^5$, and $Ra_{FT} = 3 \times 10^5$, respectively.

Considering systems with rotation, the centre and right panels of Figure 3.12 show the dominant mode and location of the mode for $Ek = 10^{-4}$ and 10^{-5}. At onset, wall modes are ubiquitous, as anticipated (Favier & Knobloch, 2020). Visually comparing Figure 3.11 to Figure 3.12, it is evident that the transition to chaotic behaviour coincides with the transition to bulk convection.

The onset of wall-localised convection, Ra^w_{FTc} and bulk convection, Ra^b_{FTc} is predicted to be

$$Ra^w_{FTc} = \frac{\pi^2 \left(6\sqrt{3}\right)^{1/2}}{Ek}, \tag{3.14}$$

and

$$Ra^b_{FTc} = \frac{3\left(\pi^2/2\right)^{2/3}}{Ek^{4/3}}, \tag{3.15}$$

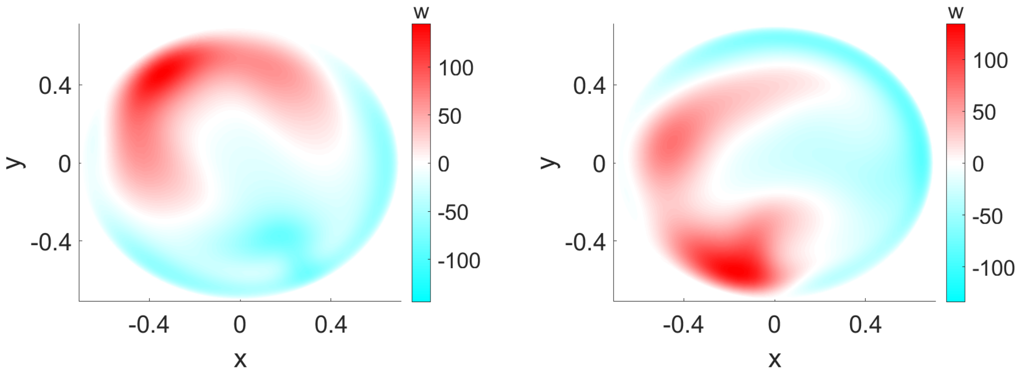

(a) FF, $Ra_{FT} = 1.6 \times 10^5$ (b) FF, $Ra_{FT} = 2 \times 10^5$

Figure 3.13: w plotted at $z = 0.3$ and $2.5 \leq t \leq 3.5$ for $Ek = \infty$, such that red indicates upward motion and blue indicates downward motion.

respectively, for any Pr and sufficiently large aspect-ratio, Γ (Chandrasekhar, 1961; Clune & Knobloch, 1993; Liao et al., 2006; Favier & Knobloch, 2020). Note that Favier and Knobloch (2020) presented results with $Pr = 1$ and $\Gamma = 0.75$ which met the predictions of Eqs (3.14) and (3.15). For $Ek = 10^{-4}$ and 10^{-5}, respectively, $Ra^w_{FTc} \approx 3 \times 10^5$ and $Ra^w_{FTc} \approx 3 \times 10^6$ and $Ra^b_{FTc} \approx 2 \times 10^6$ and $Ra^b_{FTc} \approx 4 \times 10^7$. These approximations for wall-localised and bulk convection onset are shown in Figure 3.12 by dotted lines and dashed lines, respectively.

Figure 3.12 shows that, for both $Ek = 10^{-4}$ and $Ek = 10^{-5}$, the onset to wall-localised convection meets the predicted Ra^w_{FTc} values. For $Ek = 10^{-4}$, both fixed flux and mixed configurations transition to bulk convection for lower Ra_{FT} values than predicted by Eq (3.15). Systems with fixed temperature boundary conditions were not considered at the same Ra_{FT} where fixed flux and mixed condition systems develop bulk convection, so no conclusion can be made about the fixed temperature boundary condition. Most likely, the deviation from Ra^b_{FTc} is due to the moderate Ek value which is not asymptotically small.

For $Ek = 10^{-5}$, Figure 3.12 shows that the predicted Ra^b_{FTc} value is accurate for the fixed temperature and mixed configurations. However, the fixed flux configuration causes wall-localised convection for higher Ra_{FT} values than mixed and fixed temperature conditions, which is concurrent with the transition to chaotic behaviour observed in the previous section. Figure 3.14 demonstrates the differ-

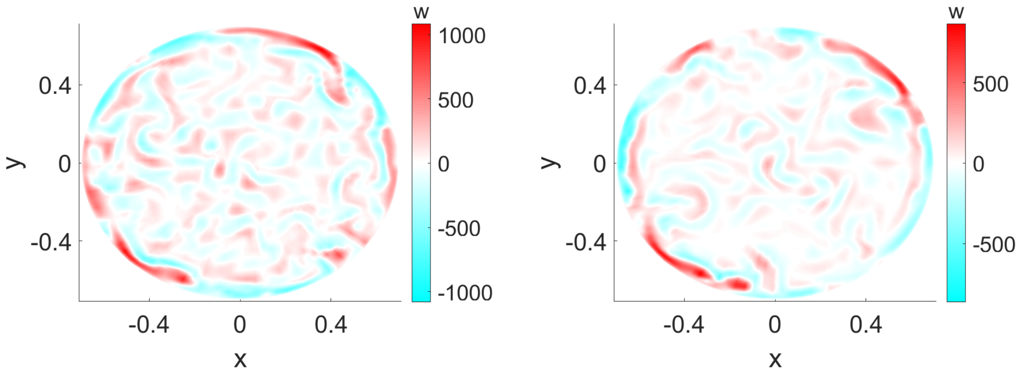

(a) FT, $Ra_{FT} = 5.67 \times 10^7$ (b) M, $Ra_{FF} = 4.2 \times 10^7$

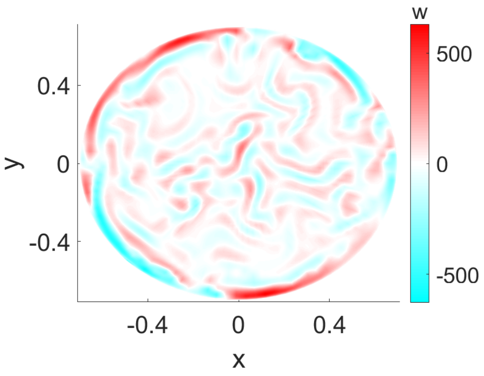

(c) FF, $Ra_{FF} = 3.9 \times 10^7$

Figure 3.14: Comparison of vertical velocity, w between boundary conditions (fixed temperature (FT), mixed (M), and fixed flux (FF)) for $Ra_{FT} \approx 4 \times 10^7$ at $z = 0.4$ for $2.5 \leq t \leq 3.5$. Blue indicates downward velocity and red indicates upward velocity.

ent horizontal solution forms around the predicted $Ra^b_{FTc} = 4 \times 10^7$. Figures 3.14a, 3.14b, 3.14c show the fixed temperature, mixed, and fixed flux systems with $Ra_{FT} = 5.7 \times 10^7$, $Ra_{FT} = 4.2 \times 10^7$, and $Ra_{FT} = 3.9 \times 10^7$, respectively.

Figure 3.14 shows that there is some flow in the bulk of each system. However, the fixed flux system has slightly weaker motion in the bulk than near the walls and is consequently categorised as a wall mode. Despite this categorisation, it is clear that the predicted onset of bulk convection is generally correct for the $Ek = 10^{-5}$ cases. We also see that for large Ra_{FT} values, that m is no longer representative of the number of convection rolls, but rather an indication of the horizontal scale of the flow structures.

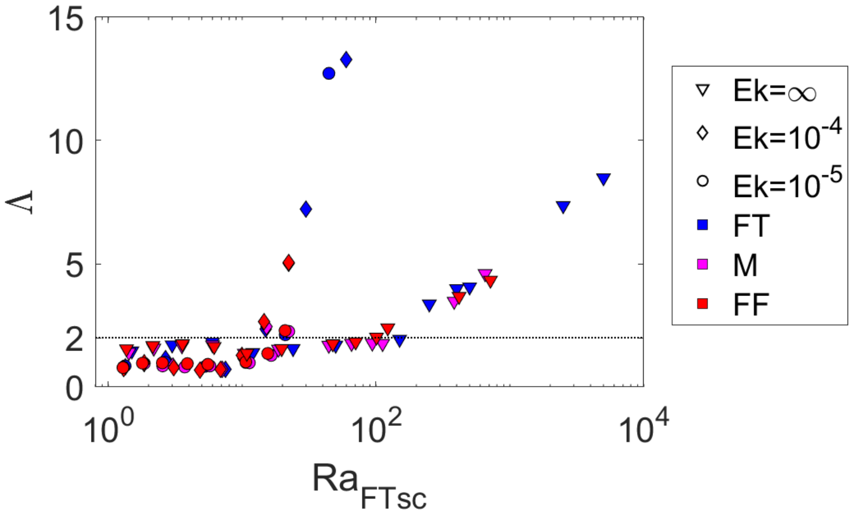

Figure 3.15: Λ calculated from Eq(3.11) vs. Ra_{FTsc} for fixed temperature (blue), mixed (magenta), and fixed flux (red) and $Ek = \infty$ (downward triangle), 10^{-4} (diamond), and 10^{-5} (circle). The dashed black line shows where $\Lambda = 2$, which indicates the transition from 2D to 3D flow.

The dominant mode number is variable across Ek and boundary conditions. For $Ek = 10^{-5}$, wall modes onset with $m = 4$. Onset predictions vary. X. Zhang et al. (2021) suggested that at onset, for $\Gamma = 0.5$ and $\Gamma = 1$, $m = 4\Gamma$. Which could be applied at present as $\Gamma = 0.7$ is in that range. While K. Zhang and Liao (2009) claims that at onset, $m = \pi\Gamma\left(2+\sqrt{3}\right)^{1/2} \approx 6\Gamma$ as $Ek \to 0$. In this case, both of the predictions are approximately correct for $Ek = 10^{-5}$ because they would each necessarily round the result to the nearest integer, thus, $m = 4$. Hence, we see that the boundary condition does not affect the solution form at onset in rapidly rotating convection.

3.5.3.2 Vertical uniformity

After the onset of bulk convection, the flow of rotating systems can enter a geostrophic regime where quasi-2D flows give way to fully 3D turbulence due to a balancing of the rotational and buoyant forces (Sprague et al., 2006). In Ecke and Niemela (2014), the onset to geostrophic turbulence is predicted at a minimum value of $Ra^g_{FTc} = 3Ra^b_{FTc}$. However there are several other suggested transition Ra_{FT} at $Ra^g_{FTc} = \frac{1.4}{Ek^{7/4}}$ (E. King et al., 2009) or $Ra^g_{FTc} = \frac{10}{Ek^{3/2}}$ (E. King et al., 2012). For

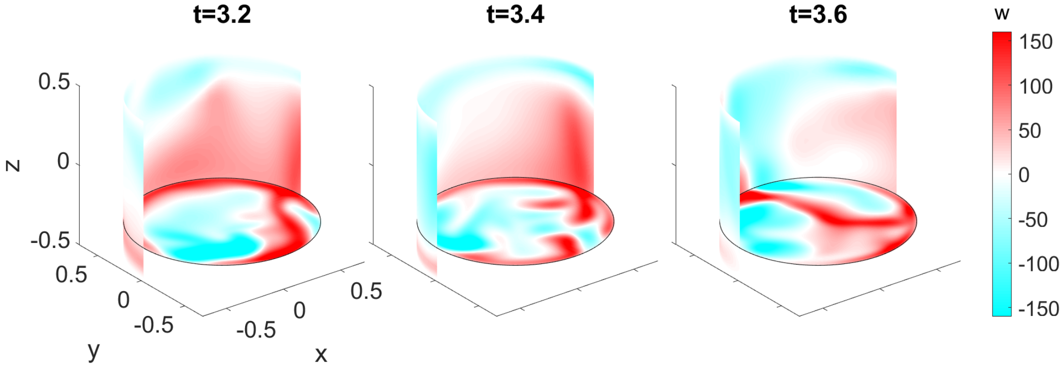

Figure 3.16: Plots of vertical velocity, w at $r = 0.685$ and $z = -0.3$ for $Ra_{FTsc} \approx 4 \times 10^2$ with $Ek = \infty$. The blue indicates downward motion and red upward, with white indicating no movement. The fixed flux configuration is shown for $Ra_{FT} = 6.6 \times 10^5$ with $\Lambda = 3$.

$Ek = 10^{-4}$, which is a larger Ek than is generally studied for geostrophic behaviour, $8\times10^6 < Ra^g_{FTc} < 2\times10^7$. When $Ek = 10^{-5}$, we consider $3\times10^8 < Ra^g_{FTc} < 8\times10^8$, which corresponds to $Ro \leq 0.33$ and the systems are consequently in the rapidly rotating regime. As seen in Figure 3.11, few of our simulated systems reach this predicted regime. Hence, we expect that relatively few systems will display 3D flow with $\Lambda > 2$.

In order to identify the transition from 2D to 3D flow, a vertical uniformity factor Λ, as described in section 3.4.3.2, is calculated. Figure 3.15 shows the Λ values, calculated using Eq (3.11), for each Ek value and boundary condition as a function of the supercriticality, $Ra_{FTsc} = Ra_{FT}/Ra^b_{FTc}$. As described in Section 3.4.3.2, $\Lambda \lesssim 2$ indicates relatively little vertical variation. As Λ increases, the vertical dimension becomes important in the flow.

Without rotation, it is clear from Figure 3.15 that 2D flow is maintained for significantly larger Ra_{FTsc} value than with rotation, as Λ does not surpass 2 until $Ra_{FTsc} \geq 10^2$. Additionally, for $Ek = \infty$, all thermal boundary conditions appear to behave similarly. It is useful to visualise an example solution for each boundary condition, here for $Ra_{FTsc} \approx 4 \times 10^2$, to understand three-dimensional flow.

Figure 3.16 compares the vertical velocity, w, for $Ek = \infty$ systems at $r = 0.685$ and $z = -0.3$. The fixed flux boundary condition system has $Ra_{FT} = 6.6 \times 10^5$ and $\Lambda = 3$. Though the solution form is not exactly consistent across thermal boundary

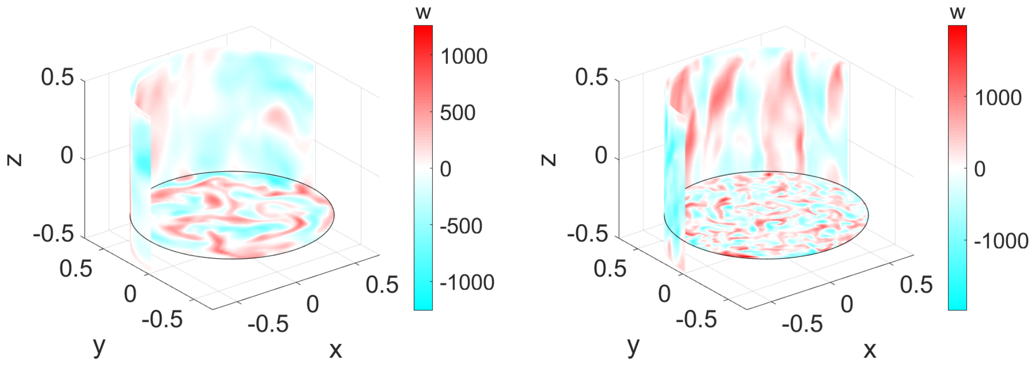

(a) $Ek = 10^{-4}$, $Ra_{FT} = 1.44 \times 10^{7}$ (b) $Ek = 10^{-5}$, $Ra_{FT} = 1.2 \times 10^{8}$

Figure 3.17: Vertical velocity, w, at $z = -0.3$ and $r = 0.665$ for fixed temperature cases with $Ra_{FTsc} > 3 \times 10^{1}$.

condition, the fixed flux case is of interest because it exemplifies the boundary behaviour at the upper boundary. The fixed $\beta = -1$ at the upper boundary causes downward velocity along the walls and near the top as the temperature difference forces fluid upward.

In rapidly rotating convection, Λ measurements agree between thermal boundary conditions. Figure 3.15 shows that, with rotation, for fixed temperature boundary conditions, the Λ factor increases rapidly as Ra_{FTsc} approaches 10^{2}. However, there are no data points for the fixed flux or mixed configurations at $Ra_{FTsc} > 30$. Thus, Figure 3.17 compares the vertical velocity, w, at $r = 0.665$ and $z = -0.3$ for the two highest Λ systems with fixed temperature boundary conditions. In Figure 3.17a, which shows a system with $Ek = 10^{-4}$ and $Ra_{FTsc} = 6 \times 10^{1}$, it is clearly very three-dimensional with many changes in velocity direction along the vertical plane, validating it's notably high Λ factor. However, Figure 3.17b, which shows vertical velocity for a system with $Ek = 10^{-5}$ and $Ra_{FTsc} = 5 \times 10^{1}$, appears at first glance to have columnar-like behaviour, not unlike that shown in systems with much lower Λ factors (such as seen in Figure 3.17a). Upon further inspection, it is clear that though the system has more columnar structure than that of Figure 3.17a, the columns are significantly broken up in the vertical and tend to lean in the horizontal, breaking vertical uniformity expected of columnar behaviour and warranting a large Λ factor.

In Figure 3.15, it is of interest to note the Ra_{FTsc} value at which the Λ factor indicates the transition from 2D to 3D flows, especially in the rotating cases, for comparison with geostrophic turbulence onset predictions. Without rotation, 3D flow begins around $Ra_{FTsc} > 10^2$, which corresponds to $Ra_{FT} = 3 \times 10^5$. For both $Ek = 10^{-4}$ and 10^{-5}, the transition occurs around $Ra_{FTsc} = 10^1$ which corresponds to $Ra_{FT} \approx 2.5 \times 10^6$ and $Ra_{FT} \approx 2.8 \times 10^7$, for the respective rotation rates. In both instances, the transition from 2D to 3D occurs at lower Ra_{FT} than the transitions predicted by E. King et al. (2009) and E. King et al. (2012), Ecke and Niemela (2014). This suggests that the aspect ratio of the system rather than the thermal boundary condition has a greater effect on the transition to geostrophic turbulence.

3.5.3.3 Zonal flow

Our final mode of investigation is the zonal solution form in the context of boundary zonal flows (BZF) which are wall-localised states coinciding with a rotation-affected bulk flow (Ecke et al., 2022). BZF is characterised by an azimuthally-periodic velocity along the walls of a given mode rotating anti-cyclonically, but time-independent in the precessing frame. Observation of the MZF as described in Section 3.4.3.3 aids in identifying wall-local modes which are independent of coinciding bulk flows.

For low Ra_{FTsc} without rotation, the mean-zonal-flow was negligible, as shown in Figure 3.18. Figure 3.18 shows the MZF value as a function of Ra_{FTsc}. The marker shape indicate the Ekman number such that circles represent systems with $Ek = \infty$, diamonds represent systems with $Ek = 10^{-4}$, and square represent systems with $Ek = 10^{-5}$. The colour of each marker shows if the simulation has fixed temperature (FT, blue), mixed (M, magenta), or fixed flux (FF, red) boundary conditions. Figure 3.18 shows a rapid decrease in MZF, which indicates the fluid is moving increasingly quickly in the clockwise direction. As expected, $Ek = 10^{-5}$ flows faster at lower Ra_{FTsc}.

It is evident that with and without rotation, the thermal boundary condition does not affect the MZF value. Hence, we suggest that boundary flows are not qualitatively affected by the thermal boundary condition. This is reasonable as the $\overline{u_{\theta t}}$ field is strongest at the wall due to the wall-localised nature of rotating

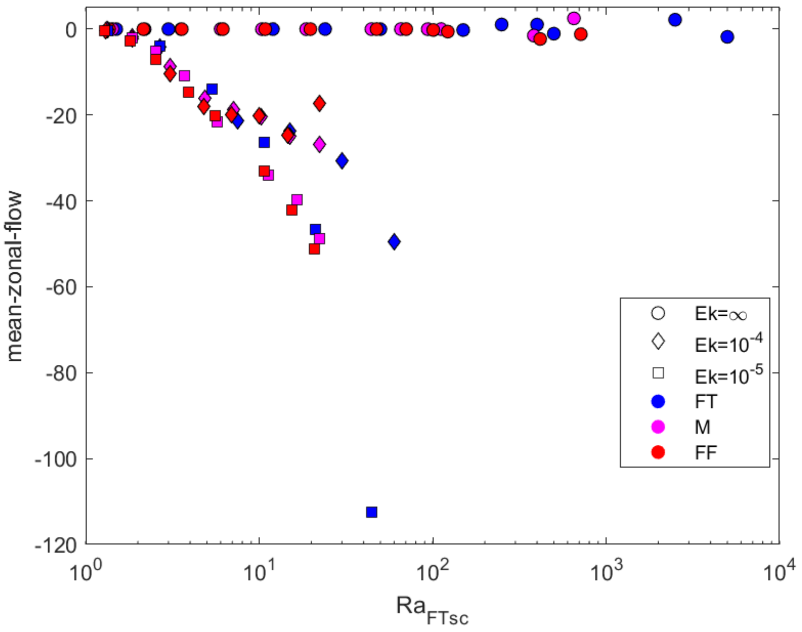

Figure 3.18: The MZF value for each boundary condition – fixed temperature (FT,blue), mixed (M,magenta), or fixed flux (FF, red) – and $Ek - \infty$ (circle), 10^{-4} (diamond), 10^{-5} (square)– as a function of Ra_{FTsc}.

convection and therefore the thermal condition of the sidewall is more important to the zonal flow dynamics than the boundary conditions in the vertical.

3.6 Summary

In summary, we have thoroughly investigated RRBC dynamics bounded with either fixed temperature, mixed, or fixed flux thermal conditions. Previous linear stability analyses in Calkins et al. (2015) and Clarté et al. (2021) found that with stress-free velocity conditions, the Ra_c and a_c values become independent of thermal boundary condition as Ek approaches 0. We provide evidence that this result also holds true for with no-slip velocity conditions and that, in a plane-layer, Ra_c and a_c converge for $Ek < 10^{-3}$. Hence, at the onset of rapidly rotating RBC in a plane-layer, the thermal boundary condition is not important.

We then consider non-linear RRBC in a cylindrical domain with $\Gamma = 0.7$ and a fluid with $Pr = 0.7$. To compare between thermal boundary conditions, we measure $\overline{Nu}$ and find Ra_{FT} value for each system using Eq (3.7). The conversion causes all boundary conditions to follow a similar $\overline{Nu} \propto Ra_{FT}^{\gamma}$ scaling for each respective Ek. However, none of our results met the predicted γ values from previous literature listed in Table 3.1. We attribute the deviation in values due to differences in calculating γ – in our case a weighted-least-square fitting while previous studies tend to use linear-regressions– and the range of Ra_{FT} values modelled along with the domain geometry and Γ, off of which vary in comparison to previous studies. Regardless, the consistency of our results suggests that universal scaling laws, such as those discussed in Plumley and Julien (2019), are applicable independent of thermal boundary condition and perhaps are independent of internal heat and cooling methods as well (Currie et al., 2020, e.g.[).

Without rotation, we see that convection onset and bulk flow structure is not generally dependent on thermal boundary condition. The main effect we have observed is that the mixed condition causes a system to transition to temporal chaos at higher Ra_{FT} values than fixed flux or fixed temperature conditions. This is concurrent with results found in Anders et al. (2020) for non-rotating fixed temperature and mixed boundary condition systems. We extend this result to rapidly rotating RBC, where it is shown that the mixed condition causes chaotic behaviour to onset at higher Ra_{FT} than fixed temperature and fixed flux cases.

Investigation into the solution forms did not find significant differences between boundary conditions at onset. This suggests that the results from our linear stability analysis – that convection onset behaviour is independent of thermal boundary condition for low Ek– is also appropriate in a small Γ cylindrical domain without rotation. Indeed our results are in agreement with the suggestion of Vieweg et al. (2021), which observed that the scale of non-rotating convection grows to fit the domain. With rotation, predictions from literature (Chandrasekhar, 1961; Favier & Knobloch, 2020) for the onset of wall-localised convection and bulk convection match well with the the results shown across boundary conditions. The only exception being the fixed flux boundary condition in the case of $Ek = 10^{-5}$ which appears to resist bulk convection to higher Ra_{FT} values. However, Figure 3.14 shows that bulk convection has begun in the fixed flux case, but is weaker than in the fixed temperature and mixed configurations. The mode of convection near onset met expectations for the $Ek = 10^{-5}$ cases (K. Zhang & Liao, 2009; X. Zhang et al., 2021). However, $Ek = 10^{-4}$ did not onset to a unanimous mode and defied predictions, likely because it has a slower rotation than the predictions are intended for.

Geostrophic turbulence, which is a regime in rotating convection which is dominated by 3D flow, is considered. Using the Λ factor defined in Section 3.4.3.2, the vertical uniformity is used to determine when the solution form transitions from rotation-affected to geostrophic turbulent flow as indicated by a vertically non-uniform solution in rotating cases (Sprague et al., 2006). However, Figure 3.15, indicates that for all boundary conditions and rotation rates the onset of 3D flow occurs before the predicted onset of geostrophic convection (E. King et al., 2009; E. King et al., 2012; Ecke & Niemela, 2014). This is not unusual, as 3D plume structures have been observed to precede geostrophic turbulence for systems with $Pr < 3$ in rotating cylindrical domains (J. S. Cheng et al., 2018).

The mean-zonal flow (MZF) is also measured in order to investigate boundary flows. As expected, any azimuthal velocity, u_θ, is negligible for systems without rotation, regardless of boundary condition and the more rapid rotation results in stronger MZF. We also find that it is evident that the development of boundary zonal flows is independent of thermal boundary condition.

In conclusion, the choice of fixed temperature, fixed flux, or mixed thermal boundary condition on the top and the bottom of an RBC or RRBC system, does not significantly affect the form of the solution to moderately high Ra_{FT}. It is very important to use the $Nu - Ra$ relationship defined in Calkins et al. (2015) in order to compare between boundary conditions and this in fact will cause the Nu scaling of all boundary conditions to collapse onto a single scaling for each Ek, as seen in Figure 3.10. The most significant difference, shown in Figure 3.11, in behaviour is the mixed thermal boundary condition's resistance to temporal chaos as fixed temperature and fixed flux systems become unstable at lower Ra_{FT}, which is in alignment with initial results found in Anders et al. (2020). Overall, the numerical thermal boundary conditions fixed temperature, mixed, and fixed flux behave very similarly, especially as Ra_{FT} increases and Ek decreases and thus may reasonably be used interchangeably in numerical studies high Ra_{FT} values.

Chapter 4

Robin Condition

In Chapter 3, we provided evidence in support of the equivalence of fixed temperature, fixed flux, and mixed (where the top boundary is fixed flux and the bottom boundary is fixed temperature) boundary conditions in rapidly rotating Rayleigh–Bénard convection (RRBC) for sufficiently large Rayleigh numbers and small Ekman numbers in a small aspect ratio cylindrical geometry. While previous studies have chosen fixed flux or mixed boundary conditions for modelling astrophysical systems and fixed temperature conditions for modelling experimental systems, the similarities between numerical thermal boundary conditions observed in Chapter 3 indicate that the fixed temperature boundary condition is sufficient for modelling dynamics in systems with the fixed flux and mixed conditions in rapidly rotating RBC models. Thus, the choice of thermal boundary condition between the three configurations considered in Chapter 3 is not the dominant factor in the interpretation of the relationship between numerical models and physical systems. However, in experimental set-ups and natural systems, the thermal behaviour at a boundary is rarely purely fixed temperature or fixed flux. Therefore, in this chapter, a novel investigation is undertaken using the Robin boundary conditions which straddles the fixed temperature and fixed flux thermal boundary conditions.

4.1 Introduction

The Robin boundary condition acts as an intermediary between fixed temperature and fixed flux conditions by relating the thermal conductivity k and depth d of the fluid to that of the bounding material through the Biot number Bi – a ratio between the height and thermal conductivity of the fluid and that of the boundary materials (Sparrow et al., 1964). The Robin condition may be formulated for several different types of boundaries (Clarté et al., 2021). In this chapter, the Robin condition such that the vertical thermal boundary condition is determined by the Bi value.

Recall from section 3.2.4, that it is useful to relate systems with different thermal boundary conditions by defining a relationship between the effective Rayleigh number Ra for each boundary condition and Ra_{FT}. There is not a ubiquitously agreed upon formulation of a Robin condition Ra. Some previous studies of the Robin boundary condition have sometimes chosen to use Ra_{FT} (O'Sullivan, 1990). Alternatively, in Gringé et al. (2007) they considered an effective Rayleigh number $Ra(Bi)$ related to Ra_{FT} such that

$$Ra_{FT} = \frac{Ra(Bi)}{1 - T_1}, \tag{4.1}$$

where T_1 is the temperature at the top of the fluid domain. Additionally, in Clarté et al. (2021) they defined

$$Ra_{FT} = \frac{Ra(Bi)}{\overline{Nu}} + \left(Ra(Bi) - \frac{Ra(Bi)}{\overline{Nu}} \right) \frac{Bi}{Bi + Bi_t}, \tag{4.2}$$

where Bi_t is a threshold found to be approximately 3. The former definition of $Ra(Bi)$ is only appropriate in a system where the lower boundary has a fixed temperature and the upper boundary is Robin. The latter appears suitable but does not follow the same logic that we have previously used to relate systems with different boundary conditions (i.e. Eq(3.7)).

Therefore, in this chapter, we seek to define a relationship for the Robin boundary condition between the effective $Ra(Bi)$ and Ra_{FT} by expanding on Eq (3.6). By defining an Ra_{FT} for each system with the Robin condition, it is possible to directly compare the heat transport scaling and temporal and spatial behaviours between the Robin condition configuration and the fixed temperature and fixed flux configurations studied in Chapter 3.

The Robin condition does not appear to have previously been studied in a rapidly rotating cylindrical geometry. Due to the applicability of the Robin condition to modelling experimental and atmospheric flows, it is of interest to study the

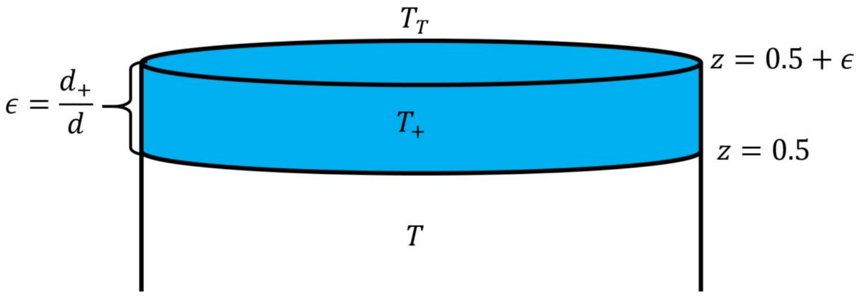

Figure 4.1: Illustration of the top boundary of a fluid domain with dimensionless parameters. See text for details.

changes in convection dynamics as the Robin condition is adjusted from the fixed temperature extreme to the fixed flux extreme with a focus on rotating systems. A concise linear stability analysis is conducted to determine the critical Rayleigh number Ra_c as a function of Bi. We calculate Bi for common experimental boundary materials to provide physical context for the Robin condition. Then, mean Nusselt number, $\overline{Nu}$ and standard deviation, σ_{Nu} from each system will be used to define a $Ra - Ra_{FT} - Nu$ relationship. Once a Ra_{FT} value is found for each system, the heat transport scaling, and temporal and spatial behaviours are compared between the various Bi values and the fixed temperature, mixed, and fixed flux boundary conditions.

4.2 Derivation of the Robin boundary conditions

In this section, we derive a thermal boundary condition on the vertical boundaries which straddles fixed temperature and fixed flux conditions. The condition is determined based on the height and thermal conductivity of the bounding materials. As described previously, the Robin condition has a formulation appropriate for boundaries with finite length and conductivity, as in an experiment (Gringé et al., 2007).

To begin, we consider the upper boundary of our fluid layer which has physical properties as indicated by subscript $\cdot_+$. The boundary has thickness d_+ which we make dimensionless following the scaling in Chapter 2 such that the nondimensional thickness is $\epsilon = \frac{d_+}{d}$. As visualised in Figure 4.1, the upper boundary (blue) has an internal temperature T_+ with a fixed temperature at the outer boundary T_T, both values are dimensionless.

We assume that heat moves through the boundary material via conduction and that the system is sufficiently wider than tall (i.e. horizontal heat transport is negligible as $\Gamma_+ \to \infty$) such that,

$$\frac{\partial T_+}{\partial t} = \frac{\kappa_+}{\kappa} \frac{\partial^2 T_+}{\partial z^2} \quad \text{at} \quad 0.5 < z < 0.5 + \epsilon, \tag{4.3}$$

where $\kappa = k/\rho c_p$ (the coefficient of thermal diffusivity) is related to thermal conductivity k, density ρ, and specific heat c_p. κ_+ measures the rate of heat transfer from the warmer boundary to the cooler boundary of the domain lid.

The fluid layer is governed by Eqs (2.11a)-(2.11c) as described in Chapter 2. The coupled system has boundary conditions

$$T_+ = T_T \quad \text{at} \quad z = 0.5 + \epsilon, \tag{4.4a}$$

$$T_+ = T \quad \text{and} \quad \frac{\kappa}{\kappa_+} \frac{\partial T}{\partial z} = \frac{\partial T_+}{\partial z} \quad \text{at} \quad z = 0.5. \tag{4.4b}$$

We further scale the system with $z = \epsilon \hat{z}$. Eq (4.3) becomes

$$\epsilon^2 \frac{\kappa}{\kappa_+} \frac{\partial T_+}{\partial t} = \frac{\partial^2 T_+}{\partial \hat{z}^2} \quad \text{at} \quad \frac{0.5}{\epsilon} < \hat{z} < \frac{0.5}{\epsilon} + 1 \tag{4.5a}$$

and the fixed temperature boundary conditions become

$$T_T = T_+ \quad \text{at} \quad \hat{z} = \frac{0.5}{\epsilon} + 1, \tag{4.5b}$$

$$T_+ = T \quad \text{at} \quad \hat{z} = \frac{0.5}{\epsilon}. \tag{4.5c}$$

Hence, at leading order ϵ, the equation of heat transport through the upper boundary is of the form $T_+ = A\hat{z} + B$. We apply the scaled boundary conditions to find that

$$T_+ = (T_T - T(\hat{z} = \frac{0.5}{\epsilon}))\hat{z} + \left(T(\hat{z} = \frac{0.5}{\epsilon}) \left(1 + \frac{0.5}{\epsilon} \right) - \frac{0.5}{\epsilon} T_T \right). \tag{4.6}$$

Then, the heat flux condition across the boundary may be approximated such that

$$\frac{k}{k_+} \frac{\partial T}{\partial z} = \frac{\partial T_+}{\partial z} = \frac{\partial T_+}{\partial \hat{z}} \frac{\partial \hat{z}}{\partial z} = \frac{T_T - T}{\epsilon} \tag{4.7}$$

at the fluid-boundary interface.

Finally, we unwrap the asymptotic scaling and find the Robin condition on an upper boundary

$$\frac{\partial T}{\partial z} = Bi_+ \left(T_T - T\right) \tag{4.8}$$

where $Bi_+ = \frac{k_+}{k}\frac{d}{d_+}$.

Generalising the Robin condition for both the top and bottom vertical boundaries,

$$\frac{\partial T}{\partial z} \cdot n_z = Bi \left(T - T_\infty\right), \tag{4.9}$$

where n_z is the vertical component of the normal vector and T_∞ is the exterior fixed temperature of the boundary (e.g. for the upper boundary $T_\infty = T_T$ and $n_z = -1$). The Biot number is generally defined as

$$Bi = \frac{k_m}{k}\frac{d}{d_m}, \tag{4.10}$$

where the subscript $\cdot_m$ indicates a property of the boundary material.

For our purposes, it is useful to prescribe T_∞ values at each boundary such that in the conducting state, the fluid maintains a linear vertical temperature profile of the form $T = -z + 0.5$ as in the fixed temperature case presented in Chapter 3. Hence,

$$T_\infty = \frac{-1}{Bi} \quad \text{at} \quad z = 0.5, \tag{4.11}$$

$$T_\infty = 1 + \frac{1}{Bi} \quad \text{at} \quad z = -0.5. \tag{4.12}$$

It is clear from Eq (4.9) that as $Bi \to \infty$, the Robin boundary condition approaches fixed temperature conditions and as $Bi \to 0$, the Robin boundary condition approaches fixed flux conditions. This makes intuitive sense, considering that large Bi indicate thin, highly conductive boundaries which would easily transfer the full T_∞ temperature to the fluid boundary and vice versa.

In order to contextualise Bi, as defined in Eq (4.10), we consider three experimental set-ups based on experiments described in Kunnen, Clercx, Geurts, et al. (2008). Table 4.1 lists the thermal conductivity k_m and thickness, d_m, of Copper, Aluminium and Plexiglas. We consider these materials to enclose a fluid layer with depth $d = 0.23$m, and thermal conductivity $k = 0.02$W/mK, which is consistent with air. In Table 4.1, the Bi values of each bounding material are found in relation to these air properties.

material	k_m (W/mK)	d_m (m)	Bi
Copper	402 (at 300K)	0.03	4.3×10^4
Aluminium	237 (at 273K)	0.03	1.1×10^3
Plexiglas	0.17	0.001	5.1×10^2

Table 4.1: The thermal conductivities for Copper (Lide, 2003), Aluminium (Touloukian et al., 1970), and Plexiglas (Morimune-Moriya & Nishino, 2021) are listed along with chosen material thicknesses are based on the experiments in Kunnen, Clercx, Geurts, et al. (2008). The Bi values are calculated for each material using Eq (4.10) assuming an interface with a layer of air 0.23m deep with thermal conductivity 0.02W/mK (Lide, 2003).

Copper has the highest Bi value, followed by Aluminium, then Plexiglas. Note that Plexiglas is generally used in a much thinner layer in experiments to compensate for low k_m. For example, if Plexiglas was considered with the same $d_m = 0.03$m as Aluminium and Copper, it would then have $Bi = 6.5 \times 10^1$, which is an order of magnitude lower than the value shown in Table 4.1.

Recall from Chapter 3, that the thermal boundary condition at the top and bottom informs the choice in thermal scaling, and thus influences the definition of the Rayleigh number. For the Robin condition, the thermal scaling is chosen to be ΔT. However, as seen in Chapter 3, as the condition becomes more similar to fixed flux, the Ra_{FT} definition is not appropriate. Therefore it is necessary to define an appropriate Rayleigh number for the Robin boundary condition dependent on the Bi value to investigate non-linear RRBC. However, linear RRBC may be considered with any Ra definition because below onset $\overline{Nu} = 1$.

4.3 Linear stability analysis

We first explore the linear aspect of RRBC with Robin boundary conditions. Using the Bi values defined for common experimental materials in Table 4.1, we investigate the importance of the Bi value in determining convection onset.

Based on the linear results presented in Clarté et al. (2021) for RRBC in a spherical shell with stress-free velocity conditions, boundaries with $Bi \geq 3 \times 10^1$ exhibit the effects of fixed temperature thermal boundary conditions. Thus, we expect that when applying each of the Bi values of the experimental setups listed in Table 4.1 to a linear RRBC system in a plane-layer, the critical Rayleigh number, Ra_c, and critial wavenumber, a_c, should be closely aligned with the fixed temperature results shown in section 3.3. Further, in Calkins et al. (2015) it is concluded that rapidly rotating systems with $Ek \leq 10^{-5}$ and stress-free velocity boundary conditions, have the same Ra_c regardless of thermal boundary condition. In Chapter 3, we determined this result to be true for systems with no-slip velocity boundary conditions and in Clarté et al. (2021) it is demonstrated that Ra_c also converges at $Ek = 10^{-5}$ for Robin condition systems with $10^0 \leq Bi \leq 10^2$ in a spherical shell.

In order to determine if the same theory is true for the range $10^{-3} \leq Bi \leq 10^3$, we utilise the Dedalus solver (Burns et al., 2016), to solve the linear RRBC equations Eqs (2.19a)-(2.19c) as described in Chapter 2. Robin thermal boundary conditions and no-slip velocity conditions are applied to the horizontal surfaces of a plane-layer geometry. Rotation rates are considered from non-rotating to rapidly rotating such that, $\infty \geq Ek \geq 10^{-6}$. The Prandtl number is $Pr = 0.7$ for consistency with the non-linear numerical set-up as well as the previous linear stability analysis in section 3.3. The Bi values are as described in Table 4.1.

Figure 4.2 visualises the results of the linear stability analysis. Results for Copper, Aluminium and Plexiglas are shown in blue, magenta, and red, respectively. Ra_c and a_c for fixed temperature and fixed flux configurations, conducted in section 3.3, are presented as dashed and dotted lines, respectively, for comparison.

The Ra_c and a_c results show that systems with $Bi \geq 5.1 \times 10^2$ behave the same at onset, regardless of rotation. Thus, we have shown, in agreement with Clarté et al. (2021), that a $Bi \geq 5 \times 10^2$ is sufficiently large Biot number to reach fixed temperature behaviour at convection onset. Fixed flux and fixed temperature systems have different Ra_c and a_c without rotation (Calkins et al., 2015), thus we anticipate that sufficiently low Bi would have different Ra_c and a_c from fixed temperature results. This result has been shown in previous non-rotating studies

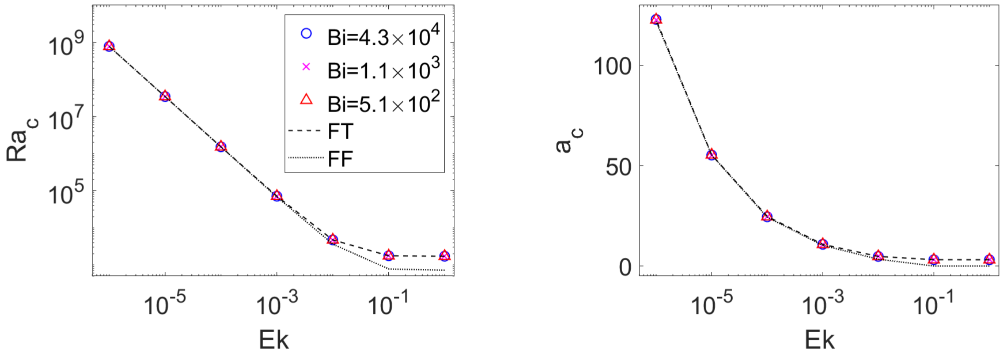

(a) Ra_c vs. Ek (b) a_c vs. Ek

Figure 4.2: Graphs of critical Rayleigh number Ra_c and wavenumber a_c as functions of Ek respectively. Results are plotted for linear stability analysis in a plane-layer with Robin thermal conditions and Bi relating to Copper (blue circle), Aluminium (magenta x) and Plexiglas (red triangle), respectively. Results for fixed temperature (dashed line) and fixed flux (dotted line) configurations are also shown.

(Dowling, 1988) and in a rotating spherical-shell with stress-free conditions (Clarté et al., 2021).

4.4 Effective Rayleigh number definition

As we increase the Rayleigh number of an RRBC system, the dynamics experience non-linear effects and $\overline{Nu}$ increases. Hence, the effective $Ra(Bi)$ deviates from Ra_{FT}. As demonstrated in Chapter 3, it is useful to define the Ra of a system in reference to the fixed temperature Rayleigh number Ra_{FT} in order to compare RRBC systems with different thermal boundary conditions. In Calkins et al. (2015), a relationship between Ra_{FT}, Nu, and the effective Rayleigh number for the fixed flux thermal boundary condition, Ra_{FF}, is defined such that $Ra_{FF} = \overline{Nu}Ra_{FT}$. Recall from Eq (3.10) that we define $Nu = \beta d/\Delta T$. In this section, we expand the relationship between $\overline{Nu}$, Ra_{FT}, and the effective Ra to determine Ra as a function of the Bi value.

4.4.1 Theory

The expression Eq (3.7) suggests that for the Robin condition, where boundary conditions range from fixed temperature to fixed flux dependent on the Biot number, Bi, there may be a relationship between the effective Ra, which depends on Bi, and the resulting Nu, and the fixed temperature Rayleigh number, Ra_{FT}. When the temperature is fixed, $Ra(Bi = \infty) = Ra_{FT}$ and when the flux is fixed $Ra(Bi = 0) = Ra_{FF} = Ra_{FT}Nu$. Thus, a definition is proposed such that,

$$Ra(Bi) = Ra_{FT}Nu^{\lambda_{Bi}}, \tag{4.13}$$

where the Ra conversion power λ_{Bi} is a function of Bi. For fixed temperature systems, $\lambda_{\infty} = 0$ and for fixed flux system, $\lambda_0 = 1$. Consequently, $0 \leq \lambda \leq 1$.

Next, we consider how Nu scales with Ra_{FT} such that,

$$\overline{Nu} \propto Ra_{FT}^{\gamma_{FT}}, \tag{4.14}$$

where $\gamma_{FT} = \gamma_{Bi=\infty}$ is a constant for fixed temperature boundary conditions. Now consider that for each respective Bi and Ek, there is a unique heat transport scaling γ_{Bi} where

$$\overline{Nu} \propto Ra(Bi)^{\gamma_{Bi}}. \tag{4.15}$$

By substituting the definition of $Ra(Bi)$ from Eq (4.13) into Eq (4.15), we find λ_{Bi} such that,

$$\overline{Nu} \propto \left(Ra_{FT}Nu^{\lambda_{Bi}}\right)^{\gamma_{Bi}},$$

and thus,

$$\overline{Nu} \propto Ra_{FT}^{\frac{\gamma_{Bi}}{1-\lambda_{Bi}\gamma_{Bi}}}. \tag{4.16}$$

The scaling of Ra_{FT} to $\overline{Nu}$ for any Bi is $\gamma_{Bi}/(1-\lambda_{Bi}\gamma_{Bi})$, wherein γ_{Bi} is calculated by fitting data from simulations to a power-law in the form of Eq (4.15). We propose that, from Eqs (4.14) and (4.16),

$$\frac{\gamma_{Bi}}{1-\lambda_{Bi}\gamma_{Bi}} = \gamma_{FT}. \tag{4.17}$$

Note that fixed temperature conditions are equivalent to $Bi = \infty$, and therefore $\gamma_{FT} = \gamma_{\infty}$ in that limit. Solving Eq (4.17) for λ_{Bi} yields,

$$\lambda_{Bi} = \frac{1}{\gamma_{Bi}} - \frac{1}{\gamma_{\infty}}. \tag{4.18}$$

We are only able to measure the Ra conversion power λ_{Bi} a posteriori.

4.4.1.1 Non-linear simulations

Hence, it is necessary to conduct a full set of non-linear simulations spanning Bi, Ra, and Ek space. The numerical RRBC set-up described in Chapter 2 with governing equations Eq(2.11a)-(2.11c) is solved with Nek5000 (Nek5000, 2019). The cylindrical domain has aspect-ratio $\Gamma = 0.7$, the Prandtl number is $Pr = 0.7$, and Ekman numbers, $Ek = \infty$, 10^{-4}, and 10^{-5}, are considered for comparison with the fixed temperature and fixed flux thermal boundary results reported in Chapter 3. The same values of Ra are modelled as for the fixed temperature configuration as listed in Appendix C. No-slip velocity conditions are applied on all surfaces and the sidewalls are thermally insulating. On the horizontal boundaries, we apply the Robin condition as defined in Eq (4.9) with $10^{-3} \leq Bi \leq 10^3$ to span the parameter range from sufficiently close to fixed flux conditions to sufficiently close to fixed temperature conditions (Clarté et al., 2021).

4.4.2 Rayleigh number conversion power as a function of Biot number

The results of the numerical model for a fixed Bi value are used to calculate λ_{Bi} using (4.18). The value of γ_∞ is measured from the fixed temperature results presented in Chapter 3 for each Ekman number. The results for γ_∞ and γ_0 (fixed flux) are reiterated in Table 4.2.

In order to find γ_{Bi}, lines of the form $\overline{Nu} \propto Ra(Bi)^{\gamma_{Bi}}$ are fitted to each set of modelled Ra values with fixed Bi and Ek values, using a weighted-least-squares method. Each γ_{Bi} measurement has an associated standard deviation σ_γ. The calculated γ_{Bi}, σ_γ, and resulting 99% confidence interval (CI) of the form $\gamma_{Bi} \pm 3\sigma_\gamma$ are summarised for $10^{-3} \leq Bi \leq 10^3$ in the first five columns of Table 4.2.

Figure 4.3 visualises the measurements for γ_{Bi} as a function of $\log(Bi)$. The fixed temperature (FT) and fixed flux (FF) results are indicated by blue lines and red lines respectively. The solid lines show $\gamma_{\infty,0}$ while the dotted lines show the 99% confidence interval of the form $\gamma \pm 3\sigma_\gamma$. Despite relating to $Bi = \infty$ and $Bi = 0$, respectively, the fixed temperature and fixed flux γ values are shown at all Bi to observe the limits at which moderate Bi tend toward each extreme. For each

Bi	Ek	γ_{Bi}	σ_{γ}	γ_{Bi} 99% CI	λ_{Bi}	σ_{λ}	λ_{Bi} 99%CI
0	∞	0.234	0.007	$0.215 - 0.254$	0.887	0.178	$0.352 - 1.42$
0	10^{-4}	0.426	0.030	$0.336 - 0.516$	0.575	0.496	$-0.912 - 2.06$
0	10^{-5}	0.512	0.068	$0.308 - 0.716$	0.830	0.473	$-0.590 - 2.25$
10^{-3}	∞	0.229	0.008	0.205 - 0.253	0.983	0.161	0.5 - 1.466
10^{-3}	10^{-4}	0.421	0.021	0.358 - 0.484	0.601	0.445	-0.734 - 1.936
10^{-3}	10^{-5}	0.512	0.079	0.275 - 0.749	0.831	0.406	-0.387 - 2.049
10^{-2}	∞	0.23	0.006	0.212 - 0.248	0.969	0.111	0.636 - 1.302
10^{-2}	10^{-4}	0.43	0.019	0.373 - 0.487	0.554	0.442	-0.772 - 1.88
10^{-2}	10^{-5}	0.524	0.057	0.353 - 0.695	0.784	0.343	-0.245 - 1.813
10^{-1}	∞	0.24	0.012	0.204 - 0.276	0.794	0.211	0.161 - 1.427
10^{-1}	10^{-4}	0.425	0.016	0.377 - 0.473	0.578	0.439	-0.739 - 1.895
10^{-1}	10^{-5}	0.523	0.064	0.331 - 0.715	0.788	0.359	-0.289 - 1.865
10^{0}	∞	0.234	0.006	0.216 - 0.252	0.892	0.104	0.58 - 1.204
10^{0}	10^{-4}	0.525	0.022	0.459 - 0.591	0.13	0.438	-1.184 - 1.444
10^{0}	10^{-5}	0.586	0.02	0.526 - 0.646	0.581	0.28	-0.259 - 1.421
10^{1}	∞	0.252	0.006	0.234 - 0.27	0.586	0.091	0.313 - 0.859
10^{1}	10^{-4}	0.526	0.043	0.397 - 0.655	0.128	0.458	-1.246 - 1.502
10^{1}	10^{-5}	0.357	0.305	-0.558 - 1.272	1.679	2.414	-5.563 - 8.921
10^{2}	∞	0.287	0.007	0.266 - 0.308	0.109	0.089	-0.158 - 0.376
10^{2}	10^{-4}	0.55	0.098	0.256 - 0.844	0.045	0.538	-1.569 - 1.659
10^{2}	10^{-5}	0.797	0.181	0.254 - 1.34	0.131	0.395	-1.054 - 1.316
10^{3}	∞	0.293	0.003	0.284 - 0.302	0.032	0.038	-0.082 - 0.146
10^{3}	-10^{-4}	0.556	0.092	0.28 - 0.832	0.023	0.524	-1.549 - 1.595
10^{3}	10^{-5}	0.88	0.15	0.43 - 1.33	0.013	0.335	-0.992 -1.018
∞	∞	0.296	0.001	$0.292 - 0.300$	0	0.033	$-0.099 - 0.099$
∞	10^{-4}	0.564	0.092	$0.289 - 0.839$	0	0.608	$-1.82 - 1.82$
∞	10^{-5}	0.889	0.145	$0.454 - 1.33$	0	0.387	$-1.16 - 1.16$

Table 4.2: A list of $\overline{Nu}-Ra(Bi)$ scaling, γ_{Bi} and corresponding standard deviation, σ_{γ}, and 99% confidence interval of the form $\gamma_{Bi} \pm 3\sigma_{\gamma}$. λ_{Bi}, standard deviation, σ_{λ}, and 99% confidence interval are calculated with Eq (4.18). Results for $Bi = 0$ and $Bi = \infty$ are from fixed flux and fixed temperature results, respectively, presented in Chapter 3.

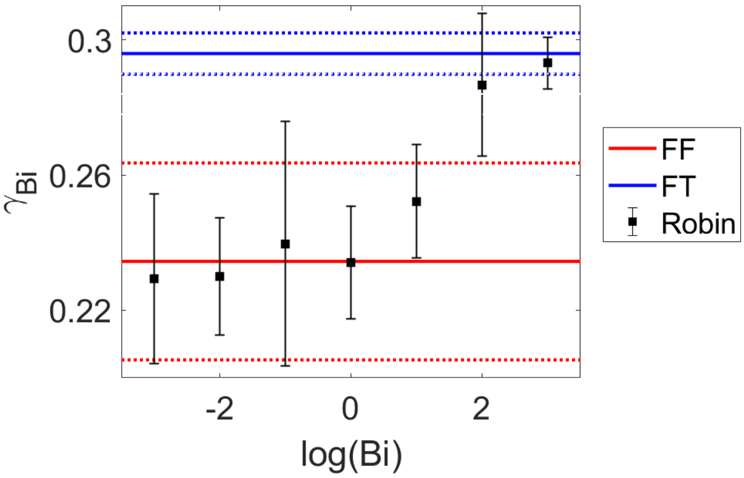

Figure 4.3: Heat transport scaling factor γ_{Bi} for $Ek = \infty$ with $10^{-3} \leq Bi \leq 10^{3}$, indicated by black square markers with error bars indicating a 99% confidence interval of $3\sigma_{\gamma}$. The blue solid line is γ_{FT} from fixed temperature simulations with confidence intervals indicated by blue dashed lines. The red solid line is γ_{FF} from fixed flux simulations with confidence intervals indicated by red dashed lines.

Bi, a square marker with error bars represent the γ_{Bi} value and the corresponding 99% confidence interval.

The γ_{Bi} results presented in Figure 4.3 show that, without rotation, as Bi increases from 10^{0}, γ_{Bi}, tends toward γ_{∞}, indicated by the black squares moving toward the blue line for larger Bi. However, by $Bi = 10^{0}$, γ_{Bi} is very close to γ_{0}, and as Bi decreases, γ_{Bi} varies slightly about γ_{0}. We anticipated that systems would imitate the fixed flux configuration for $Bi \leq 10^{-2}$ (Clarté et al., 2021). However, that prediction was derived in a spherical-shell geometry with a fixed temperature inner core. Hence, the deviations between our results and those presented in Clarté et al. (2021) are likely due to the differences in geometry and boundary condition arrangements between the two studies. Additionally, the ranges of uncertainty for γ_{0} and $Bi \leq 10^{0}$ are relatively large, and the predicted behaviour is within the confidence interval.

The γ_{Bi} and σ_{γ} values are measured for $Ek = \infty$, 10^{-4} and 10^{-5} are presented in Table 4.2. Using Eq (4.18), λ_{Bi} is found for each Bi and Ek and uses error

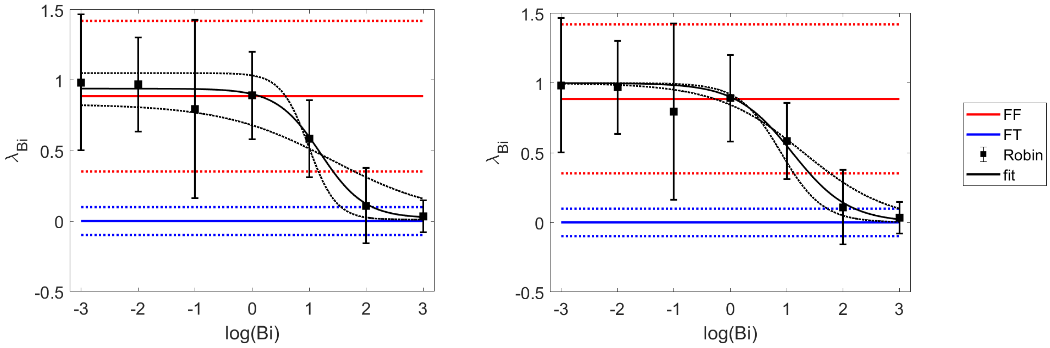

(a) ‘Full’ fit

(b) ‘Constrained’ fit

Figure 4.4: Plot of the λ_{Bi} as a function of Bi calculated from Eq(4.18) for non-rotating systems. Values of λ_∞ and λ_0 are indicated in blue (red) for fixed temperature (fixed flux) configurations. The dashed line indicates the bounds of the 99% CI. For each Bi, λ_{Bi} is given by a black square with error bars of $3\sigma_\lambda$ which represents a 99% CI. The data points are fitted to a line of the form in Eq (4.20) with two methods. The coefficients for the ‘full’ and ‘constrained’ equations are provided in Tables 4.3 and 4.4, respectively.

propagation to find a standard deviation σ_λ for each such that,

$$\sigma_\lambda = \sqrt{\left(\frac{\sigma_\gamma}{\gamma_{Bi}^2}\right)^2 + \left(\frac{\sigma_{\gamma_\infty}}{\lambda_\infty^2}\right)^2} \tag{4.19}$$

(Ku et al., 1966).

The λ_{Bi} values with corresponding confidence intervals for the non-rotating case are visualised in Figure 4.4. These values, as well as those for $Ek = 10^{-4}$ and 10^{-5} (not pictured), appear to have a $\tanh(\log(Bi))$ form. Alternatively, λ_{Bi} could be of the form $Bi/(Bi+j)$ where j is a constant unique for each Ek. However, it was not found to successfully collapse data onto γ_{FT} in the current study. Therefore, it is assumed that λ has the form,

$$\lambda_{Bi} = -A\tanh\left(B\left(\log\left(Bi\right) + D\right)\right) + E, \tag{4.20}$$

where A, B, D, and E are constants to be determined through line-fitting. Using a weighted - least - squares fitting method, all constants were determined for each Ek in two methods: ‘full’ and ‘constrained’. The ‘full’ approach allows all variables to be fitted to the data, while the ‘constrained’ method sets $A = 0.5$ and $E = 0.5$

Ek	A	B	D	E
∞	0.46 ± 0.06	1.3 ± 0.78	-1.2 ± 0.21	0.48 ± 0.05
10^{-4}	0.25 ± 0.06	4.5 ± 160	0.22 ± 8.0	0.32 ± 0.06
10^{-5}	0.46 ± 0.56	0.54 ± 1.2	-1.0 ± 2.8	0.37 ± 0.41

Table 4.3: Results for λ_{Bi} coefficients for an equation of the form in Eq (4.20) by Ek with 99% confidence interval.

Ek	A	B	D	E
∞	-0.5	1.0 ± 0.35	-1.1 ± 0.20	0.5
10^{-4}	-0.5	0.32 ± 0.24	1.7 ± 1.0	0.5
10^{-5}	-0.5	0.42 ± 0.31	-0.23 ± 0.89	0.5

Table 4.4: Results for λ_{Bi} coefficients for an equation of the form Eq (4.20) by Ek with 99% confidence interval, in the 'constrained' method fixing A and E.

such that the line matches the bounds of the under pinning theory. The coefficients determined by the 'full' method are recorded in Table 4.3 and by the 'constrained' method results are in Table 4.4. Each coefficient is presented in the form $A \pm \sigma_A$, where σ_A is the standard deviation. It is evident from both tables that there is significant uncertainty in the fitting for $Ek = 10^{-4}$, though more so from the 'full' method. This is likely due to fewer $Ra(Bi)$ considered for $Ek = 10^{-4}$ than for other rotation rates.

Figure 4.4 exemplifies the two fitting methods for $Ek = \infty$, where the dashed line is the 'full' method and the solid line is the 'constrained' approach. In this case, both lines appear to fit the data well and generally approach 0 and 1 as Bi approaches ∞ and 0, respectively. However, it is favourable to use the 'constrained' method as it enforces the limits of the theory which underpinned the development of this scaling.

4.4.3 Method comparison

Recall that the motivation for calculating λ_{Bi} is to find the Ra_{FT} for each $Ra(Bi)$ using Eq (4.13). Also, recall our assumption that by using Eq (4.13), for a set of systems with varying $Ra(Bi)$ and Bi and fixed Ek, the γ values should be the same. The same assumption is applicable to the $Ra(Bi)$ definitions, Eqs (4.1) and (4.2), used in Gringé et al. (2007) and Clarté et al. (2021), respectively. It is of interest to compare the resultant $Ra(Bi)$ values from the 'full' and 'constrained' methods of defining λ_{Bi} for Eq (4.13) to the $Ra(Bi)$ values calculating using methods from the previous literature.

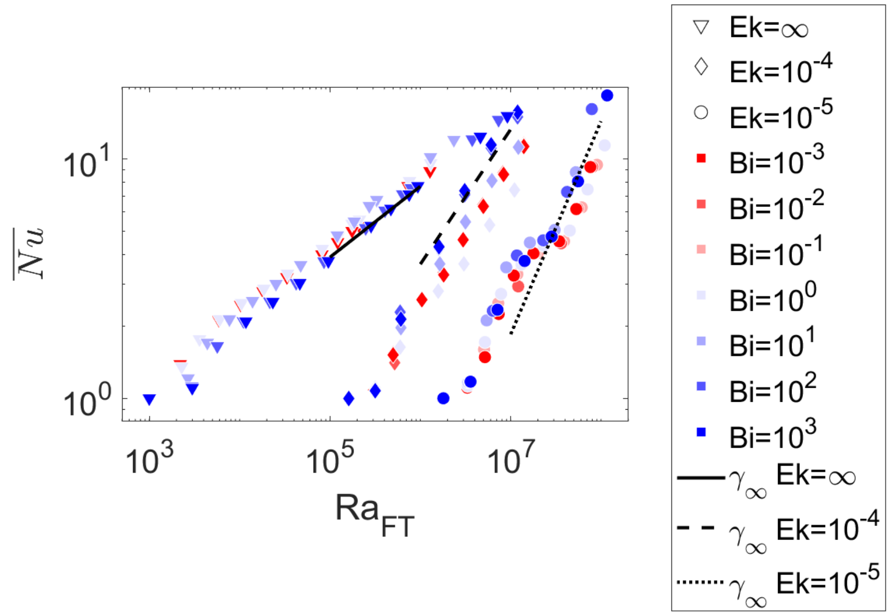

(a) 'Full' method

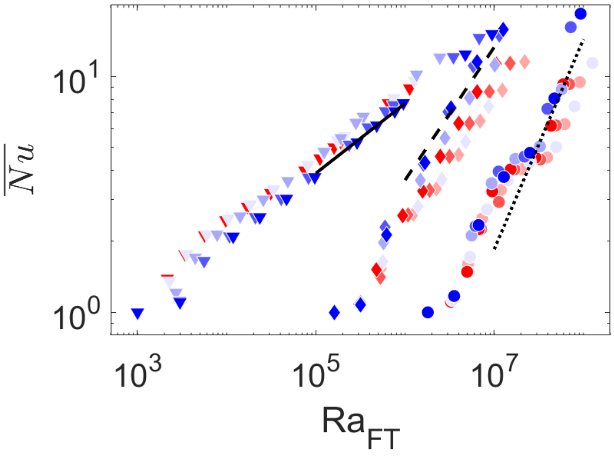

(b) 'Constrained' method

Figure 4.5: Plots of $\overline{Nu} - Ra_{FT}$ vs Ra_{FT} calculated using Eq (4.13) and the two different methods of defining λ_{Bi} as in Eq (4.20): 'full' and 'constrained'. See Figure 4.5d for further details.

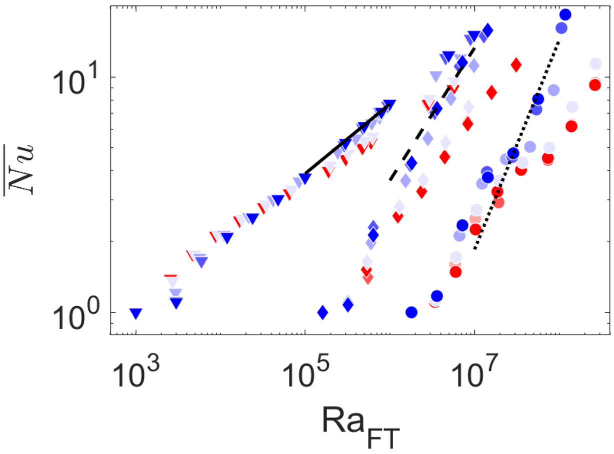

(c) Eq (4.1) from Gringé et al. (2007)

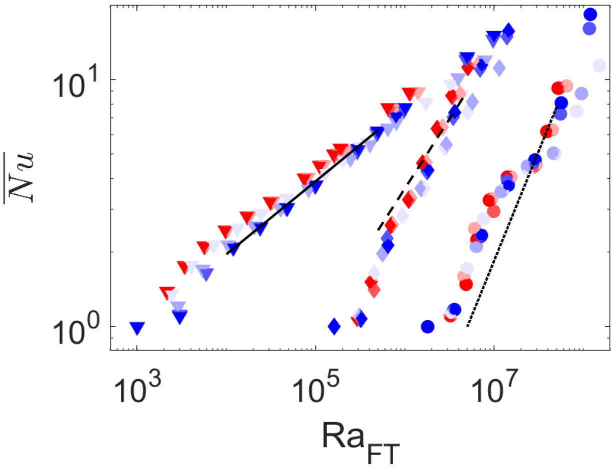

(d) Eq (4.2) from Clarté et al. (2021)

Figure 4.5: Plots of $\overline{Nu}$ vs. Ra_{FT} calculated three ways. The first two methods use Eq (4.13) and the two different methods of defining λ_{Bi} as in Eq (4.20): 'full' and 'constrained'. The third method follows Eq (4.1) as suggested in Gringé et al. (2007). Finally, we use the definition in Eq (4.2) from Clarté et al. (2021). Each Ek is represented by a marker shape: inverted triangles for $Ek = \infty$, diamonds for $Ek = 10^{-4}$, and circles for $Ek = 10^{-5}$. As $\log(Bi)$ approaches -3, it becomes more red, and as $\log(Bi)$ approaches 3 it becomes more blue. $Bi = 10^0$ is a very light blue shade, rather than white, for visibility. The black lines indicate the fixed temperature, or $Bi = \infty$ $\overline{Nu} - Ra_{FT}$ scaling, γ_∞ for each Ek such that the scaling for: $Ek = \infty$ is a solid line, $Ek = 10^{-4}$ is a dashed line, and $Ek = 10^{-5}$ a dotted line.

Figure 4.5 visualises the result of transforming $Ra(Bi)$ to Ra_{FT} using four different methods. The first two methods use Eq (4.13) where λ_{Bi} is defined by Eq (4.20). The coefficients for Eq (4.20) are determined in two ways: the ‘full’ method, shown in Figure 4.5a, and the ‘constrained’ method, shown in Figure 4.5b. The third method, shown in Figure 4.5c, follows Eq (4.1) from Gringé et al. (2007). The final definition considered is Eq (4.2) from Clarté et al. (2021), with results shown in Figure 4.5d.

In each plot, Ek values are indicated by the marker shape. Inverted triangles represent systems with $Ek = \infty$, diamonds represent systems with $Ek = 10^{-4}$, and circles represent systems with $Ek = 10^{-5}$. The distinct Biot numbers, Bi, are indicated by marker colour. As Bi approaches 10^{-3}, the colour becomes darker red, and as Bi approaches 10^{3}, the colour becomes darker blue. Note $Bi = 10^{0}$ is faint blue rather than white to be visible on the plot. An assumption made in Eq (4.13) is that after converting Ra_{Bi} to Ra_{FT}, all systems of the same Ek will have the same $\overline{Nu} - Ra_{FT}$ scaling as fixed temperature systems, γ_{∞}. Therefore, γ_{∞} for each Ek, as listed in Table 4.2, is shown on each plot as such: $Ek = \infty$ is shown as a solid line, $Ek = 10^{-4}$ is shown as a dashed line, and $Ek = 10^{-5}$ is shown as a dotted line.

All methods visualised in Figure 4.5 demonstrate reasonable ability to collapse data with the Robin condition and different Bi onto a $\overline{Nu} - Ra_{FT}$ scaling like that of the fixed temperature configuration. This is evident by the data in each figure, for each Ek grouping around the black lines indicating γ_{∞}. However, in each case, the Bi which scale most similarly to the fixed temperature case are the $Bi \geq 10^{2}$ systems. This makes sense because their Ra_{Bi} are naturally closest to Ra_{FT} because of the nature of their thermal boundary condition. For the ‘full’ and ‘constrained’ methods, it appears from Figures 4.5a and 4.5b, respectively, that systems with $10^{-2} > Bi > 10^{2}$ scale less similarly to γ_{∞} than the more extreme values of Bi. This could be due to differences in solution form, or because the uncertainty in the λ_{Bi} definition is strongest for moderate Bi, causing their Ra_{FT} values to be less accurate. This could be remedied in future studies by simulating more moderate Bi. Alternatively, Eq (4.1), does not collapse low Bi systems to γ_{∞} very well for any Ek, as seen in Figure 4.5 by the red shaded markers being

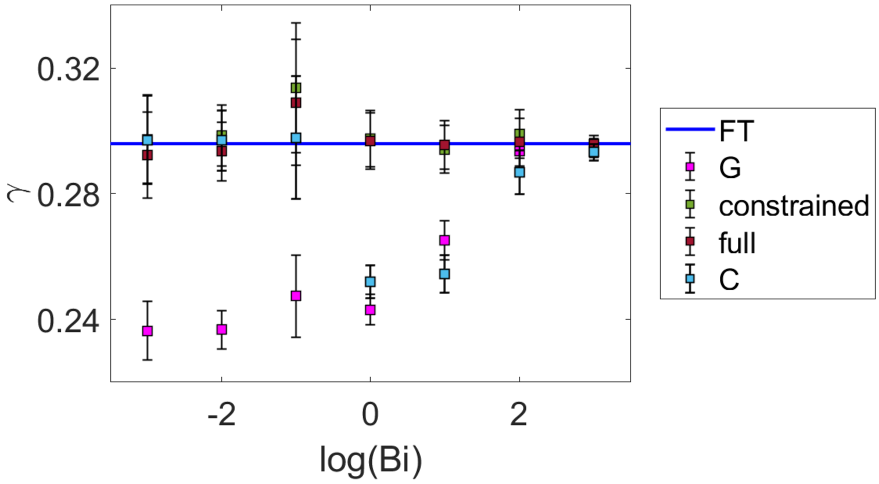

Figure 4.6: γ as a function of Bi compared with γ_∞ (blue line) as measured from each method of Ra_{FT} calculation. The $Nu \propto Ra_{FT}^{\gamma}$ scaling for each Bi for systems without rotation are shown for the Ra_{FT} measure from Gringé et al. (2007) by magenta squares (G) and Clarté et al. (2021) by cyan squares (C). The 'constrained' ('full') method results are green (dark red). The error bars are σ_γ.

furthest from the black lines. Notably, using the method defined in Clarté et al. (2021) resulted in the best agreement of scaling for the full range of Bi. Though, as in the other methods, the moderate Bi values deviate most from the γ_∞ scaling while the high and low Bi scale very closely with γ_∞.

Figure 4.6 exemplifies the differences in $\overline{Nu} - Ra_{FT}$ scaling corresponding to the respective Ra_{FT} calculation methods for $Ek = \infty$. The results from the 'constrained' and 'full' configurations of Eq(4.13), Eq (4.1) from Gringé et al. (2007), and Eq (4.2) from Clarté et al. (2021) are indicated by square of green, dark red, magenta, and cyan colours, respectively. The error bars indicate σ_γ, which is a 65% confidence interval. The blue line shows γ_{FT} from the fixed temperature simulations to which all Bi should collapse if the Ra_{FT} calculation is accurate enough.

The magenta squares in Figure 4.6, which represent the calculation suggested in Gringé et al. (2007), are evidently the least appropriate method, closely followed by the $Ra(Bi)$ definition suggested in Clarté et al. (2021), to enable all Bi results to follow the fixed temperature heat transport scaling. The 'constrained' case and the 'full' configurations result in γ values closer to γ_∞ for majority of Bi values. There is no obvious superior fitting between the two configurations of Eq(4.13).

Thus, as there is not much disparity in their ability to convert Ra_{Bi} to Ra_{FT}, it is preferable to choose the 'constrained' method as this ensures the theoretical limits of Eq (4.13) are met.

Hence, we have defined an effective Rayleigh number $Ra(Bi)$, which is a function of the Biot number, in relation to the fixed temperature Rayleigh number Ra_{FT} such that $Ra(Bi) = Ra_{FT} Nu^{\lambda}_{Bi}$. The equation for λ_{Bi} has been derived in Eq (4.18) with 'constrained' coefficients listed in Table 4.4.

4.5 Analysis of non-linear results

By applying Eq (4.13) with Eq(4.20) and coefficients in Table (4.4), the effective Rayleigh number for each Bi, Ra_{Bi}, is transformed into the fixed temperature Rayleigh number, Ra_{FT}. Hence, we are able to compare the heat transport, temporal and spatial behaviours between systems with varying Bi values as well as between systems with Robin, fixed temperature, and fixed flux boundaries. Thus, the numerical results of the model discussed in section 4.4.1.1 are analysed using the same tools as described in section 3.4.

4.5.1 Heat transport scaling

In section 4.4, we transformed $Ra(Bi)$ into Ra_{FT} using Eqs (4.13) and (4.20) with the coefficients listed in Table 4.4. Recalling the relationship been the Nusselt number and Ra_{FT}, $\overline{Nu} \propto Ra^{\gamma}_{FT}$, we compared the γ values of the systems with Robin boundaries to those with fixed temperature boundaries as reported in Chapter 3. Observing Figures 4.5b and 4.5b, it was shown that the γ values measured for the Robin configurations were sufficiently close to γ_{FT} without rotation. However, in Chapter 3, we found that γ_{FT} did not align with γ values from previous literature. Hence, it is of interest to compare γ values of RRBC systems with Robin boundaries to γ values from previous studies, which are listed in Table 3.1. Note that we are unaware of any prior measurements of γ for RRBC in a cylindrical domain with Robin boundary conditions.

Figure 4.7 shows the $\overline{Nu} - Ra_{FT}$ relationship for Robin condition systems in comparison with γ from previous literature. The Bi and Ek parameter values of

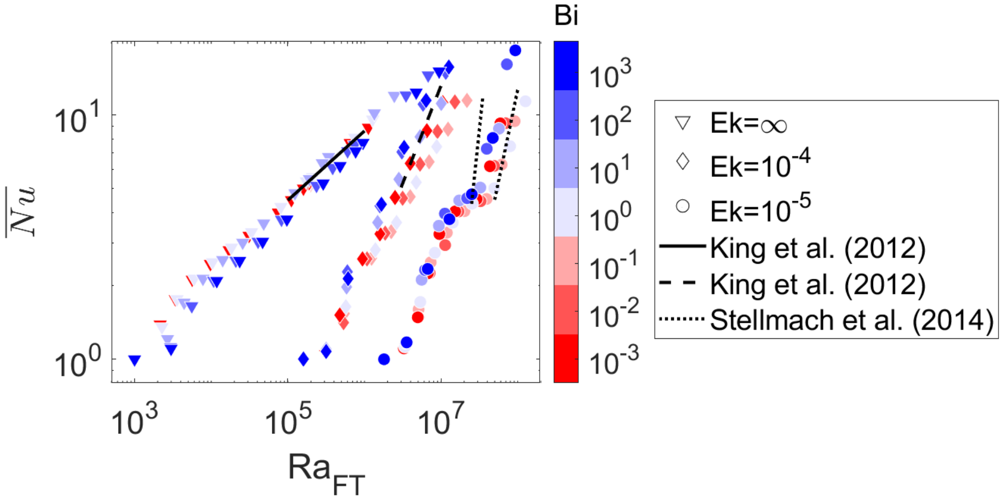

Figure 4.7: Plot of $\overline{Nu}$ vs. Ra_{FT} for RRBC systems with Robin boundary conditions. Each system has unique Bi and Ek values, shown by the colour and shape of each marker, respectively. The black lines show the γ values from previous literature where the solid, dashed, and dotted lines indicate $\gamma = 0.284$, 0.8 (E. King et al., 2012), and $1.5 \leq \gamma \leq 3$ (Stellmach et al., 2014), respectively.

each simulation are shown by colour and marker shape, respectively. The colour becomes more blue (red) as Bi approaches 10^3 (10^{-3}). For each Ek value represented in figure 4.7 there is a corresponding γ from previous literature indicated by a black line. In E. King et al. (2012), it is reported that $\gamma = 0.284$ (solid line) and 0.8 (dashed line) for $Ek = \infty$ and 10^{-4}, respectively, from physical experiments in a cylinder with aspect-ratio $0.5 \leq \Gamma \leq 2$ and $Pr = 7$. In Stellmach et al. (2014), they find that $1.5 \leq \gamma \leq 3$ (dotted lines) from numerical and asymptotic results in a plane-layer with $Pr = 1$ and 7. The γ measurements for each configuration with fixed Bi and Ek values are recorded in Table 4.5.

Observing the relationship between $\overline{Nu}$ and Ra_{FT} in cases without rotation, Figure 4.7 shows that for $Ra_{FT} > 10^5$, configurations with all Bi values behaviour similarly. In the same range of Ra_{FT} values, systems with each Bi appear to scale similarly to the $\gamma = 0.284 \pm 0.006$ prediction from E. King et al. (2012). According to the γ measurements recorded in Table 4.5, the 99% confidence intervals for each Bi value overlaps with the CI of the predicted γ value. However, the mean predicted $\gamma > 0.285$ for all Bi values, which is similar to our findings for fixed temperature and fixed flux configurations in Chapter 3.

For $Ra_{FT} < 10^5$, the γ value increases as Bi increases. This suggests that either the relationship $Ra_{eff} = Ra_{FT}Nu^{\lambda}$ is not appropriate at low Ra_{FT} or that the form of the fluid behaviour is significantly different between boundary conditions for low Ra_{FT} without rotation. We expect the latter to be the case because the coefficients of λ have been calculated for $Ra_{FT} > 10^5$ to align with the ranges of Ra_{FT} values used in previous literature. Hence, we have shown that without rotation, systems with Robin boundary conditions and $10^{-3} \leq Bi \leq 10^3$ have similar global heat transport.

Considering RRBC, we compare the 99% CIs reported in Table 4.5 for systems with $Ek = 10^{-4}$ to the fixed temperature $\gamma = 0.564 \pm 0.276$, as reported for $Bi = \infty$ in Table 4.2. All Bi values considered have CIs which overlap with the fixed temperature value. As for the fixed temperature and fixed flux boundary conditions in Chapter 3, the γ measurements for Robin condition systems with $Ek = 10^{-4}$ are much lower than the $\gamma = 0.8$ predicted in E. King et al. (2012). We observe from Figure 4.7 that systems with $Ek = 10^{-4}$ and moderate Bi values deviate from the fixed temperature γ measurement. However, the deviation of systems with moderate Bi values is indicative of different spatial and temporal behaviours to those in the extreme Bi value systems.

Though RRBC with $Ek = 10^{-4}$ was considered in Clarté et al. (2021), their results demonstrate significantly different behaviour to the $Ek = 10^{-4}$ results found here. Clarté et al. (2021) did not contain quantitative measurements of γ for systems with Robin boundary conditions. However, we do not believe their qualitative results are comparable to the systems studied in this thesis because they found that convection onset at $Ra_{FT} = 2 \times 10^6$ with $Ek = 10^{-4}$, which is an order of magnitude larger than our findings. This difference is not due to the cylindrical geometry used in this thesis compared to the spherical-shell domain used in Clarté et al. (2021) because previous studies of fixed temperature convection in a spherical shell, such as Gastine et al. (2016), have shown convection onset around $Ra_{FT} = 2 \times 10^5$. Hence, we will not compare quantitative heat transport results for the RRBC systems shown in Figure 4.7 to the results in Clarté et al. (2021).

Increasing rotation, we observe that systems with Robin boundary conditions and $Ek = 10^{-5}$ exhibit the same heat transport relationship as systems with fixed

$\log(Bi)$	$\log(Ek)$	γ	σ	99%CI
-3	∞	0.297	0.014	0.276 - 0.318
-3	-4	0.595	0.041	0.534 - 0.656
-3	-5	0.971	0.290	0.540 - 1.403
-2	∞	0.298	0.010	0.284 - 0.313
-2	-4	0.561	0.032	0.514 - 0.608
-2	-5	0.957	0.192	0.672 - 1.243
-1	∞	0.314	0.021	0.283 - 0.345
-1	-4	0.509	0.023	0.475 - 0.543
-1	-5	0.849	0.170	0.596 - 1.102
0	∞	0.297	0.009	0.284 - 0.311
0	-4	0.604	0.030	0.560 - 0.649
0	-5	0.865	0.045	0.799 - 0.931
1	∞	0.294	0.008	0.283 - 0.306
1	-4	0.570	0.051	0.494 - 0.647
1	-5	0.391	0.394	-0.197 - 0.978
2	∞	0.299	0.008	0.288 - 0.311
2	-4	0.576	0.107	0.417 - 0.736
2	-5	0.930	0.248	0.561 - 1.299
3	∞	0.295	0.003	0.291 - 0.299
3	-4	0.571	0.097	0.426 - 0.716
3	-5	0.952	0.176	0.691- 1.213

Table 4.5: The scaling, γ, between $\overline{Nu}$ and Ra_{FT} for systems with the Robin thermal boundary condition with $10^{-3} \leq Bi \leq 10^{3}$ and $Ek = \infty$, 10^{-4}, or 10^{-5}. The standard deviation for each γ measurement, σ, is derived from the uncertainty due to time-averaging and line-fitting. The 99% confidence interval is reported as $\gamma \pm 3\sigma$.

temperature boundary conditions, as shown in Chapter 3. That is, configurations with both fixed temperature and Robin boundary conditions have a change in $\overline{Nu} = Ra_{FT}$ slope around $Ra_{FT} = 3 \times 10^{7}$. Quantitatively comparing γ results for the Robin condition in Table 4.5 to the fixed temperature results, noted as $Bi = \infty$ in Table 4.2, RRBC with the Robin condition generally has $\gamma > \gamma_{FT}$, though the γ values are within the fixed temperature CI. Note that as in the fixed temperature and fixed flux cases, the scaling is much lower than the predicted range of $1.5 \leq \gamma \leq 3$ from Stellmach et al. (2014). These differences are likely due to the shift in scaling around $Ra_{FT} = 3 \times 10^7$.

The deviation of γ measurements for systems with moderate Bi values from the behaviour of extreme Bi is less evident for $Ek = 10^{-5}$ than $Ek = 10^{-4}$. However, as Ra_{FT} increases, the configuration with $Bi = 10^0$ appears to scale less steeply than systems with other Bi values.

In this section, we have shown that the global heat transport behaviour rotating and non-rotating RBC with Robin boundary conditions are similar to those measured in systems with fixed temperature conditions in Chapter 3. In non-rotating RBC systems with Robin boundary conditions Nu scaling is not dependent on the Bi value. Alternatively, moderately and rapidly rotating systems where $Ek \leq 10^{-4}$ demonstrate Bi-dependent heat transport scaling. This is in contrast to qualitative results presented in Clarté et al. (2021) which showed that the $\overline{Nu} - Ra_{FT}$ relationship is independent of Bi value. This difference in heat transport behaviours may be due to the different $Ra(Bi)$ definition, geometry, or Pr value used in Clarté et al. (2021). In order to determine if the Bi-dependence observed in this section is an artefact of our $Ra(Bi)$ definition or if the flow is affected by the Robin condition, we will investigate temporal and spatial behaviours with varying Bi values.

4.5.2 Time-dependence

Having observed that the heat transport behaviour is dependent on Bi value in RRBC configurations with Robin thermal boundary conditions, we aim to identify differences in temporal behaviour related to changes in Bi value. Results are also compared to those found for the fixed temperature and fixed flux configurations in Chapter 3. The analysis is conducted using the same process as reported in section 3.4.2. Thus, in this section, each RRBC system is categorised as either: conducting, time-independent, oscillating, quasi-oscillating, or temporally chaotic.

The temporal behaviour category of each system with unique Ek, Ra_{FT}, and Bi values is summarised in Figure 4.8. Plots of $\log(Bi)$ vs. Ra_{FT} are shown for fixed Ek values. Temporal behaviour is indicated by the marker shape. Circles are used to represent conducting systems which are not convecting. Diamonds

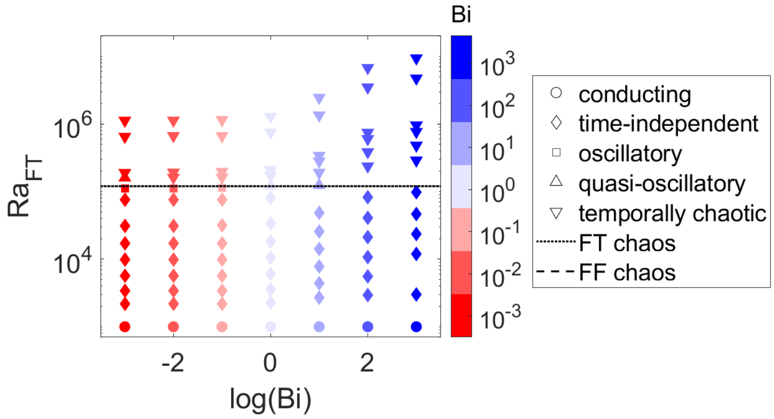

(a) $Ek = \infty$

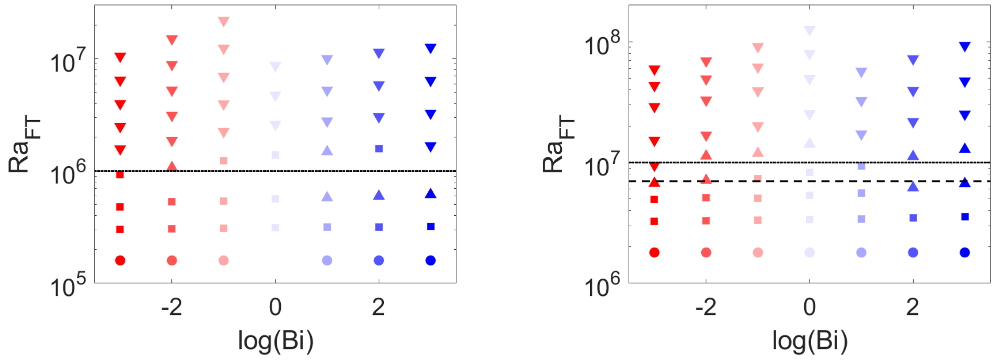

(b) $Ek = 10^{-4}$

(c) $Ek = 10^{-5}$

Figure 4.8: Plots of $\log(Bi)$ vs. Ra_{FT} for fixed Ek values of RRBC systems with Robin boundary conditions. The shapes indicate time-dependence category as such: circles represent conduction, diamonds represent time-independence, squares represent oscillation, upright triangles represent quasi-oscillation, and inverted triangles represent temporal chaos. The black lines show the Ra_{FT} values of the transition to temporal chaos in systems with fixed temperature (FT, dotted) and fixed flux (FF, dashed) conditions.

represent time-independent systems. Squares represent oscillating systems and upright triangles show quasi-oscillating systems. Finally, inverted triangles represent temporally chaotic systems. Dotted and dashed black lines respectively show the Ra_{FT} values at which fixed temperature and fixed flux systems transition to temporal chaos. Note where only one line is shown the Ra_{FT} values are the same for the transition to chaos in both fixed temperature and fixed flux configurations.

Consider Figure 4.8a which shows the temporal variation of non-rotating systems. Convection onset occurs at similar Ra_{FTc} values across Bi value, which we anticipated due to the similarity of Ra_{FTc} values for fixed temperature and fixed flux systems found in Chapter 3. Time-independent behaviour is ubiquitous across Bi from onset to $Ra_{FT} = 8 \times 10^4$.

The transition to time-dependent behaviour is observed to be affected by Bi value. Systems with $Bi \leq 10^1$ transition into oscillatory and quasi-oscillatory behaviour for $8 \times 10^4 \leq Ra_{FT} \leq 1.6 \times 10^5$. However, cases with $Bi > 10^1$ were not simulated for that range of Ra_{FT} values. In Chapter 3, it was shown that fixed flux and fixed temperature boundary conditions led to the onset of temporally chaotic behaviour at $Ra_{FT} = 1.2 \times 10^5$. Ubiquitously, the Robin condition systems transition to chaotic behaviour for $Ra_{FT} > 2 \times 10^5$, which is in good agreement with the fixed temperature and fixed flux transition. Overall, it is evident that without rotation, the temporal behaviour of RBC is not affected by Bi value.

Considering $Ek = 10^{-4}$, convection onset is shown in Figure 4.8b by the transition from circular to square markers. For all Bi values, onset consistently occurs around $Ra_{FT} = 2.5 \times 10^5$, which is in agreement with previous studies, and our previous results that found that as Ek decreases Ra_{FTc} converges for all thermal boundary conditions (Calkins et al., 2015; Clarté et al., 2021). Further, at onset, RRBC is oscillatory for all Bi values, driven by the rotation. Configurations with the highest and lowest Bi values transition to temporal chaos by $Ra_{FT} = 1.5 \times 10^6$, which is appropriate for the fixed flux and fixed temperature predictions. However, as the Bi approaches 10^0, the transition to chaos occurs at higher Ra_{FT}. This is an interesting result which suggests that systems with moderate Bi values resist chaotic behaviour to higher Ra_{FT}.

Let us investigate the cases with $Ek = 10^{-5}$ to see if moderate Bi values cause changes in temporal behaviour in rapidly rotating RBC. As anticipated, Figure 4.8c shows that the onset of convection occurs around $Ra_{FTc} = 2.5 \times 10^6$ across all Bi values. Configurations with moderate Bi values transition to temporal chaos at $Ra_{FT} = 3 \times 10^7$ while cases with $Bi = 10^3$ transition at $Ra_{FT} = 2 \times 10^7$ and $Bi = 10^{-3}$ transition at the lowest $Ra_{FT} = 10^7$. The early onset of chaotic behaviour in fixed flux-like system with Robin condition and $Bi = 10^{-3}$ is in agreement with the results in Chapter 3. Additionally, the resistance of Robin condition systems with moderate Bi to chaotic behaviour gives further merit to the hypothesis that moderate Bi behave differently from extreme Bi systems.

Overall, it is found that the time dependence of non-rotating convection is not affected by the Bi value in systems with Robin thermal boundary conditions. At onset, the rotating systems show the results which agree with the linear prediction that thermal boundary conditions do not affect convection onset in rapidly rotating systems (Calkins et al., 2015). However, the transition to temporal chaos is dependent on Bi value in RRBC. Moderate Bi values – that is $10^{-1} \leq Bi \leq 10^1$ – are non-chaotic to higher Ra_{FT} values than extreme Bi values. An investigation of spatial behaviour of the fluid motion will further illuminate the causes of these differences in temporal variation.

4.5.3 Spatial structures

In the previous sections, it was shown that applying the Robin condition to RRBC systems causes changes in both heat transport and temporal behaviour when the Biot number approaches $Bi = 10^0$. However, rotating systems with extreme Bi values and non-rotating systems behave similarly to configurations with fixed flux or fixed temperature boundary conditions, respectively. In order to understand the flow dynamics, we use the tools described in section 3.4.3 to analyse spatial structures in the horizontal, vertical, and zonal directions. Each direction provides insight to why $\overline{Nu} - Ra_{FT}$ scaling and time-dependence does or does not vary between systems with different Bi values. Additionally, vertical uniformity and zonal flow measurements are used to determine transition from the rotation-affected flow to the geostrophic regime, which is predicted to onset for $Ra_{FT} \geq 3Ra_{FTc}$ (Ecke et al., 2022).

4.5.3.1 Horizontal flow structure

The flow in the horizontal plane is first considered. As described in section 3.4.3.1, we identify the number m and location of convection rolls. Figure 4.9 shows plots of $\log(Bi)$ vs. Ra_{FT} for each Ek value. The m value is shown by the colour of each marker. The dominant convection can take place either along the wall, in the bulk, or distinct modes in both the bulk and along the wall, as indicated by square, circle, or diamond markers, respectively. The predicted onset of wall-localised (Eq (3.14)), bulk (Eq (3.15)), and geostrophic convection ($Ra^g_{FTc} = 3Ra_{FTc}$) are shown by the dotted, dashed, and dash-dotted lines, respectively (Chandrasekhar, 1961; Ecke & Niemela, 2014; Favier & Knobloch, 2020).

Without rotation, the Robin condition has uniform behaviour for all Bi values. Figure 4.9a shows that convection is ubiquitously in the bulk with $m = 1$ convection rolls. This result agrees with the findings for both fixed temperature and fixed flux systems discussed in section 3.5. The bulk convection is expected because wall-localised convection is driven by rotation (Chandrasekhar, 1953). The critical wavenumbers a_c for $0 < Bi < \infty$ are predicted to span the range $0 < a < 3.2$ in a plane-layer (Hurle et al., 1967; Dowling, 1988). Using Eq (3.8) from Gao and Behringer (1984), a_c is related to m and predicts $m = 0$ as $Bi \to 0$ and $m = 1$ for $Bi \to \infty$. However, as mentioned in Chapter 3, the effect of lateral boundaries causes $m = 0$ to be nonphysical and hence we also anticipate $m = 1$ for systems with fixed flux-like boundaries. Therefore, we have shown that the horizontal flow structure is not affected by Bi value in non-rotating convection.

On the other hand, we have previously observed Bi- dependent temporal and heat transport behaviours in rotating convection. Considering Figure 4.9b, which shows the horizontal behaviour for RRBC with Robin conditions and $Ek = 10^{-4}$, it is clear that at onset, all systems have wall-localised $m = 3$ rolls. Section 3.3 found that in a plane layer systems with fixed temperature and fixed flux thermal boundary conditions should have $a = 25$, which, using Eq (3.8), would relate to $m = 11$. Thus, it is clear that the onset wavenumber is significantly different in

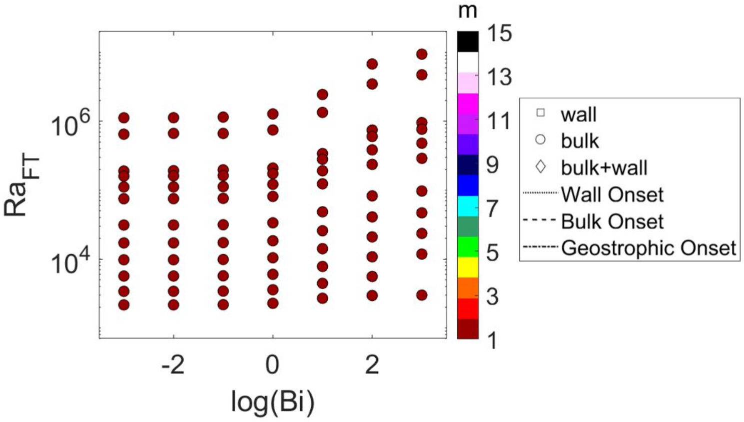

(a) $Ek = \infty$

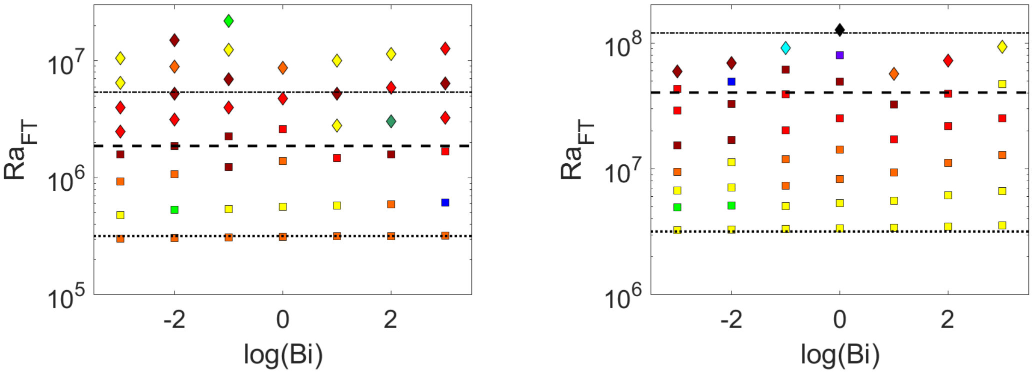

(b) $Ek = 10^{-4}$ (c) $Ek = 10^{-5}$

Figure 4.9: Plots of $\log(Bi)$ vs Ra_{FT} for each respective Ek with markers indicating the number of convection rolls m and the location of the dominant convection structure. The colours show m, as defined in the colour-bar. The marker shape represents the location of dominant convection: along the wall (square), in the bulk (circle), or both (diamond). In rotating systems, the onset of wall-localised convection (dotted lines), bulk convection (dashed lines), and geostrophic convection (dot dashed lines) are predicted from Eq (3.14), Eq (3.15), and $Ra_{FTg} = 3Ra^{b}_{FTc}$ (Ecke & Niemela, 2014) respectively.

the narrow aspect-ratio considered here than in the plane layer used in the linear stability analysis which does not develop wall modes. However, the uniformity across Bi suggests that the different thermal condition does not strongly affect horizontal behaviour at onset.

As Ra_{FT} increases away from onset, the horizontal form of the flow becomes dependent on Bi value. The critical Rayleigh number for wall-localised convection Ra^w_{FTc} and bulk convection Ra^b_{FTc} are predicted for fixed temperature conditions by Eqs (3.14) and (3.15), respectively (Chandrasekhar, 1961; Favier & Knobloch, 2020). Though derived for infinite plane layers, these equations have been shown to be appropriate for similar Γ in Favier and Knobloch (2020) where $\Gamma = 0.75$ and $Pr = 1$ with fixed temperature boundaries. For $Ek = 10^{-4}$, it is predicted that $Ra^w_{FTc} = 3 \times 10^5$ and $Ra^b_{FTc} = 2 \times 10^6$, as shown by the dotted and dashed lines in Figure 4.9b. While the onset of bulk convection meets the prediction for some Bi values, when $Bi \to 10^0$ the Ra^b_{FTc} value increases. The transition to bulk convection coincides with the transition to temporal chaos as seen by comparing Figure 4.8b to Figure 4.9b.

Figure 4.10 shows vertical velocity w at $z = 0.3$ and $t = 3$ behaviour around transitions to bulk convection and temporal chaos for RRBC with Robin conditions and $Ek = 10^{-4}$. Cases with $Bi = 10^{-3}$, 10^0 and 10^{-3} are compared in side-by-side plots of vertical velocity, w, at $z = 0.3$. For each Bi value, an $1.4 \times 10^6 \leq Ra_{FT} \leq 1.6 \times 10^6$ and $2.5 \times 10^6 \leq Ra_{FT} \leq 3.2 \times 10^6$ are each considered to visualise behaviour on either side of the predicted transition to bulk convection $Ra^b_{FTc} = 2 \times 10^6$.

For each Bi value, it is clear that flow velocity increases in the bulk and becomes more spatially complex as the Ra_{FT} value increases. However, as seen in Figure 4.9b, the convection in the bulk of $Bi = 10^{-3}$ and 10^3 has less relative strength than the case with $Bi = 10^0$ for the same Ra_{FT}. Additionally, $Bi = 10^3$ has the most spatially chaotic behaviour, where convection is equally dominant in the bulk as along the walls, while $Bi = 10^{-3}$ has strong bulk convection, but retains clear wall-localised behaviour. At a similar Ra_{FT} value, $Bi = 10^0$ has relatively weak bulk convection, in comparison with its wall-localised flow. These observations support the hypothesis that RRBC with moderate Bi values resist both temporal and spatial chaos to larger Ra_{FT} values than extreme Bi.

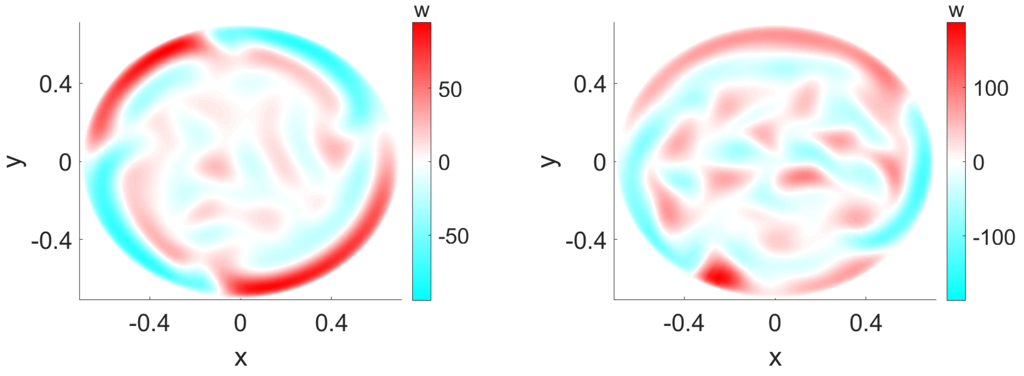

(a) $Bi = 10^{-3}$, $Ra_{FT} = 1.5 \times 10^6$ (b) $Bi = 10^{-3}$, $Ra_{FT} = 2.5 \times 10^6$

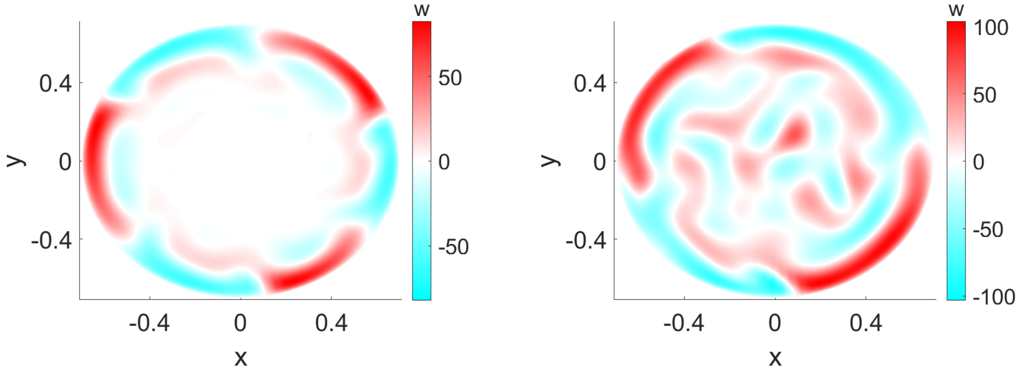

(c) $Bi = 10^0$, $Ra_{FT} = 1.4 \times 10^6$ (d) $Bi = 10^0$, $Ra_{FT} = 2.6 \times 10^6$

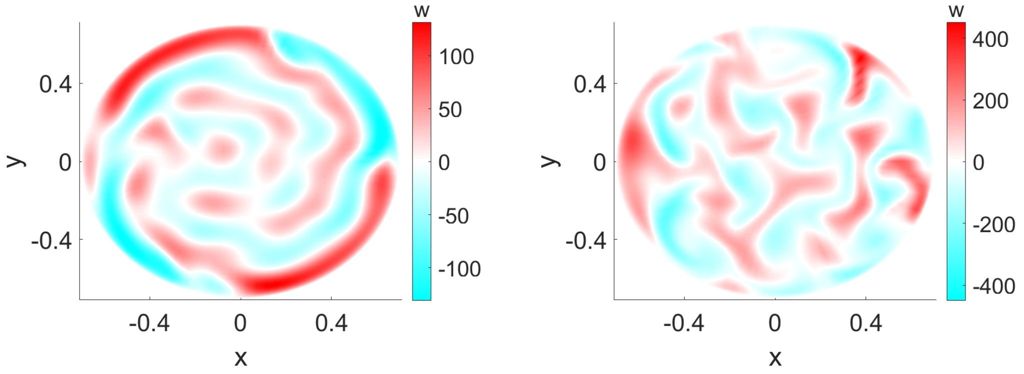

(e) $Bi = 10^3$, $Ra_{FT} = 1.6 \times 10^6$ (f) $Bi - 10^3$, $Ra_{FT} = 3.2 \times 10^6$

Figure 4.10: Plots of vertical velocity w at $z = 0.3$ and $t = 3$ for systems with $Ek = 10^{-4}$ and $Bi = 10^{-3}$, 10^0, or 10^3. On the left (right) are systems with Ra values just below (above) the predicted transition to bulk convection, $Ra^b_{FTc} = 2 \times 10^6$ and the observed transition to time dependence (see Figure 4.8).

Observing the horizontal flow behaviour for RRBC with $Ek = 10^{-5}$, summarised in Figure 4.9c we note that at onset, all systems exhibit a $m = 4$ wall-localised mode. This behaviour is consistent with the fixed temperature and fixed flux results. After convection onset, it is evident that the number of convection rolls is dependent on Bi number. Though for $Bi > 10^{-2}$, as Ra_{FT} increases, m transitions from 4 to 3 then 2 until bulk convection onset.

The critical Rayleigh numbers for wall-localised convection and bulk convection are predicted from Eqs (3.14) and (3.15) to be $Ra^w_{FTc} = 2\times10^6$ and $Ra^b_{FTc} = 4\times10^7$. Figure 4.9c shows that the wall onset results match the prediction well. However, the transition to bulk convection is dependent on Bi value, where $Bi = 10^1$ and 10^{-3} appear to meet the prediction best. This is inconsistent with results for fixed temperature and fixed flux systems, where it was shown that fixed temperature systems meet the transition to bulk convection predictions better than the fixed flux systems with $Ek = 10^{-5}$. In section 3.5, we determined that fixed temperature systems transitioned to bulk convection at the predicted Ra^b_{FTc} while fixed flux systems retained wall-localised convection for higher Ra_{FT}. Therefore, we expected that high Bi better fit the predicted critical Rayleigh number than low Bi, which is the opposite of the behaviour indicated in Figure 4.9c. Recall that the transition to temporal chaos followed a similar pattern in Figure 4.8c.

Figure 4.11 shows horizontal plots of w for $Bi = 10^{-3}$, 10^0, and 10^3 at Ra_{FT} values slightly above and below the predicted $Ra^b_c = 4 \times 10^7$. The results for $Bi = 10^3$ support the observations in Figure 4.9c, showing that wall modes are dominant for $Ra_{FT} > 4 \times 10^7$, the predicted Ra^b_{FTc}. For $Bi = 10^{-3}$, both Ra_{FT} values visualised show bulk convection but at low magnitudes relative to the wall modes. Meanwhile, for $Bi = 10^0$, the lower Ra has no bulk movement, but when Ra_{FT} is increased some small bulk convective motion is shown. While the wall-localised convection is clearly dominant in all cases shown in Figure 4.11, as Bi increases, it is seen that bulk convection is slower to develop. However, note that the Ra_{FT} visualised for the high Bi cases is somewhat lower than that of the moderate cases, which could account for the difference in solution form.

Overall, it is evident that, as with heat transport and time-dependence, the horizontal structure of flow in non-rotating convection is not affected by the Robin

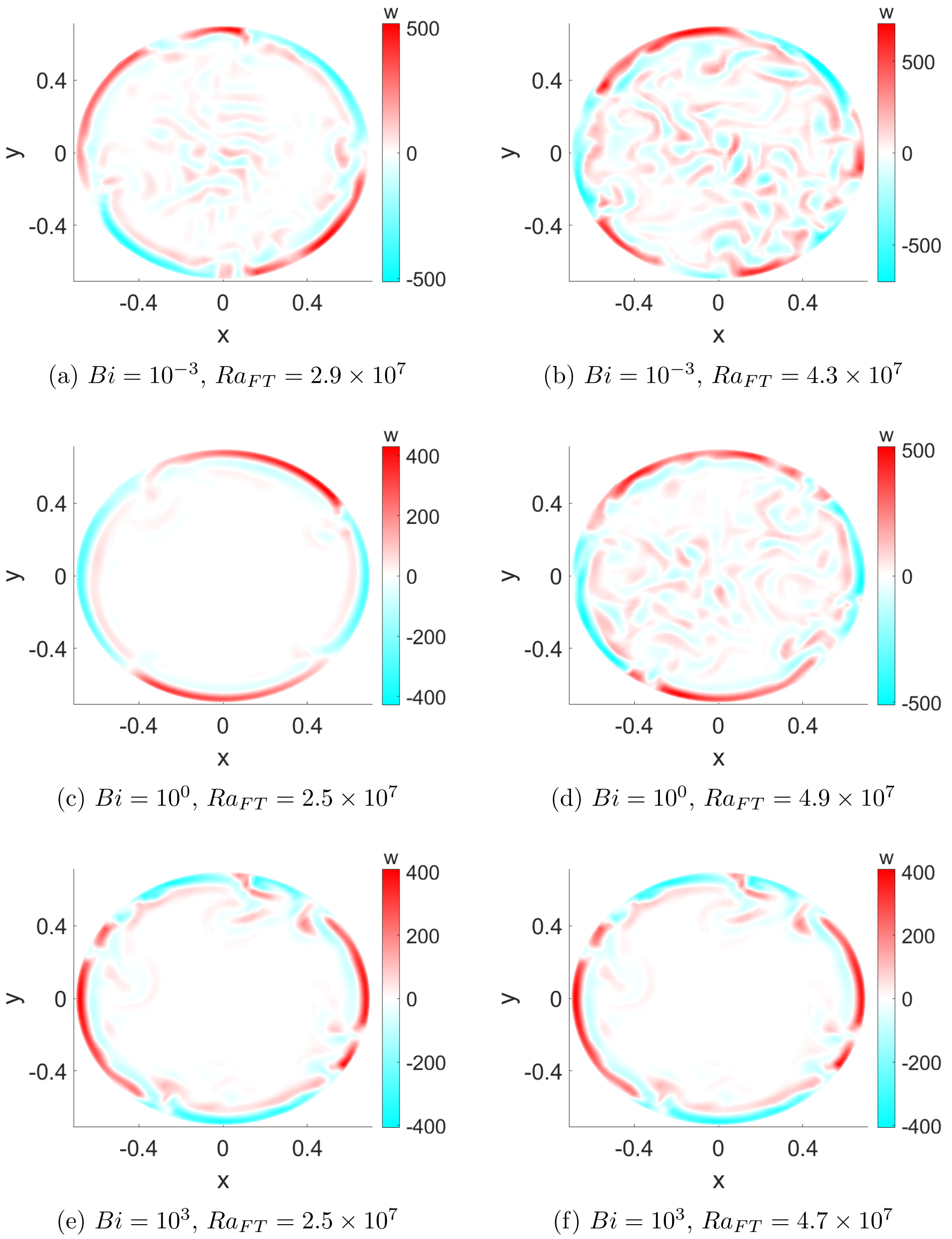

(a) $Bi = 10^{-3}$, $Ra_{FT} = 2.9 \times 10^7$ (b) $Bi = 10^{-3}$, $Ra_{FT} = 4.3 \times 10^7$

(c) $Bi = 10^{0}$, $Ra_{FT} = 2.5 \times 10^7$ (d) $Bi = 10^{0}$, $Ra_{FT} = 4.9 \times 10^7$

(e) $Bi = 10^{3}$, $Ra_{FT} = 2.5 \times 10^7$ (f) $Bi = 10^{3}$, $Ra_{FT} = 4.7 \times 10^7$

Figure 4.11: Plots of vertical velocity w at $z = 0.3$ and $t = 3$ for $Bi = 10^{-3}$, 10^0, and 10^3 around the predicted transition to bulk convection, $Ra^b_{FTc} = 4 \times 10^7$ and the observed transition to time dependence (see Figure 4.8) in systems with $Ek = 10^{-5}$. The red colour indicates upward motion and the blue indicates downward motion.

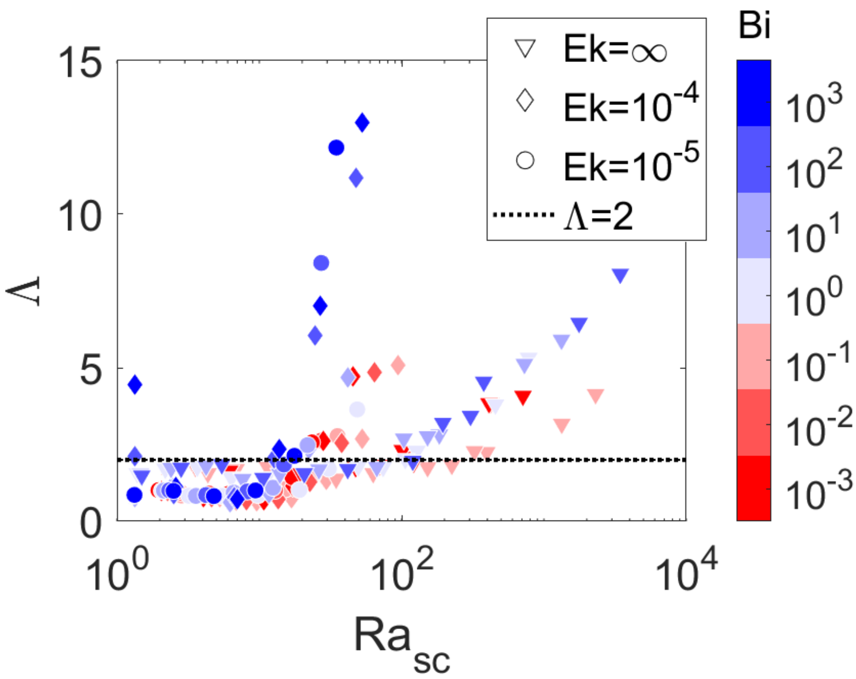

Figure 4.12: Plot of vertical uniformity factor, Λ, defined in Eq (3.11) as a function of the supercriticality $Ra_{FTsc} = Ra_{FT}/Ra^b_{FTc}$. The marker shape indicates the Ek value of each system. The marker colour relates to the Biot number, Bi. The dashed line shows $\Lambda = 2$ where vertical behaviour becomes 3D. Note all rotating systems with $Ra_{FTsc} > 2$ have $Ro < 1$ and are weakly or rapidly rotating.

condition. With rotation, there is evidence that systems with moderate Bi values retain wall-localised convection to higher Ra_{FT} values than systems with extreme Bi numbers.

4.5.3.2 Vertical structure

The vertical solution form can provide further insight into the dynamics of RRBC with Robin boundary conditions. The vertical uniformity of w within the domain is measured by factor Λ, as defined in Eq (3.11). As Λ becomes large, the fluid motion has significant 3D behaviour. We consider here that when $\Lambda \leq 2$, the flow is predominantly 2D. In rapidly rotating systems, 3D flow can be indicative of geostrophic turbulence (Ecke et al., 2022).

Figure 4.12 shows the Λ measurements as a function of supercriticality Ra_{FTsc}. The Ek and Bi value of each system is shown by the marker shape and colour, respectively. The predicted transition from 2D to 3D flow at $\Lambda = 2$ is shown by

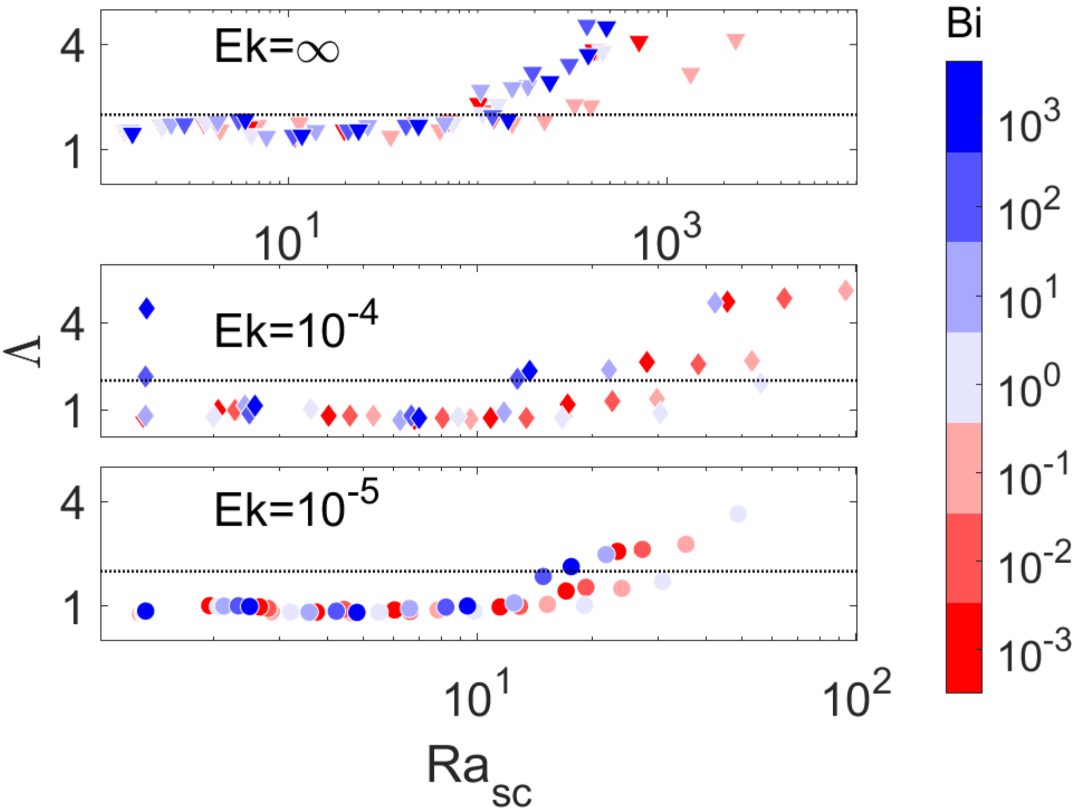

Figure 4.13: Plot of vertical uniformity factor Λ defined in Eq (3.11) as a function of the super-critical Rayleigh number, $Ra_{FTsc} = Ra_{FT}/Ra^b_{FTc}$. The marker shape indicates Ek as such: inverted triangles are $Ek = \infty$, diamonds are $Ek = 10^{-4}$, and circles are $Ek = 10^{-5}$. The marker colour relates to the Biot number, Bi, as indicated by the colour-bar. The dashed line shows $\Lambda = 2$ where vertical behaviour becomes non-uniform.

the dotted line. The range of $Ra_{FTsc} < 10^2$ and $\Lambda < 5$ is clustered so Figure 4.13 provides a closer look for each Ek individually. As before, Bi is indicated by colour shown in the colour-bar. The top panel shows $Ek = \infty$ for $10^0 \leq Ra \leq 10^2$ and $\Lambda \leq 5$. The centre panel shows $Ek = 10^{-4}$ and the bottom panel shows $Ek = 10^{-5}$ both for the ranges $10^0 \leq Ra_{FTsc} \leq 10^2$ and $\Lambda \leq 6$.

As in the fixed temperature case, the non-rotating systems transition to 3D flow at larger Ra_{FTsc} than rotating systems with Robin conditions, regardless of Bi value. Without rotation, flow becomes vertically non-uniform around $Ra_{FTsc} = 10^2$, while rotating system have 3D flow by $Ra_{FTsc} \leq 5 \times 10^1$. Both with and without rotation, $Bi \leq 10^{-1}$ systems have $\Lambda < 2$ to higher Ra_{FTsc} than higher Bi systems.

Considering only non-rotating systems, Figure 4.12 and the top panel of Figure 4.13, show that the configuration with $Bi = 10^{-1}$ exhibits 3D flow at the highest Ra_{FTsc} compared to other Bi values. Systems with $Bi = 10^{-1}$ achieves $\Lambda \geq 2$ at $Ra_{FTsc} = 3 \times 10^2$ while all other Bi configurations have $\Lambda \geq 2$ around $Ra_{FT} = 10^2$.

We visualise the vertical velocity, w, for three examples of different Bi systems for $3.7 \times 10^2 Ra_{FTsc} \leq 4.1 \times 10^2$ in Figure 4.14.

Figure 4.14a shows vertical behaviour for RBC with $Bi = 10^{-3}$ and $Ra_{FTsc} = 4.1 \times 10^2$, which has $\Lambda = 3.8$. The vertical plane shows that there are significant changes in w in the z-plane, changing from downward to upward motion in the upper part of the domain. When $Bi = 10^{-1}$, the vertical behaviour is visibly different from the previous case. The velocity is downward consistently until the very upper reaches of the domain, which, as described in section 3.4.3.2, are not considered for Λ calculation to avoid boundary layers. The deviation in vertical motion in the system with $Bi = 10^3$ is significantly different from the $Bi = 10^{-1}$ case, but to the eye is not necessarily different from the $Bi = 10^{-3}$ case. Thus, it is clear that the $Bi = 10^{-1}$ configuration has different vertical behaviour than the other cases. It is also evident that once $\Lambda > 2$ the behaviour causing increases in Λ is not necessarily visible from a fixed frame of r and time, due to increasingly time- dependent flow. Also recall that the thermal boundary layer is assumed to be of fixed length for the Λ calculation which may be insufficient for all cases and cause errors for low Ra values.

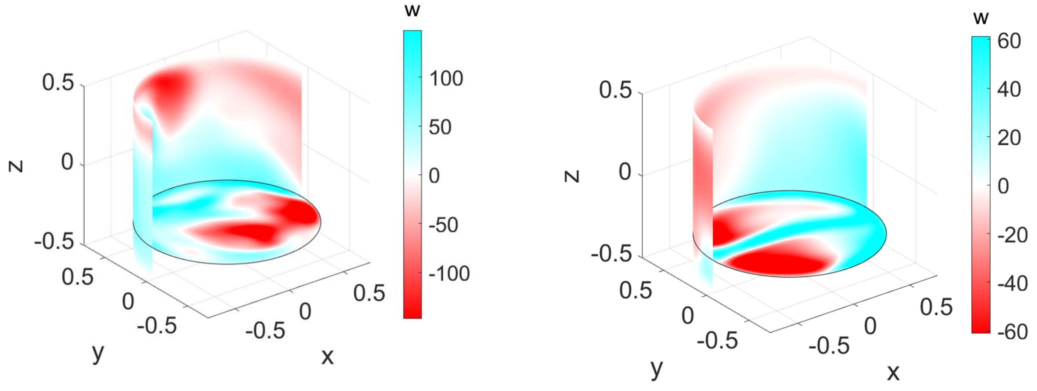

(a) $Bi = 10^{-3}$, $Ra_{FTsc} = 4.1 \times 10^2$, $Ra_{FT} = 6.5 \times 10^5$, $\Lambda = 3.8$

(b) $Bi = 10^{-1}$, $Ra_{FTsc} = 4 \times 10^2$, $Ra_{FT} = 1.2 \times 10^5$, $\Lambda = 2.2$

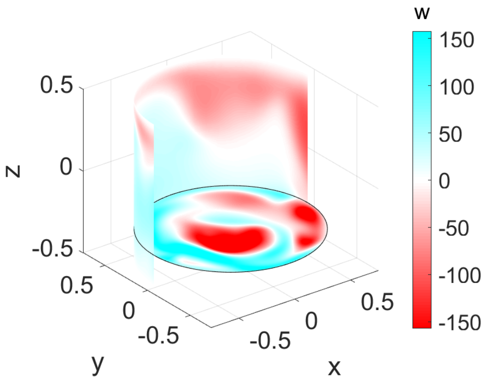

(c) $Bi = 10^2$, $Ra_{FTsc} = 3.7 \times 10^2$, $Ra_{FT} = 7.5 \times 10^5$, $\Lambda = 4.5$

Figure 4.14: Plots of vertical velocity w at $r = 0.685$, $z = 0.3$, and $t = 3$ for non-rotating systems. The blue colour indicates downward motion and the red indicates upward motion.

We next look into the systems rotating with $Ek = 10^{-4}$. Figure 4.12, indicates that above $\Lambda = 2$, the moderate and low Bi systems have less vertical deviation at the same Ra_{sc} than high Bi configurations. Looking only at $\Lambda \leq 5$ in the middle panel of Figure 4.13, it is evident that for $Bi \geq 10^2$, the transition above $\Lambda = 2$ occurs at $Ra_{FTsc} = 10$ while all other Bi configurations transition at $Ra_{FTsc} \geq 2 \times 10$. Additionally, there are two anomalies for $Bi = 10^3$ and 10^2 which show $\Lambda \geq 2$ at $Ra_{FTsc} < 2$. These occur because of low velocity magnitudes throughout the system which are in the divisor of Eq (3.11) causing the Λ value to be larger than expected.

In order to examine the differences in vertical behaviour between different Bi, the range of $4.5 \times 10^1 \leq Ra_{FTsc} \leq 5.5 \times 10^1$ is considered. Note from Figure 4.12 and the centre panel of Figure 4.13 that all Bi are considered in this range of Ra_{FTsc} but have significant variation in Λ value. Let us look at $Bi = 10^3$, which has the highest Λ, $Bi = 10^{-3}$ which has a similar Λ to $Bi = 10^1$, and $Bi = 10^0$ which has the lowest Λ, which is also similar to the $Bi = 10^{-1}$ value.

Figure 4.15 contains three plots of w at time $t = 3$, $z = -0.3$ and $r = 0.685$. Figure 4.15a shows a configuration with $Bi = 10^3$ and $Ra_{FTsc} = 5.2 \times 10^1$ which has $\Lambda = 13$. Figure 4.15b shows a system with $Bi = 10^0$ and $Ra_{FTsc} = 5.5 \times 10^1$ which has $\Lambda = 1.9$, just below transition to 3-dimensional flow. Finally, Figure 4.15c visualises a configuration with $Bi = 10^{-3}$ and $Ra_{FTsc} = 4.5 \times 10^1$ which has $\Lambda = 4.7$.

Comparing the plots in Figure 4.15, it is obvious that columnar vertical structure is only present for $Bi = 10^0$ and not $Bi = 10^{-3}$ or $Bi = 10^3$. This demonstrates that systems with moderate Bi, which are similar to neither fixed temperature nor fixed flux configurations, maintain 2D behaviour to higher Ra_{sc} values. Also note that while the $Bi = 10^3$ case, shown in Figure 4.15a, appears to have some columnar-like behaviour, this is a single snapshot in time and temporal variation analysis determined that this Ra_{FT} considered is chaotic. Therefore a single frame of w cannot fully visualise the changes in vertical behaviour. In comparison, the configuration with $Bi = 10^{-3}$ shows no columnar-like behaviour.

The investigation of RRBC dynamics when $Ek = 10^{-4}$ demonstrates different spatial behaviours between Robin condition configurations with different Bi values.

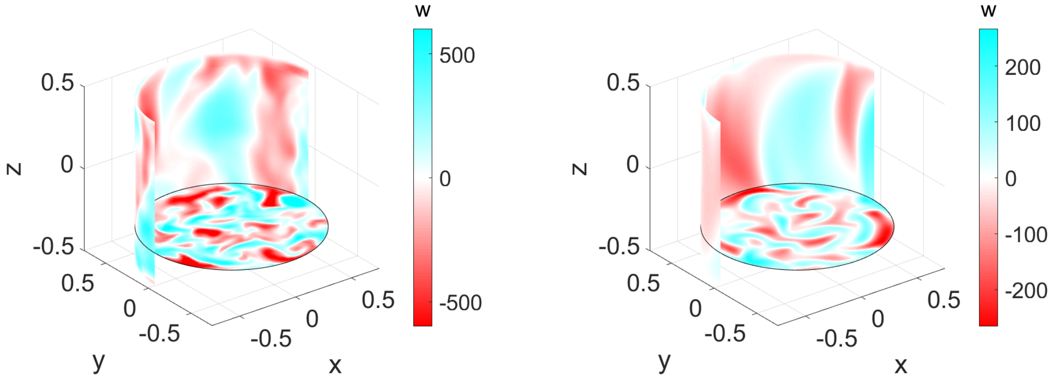

(a) $Bi = 10^3$, $Ra_{FTsc} = 5.2 \times 10^1$, $Ra_{FT} = 1.3 \times 10^7$, $\Lambda = 13$

(b) $Bi = 10^0$, $Ra_{FTsc} = 5.5 \times 10^1$, $Ra_{FT} = 8.7 \times 10^6$, $\Lambda = 1.9$

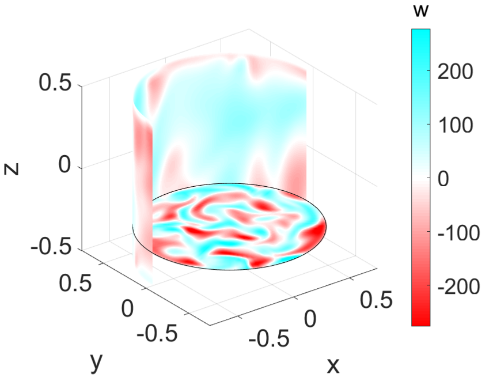

(c) $Bi = 10^{-3}$, $Ra_{FTsc} = 4.5 \times 10^1$, $Ra_{FT} = 1.0 \times 10^7$, $\Lambda = 4.7$

Figure 4.15: Plots of vertical velocity, w, at $r = 0.685$, $t = 3$, and $z = 0.3$ for RRBC with $Ek = 10^{-4}$. The blue colour indicates downward motion and the red indicates upward motion. Each plot is for a specific Biot number, Bi, and supercritical Rayleigh number, Ra_{FTsc}.

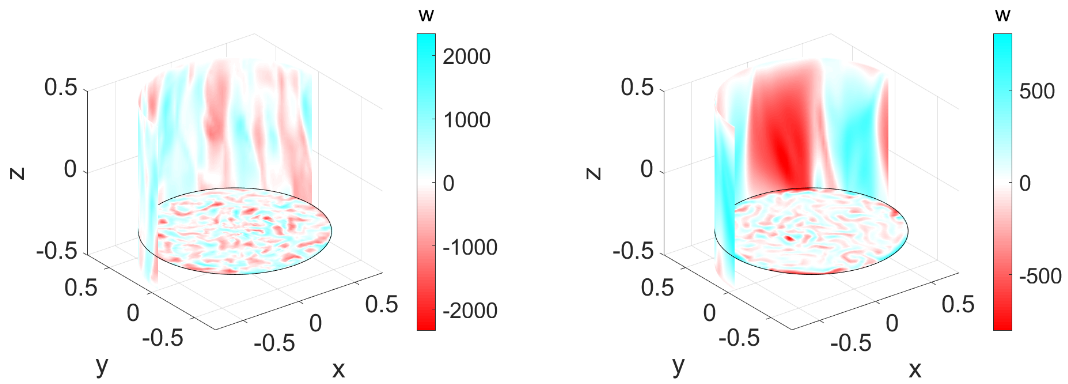

(a) $Bi = 10^3$, $Ra_{FTsc} = 3.5 \times 10^1$, $Ra_{FT} = 9.3 \times 10^7$, $\Lambda = 12$

(b) $Bi = 10^0$, $Ra_{FTsc} = 3.0 \times 10^1$, $Ra_{FT} = 7.9 \times 10^7$, $\Lambda = 1.7$

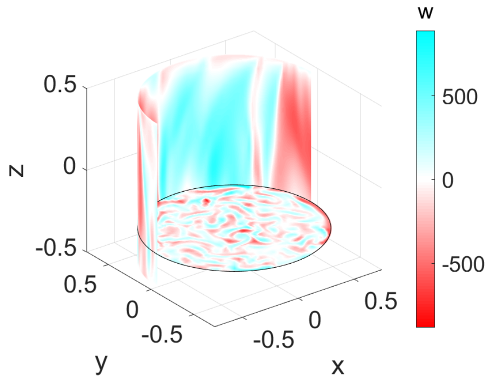

(c) $Bi = 10^{-2}$, $Ra_{FTsc} = 2.7 \times 10^1$, $Ra_{FT} = 6.9 \times 10^7$, $\Lambda = 2.7$

Figure 4.16: Plots of vertical velocity, w, at $r = 0.685$, $t = 3$, and $z = 0.3$ for RRBC systems with $Ek = 10^{-5}$. The blue colour indicates downward motion and the red indicates upward motion. Each plot is for a specific Biot number, Bi, and super-critical Rayleigh number, Ra_{FTsc}.

Let us consider systems with $Ek = 10^{-5}$ to determine if these observations are present in more rapidly rotating systems. From Figure 4.12, it is evident that Λ grows much faster for configurations with $Bi > 10^1$ than for lower Bi values. In the lowest panel of Figure 4.13, we observe the Λ values for low Bi, which shows that $Bi = 10^0$ exhibits below $\Lambda = 2$ to the highest Ra_{FTsc}.

Comparing the vertical behaviour for different Bi values applied to systems with $2.5 \times 10^1 \leq Ra_{FTsc} \leq 3.5 \times 10^1$, we visualise different Λ values in Figure 4.16. In each plot, w is shown at $z = -0.3$, $t = 3$, and $r = 0.685$. A system with $Bi = 10^3$ at $Ra_{FTsc} = 3.5 \times 10^1$ which has $\Lambda = 12$ is shown in Figure 4.16a. A configuration with $Bi = 10^0$ and $Ra_{FTsc} = 3.0 \times 10^1$ which has $\Lambda = 1.7$ is shown in Figure 4.16b. Finally, a system with $Bi = 10^{-2}$ and $Ra_{FTsc} = 2.7 \times 10^1$ which has $\Lambda = 2.6$ is visualised in Figure 4.16c.

At first glance, all three plots in Figure 4.16 show more columnar-like behaviour than the $Ek = 10^{-4}$ systems, shown in Figure 4.15, did. This is due to the increased effects of rotation from decreasing the Ekman number which encourages vertical columns (Chandrasekhar, 1961). A closer examination of the $Bi = 10^3$ case in Figure 4.16a shows that there are breaks and curves in the vertical columns, which would cause Λ to be large especially taken over time (recall this plot is a snapshot in time). In comparison, the $Bi = 10^0$ and 10^{-2} plots show much more vertical uniformity with much wider and more consistent vertical columns. This verifies that low and moderate Bi maintain vertical uniformity to higher Ra_{FTsc} than large Bi.

The results of vertical and horizontal spatial behaviour are consistent with the temporal variation results all of which show that systems with Robin conditions with moderate Bi values resist chaotic behaviour to higher Ra_{FT} values than extreme Bi configurations. While horizontal behaviour and temporal variation suggest similar transitions to chaos for extreme Bi values, both low and high, the vertical behaviour of RRBC shows low Bi numbers retains vertical uniformity to larger Ra_{FT} than high Bi systems.

4.5.3.3 Zonal structure

Finally, let us consider zonal flow behaviour, which, along with horizontal and vertical spatial behaviour can determine if a system geostrophically turbulent (Ecke et al., 2022). Figure 4.17 shows the time-and-volume-averaged mean-zonal-flow MZF, see Eq(3.13), as a function of super-critical Rayleigh number, Ra_{FTsc}. The Bi and Ek values of each system are indicated by the colour and shape of each marker.

From Figure 4.17, it is evident that non-rotating systems do not have significant zonal flows, even at high Ra_{FTsc}. That is expected because convection is a primarily vertical phenomena and rotation excites zonal flows. The same behaviour was exhibited in the fixed temperature and fixed flux configurations.

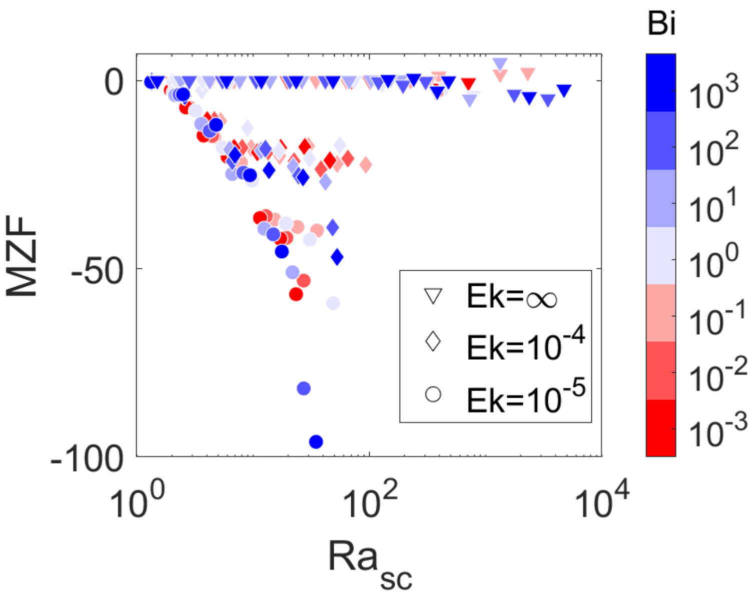

Figure 4.17: The volume and time averaged mean-zonal-flow (MZF) as a function of supercriticality Ra_{FTsc} for systems with Robin thermal boundary conditions with varying Biot numbers. The Bi value is indicated by colour as shown by the colour-bar. The Ekman number, Ek is indicated by the marker shape.

With moderate rotation, it is clear that low and moderate Bi value systems have lower MZF than $Bi \geq 10^2$ for the same Ra_{FTsc}. Moderate Bi are again seen to have lower MZF when $Ek = 10^{-5}$, in comparison to both high and low Bi. This is congruent with the temporal variation which showed that for $Ek = 10^{-5}$, the moderate Bi became chaotic at higher Ra_{FT} than extreme Bi. Hence, unlike in the fixed flux and fixed temperature cases, we do note some deviation in zonal flow behaviour between different thermal boundary conditions.

To investigate the differences in zonal flow structure, we plot Figure 4.18 which visualised $\overline{u_{\theta t}}$ for two systems with $Ra_{FTsc} = 3.5 \times 10^1$ and 10^{-5}. The volume averaged zonal flow for the $Bi = 10^3$ case has $MZF = -100$ while the configuration with $Bi = 10^{-1}$ is $MZF = -40$. The difference in zonal structure and cause of the great variation in MZF values between the two systems is evident from Figure 4.18. The higher Bi configuration has a chaotic zonal flow with much larger magnitude of velocity than the moderate Bi configuration which exhibits both columnar bulk flow and a strong wall-localised flow. This further shows that RRBC with moderate Bi values resists chaotic flow to higher Ra_{FT} values than systems with extreme Bi

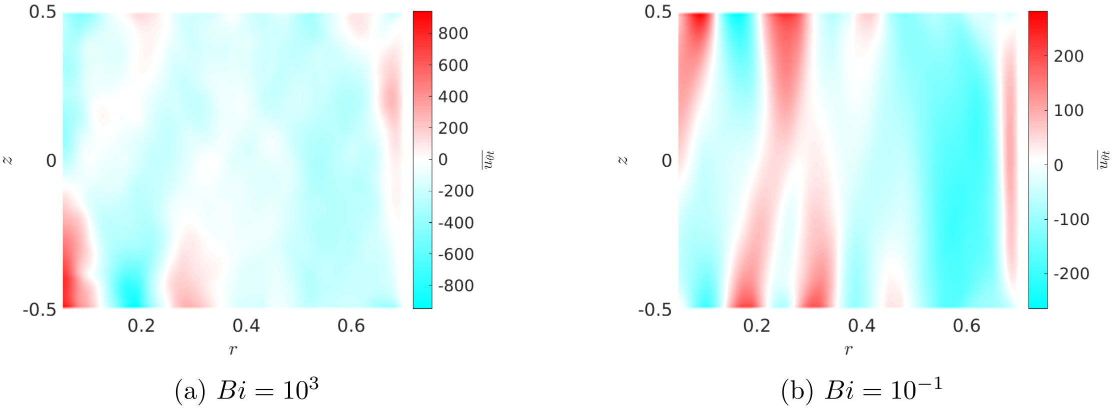

(a) $Bi = 10^3$ (b) $Bi = 10^{-1}$

Figure 4.18: $\overline{u_{\theta t}}$ for two Robin RRBC systems with $Ra_{FTsc} = 3.5 \times 10^1$ and $Ek = 10^{-5}$ plotted at $t = 3$.

values.

4.6 Summary

In overview, we have introduced and defined the Robin condition– a thermal boundary condition which straddles fixed temperature and fixed flux conditions. The Robin condition, as defined in Eq (4.9), is controlled by the Biot number Bi, a ratio involving the height and thermal conductivity between the boundary and the fluid layer, defined in Eq (4.10). The Bi value indicates how similar a boundary is to fixed temperature ($Bi \to \infty$) or fixed flux ($Bi \to 0$). In order to compare results between RRBC systems with different Bi values, it is necessary to define the effective Rayleigh number, $Ra(Bi)$, as a function of the fixed temperature Rayleigh number, Ra_{FT}. We choose to extend the relationship between Ra_{FT} and Ra_{FF} presented in Eq (3.7) to a novel relationship between Ra_{FT} and $Ra(Bi)$, described by Eq (4.13). We find that our definition of $Ra(Bi)$ causes the $\overline{Nu} - Ra_{FT}$ scaling γ to converge to the fixed temperature γ value for a range of Bi values better than the $Ra(Bi) - Ra_{FT}$ relationships defined in Gringé et al. (2007) and Clarté et al. (2021).

Employing our $Ra(Bi) - Ra_{FT}$ transformation, Figure 4.7 showed the γ values for RBC systems with varying Ek and Bi values are generally within the 99%

confidence interval of the fixed temperature configuration γ value. Without rotation, it was ubiquitously observed that heat transport, spatial behaviour and time-dependence were not affected by Bi value. We further observe that systems with moderate Bi – that is $10^{-1} \leq Bi \leq 10^{1}$– have differences in flow, when rotating. An investigation into temporal variation showed that moderate Bi are non-chaotic to higher Ra_{FT} than extreme Bi when rotating.

Spatial behaviour was considered in three directions: horizontal, vertical, and zonal. The horizontal structures showed that with rotation, behaviour at the onset of wall-localised convection is uniform across Bi. However, for $Ra_{FT} > Ra^{w}_{FTc}$, the number of convection rolls m and location of dominant convection within the domain vary with Bi value. The transition to bulk convection occurs at higher Ra_{FT} than fixed temperature theory predicts for moderate Bi systems.

When considering vertical behaviour, Λ, defined in Eq(3.11), was used to determine the vertical uniformity. When $\Lambda > 2$, a system is considered to have 3D flow. With and without rotation, both moderate and low Bi are shown to become 3-dimensional at higher super-critical Rayleigh number, $Ra_{FTsc} = Ra_{FT}/Ra_{FTc}$, than large Bi. Finally, the mean-zonal-flow (MZF) was time and volume averaged to show that without rotation, even chaotic behaviour does not cause significant zonal flow. However, with rotation, it was seen that moderate Bi had lower MZF than high Bi for the same Ra_{FTsc}.

Overall, we have made a unique observation that moderate Bi values cause rapidly rotating RBC systems to remain non-chaotic to higher Ra_{FT} values than systems similar to fixed temperature or fixed flux conditions. Though, we have considered only a single geometry and Pr value, this has implications for the way we relate physical systems to numerical models. In the experimental context, it is useful to ensure the boundary materials and fluid relate such that $Bi > 10^{2}$ if a corresponding numerical model applied fixed temperature boundary conditions. Further, if we consider the Earth's core-mantle boundary (cautiously due to the convective nature of the mantle)– where the molten core has $d = 2.2 \times 10^{3}$km depth and approximately $k = 30$W/mK (Ohta & Hirose, 2020) and the mantle has $d_m = 2.9 \times 10^{2}$W/mK and approximately $k_m = 3.5$W/mK (Tang et al., 2014)– the Biot number is on the order of 10^{-1} which is considered to be moderate. Hence, the differences between RRBC dynamics in systems with moderate Bi values and either fixed temperature or fixed flux conditions are relevant to the interpretation of numerical models of the Earth's core.

Chapter 5

Inhomogeneous Sidewall Insulation

In Chapter 4, we studied the dynamics of a fluid undergoing rotating Rayleigh–Bénard convection (RRBC) in a cylindrical domain with Robin boundary conditions on the horizontal boundaries. The investigation of RRBC with by Robin conditions, revealed that flow dynamics are moderately affected by the properties of the bounding material. While many experimental studies use materials which create conditions similar to fixed temperature conditions, the thermal conditions at the core-mantle boundary (CMB) are not clearly similar to either fixed flux or fixed temperature conditions.

In our endeavour to investigate physically realisable thermal boundary conditions, we must consider the lateral boundaries. As discussed in Chapter 1, the Earth's core is affected by a large-length scale variation in heat flux at the CMB. Hence, in this chapter, we explore the effects of inhomogeneous insulation by applying nonuniform heat flux to the sidewalls of the cylindrical domain. The cylindrical geometry enables the numerical model to be compared to potential future experiments. Hence, the boundary conditions are chosen to be both experimentally feasible and representative of the heat flux at the CMB.

5.1 Introduction

Previous studies of inhomogeneous heat flux boundary conditions have considered either variations in temperature (C. J. Davies et al., 2009; Reiter et al., 2022) or heat flux (Mound & Davies, 2017; Sahoo & Sreenivasan, 2017, 2020). In a rotating spherical-shell with azimuthal variation in fixed temperature boundary conditions, it was found that the large length-scale variations caused steady state solutions in RRBC while convective length-scale variations had different effects dependent on the amplitude of the variations (C. J. Davies et al., 2009). An experimental model in a rotating cylindrical annulus described in Sahoo and Sreenivasan (2020) supported the large-length scale result when the heat flux was varied. In a non-rotating cylindrical domain where the temperature is varied vertically and not azimuthally, bulk convection for high Ra systems was not observed to be affected by the thermal boundary condition (Reiter et al., 2022). However, we are unaware of a numerical study which considers the effects of azimuthally varying heat flux thermal condition on a rotating cylindrical domain.

Therefore, this chapter will investigate RRBC dynamics in a rotating cylinder with heat flux varying in sinusoidal patterns azimuthally and vertically. In Sahoo and Sreenivasan (2020) it is noted that, in a physical experiment, without vertical variation in heat flux, the RRBC system reaches the quasi-geostrophic regime, where convection loses its columnar structure. However, vertical variation is necessary to conform with homogeneous fixed temperature boundary conditions at the top and bottom of the domain. We consider two patterns of sinusoidal heat flux: Positive/Negative which oscillates from positive to negative values and Positive/Zero which oscillates from positive values to zero. In the latter case, the boundary heat flux is never negative, which is more appropriate for modelling the Earth's core (Mound & Davies, 2017) and is more experimentally realisable (Sahoo & Sreenivasan, 2020).

In both cases, we fix the azimuthal mode m_θ of the boundary condition in reference to be the preferred mode m_{UI} of the uniformly insulated case. Note that we use a fluid with $Pr = 0.7$ such that m_{UI} is determined from the fixed temperature vertical thermal boundary condition systems reported in Chapter 3. There are three configurations for the azimuthal mode:

1. large length-scale $m_\theta = 1$, which is most geophysically appropriate (Mound & Davies, 2017);

2. convective length-scale $m_\theta = m_{UI}$; and

3. secondary convective length-scale $m_\theta = bm_{UI}$ where $b = 0.5$ or 2.

The latter two cases are of interest because of their ability to 'pin' convection rolls such that rolls which may rotate about the domain in a homogeneously insulated system become stationary.

In Section 5.2, we define the Positive/Negative and Positive/Zero configurations. Then, in section 5.3, we derive a solid steady state solution for the Positive/Negative case and a heat flux analysis provides analytic results against which the Positive/Zero numerical setup is tested for accuracy. In section 5.4, the results are presented for each case of m_θ with and without rotation. We aim to identify global effects of inhomogeneous insulation on rotating RBC by observing changes in heat transport, temporal behaviour, and flow structure.

5.2 Boundary conditions

In order to solve the fluid system described in Chapter 2 – an air-like fluid with $Pr = 0.7$ undergoing rotating RBC in a cylindrical domain, governed by Eqs (2.11a)-(2.11c)– it is necessary to define boundary conditions on the horizontal and lateral boundaries. On all surfaces, velocity is no-slip, as in Eq (2.15). The top and bottom thermal boundary conditions are fixed temperature, as described in Eq (3.1). Due to the fixed temperature conditions, we consider the fixed temperature Rayleigh number, which we refer to as Ra in this chapter.

On the sidewalls, the heat flux is a sinusoidal function in both the vertical and azimuthal directions. We require a vertical variation in heat flux to accommodate the fixed temperature condition at the top and bottom of the system. We consider two forms of inhomogeneous thermal boundary condition on the sidewalls: Positive/Negative and Positive/Zero.

5.2.1 Positive/Negative inhomogeneity

The Positive/Negative lateral thermal boundary condition has oscillations both vertically and azimuthally. For simplicity, we fix the vertical variation as mode

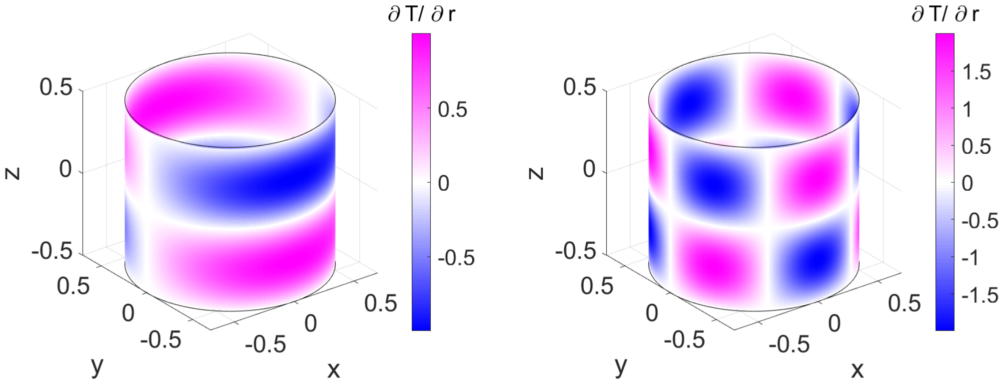

(a) $A_n = 1$, $m_\theta = 1$ (b) $A_n = 2$, $m_\theta = 3$

Figure 5.1: Plots of the Positive/Negative heat flux applied on the sidewalls, as defined in Eq (5.1), for varied values of A_n and m_θ. The magenta indicates positive heat flux and blue is negative heat flux.

$n = 1$ for all models. Hence, the Positive/Negative condition is defined as,

$$\nabla T \cdot \boldsymbol{n} = \frac{\partial T}{\partial r} = A_n \sin\left(f_n z\right) \sin\left(m_\theta \theta\right) \qquad \text{at} \quad r = 0.7, \tag{5.1}$$

where $f_n = 2n\pi$ is the modified vertical mode. The azimuthal mode m_θ, and the amplitude A_n are prescribed for each system.

Figure 5.1 visualises two forms that the Positive/Negative condition can take by varying m_θ and A_n. Increasing the amplitude increases the maximum and decreases the minimum heat flux, as seen in the colour-bar magnitude differences between Figure 5.1a and 5.1b, where A_n increases from 1 to 2. Increasing m_θ causes more fluctuations in the azimuthal direction. Note that between the peaks and troughs and at the top and bottom of the system, the figures show white, which indicates $\partial T/\partial r = 0$.

5.2.2 Positive/Zero inhomogeneity

Due to experimental considerations, it is reasonable to have a system which has some positive heat flux and is otherwise zero, rather than negative (Sahoo & Sreenivasan, 2020). By adjusting Eq (5.1) such that it cannot be negative, we define the Positive/Zero boundary condition such that

$$\frac{\partial T}{\partial r} = A_n \sin(\pi\left(z + 0.5\right))(1 + \sin(m_\theta \theta)). \tag{5.2}$$

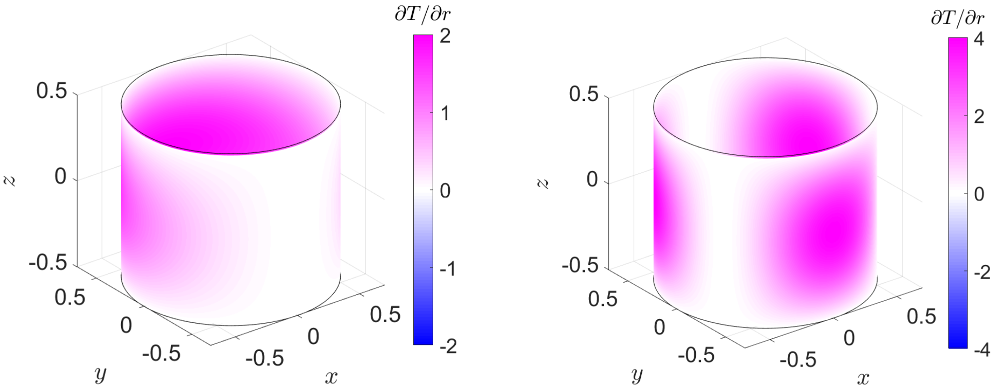

(a) $A_n = 1$, $m_\theta = 1$ (b) $A_n = 2$, $m_\theta = 3$

Figure 5.2: The Positive/Zero condition, as in Eq (5.2), applied to the sidewalls with (left) $A_n = 1$ and $m_\theta = 1$ and (right) $A_n = 2$ and $m_\theta = 3$. The magenta indicates positive heat flux and the white indicates zero heat flux.

Note that in order to maintain a fully positive heat flux, the vertical variation is now only half of a sine wave.

Figure 5.2 illustrates the Positive/Zero heat flux applied on the sidewalls. Figure 5.2a shows a case where $A_n = 1$ and $m_\theta = 1$ and Figure 5.2b shows the case where $A_n = 2$ and $m_\theta = 3$. As prescribed by Eq (5.2), $dT/dr \geq 0$. Note also that at the top and bottom, the heat flux is zero, which is necessary to satisfy the fixed temperature condition on the top and bottom of the system.

5.2.3 Boundary condition parameters

In both the Positive/Zero and Positive/Negative cases, the value of m_θ, for a given fixed set of Ek and Ra parameters, is chosen in three ways. First, $m_\theta = 1$ is considered for every case. This is to simulate heat flux variation at the sidewalls with a larger length-scale than the convection, as in Mound and Davies (2017). The second case will be $m_\theta = m_{UI}$ where m_{UI} is the dominant horizontal mode determined for homogeneous sidewall insulation in Chapter 3. In non-rotating cases, the first two cases are the same because $m_{UI} = 1$. The third option is $m_\theta = bm_{UI}$ where $b = 0.5$ or 2. The latter two cases are of interest to investigate the ability of sidewall boundary conditions to pin convection rolls which are time-dependent with homogeneous sidewall conditions. In C. J. Davies et al. (2009), convection-length temperature variations pinned convection in a spherical-shell domain. However, we are unaware of any previous studies into convective length-scale oscillations in heat flux conditions.

The amplitude, A_n, is increased to determine what amplitude of heat flux is necessary to cause changes in behaviour from the homogeneous case and to see if different amplitudes cause different behaviours in the inhomogeneous case.

5.3 Numerical testing

In the previous section, two inhomogeneous thermal boundary conditions were defined to be applied on the lateral boundaries of the fluid system defined in Chapter 2. We apply the Positive/Negative Eq (5.1) and Positive/Zero Eq (5.2) conditions individually with governing equations Eqs (2.11a)-(2.11c). The system is solved using Nek5000 (Nek5000, 2019) as described in Chapter 2. The parameter list of simulated Positive/Negative and Positive/Zero configurations are in Appendix D.1.

Though, a kinetic energy balance, as described in section 2.2.2.1, is conducted and $err < 1\%$ is confirmed, we hope to gain further confidence in our numerical implementations. Thus, in this section, an analytic result is determined for each boundary condition against which nonlinear numerical results are compared.

5.3.1 Solid steady state solution for the Positive/Negative condition

Considering the RRBC system with the Positive/Negative condition, we posit that an analytical solution exists for a solid steady state solution where the fluid is both time-independent and has no velocity. This solution can be compared with the results of numerical simulations conducted in parameter ranges when time-independence and no flow is expected.

The solid steady state is characterised by time-independence and no fluid motion such that $\frac{dT}{dt} = 0$ and $\boldsymbol{u} = 0$. By applying these conditions to the dimensionless energy equation, Eq (2.11c), we recover the Laplace equation:

$$\nabla^2 T = 0. \tag{5.3}$$

Hence, the temperature must satisfy the fixed temperature boundary condition and the inhomogeneous sidewall condition, Eq (5.1), as well as Eq (5.3).

By converting into cylindrical coordinates, a solution may be derived of the form

$$T = \tau(z) + \tau'(z, \theta, r), \tag{5.4}$$

where τ is a linear vertical temperature profile and τ' is the perturbation from τ.

For the sake of brevity, the details of the derivation are located in Appendix D.2. We find that the solution is the sum of τ and a product of sines in z and θ with an r dependence such that

$$T\left(z, \theta, r\right) = -z + 0.5 + \frac{A_n}{\frac{\mathrm{d}I_m(0.7f_n)}{\mathrm{d}r}} \sin\left(f_n z\right) \sin\left(m_\theta \theta\right) I_m\left(f_n r\right), \tag{5.5}$$

where I_m is the modified Bessel's function.

5.3.1.1 Conductive solutions

The relationship between the solid steady state solution and the numerical conductive solution, where $Ra < Ra_c$ (Ra_c is estimated from the homogeneous case) is quantified using a $||\Delta_\infty||$ norm of the temperatures and the time averaged Nusselt number, $\overline{Nu} =< \Delta T/\beta d >_t$, of the numerical solution. Designating the solid steady state solution, the result of Eq (5.5), $\hat{T}$ and the numeric temperature solution is as T, the $||\Delta_\infty||$ norm is defined as

$$||\Delta_\infty|| = |\max(\hat{T} - T)|. \tag{5.6}$$

We expect that for $Ra = 0$, where $\boldsymbol{u} = 0$ is intuitively a solution, $||\Delta_\infty|| = 0$. However, it is not obvious if the inhomogeneous sidewall condition will cause a thermally driven flow in the conductive state, resulting in $||\Delta_\infty|| > 0$.

Additionally, Ra_c is predicted to decrease from the homogeneous case (Sahoo & Sreenivasan, 2017, 2020). Therefore, we observe the $\overline{Nu}$ as a function of Ra to identify Ra_c, the lowest Ra value where $Nu > 1$.

The $||\Delta_\infty||$ and $\overline{Nu}$ values are plotted as functions of Ra, in Figures 5.3a and 5.3b, respectively. In both plots, the Ek value of each system is indicated by a marker shape while the amplitude A_n and azimuthal mode m_θ are represented by

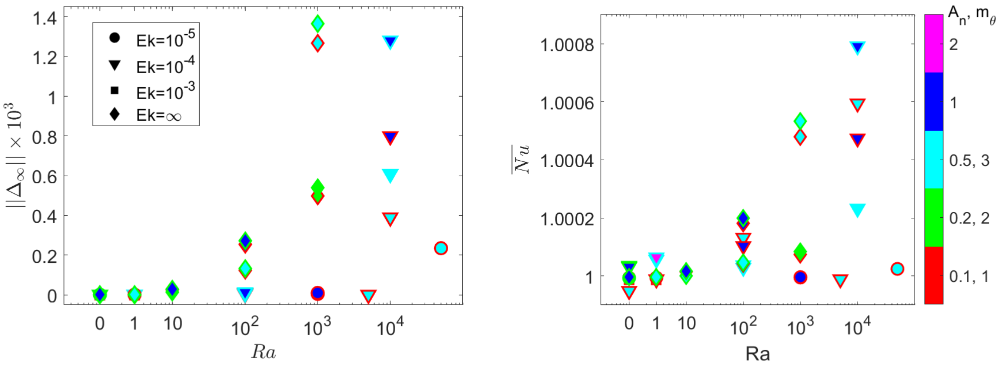

(a) $||\Delta_\infty|| \times 10^3$ vs. Ra

(b) $\overline{Nu}$ vs. Ra

Figure 5.3: Plots of $||\Delta_\infty|| \times 10^3$, calculated from Eq (5.6), and average Nusselt number, $\overline{Nu}$ vs. Ra. Each Ekman number, Ek, is represented by a marker shape. The amplitude A_n and azimuthal mode, m_θ, are indicated by the colour of the marker face and edge, respectively. Note the horizontal axes do not have consistent logarithmic scales in order to visualise $Ra = 0$ distinctly from $Ra = 1$.

the marker face and edge colours, respectively. The horizontal axes are a manipulated logarithmic scale such that $Ra = 0$ and $Ra = 1$ are visible.

Comparing the spread of $||\Delta_\infty||$ and $\overline{Nu}$ in Figure 5.3, it is clear that the metrics are strongly related. The corresponding $||\Delta_\infty||$ and $\overline{Nu}$ values are located in the same position, though different magnitude, for the two metrics. This is as expected due to the no velocity assumption of the solid steady state solution, as velocity increases due to convective motion, the system deviates from Eq (5.5), increasing the $||\Delta_\infty||$ value. As in the uniformly insulated case, convection is suppressed to higher Ra with decreasing Ek (Chandrasekhar, 1961; Buell & Catton, 1983a). Each $Ra - Ek$ set in Figure 5.3b is $Ra < Ra_c$, calculated for the homogeneous case, however $\overline{Nu} > 1$ is present within this range, indicated that $Ra_c \leq 100$ for $Ek = \infty$ and $Ra_c \leq 10^4$ for $Ek = 10^{-4}$. Thus, we agree with previous results in experimental cylindrical domains and numerical spherical shells that Ra_c decreases with inhomogeneous insulation (Sahoo & Sreenivasan, 2017, 2020).

Additionally, the low $||\Delta_\infty||$ values in Figure 5.3a correspond to the systems with $\overline{Nu} < 1.0002$. Thus, it is clear there is no thermally driven flows in the conductive state and consequently, the solid steady state solution Eq (5.5) is an appropriate solution for the conductive flow. Further, the low $||\Delta_\infty||$ values are indicative of a suitably accurate numerical implementation of the Positive/Negative boundary condition.

5.3.2 Heat flux accounting for the Positive/Zero condition

With respect to the Positive/Zero condition, the heat flux throughout the system is considered with two aims: to gain confidence in the numerical methods and define an appropriate heat transport metric. Previously, we have quantified global heat transport with the Nusselt number, Nu. We have previously defined $Nu = \beta d/\Delta T$. Consequently, in systems with uniformly insulated sidewalls and fixed temperature vertical boundaries, Nu is dependent on the heat flux, β, at the top of the system. However, in the Positive/Zero case, the introduction of heterogeneity to the sidewall insulation causes heat to enter or leave the system. Therefore, it is useful to further investigate definitions of Nu and the impact of varied heat flux on global heat transport. By measuring the global heat transport, we are also able to test our numerical methods.

The Nusselt number is the ratio between the total heat flux (conductive and convective) to the conductive heat flux without convection. Hence to investigate the heat flux, following the derivation of Nu in Hepworth (2014), we consider the non-dimensional heat equation, $\frac{DT}{Dt} = \nabla^2 T$. Integrating over the volume of the domain,

$$\int_V \left(\frac{\partial T}{\partial t} + (\boldsymbol{u}\cdot\nabla)\, T\right) \mathrm{d}V = \int_V \left(\nabla^2 T\right) \mathrm{d}V. \tag{5.7}$$

To define heat flux for a statistically steady state, we assume either a time-independent solution or a time-averaged solution. Hence,

$$\int_V \left((\boldsymbol{u}\cdot\nabla)\, T\right) \mathrm{d}V = \int_V \left(\nabla^2 T\right) \mathrm{d}V. \tag{5.8}$$

Applying the 3D divergence theorem, no-slip conditions, and fixed temperature horizontal conditions as described in section 5.2, Eq (5.8) becomes

$$\int_0^{0.7}\int_0^{2\pi} \frac{\partial T}{\partial z} r\mathrm{d}\theta\mathrm{d}r|_{z=-0.5} = \int_0^{0.7}\int_0^{2\pi} \frac{\partial T}{\partial z} r\mathrm{d}\theta\mathrm{d}r|_{z=0.5} + r\int_{-0.5}^{0.5}\int_0^{2\pi} \frac{\partial T}{\partial r}\mathrm{d}\theta\mathrm{d}z|_{r=0.7}. \tag{5.9}$$

See Appendix D.3 for a detailed derivation.

From Eq (5.9), it is clear that the heat flux at top and bottom of the domain are dependent on the heat flux removed or added through the sidewalls. Hence, values of m_θ and A_n may affect total heat transfer.

For the Positive/Zero case, Eq (5.2) is applied to the radial term of Eq (5.9) and solved as such:

$$\begin{aligned}
r\int_{-0.5}^{0.5}\int_{0}^{2\pi}\frac{\partial T}{\partial r}d\theta dz|_{r=0.7} &= R\int_{-0.5}^{0.5}\int_{0}^{2\pi}A_n\sin(\pi\,(z+0.5))(1+\sin(m\theta))d\theta dz,\\
&= 0.7A_n\int_{-0.5}^{0.5}\sin(\pi\,(z+0.5))\int_{0}^{2\pi}1+\sin(m\theta))d\theta dz,\\
&= 0.7A_n 2\pi\int_{-Z}^{Z}\sin(\pi\,(z+0.5))dz,\\
&= 0.7A_n 2\pi(\frac{2}{\pi}),\\
&= 2.8A_n. \qquad (5.10)
\end{aligned}$$

Therefore, the difference between heat flux at the bottom and top of the domain is

$$\int_{0}^{R}\int_{0}^{2\pi}\frac{\partial T}{\partial z}r\mathrm{d}\theta\mathrm{d}r|_{z=-0.5}-\int_{0}^{R}\int_{0}^{2\pi}\frac{\partial T}{\partial z}r\mathrm{d}\theta\mathrm{d}r|_{z=0.5}=2.8A_n. \qquad (5.11)$$

From this relationship, we may determine the accuracy of the numerical model for the Positive/Zero configuration.

5.3.2.1 Numerical testing for Positive/Zero configuration

To gain confidence in our numerical model, we first compare the analytic global heat flux prediction Eq (5.11) to numeric results. From Eq (5.11), the difference in heat flux between the top of the domain and the bottom should be related to the amplitude of the applied insulation by a factor of 2.8. The parameter ranges listed in Appendix D.1 are modelled and the vertical temperature gradient at the upper and lower boundaries are calculated.

In Figure 5.4 the difference between the heat flux at the top and bottom of the domain is divided by the amplitude A_n of each simulation. The Ek, A_n, and m_θ values are represented by the marker shape, edge colour, and fill colour, respectively. The A_n and m_θ values are shown by the colours in the colour-bar and legend, respectively. The error bars show the heat flux standard deviation

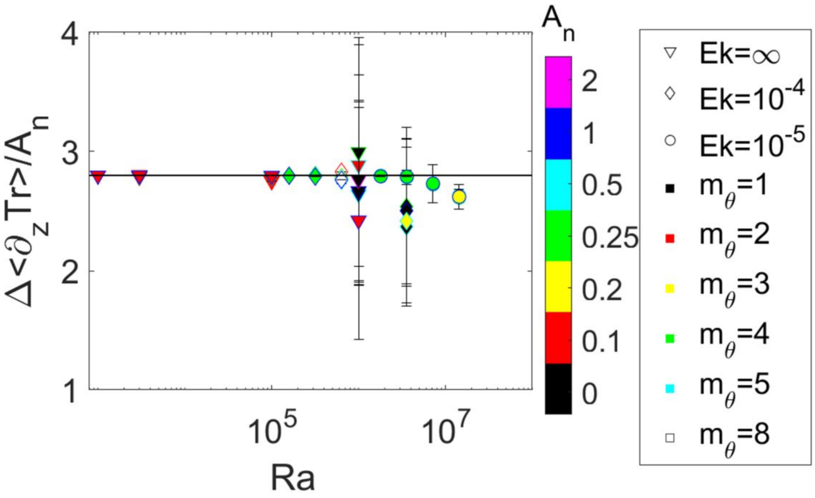

Figure 5.4: The difference in heat flux between the top and bottom of the domain $\Delta < \partial_z Tr >_{t,A} / A_n$ as a function of Ra. The result expected from Eq (5.11) is 2.8 (black line). Each simulation has an Ek, A_n, and m_θ value represented by the marker shape, edge colour, and fill colour, respectively. The error bars show the standard deviation in heat flux measurement.

due to time averaging. As determined in Eq (5.11), each simulation should have a difference in heat flux of $2.8A_n$.

From Figure 5.4, it is clear that for $Ra_{FT} < 10^6$, all systems considered display the expected heat flux behaviour. Though as Ra increases, larger error ranges and deviations from 2.8 occur. This is because, as seen in Chapter 3, as Ra_{FT} increases, the fluid behaviour becomes increasingly time-dependent. This variation in behaviour causes uncertainty in the calculation of an average heat flux. The standard deviation from the calculated differences contain 2.8 in each case. The only exception is the case where $Ek = 10^{-5}$ and $Ra = 1.44 \times 10^7$ which likely needs additional time-stepping to saturate such that the heat flux difference is 2.8. Thus, we conclude that the simulations are sufficiently accurate.

5.3.2.2 New Nusselt number definition

In the previous section, it was shown that measuring the heat flux at the top and bottom of the domain is not sufficient to describe heat transport in a system with Positive/Zero insulation. Therefore, a widely accepted Nu definition for fixed temperature and uniformly insulated systems (Verzicco & Camussi, 2003; Kunnen, Clercx, & Geurts, 2008) is adapted such that,

$$Nu_k = 1+ < wT >_V \ . \tag{5.12}$$

In Kunnen, Clercx, and Geurts (2008) and Verzicco and Camussi (2003), Eq (5.12) is compared with $\overline{Nu} =< \partial T/\partial z >_t$ measured at the top and bottom of the domain to determine sufficient numerical mesh resolution. According to Verzicco and Camussi (2003), disparity between values indicates insufficient resolution.

To further confirm this theory for the fixed temperature, uniformly insulated model, the $\overline{Nu_k}$ value is measured for each system and compared to the previous $\overline{Nu}$ value. In Figure 5.5 both Nusselt numbers are plotted as functions of Ra. The results for the range of Ek numbers are plotted, each as a unique marker shape, as indicated in the legend. The $\overline{Nu}$ values using Eq (3.10) is plotted in magenta while the $\overline{Nu_k}$ values are plotted in red.

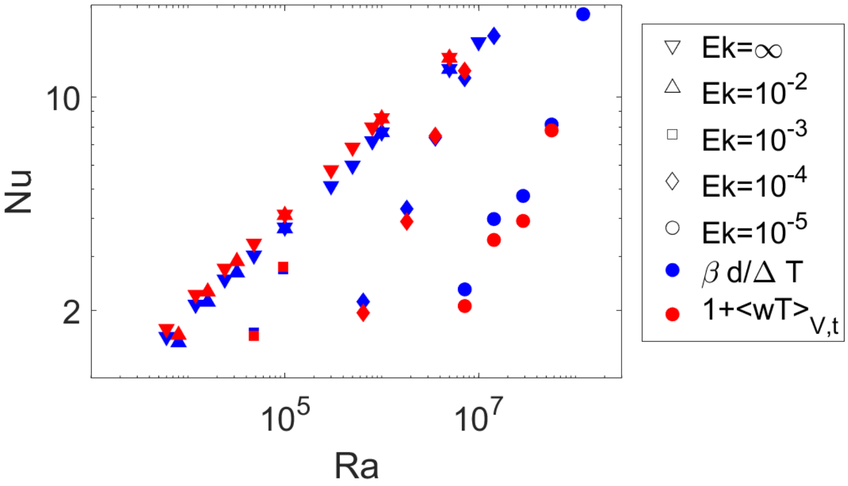

Figure 5.5: Comparison of two Nusselt number definitions for uniformly insulated RRBC systems. The definition from Calkins et al. (2015) (Eq (3.10)) is in magenta and the definition from Kunnen, Clercx, and Geurts (2008) (Eq (5.12)) is in red. Each Ek is indicated by shapes as shown in the legend.

For all Ek, the proximity of red and magenta markers in Figure 5.5 indicates sufficient mesh resolution in the bulk and along the walls. Note there are some deviations in Nusselt number value for a give Ra value. We attribute this to a difference in the methods for calculating Nu_k and Nu (i.e. Nu_k is calculated using data closer to the boundaries than Nu). Additionally, the agreement between values improves our confidence in the Nu_k measurement defined in Eq (5.12). Thus, we have determined an appropriate metric of global heat transport measurement for inhomogeneously insulated systems, Nu_k. We also have a understanding of the heat flux through the vertical boundaries as effected by the inhomogeneity at the sidewalls and have confirmed the accuracy of the numerical methods.

5.4 Analysis of results

In this section, we analyse the numerical results of applying inhomogeneous sidewall insulation with both Positive/Negative and Positive/Zero heat flux to a rotating cylindrical domain. The systems considered include those listed in Appendix D.1 where $Ra > Ra_c$.

Recall that the azimuthal mode of the sidewall heat flux m_θ is chosen in relation to the dominant mode of the uniformly insulated system (i.e. $A_n = 0$) m_{UI} which is determined from results presented in Chapter 3. Each m_θ value is then chosen to fit one of the following categories:

1. $m_\theta = 1$ such that the length-scale of heat flux applied at the sidewall is larger than the length-scale of the dominant azimuthal mode in the homogeneously insulated configuration;
2. $m_\theta = m_{UI}$ to pin convection rolls; and
3. $m_\theta = bm_{UI}$ where $b = 0.5$ or 2 to observe if secondary modes can be excited by sidewall heat flux.

Note that without rotation, the first two instances are the same because $m_{UI} = 1$.

Each case of m_θ is investigated individually. We begin by testing the large length-scale case. The heat transport behaviour is quantified by Nu_k and compared against homogeneous results. Next, spatial and temporal behaviours are explored. The same aspects are considered for the convective length-scale configuration and the secondary convective length-scale case.

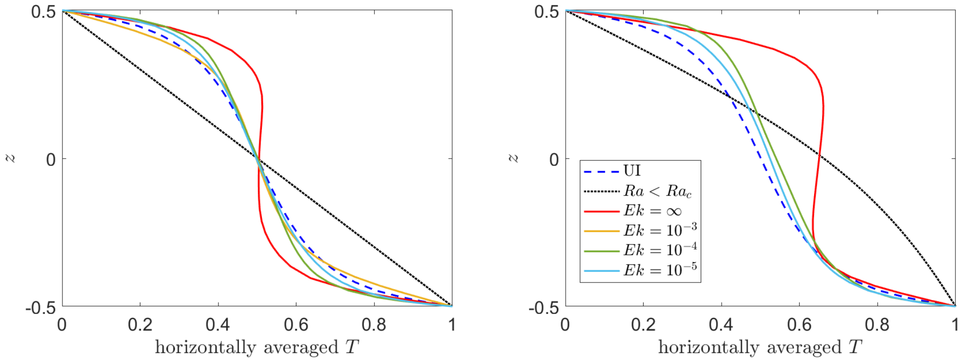

(a) Positive/Negative

(b) Positive/Zero

Figure 5.6: Plots of horizontally averaged temperature T vs. height z for configurations with Positive/Negative and Positive/Zero configurations for supercriticality Ra_{sc} on the order of 10. The blue dashed line indicates the uniformly insulated case of the same Ra_{sc} value. The black dotted line shows the conducting case with $A_n = 0.5$. The colour of each solid line indicates the Ekman number of the systems which each have $m_\theta = 1$ and $A_n = 1$.

5.4.1 Large length-scale heat flux

We first consider the case where the applied inhomogeneous heat flux has a larger length-scale than that of the convective motion. In the Earth's core, tomographic measurements indicate that the heat flux at the CMB has a large length-scale and is generally positive (Mound & Davies, 2017). Hence, the Positive/Zero configuration explored in this section is the most geophysically appropriate boundary condition that we will consider.

Our exploration of RRBC dynamics begins with observing the vertical temperature profile.

The vertical temperature profiles of systems which have approximately Ra_{sc} on the order of 10 are plotted for each Ek value in Figure 5.6. Note the Ra_{sc} values are calculated from the uniformly insulated case, which is shown by the dashed line. In the left (right) panel, the Positive/Negative (Positive/Zero) condition is applied. Each Ek is indicated by colour. The case where $Ra < Ra_c$ has $m_\theta = 1$ and $A_n = 0.5$ and all other instances have $m_\theta = 1$ and $A_n = 1$.

Comparing the conductive profiles, from Figure 5.6a, it is clear that the Positive/Negative condition allows for the linear profile expected from a homogeneously

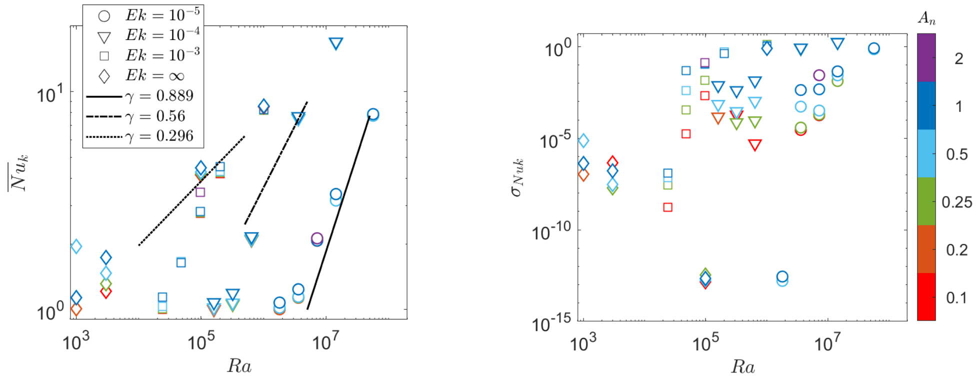

(a) $\overline{Nu_k}$ vs. Ra

(b) σ_{Nuk} vs. Ra

Figure 5.7: Plots of $\overline{Nu_k}$ as defined in Eq (5.12) and the standard deviation of the Nu_k time series from $\overline{Nu_k}$ as functions of Ra. The sidewalls are inhomogeneously insulated with the Positive/Zero case as in Eq (5.2) with azimuthal mode $m_\theta = 1$. The amplitude of the boundary condition A_n is indicated by the marker outline colour. The Ek of each system is shown by the marker shape. In the left panel, the black lines show the $\overline{Nu} \propto Ra^\gamma$ relationship for $Ek = \infty$, 10^{-4}, and 10^{-5} using results from Chapter 3.

insulated system (Chandrasekhar, 1961). However, Figure 5.6b shows that the Positive/Zero case does not have a linear temperature profile. In both cases, the non-rotating system develops an adverse temperature gradient. The Positive/Zero case appears not to centre on an averaged temperature of 0.5 as the Positive/Negative and homogeneous case does.

5.4.1.1 Heat transport

To investigate global heat transportation, the time-averaged Nusselt number, as defined in Eq (5.12), is measured for each system. Figure 5.7 shows the $\overline{Nu_k}$ value and corresponding standard deviation σ_{Nu} for the Positive/Zero case in side-by-side panels, each as a function of Ra. The sidewall heat flux in all cases has $m_\theta = 1$. Marker shape indicates the Ek value and marker colour represents the A_n value for each system. In the left panel, $\overline{Nu_k} - Ra$ scalings calculated in Chapter 3 for the uniformly insulated configuration are shown by the black lines.

Overall, it is evident from the left panel in Figure 5.7, that for Positive/Zero configurations near onset with $m_\theta = 1$, increasing A_n, increases $\overline{Nu_k}$. It is evident that changes in A_n have a smaller effect on global heat transport as Ra increases. Furthermore, near onset, non-rotating systems exhibit larger increases in $\overline{Nu_k}$ as A_n increases than rotating systems.

In contrast, we observe in the right panel of Figure 5.7, that variations in σ_{Nuk} with changes in A_n are not generally dependent on Ra. Rather, for the rotating Positive/Zero systems, the effect of increasing A_n decreases as Ra increases. Without rotation, there is no consistent relationship between A_n and σ_{Nuk}. There are two cases where σ_{Nuk} is exceptionally low and has little variation between A_n values. One is rotating with $Ek = 10^{-5}$ and $Ra = 1.8 \times 10^6$, which is very near to onset. The other instance is not rotating with $Ra = 10^5$. These results are also representative of the global heat transport in Positive/Negative configurations.

We next compare the spread of $\overline{Nu_k}$ for the $Ek = \infty$, 10^{-4}, and 10^{-5} systems with inhomogeneous insulation to the Nusselt number scaling results for uniformly insulated cases. Table 5.1 lists the γ values and the 99% confidence intervals (CI) from the for fixed Ek and A_n values, following the process explain in section 3.4.1. The magenta (black) values are from the Positive/Negative (Positive/Zero) case. Where $A_n = 0$, the results are from the uniformly insulated case found in Chapter 3. Note that there is no $A_n = 0$ scaling for $Ek = 10^{-3}$. Note in some instances there are insufficient Ra values modelled to calculate a γ.

Though visually similar in Figure 5.7, Table 5.1 shows that no system with inhomogeneous insulation and $m_\theta = 1$ has the same γ as the uniformly insulated case. Generally, the γ value is lower in the inhomogeneous case than the uniformly insulated case, suggesting that the varied insulation weakens vertical heat transport. Without rotation, the confidence intervals between the inhomogeneous cases and the uniform case do not overlap. When $Ek = 10^{-4}$, the $A_n = 0$ confidence interval is large and therefore overlaps with the intervals of the inhomogeneous configuration. When $Ek = 10^{-5}$, the $A_n = 0.5$ and $A_n = 1$ amplitudes for the Positive/Negative and Positive/Zero configurations, respectively, have confidence intervals on the scaling which aligns with the uniformly insulated case. Hence, it is evident that inhomogeneous insulation significantly affects the global heat transport behaviour of convection in comparison to a uniformly insulated configuration.

Ek	A_n	γ	γ 99% CI	γ	γ 99% CI
∞	0	0.296	0.293 – 0.298	-	-
	0.1	0.352	0.351 – 0.352	-	-
	0.5	0.306	0.304 – 0.308	-	-
	1.0	0.269	0.269 – 0.270	0.285	0.284 – 0.285
10^{-3}	0	0.763	0.763 – 0.764	-	-
	0.1	0.747	0.744 – 0.749	-	-
	0.25	0.513	0.267 – 0.660	-	-
	0.5	0.499	0.350 – 0.647	0.504	0.396 – 0.612
	1.0	0.525	0.290 – 0.760	0.486	0.394 – 0.579
10^{-4}	0	0.567	0.427 – 0.700	-	-
	0.25	0.712	0.621 – 0.802	-	-
	0.5	0.707	0.619 – 0.796	0.716	0.623 – 0.811
	1.0	0.712	0.606 – 0.797	0.593	0.455 – 0.731
10^{-5}	0	0.889	0.673 – 1.11	-	-
	0.25	0.620	0.617 – 0.623	-	-
	0.5	0.606	0.596 – 0.615	0.774	0.771 – 0.777
	1.0	0.707	0.682 – 0.7316	0.651	0.651 – 0.651

Table 5.1: Nusselt number scalings such that $\overline{Nu} \propto Ra^{\gamma}$ with the 99% confidence interval of γ in black (magenta) for the Positive/Zero (Positive/Negative). Note that the $A_n = 0$ cases are the uniformly insulated configuration reported in Chapter 3 and calculated with Nu from Eq (3.10). Where $A_n > 0$, the inhomogeneous insulated systems use Nu_k from Eq (5.12). The '-' symbol indicates that insufficient Ra values were modelled to measure γ.

In (Mound & Davies, 2017), inhomogeneous sidewall insulation in a form similar to the Positive/Zero $m_\theta = 1$ configuration was found to enhance γ measurements in spherical-shell geometry with $10^{-4} \geq Ek \geq 10^{-6}$. The results presented in Table 5.1 show that γ is enhanced for Positive/Zero configurations with $Ek = 10^{-4}$ when $A_n > 0$. However, all other Ek values result in diminished γ values. This is likely because higher Ra are considered in (Mound & Davies, 2017). Indeed, Figure 7 in (Mound & Davies, 2017), shows that for $Ra < 10^8$, the inhomogeneously insulated cases have lower γ than that of the homogeneous case.

Furthermore, in Mound and Davies (2017), the γ enhancement increased with increased applied heat flux amplitude. We do not see the same relationship between A_n and γ in Table 5.1. This difference may be due to inconsistency between the definition of amplitude used in (Mound & Davies, 2017), such that $A_n^* = \frac{\max(\partial_r T) - \min(\partial_r T)}{<\partial_r T>_V}$ at $r = 0.7$, and the amplitude definition of A_n used here. Additionally, the Positive/Negative configuration appears to decrease γ as A_n increases.

Hence, we have shown that in RRBC away from onset, global heat flux relative to the conductive heat flux is generally diminished by large length-scale sidewall insulation. Next, the fluctuation of Nu_k over time is used to investigate temporal behaviour for a representative selection of $Ek - Ra$ configurations.

Measuring global heat transport with the Nusselt number Nu_k provides insight into both temporal and thermal behaviour. Figure 5.8 contains plots of Nu vs. t for four unique systems with $m_\theta = 1$ with varying Ra, Ek, and A_n values. In each panel, from top to bottom, results for RBC configurations with $Ek = 10^{-5}$-$Ra = 1.44 \times 10^7$; $Ek = 10^{-4}$-$Ra = 6.4 \times 10^5$; $Ek = 10^{-3}$-$Ra = 9.6 \times 10^5$; and $Ek = \infty$-$Ra = 1 \times 10^5$, are respectively shown. The A_n value of each Positive/Zero case is indicated by the line colour specified in the legend. The $A_n = 1$ case of the Positive/Negative condition is plotted in magenta.

Figure 5.8 shows that, of the Ra-Ek configurations considered, the homogeneous case has time-independent Nu_k time series. Note that this may differ from the temporal behaviour noted in Chapter 3 based on a Nu time series due to the different calculation methods for Nu and Nu_k.

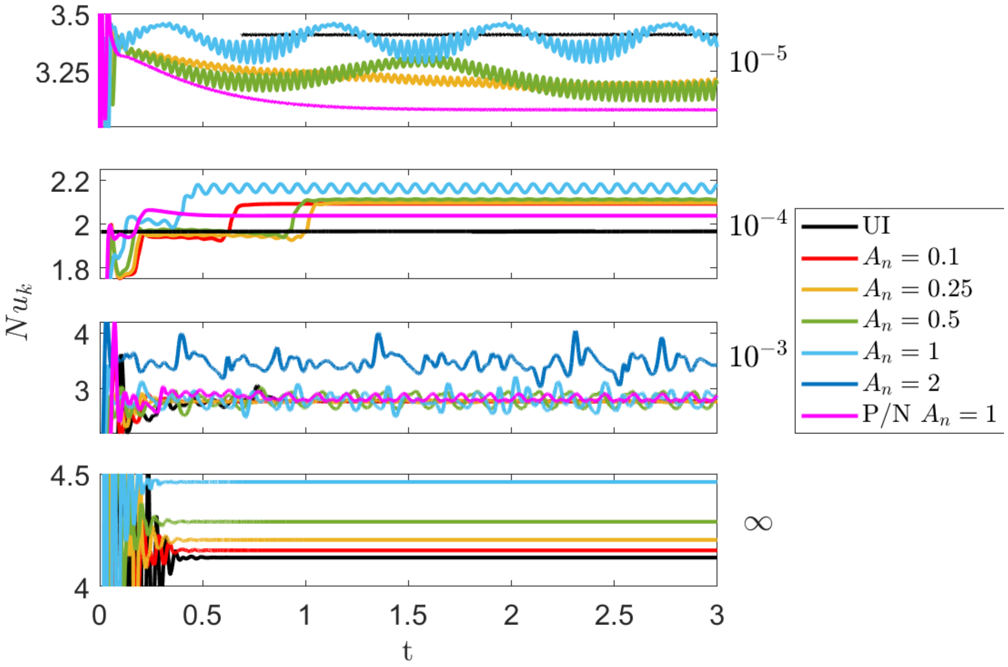

Figure 5.8: Nusselt number, Nu_k, time series for configurations of inhomogeneous sidewall insulation with $m_\theta = 1$. The panels contain, from top to bottom, $Ek = 10^{-5}$- $Ra 1.44 \times 10^7$; $Ek = 10^{-4}$-$Ra = 6.4 \times 10^5$; $Ek = 10^{-3}$-$Ra = 9.6 \times 10^5$; and $Ek = \infty$-$Ra = 1 \times 10^5$. Within each plot, the uniformly insulated ($A_n = 0$) time series is plotted in black along with the Positive/Zero condition for varying A_n is varied according to colour. The $A_n = 1$ case for the Positive/Negative condition is plotted in magenta. Note that the vertical axis is not consistent for all panels.

In the upper two panels of Figure 5.8,as A_n increases, the temporal behaviour becomes oscillatory for Positive/Zero configurations. Further, in the $Ek = 10^{-5}$ and $Ra = 1.44 \times 10^7$ system, the Nu_k time series becomes quasi-oscillatory with decreasing envelope wavelength as A_n increases. The superposition of temporal modes in quasi-oscillatory behaviour may be representative of a superposition of spatial modes within the system. For the same systems, the Positive/Negative configuration is ubiquitously time-independent.

The weakly rotating systems in the third panel has chaotic behaviour for all configurations shown in Figure 5.8. The Positive/Zero case increases in $\overline{Nu_k}$ when $A_n = 2$. The non-rotating system shown in the bottom panel did not have a Positive/Negative equivalent simulation, but all Positive/Zero configurations have time-independent flow and $\overline{Nu_k}$ increases with A_n.

Hence, we have observed that while $\overline{Nu_k} - Ra$ scaling decreases with inhomogeneous insulation, it does not necessarily correspond to more temporally steady systems. Non-rotating systems are not temporally affected by the applied heat flux. With rotation, the Positive/Negative configurations remain time-independent, though the Positive/Zero configurations tend toward oscillatory behaviour. It is now of interest to explore the spatial implications of these noted variations in heat transport and temporal behaviour.

5.4.1.2 Spatial structure

To investigate the flow structure, we examine the patterns of vertical velocity w over time and about a fixed radius.

Beginning with a rapidly rotating system with parameters $Ek = 10^{-5}$ and $Ra = 1.44 \times 10^7$, Figure 5.9 shows on the left Hövmoller diagrams of w at $r = 0.68$ over time and on the right plots of w at $t = 3$ and $r = 0.685$. The homogeneously insulated case is shown in the upper set of plots. The lower two plots have inhomogeneous insulation on the sidewalls in the Positive/Negative or Positive/Zero configuration as indicated by the sub-captions. For each inhomogeneous system, $m_\theta = 1$ and $A_n = 1$.

It is evident from the right-side plots of Figure 5.9 that each system has 3 convection rolls. However, the placement and motion of the rolls about the az-

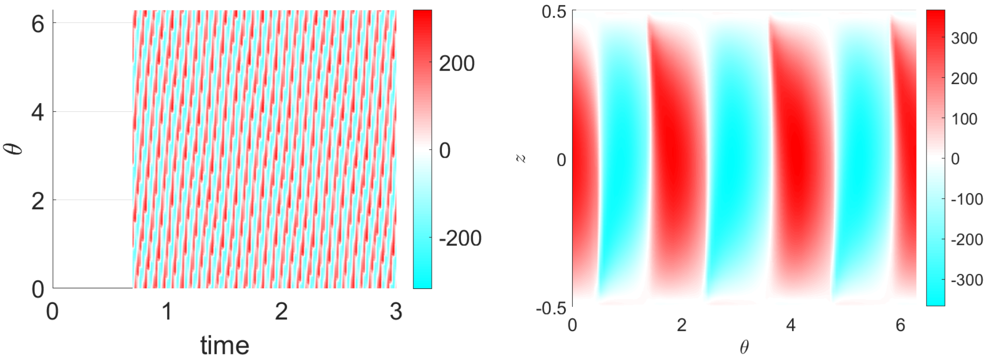

(a) Homogeneous, $A_n = 0$

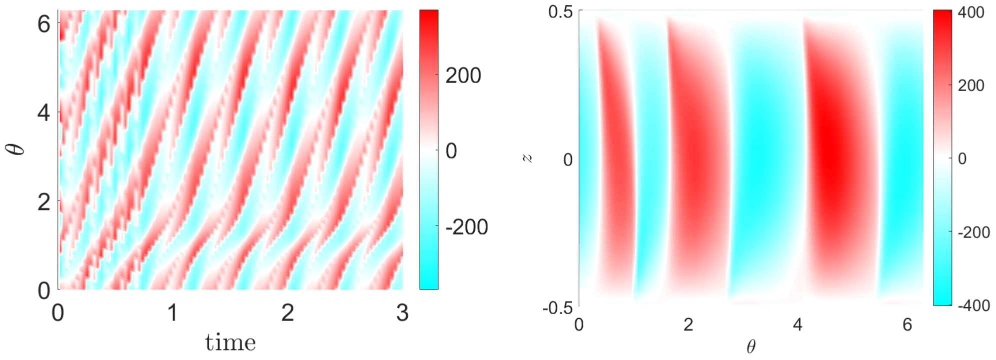

(b) Positive/Negative, $A_n = 1$

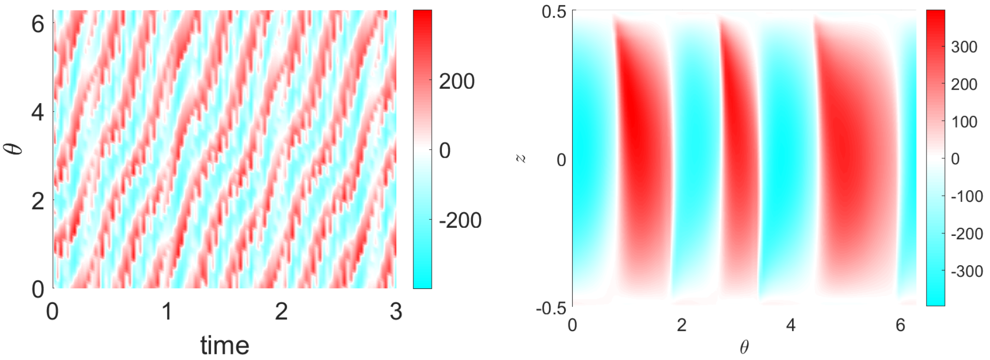

(c) Positive/Zero, $A_n = 1$

Figure 5.9: Plots of vertical velocity w in two forms: (left) Hövmoller diagrams at $z = 0.3$ and $r = 0.68$ over time and (right) slices at time $t = 3$ and $r = 0.685$. The RRBC system has $Ek = 10^{-5}$ and $Ra = 1.44 \times 10^7$. The upper plots are homogeneously insulated. The middle and lower plots are inhomogeneously insulated with $m_\theta = 1$ and $A_n = 1$ as in Eq (5.1) and Eq (5.2), respectively.

imuthal axis varies dependent on the boundary condition. By observing the slope of the lines in the left-side Hövmoller diagrams, the rate of rotation of the convection rolls about the vertical axis is estimated. The homogeneous case completes approximately 8.7 rotations per unit of time while the Positive/Negative and Positive/Zero configurations complete 2.3 and 3 rotations per unit of time, respectively. Additionally, we find that as A_n increases, the overall rotation rate is decreases. Thus, it is clear that the application of inhomogeneous insulation of large-length scale at the sidewall causes convection cells to rotate slower in rapidly rotating RBC systems.

Further, in the Positive/Negative case, the rotation rate is slowed in the region $\theta < \pi$ where the boundary condition applies $\partial T/\partial r > 0$. This shows that the positive heat flux causes the rotation to slow more than the negative heat flux. However, with the Positive/Zero condition where $\partial T/\partial r \geq 0$ ubiquitously, the overall rotation is faster than the Positive/Negative case. This difference suggests the maximum applied heat flux is not the only factor determining convection roll rotation.

The structure of the rolls may also influence the rotation rate of the convection rolls. As seen in the right-hand plots of Figure 5.9, the homogeneous case has three rolls each of relatively similar wavelength. The Positive/Negative configuration causes the wavelength of the convection rolls to narrow as the heat flux applied at the sidewalls increases. In contrast, the Positive/Zero case shows a narrowing of convection rolls in the region near $\theta = \pi$ where the applied heat flux transitions from the maximum to minimum amplitude. The location of the narrower convection rolls changes with time and is likely a physical manifestation of the quasi-oscillatory temporal behaviour seen in Figure 5.8.

It it worth noting that the convection illustrated in Figure 5.9 is wall-localised. The application of inhomogeneous sidewall insulation does not affect the flow of the bulk fluid in rapidly rotating RBC for these parameters. This is also true for moderately rotating RBC, including the case $Ek = 10^{-4}$ and $Ra = 6.4 \times 10^5$.

However, as rotation decreases, the effects of inhomogeneous sidewall insulation on flow structure change. For the case with $Ek = 10^{-4}$ shown in Figure 5.8, the homogeneous case has $m_{UI} = 4$ and the convection rolls do no rotate. Figure 5.10

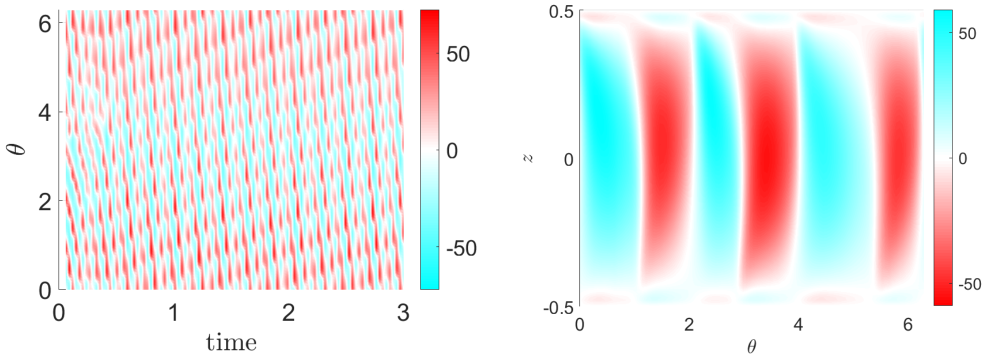

Figure 5.10: Vertical velocity w for the rotating RBC system with $Ek = 10^{-4}$ and $Ra = 6.4 \times 10^5$. The sidewalls have the Positive/Zero with $m_\theta = 1$ and $A_n = 1$. The left-hand plot is a Hövmoller diagram at $z = 0.3$ and $r = 0.68$. The right-hand plot is taken at time $t = 3$ and $r = 0.685$.

shows the w structure with Positive/Zero sidewall insulation with azimuthal mode $m_\theta = 1$ and amplitude $A_n = 1$. The homogeneous and Positive/Negative results are shown in Appendix D.4.

From Figure 5.10, it is clear that the system has become time-dependent and now has 3 convection rolls. This is also true for the Positive/Negative case. This choice of spatial structure is a secondary convection form, excited by the inhomogeneity. In Figure 5.7, the panel showing the $Ek = 10^{-4}$ case shows that the inhomogeneously insulated systems briefly choose a state of convection where Nu_k is the same as the uniformly insulated case before jumping to a higher Nu_k value. However, it is unclear why the chosen number of convection rolls does not match the applied heat flux in this case.

The weakly rotating case which has temporally chaotic behaviour in Figure 5.8 $Ek = 10^{-3}$ and $Ra = 9.6 \times 10^4$, transitions from non-rotating convection rolls to rotating rolls with the application of inhomogeneous sidewall insulation. However, the dominant mode remains $m_{UI} = 2$. See Appendix D.4 for figures of the weakly rotating system.

Without rotation, no notable difference in flow structure is observed. Hence, the change in σ_{Nuk} observed in Figure 5.7 for $Ek = \infty$ and $Ra = 1 \times 10^5$ is likely not due to the inhomogeneous insulation.

In summary, we have identified several effects on rotating convection due to the application of large length-scale heat flux variations as the lateral boundary condition. We first saw that the Positive/Negative condition has a similar vertical temperature profile as the homogeneous configuration while the Positive/Zero case deviates from this behaviour. However, the scaling of the Nusselt number Nu_k with the Rayleigh number Ra such that $Nu_k \propto Ra^{\gamma}$, changes dependent on the lateral boundary condition. In Mound and Davies (2017), it was found that in spherical shells, large length-scale heat flux boundary conditions caused an enhancement of heat transport in rapidly rotating systems. Our results oppose the literature, finding that heat transport is diminished with and without rotation. Though, the limited range of Ra considered here may contribute to the discrepancy.

Next, it was shown that temporal behaviour is affected by inhomogeneous insulation. Though the Positive/Negative condition did not cause changes in temporal dependence, the Positive/Zero condition causes oscillatory behaviour in rapidly and moderately rotating systems. The spatial structure did not necessarily reflect the temporal behaviour.

All rotating systems exhibited a change in fluid rotation in wall modes due to the inhomogeneity. However, the rapidly rotating system rotated slower while the weakly rotating systems only rotating with inhomogeneous insulation, not in the uniformly insulated case. Within the rotating systems, when Positive/Negative heat flux is applied, the rotation slows within the region where $\partial T/\partial r > 0$ at the sidewall. This contrast to results from Sahoo and Sreenivasan (2020) in which it was shown that increased heat flux slowed flow rotation. Generally, the dominant number of convection rolls was not affected by the large length-scale applied heat flux, with exception for the moderately rotating case which changed from $m_{UI} = 4$ to a dominant $m = 3$ with either Positive/Negative or Positive/Zero heat flux. The non-rotating system also retains the dominant mode when $m_\theta = 1$ is applied. However, without rotation, $m_{UI} = 1$ and hence is better investigated in the context of convective length-scale sidewall inhomogeneities.

5.4.2 Convective length-scale heat flux

We next explore the application of convection length heat flux variations at the sidewalls of RRBC. In terms of the Positive/Negative– Eq (5.1) – and Positive/Zero

– Eq (5.2)– the azimuthal mode is set to be $m_\theta = m_{UI}$, where m_{UI} is the dominant mode of the uniformly insulated configuration as determined in Chapter 3. Hence, the lateral boundary condition should align with the dominant convection rolls.

The vertical temperature profiles are unchanged from the $m_\theta = 1$ case such that the Positive/Negative condition follows similar behaviour as uniformly insulated systems. As in section 5.4.1, the Positive/Zero configuration becomes increasingly vertically uniform in the bulk of the domain but is not centred on $T = 0.5$ (see Appendix D.4).

Thus, we focus on heat transport in the context of the Nusselt number. In this section, Nu_k is considered as both the time averaged value and time series. We additionally, consider the spatial behaviours with a particular interest in the arrangement and movement of convection rolls.

5.4.2.1 Heat transport

In section 5.4.1, it was found that applying large length-scale heat flux to the sidewalls of a cylindrical rotating RBC system caused $\overline{Nu_k}$ to deviate from the homogeneous value. However, we are unaware of any study which compares $\overline{Nu} - Ra$ scaling for an inhomogeneously insulated system with convective length-scale heat flux applied at the sidewalls.

Figure 5.11 shows plots of the time averaged Nusselt number $\overline{Nu_k}$ and corresponding standard deviation σ_{Nuk} against Rayleigh number. The results are calculated from rotating RBC systems with Positive/Zero conditions where the azimuthal mode $m_\theta = m_{UI}$ where m_{UI} is the dominant mode of the uniformly insulated system. The amplitude of the boundary condition and Ek of the system are indicated by the colour and shape of the marker, respectively. Scalings of the form $\overline{Nu} \propto Ra^\gamma$ measured for the uniform case are indicated by the black solid, dot-dashed, and dotted lines for $Ek = 10^{-5}$, 10^{-4}, and ∞, respectively.

From Figure 5.11, it is evident that at Ra value increases, changes in A_n stop affecting $\overline{Nu_k}$. However, the right panel in Figure 5.11 shows that σ_{Nuk} does not follow the same pattern, varying with A_n independently of Ra. With few exceptions, σ_{Nuk} increases as A_n increases which indicates that the amplitude of oscillations or chaotic fluctuations increase with A_n.

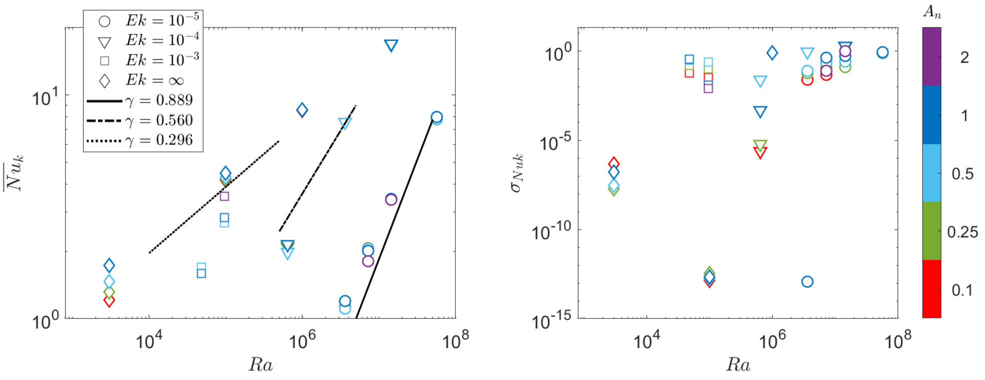

(a) $\overline{Nu_k}$ vs. Ra

(b) σ_{Nuk} vs. Ra

Figure 5.11: Plots of time averaged Nusselt number $\overline{Nu_k}$ and corresponding standard deviations σ_{Nuk} as functions of Rayleigh number Ra. The RBC systems have Ek as noted by the marker shape and Positive/Zero thermal insulation with azimuthal mode $m_\theta = m_{UI}$ where m_{UI} is the dominant mode of the uniformly insulated system. The applied heat flux amplitude A_n is indicated by the marker colour. Heat transport scalings of the form $\overline{Nu_k} \propto Ra^\gamma$ are shown for the uniformly insulated cases with $Ek = \infty$, 10^{-4}, and 10^{-5}.

Visually, comparison between the $\overline{Nu_k}$ spread and the uniformly insulated scalings in Figure 5.11 suggests that the Positive/Zero condition results in similar γ measurements as the uniform case. These results are quantified in Table 5.2 for both the Positive/Negative and Positive/Zero configurations. See the $A_n = 0$ listings in Table 5.1 for the homogeneous γ measurements.

The γ values presented in Table 5.2 do not align with the uniformly insulated results being lower in the non-rotating and rapidly rotating systems but higher in the moderately rotating system. This is true for both the Positive/Zero and Positive/Negative configurations. In comparison to the $m_\theta = 1$ case, as listed in Table 5.1, the scalings for moderate rotation are higher when $m_\theta = m_{UI}$, while rapidly rotating systems have lower γ values. Hence, we anticipate differences in flow structure due to changes in global heat transport indicated by variation in γ value.

To investigate the heat transport further, the Nusselt number time series are illustrated in Figure 5.12. In each panel, the Nu_k values over time are plotted for systems with fixed Ek (as indicated by the right side label) and $Ra = 1.44 \times 10^7$,

Ek	A_n	γ	γ 99% CI	γ	γ 99% CI
∞	0.1	0.351	0.351 – 0.352	-	-
	1	0.269	0.269 – 0.270	0.285	0.284 – 0.285
10^{-4}	0.5	0.738	0.624 – 0.851	0.778	0.435 – 1.07
10^{-5}	0.5	0.680	0.541 – 0.820	0.654	0.652 – 0.656
	1	0.677	0.550 – 0.804	0.722	0.695 – 0.748

Table 5.2: List of scaling γ where $\overline{Nu_k} \propto Ra^{\gamma}$ for inhomogeneously insulating RBC systems. The Positive/Negative condition results are shown in magenta and Positive/Zero condition results are in black. For each the 99% confidence interval (CI) is also listed.

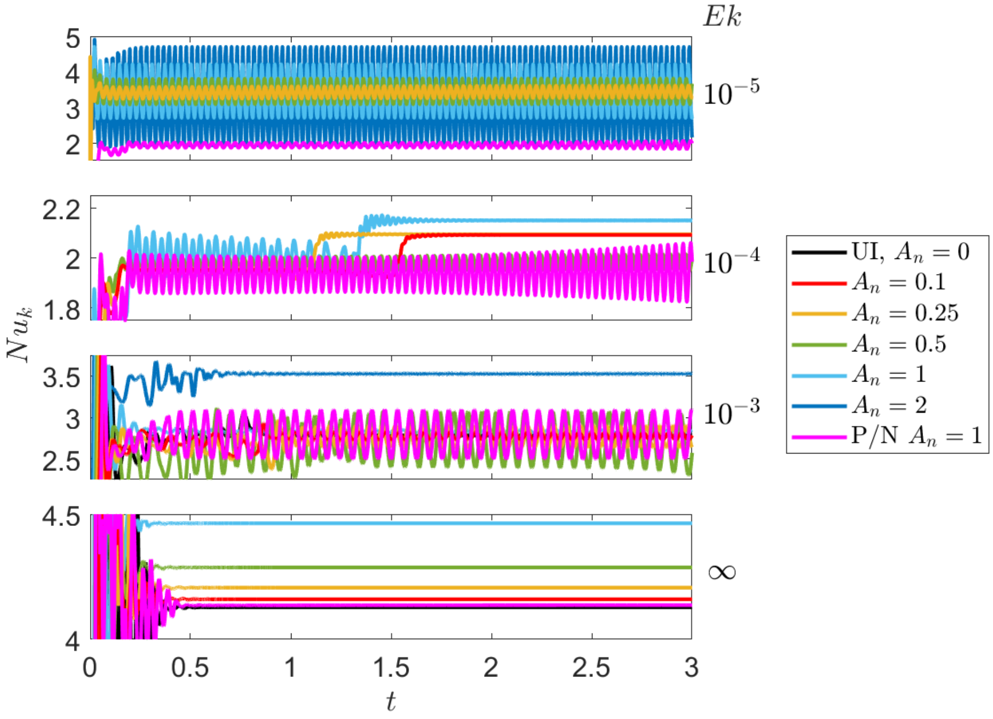

Figure 5.12: Nu_k time series for configurations of inhomogeneous sidewall with $m_\theta = m_{UI}$. The panels contain, from top to bottom, $Ek = 10^{-5}$- $Ra 1.44 \times 10^7$; $Ek = 10^{-4}$-$Ra = 6.4 \times 10^6$; $Ek = 10^{-3}$-$Ra = 9.6 \times 10^4$; and $Ek = \infty$-$Ra = 3 \times 10^3$. Within each plot, A_n of the Positive/Zero boundary condition is varied according to colour, as indicated in the legend. The magenta line shows Positive/Negative case with $A_n = 1$. Note that the vertical axis is not consistent for all panels.

6.4×10^5, 9.6×10^4, and 1×10^5, individually. The black line shows the uniformly insulated result and the magenta line shows the Positive/Negative case with $A_n = 1$. The other colours represent the Positive/Zero configuration with A_n as indicated by the legend. Both inhomogeneous conditions have $m_\theta = m_{UI}$ for each case.

An overview of Figure 5.12 shows that the temporal dependence is strongly affected by the type of inhomogeneity. The Positive/Negative condition causes oscillatory behaviour in all rotating systems. In contrast, the Positive/Zero condition causes time-independence in moderately rotating and weakly rotating systems and oscillatory behaviour in the rapidly rotating case. Further, the $\overline{Nu_k}$ value tends to be increased by increasing A_n with the Positive/Zero condition but not the Positive/Negative condition.

In order to thoroughly investigate these systems individually, it is useful to visualise the flow structure.

5.4.2.2 Convection roll pinning

We first visualise the vertical arrangement of w in several rotating systems. Then, the horizontal arrangement of w is considered particularly in weakly and non-rotating systems.

In the top panel of Figure 5.12, the Nu_k time series for a system with $Ek = 10^{-5}$ and $Ra = 1.44 \times 10^7$ is shown. There is a significant variation between the temporal behaviours of the Positive/Zero and Positive/Negative configurations. To explore how the temporal differences relate to flow structure, we observe Figure 5.13 which shows the vertical velocity both for fixed r and z (left); and for fixed r and t (right). The upper panel has Positive/Negative inhomogeneity with $A_n = 1$ and the lower two panels have Positive/Zero variation with $A_n = 1$ and 2, respectively. All plots have an azimuthal mode of $m_\theta = 3 = m_{UI}$.

The upper panel of Figure 5.13 shows that the Positive/Negative configuration has a similar pattern to the Positive/Zero condition when large length-scale variations were applied (see Figure 5.9c) such that the convection rolls continue rotating about the domain. This differs from previous Positive/Negative results where slowing of rotation was noted in regions where positive heat flux is applied. This is also evident in the snapshot of the vertical axis in the right-hand panel

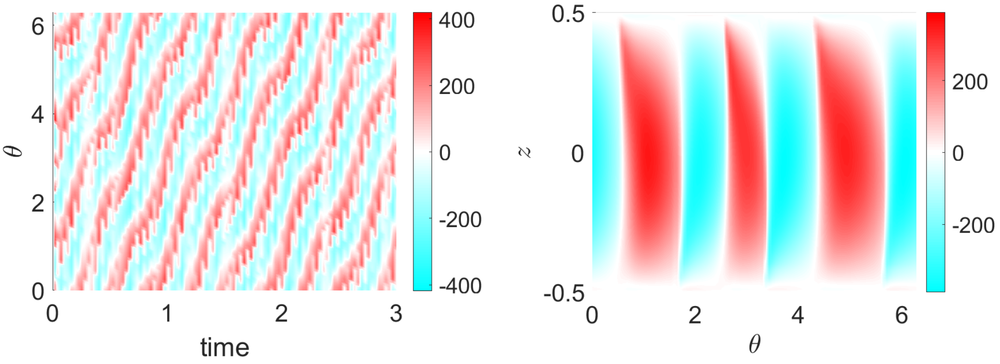

(a) Positive/Negative, $A_n = 1$

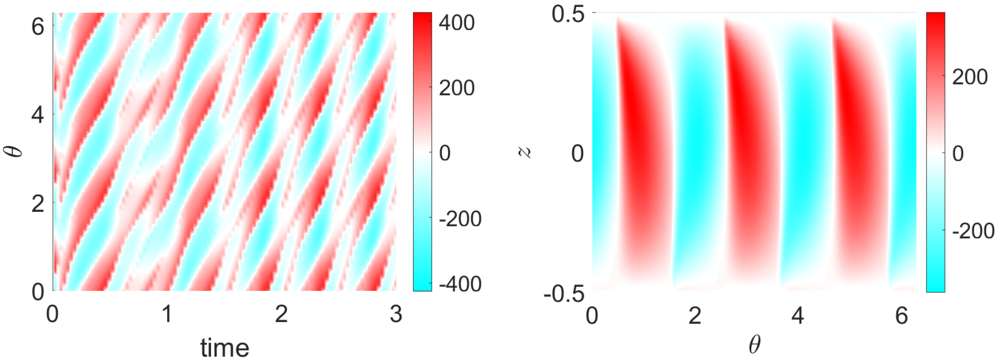

(b) Positive/Zero, $A_n = 1$

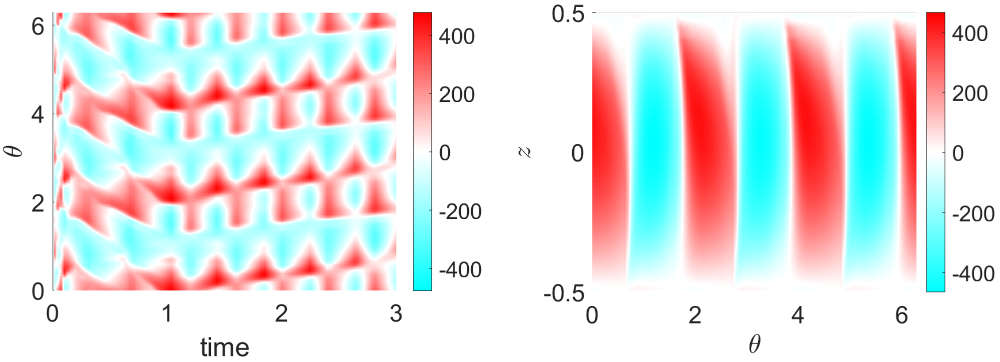

(c) Positive/Zero, $A_n = 2$

Figure 5.13: Visualisations of w in RRBC system with $Ek = 10^{-5}$ and 1.44×10^7 with inhomogeneous sidewall insulation. On the left (right) are Hövmoller diagrams with fixed $r = 0.68$ and $z = 0.3$ (w at fixed $t = 3$ and $r = 0.685$). For each $m_\theta = 3 = m_{UI}$. The homogeneous results are shown in the upper panel of Figure 5.9c.

which shows that some convection rolls are narrower but with no clear dependence on the heat flux variations.

In contrast, the lower panels of Figure 5.9 show that the Positive/Zero case begins to form a regular pattern and decreases in rotation rate in comparison to the Positive/Negative configuration for $A_n = 1$. When the amplitude is doubled, the bottom panel shows evidence of convection roll pinning. Though the rolls are not in a constant location, the average θ range for a fixed w value does not rotate strongly about the system, not completing even a single rotation during the 3 time unit simulation. The variation of upward and downward flow is limited to azimuthal regions of width $\theta = 3/2\pi$. Further, right plot of the lowest panel shows that the upward modes split toward the top of the domain. This split alternates between the downward and upward columns over time and causes the zigzag pattern in the Hövmoller diagram. We see the same kind of behaviour in the $Ek = 10^{-4}$ and $Ra = 6.4 \times 10^5$ case (see Appendix D.4).

In weakly and non-rotating systems, the pinning is more efficient, minimising the regional oscillations. For example, Figure 5.14 illustrates w for the system $Ek = 10^{-3}$ and $Ra = 9.6 \times 10^4$ with Positive/Zero configuration and $m_\theta = 4 = m_{UI}$ and $A_n = 2$. In the left panel, the Hövmoller diagram shows two clear convection rolls, oscillating with weak velocities within azimuthal regions of width $\theta = 2/2\pi$. While the homogeneous case had negligible rotation of the convection rolls, the applied heat flux alters the flow structure.

From the right-hand panels of Figure 5.14, it is evident that the bulk spatial behaviour is altered by the inhomogeneous insulation. Rapidly and moderately rotating systems did not exhibit such alterations, having wall-localised convection with and without inhomogeneity in the sidewall thermal condition. Further investigation of the bulk flow shows that while the wall-localised flow is time-independent, the bulk flow has become time-dependent.

Figure 5.15 shows two snap-shots of vertical velocity at $z = 0.3$ in the weakly rotating system. Comparing the plots at time $t = 2.7$ (left) and $t = 2.9$ (right), it is clear that the fluid in the interior of the domain is fluctuating while the convection rolls at walls remain fixed. Hence, the Positive/Zero condition has caused both

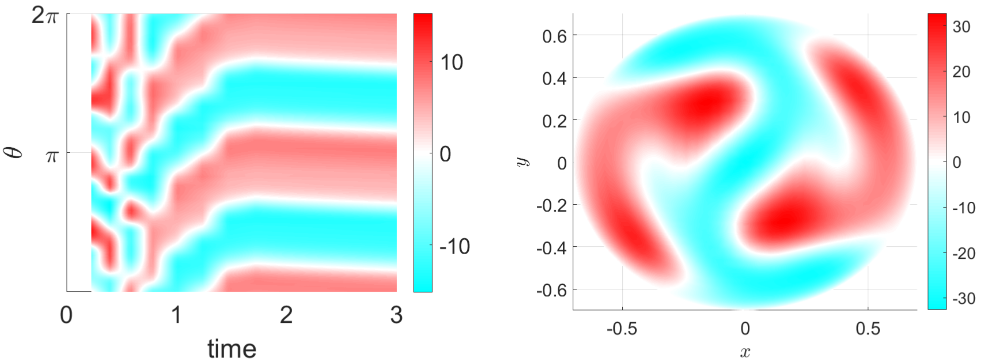

(a) Homogeneous

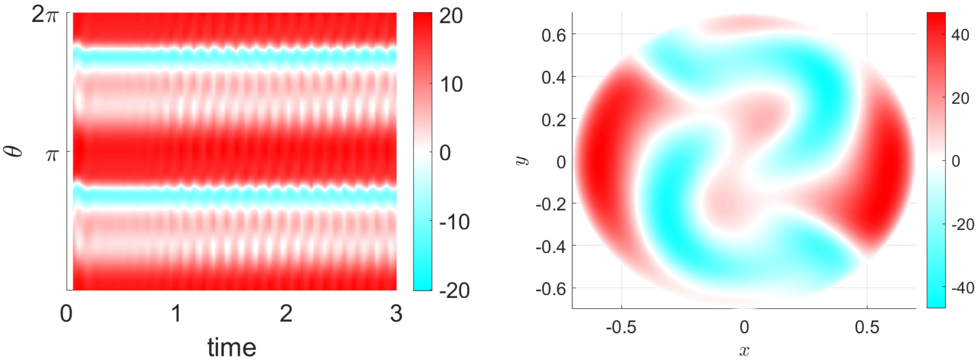

(b) Positive/Zero

Figure 5.14: Plots of vertical velocity in a weakly rotating system with $Ek = 10^{-3}$ and $Ra = 9.6 \times 10^4$. On the left are Hövmoller plots at $r = 0.68$ and $z = 0.3$. On the right, $z = 0.3$ and $t = 3$ are fixed. The inhomogeneous Positive/Zero insulation has $m_\theta = 2 = m_{UI}$ and $A_n = 2$.

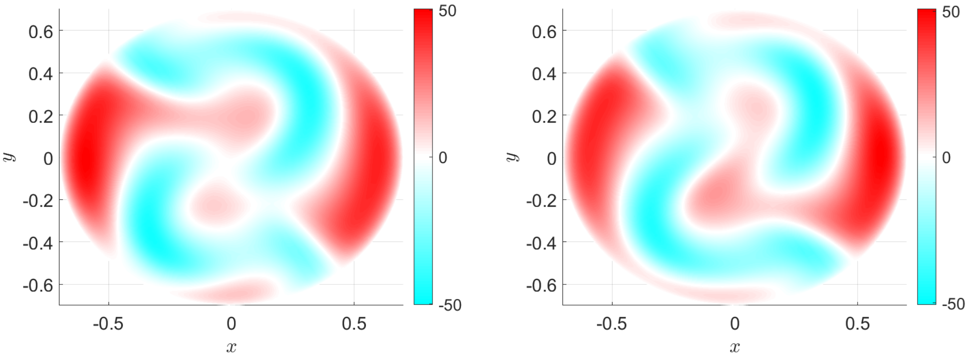

(a) $t = 2.7$ (b) $t = 2.9$

Figure 5.15: Vertical velocity in a weakly rotating RBC with parameter $Ek = 10^{-3}$ and $Ra = 9.6 \times 10^5$. Inhomogeneous insulation is applied in the Positive/Zero configuration with $m_\theta = 2 = m_{UI}$ and $A_n = 2$.

pinning and time-dependence. This behaviour is also exhibited in non-rotating flows.

Thus, we have seen that applying convective length-scale inhomogeneity to sidewall insulation can cause pinning of convection rolls to varying degrees for different rotation regimes. Rapidly and moderately rotating systems have wall-localised modes pinned within azimuthal regions of width $\theta = m_\theta/2\pi$ for sufficiently large amplitudes of heat flux. Weakly and non-rotating systems also have wall-localised convection pinning however they also exhibit time-dependent flow in the fluid bulk. Having established that matching the length-scale of the lateral heat flux condition to the convective length-scale results in pinning, we consider m_θ which match secondary convective length-scales.

5.4.3 Secondary convective length-scale heat flux

The ability of convective length-scale insulation variations to pin convection rolls motivates us to explore the application of secondary convective length-scale inhomogeneity, i.e. for a system with $m_{UI} = 4$ we apply $m_\theta = 2$, or 8. These secondary structures tend to have a significant but not dominant presence in convection. For example, a fast Fourier Transform of the vertical velocity at a fixed $z = 0.3$ and $r = 0.65$ of the uniformly insulated case with $Ek = 10^{-4}$ and $Ra = 1.44 \times 10^7$ has a

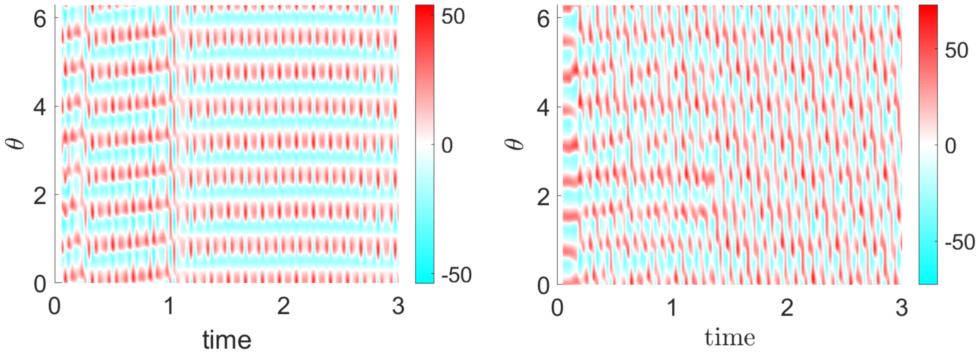

(a) Positive/Negative, $A_n = 2$ (b) Positive/Zero, $A_n = 1$

Figure 5.16: Vertical velocity for RRBC system with $Ek = 10^{-4}$ and $Ra = 6.4 \times 10^5$. Inhomogeneous insulation is applied in two different configurations: Positive/Negative and Positive/Zero. Both cases have azimuthal mode of $m_\theta = 8 = 2m_{UI}$ and amplitude of $A_n = 2$.

peak amplitude at mode $m_{UI} = 4$ with secondary peaks of 20% and 16% strength at $m = 8$ and 12, respectively. In this section, we apply $m_\theta = bm_{UI}$ where b is a positive integer or 1/2.

Considering our example case with $Ek = 10^{-4}$ and $Ra = 6.4 \times 10^5$, we apply azimuthal mode $m_\theta = 8$. Figure 5.16 shows two Hövmoller diagrams with Positive/Negative (left) and Positive/Zero (right) boundary conditions. In both panels, there is evidence of a dominant $m_\theta = 8$ mode. However, the Positive/Negative panel has a less oscillatory structure than the Positive/Zero case. This is likely due to the larger heat flux amplitude applied in the Positive/Negative configuration rather than a more efficient pinning mechanism.

For a fixed amplitude, weakly rotating systems exhibit differences in flow structure between the Positive/Negative and Positive/Zero configurations. Considering the weakly rotating system with parameters $Ek = 10^{-3}$ and $Ra = 9.6 \times 10^4$, we apply $m_\theta = 4 = 2m_{UI}$. Figure 5.17 shows Hövmoller diagrams and horizontal slices at $z = 0.3$ and $t = 3$ for both Positive/Negative and Positive/Zero configurations.

The lower panels of Figure 5.17 show four efficiently pinned convection rolls near the walls with relatively distinct interior flow when bounded with Positive/Zero heat flux. In contrast, the Positive/Negative configurations results exhibit weakly pinned rolls, with significant oscillations. Further, the bulk structure appears to

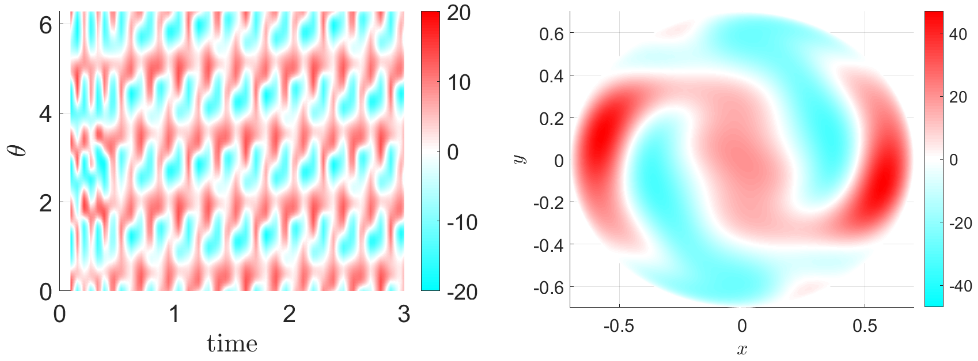

(a) Positive/Negative

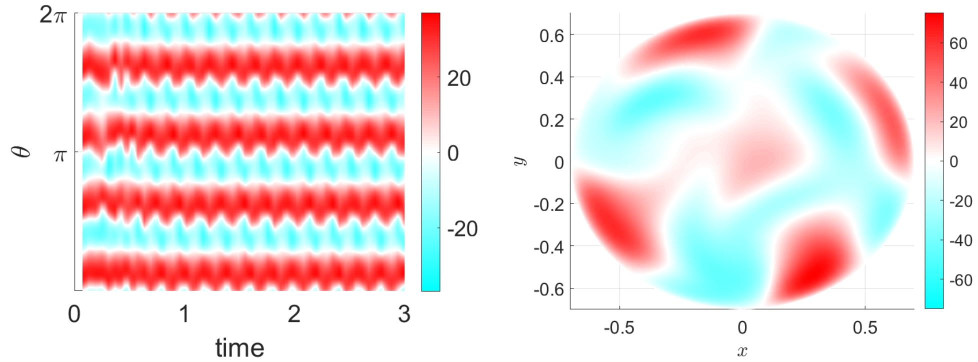

(b) Positive/Zero

Figure 5.17: Plots of vertical velocity in a rotating RBC system with $Ek = 10^{-3}$ and $Ra = 9.6 \times 10{-}^{4}$. Positive/Negative and Positive/Zero inhomogeneous heat flux is applied at the sidewall with $m_\theta = 4 = 2m_{UI}$ and $A_n = 2$.

dominate the flow the domain, with only weak wall-localised modes appearing to match the applied heat flux. However, in both the cases, the flow structure in the bulk differs from the homogeneous case as shown in the top panel of Figure 5.14. Thus, even weakly generated convection rolls at the wall due to inhomogeneous insulation affect the bulk flow in the weakly rotating RBC.

In summary, we have found that both Positive/Zero and Positive/Negative heat flux boundary conditions, when applied with azimuthal mode of $m_\theta = bm_{UI}$, can cause a change in the dominant mode of convection in moderately and weakly rotating systems. However, we note that in weakly rotating flows, where bulk convection dominates rather than wall-localised convection, the applied number of convection rolls does not necessarily dominate the interior flow. The bulk flow does change structure due to the presence of wall-localised modes but is not subject to the same form. Note we disregard the non-rotating case in this instance because the dominant mode $m_{UI} = 1$ is significantly more powerful than any secondary modes.

5.5 Summary

In this chapter we investigated a rotating cylinder with sidewall heat flux varying in sinusoidal patterns azimuthally and vertically. We were motivated by the variation in heat flux surrounding planetary cores due to non uniform heating from the mantle and sought to investigate experimentally viable numerical models. We considered sinusoidal variations about the azimuthal axis such that the mode could be applied wither either a larger length-scale, the same length-scale, or a multiple of the convective length-scale. The first case is applicable in a geophysical context because in the planetary core, the heat flux at the mantle is at a larger wavelength than the convection in the core (Mound & Davies, 2017). Hence, we ubiquitously modelled the large length-scale with azimuthal mode $m_\theta = 1$. In the latter two cases, we hypothesised that by matching the uniform length scale m_{UI}, the convection rolls could become zonally stable, overcoming the force of rotation in RRBC.

In section 5.2, we defined two inhomogeneous boundary conditions: Positive/Negative and Positive/Zero. The first configuration oscillates heat flux between positive and negative and the second oscillates with $\partial T/\partial r \geq 0$. The latter is more geophysically and experimentally appropriate (Mound & Davies, 2017; Sahoo & Sreenivasan, 2020). Both conditions are dependent on the prescribed amplitude A_n and azimuthal mode m_θ.

Next, in section 5.3, an analytical result is derived for each boundary condition to compare with numerical results in order to test the accuracy of the numerical methods. For the Positive/Negative condition, the solid steady state solution is derived resulting in Eq (5.5). Using the solid steady state solution, we determined that there is no thermally driven though non-convective flow and that convection onsets at a lower Ra_c than in the uniform case, agreeing with previous literature (Sahoo & Sreenivasan, 2017, 2020). For the Positive/Zero configuration, we calculate the heat flux through the domain, finding that the difference between the heat flux at the top and bottom of the domain is proportional to the amplitude of the sidewall boundary heat flux. This relationship enabled us to compare the analytic prediction to numeric results.

Further, given the dependence of heat transport on the lateral boundary condition, we sought to redefine the Nusselt number. In Eq (5.12), we define Nu_k as in Kunnen, Clercx, and Geurts (2008) and compare $\overline{Nu_k}$ and $\overline{Nu}$ values for the fixed temperature, uniformly insulated configuration. Finding sufficient similarity, we established the use of Nu_k as the metric of heat transport throughout this chapter.

We next applied a large length-scale heat flux to the sidewalls of RRBC systems. In section 5.4.1, we fixed $m_\theta = 1$ and investigated vertical temperature profiles, $\overline{Nu_k} \propto Ra^\gamma$ scaling, temporal behaviour, and spatial behaviour. The temperature profiles show that the Positive/Negative condition causes the same average temperature structure as the homogeneous case while the Positive/Zero configuration has a higher average temperature in the domain bulk.

Considering the $\overline{Nu_k}$ measurements, Mound and Davies (2017) previously found that large length-scale inhomogeneities caused enhancement of γ in a rapidly rotating spherical shell. The results recorded in Table 5.1 show the opposite for this case such that as the heat flux amplitude A_n increases, the γ value decreases for both the Positive/Negative and Positive/Zero configurations. The discrepancy between our results and those in Mound and Davies (2017) is likely due to differences in definition of heat flux amplitude and in the range of Ra values modelled, as well as the domain geometry.

We chose a representative set of systems to explore more closely, one Ra for each $Ek = \infty$, 10^{-3}, 10^{-4}, and 10^{-5}. In each case, it was shown that temporal behaviour is affected by Positive/Zero, but not Positive/Negative inhomogeneous insulation. However, the spatial structure was affected for both configurations. Rotating systems exhibited a change in rotation of convection rolls about the vertical axis. In rapidly rotating systems, rolls rotated slower while the weakly rotating systems only rotated with inhomogeneous insulation, not in the uniformly insulated case. In contrast to results from Sahoo and Sreenivasan (2020), in which it was shown that increased heat flux slowed flow rotation, when Positive/Negative heat flux was applied, the rotation slows within the region where $\partial T/\partial r > 0$ at the sidewall. Generally, the dominant number of convection rolls was not affected by the large length-scale applied heat flux, with exception for the moderately rotating case which changed from $m_{UI} = 4$ to a dominant $m = 3$ with either Positive/Negative or Positive/Zero heat flux. The non-rotating system also retained the dominant mode when $m_\theta = 1$ is applied. However, without rotation, $m_{UI} = 1$ and hence is better investigated in the context of convective length-scale sidewall inhomogeneities.

Next, in section 5.4.2, the convective-length scale was applied such that $m_\theta = m_{UI}$ where m_{UI} is the dominant mode of the uniformly insulated system. The γ calculations were decreased from those in the $m_\theta = 1$ cases. Investigation of the spatial behaviour showed that that applying convective length-scale inhomogeneity can cause pinning of convection rolls. Rapidly and moderately rotating systems have dominant wall-localised convection pinned within azimuthal regions of width $\theta = 2\pi/m_\theta$ for sufficiently large amplitudes of heat flux. While weakly and non-rotating systems also have wall-localised convection pinning, the convection rolls on the interior do not conform to time-independent behaviour.

In section 5.4.3, we applied $m_\theta = bm_{UI}$ where $b = 0.5$ or 2, such that the inhomogeneity has the length scale of a secondary convective mode. We found that both Positive/Zero and Positive/Negative heat flux boundary conditions caused the

m_θ value to become the dominant mode of convection. However, we again note that the applied mode is only dominant in wall-localised flow. In weakly rotating systems, the bulk flow changes structure and becomes time-dependent while the wall-local flow is time-independent due to the boundary conditions.

Overall, we suggest that inhomogeneous insulation, as present in planetary cores, does effect convection, though the effect decreases as rotation becomes more rapid. We show that positive heat flux has a stronger effect than negative heat flux on the sidewall boundaries of the system. Notably, we observe that larger wavelengths applied to the sidewall than are dominant in the domain, as is the case in planetary cores, demonstrated changes in flow behaviour dependent on the amplitude of the sidewall boundary condition. This result suggests that studies motivated by planetary cores and interested in moderate Ra number must necessarily consider variation in heat flux at the mantle, particularly for the investigation of boundary layers, due to our observation that wall-localised convection is most strongly affected by inhomogeneous insulation. Further, it is of interest to experimentalists that by matching the applied azimuthal mode to the dominant mode of the insulated system, a rotating system can have pinned convection rolls in rapidly rotating systems. Additionally, the location of convection rolls within non-rotating systems can be adjusted within the domain using inhomogeneous sidewall insulation. These results provide a basis for further investigation into more realistic astrophysical systems with heterogeneous sidewall insulation and a background for an experimental design to study the same effects.

Chapter 6

Experimental Design

6.1 Introduction

Previously, we have focused on relating numerical simulations to physical systems, both experimental and natural, by determining the effect of choosing an idealised thermal boundary condition in comparison to a physically appropriate condition. In Chapter 3, we determine that, for sufficiently rapidly rotating and strongly convecting systems, systems with fixed flux and fixed temperature thermal boundary conditions behave similarly. In Chapter 4, we expand this knowledge, applying the Robin boundary condition, which uses the Biot number Bi –a ratio of thermal conductivity and thickness of the boundary to that of the fluid– to determine if the boundary is closer to fixed temperature or fixed flux conditions. In that chapter, we determine a range of Biot numbers which constitute sufficiently fixed temperature or fixed flux conditions. Thus, having thoroughly described the traditional numerical thermal boundary conditions to model physical systems, we turn our attention to designing an experiment.

As discussed in Chapter 1, there have been interesting developments in the field of simplified moist convection. Of particular interest is the Fast Autoconversion and Rain Evaporation (FARE) model proposed in Hernadez-Duenas et al. (2012), which is a two-fluid system, is capable of modelling cloud dynamics such as squall lines with only two-phases of fluid. However, such models have not been experimentally studied in a rotating system, which would provide both validation of the numerical model and the opportunity to improve forecasting by testing data assimilation between the numerical model and the observational data from the experiment. Therefore, an experimental set-up is proposed to model a system akin to that of the FARE model, such that the system contains two fluids: air in the gaseous form, and a second fluid which co-exists in two phases. This experiment provides the opportunity to better understand convection dynamics with both precipitants and phase change. Such weather-related processes are becoming increasingly important to understand due to severe and rapid fluctuations in weather patterns due to climate change (Trapp, 2018).

We propose an experiment which would be able to validate the FARE model and an equivalent rotating model. In order to design the proposed experiment, each specification of the model must be explained and rationalised. In this chapter, we will describe the choice and reasoning for each part of the experiment to thoroughly provide the design for a future study. We discuss the aspects of the experiment: the general design, determination of independent variables, and identification of suitable specific materials.

In regard to the general design, the experiment uses a cylindrical cell with clear sidewalls, on a rotation table. The experiment aims to control the convection within the cell to a few ($1 \leq m \leq 3$) non-chaotic convection rolls to enable easy observation and measurement of behaviours and pattern formation. In order to design the experiment, a number of independent variables must be chosen including: what precipitant is used and in which phases, what aspect ratio Γ of the cylindrical domain, what materials the cylinder should be made of and their dimensions, as well as temperature difference $\Delta\tilde{T}$, pressure $\tilde{p}$, rotation rate Ω, and domain height d. Recall that the tildes indicate dimensional variables.

6.2 Precipitant

The experiment requires the presence of a precipitant– preferably one which is visible in both gaseous and precipitating phases– to coexist in a system of gaseous air. The FARE model considered uses water as a liquid and vapour, neither of which are visible. Additionally, the low energy state, either liquid or solid, will settle at the bottom of the cylindrical cell. If the low energy phase is liquid, the thermal boundaries at the bottom of the system are difficult to control due to fluctuations in the volume of liquid at the lower boundary, causing changes in thermal conductivity. Therefore, it is desirable to use a solid phase material which will sublimate into a gas.

Hence, our choice is a sublimating material which is visible in both the gaseous and solid form. These constraints significantly limit the number of fluids available. Further limitations on the system require that the pressure remain in an achievable range with a low vacuum, and a temperature above room temperature such that the entire system does not need to be cooled. These restrictions will be further discussed in section 6.4. To understand the conditions which enable sublimation, we identify the triple point of each potential fluid. The triple point is the temperature and pressure at which gaseous, liquid, and solid phases can coexist. Generally, for temperatures and pressures above the triple point, the gaseous phase is preferred (Pavia et al., 2015).

Table E.1 in Appendix E details fluids which meet our requirements, their triple points, visibility, and hazards. Due to health risks, Hexachloroethane and Camphor will not be considered, leaving Iodine as the most likely choice, followed by Ferrocene which is not confirmed to have a visible gas phase. For the sake of brevity, this Chapter considers only Iodine, but provides a protocol which can be used to adjust the design for Ferrocene.

We next consider the conditions for the sublimation of Iodine. To guarantee sublimation there must be some portion of the domain where pressure $\tilde{p}$ is at or below the triple point and temperature $\tilde{T}$ is at or above the triple point. Because convection is thermally driven, $\tilde{T}$ varies within the system, allowing for both solid and gaseous states as the fluid moves through the triple point $\tilde{T}$. Practicality also requires $\tilde{p}$ be approximately constant throughout the system, therefore it is ideal to have a $\tilde{p}$ value similar to the triple point $\tilde{p}$ value, unless the $\tilde{T}$-gradient is sufficiently steep such that the fluid does not have enough time to change into the liquid phase as $\tilde{T}$ transitions within the domain. Hence, we constrain pressure and temperature such that $\tilde{p} \leq 1.12 \times 10^4$Pa, and average temperature, $\overline{\tilde{T}} = 114^o$C.

6.3 Aspect ratio

Our experiment is required to be a sealed cylinder with clear sidewalls which contains air and Iodine and is able to spin on a rotating table. In order to make confident measurements and observations of the gaseous form of Iodine, a non-chaotic pattern of convection is preferred. Therefore, it is essential to choose a cylindrical aspect ratio, $\Gamma = R/d$, which maintains regularly patterned convection cells to the highest Rayleigh number, Ra. Recalling that $Ra = \alpha g \Delta\tilde{T} d^3/\nu\kappa$ (assuming boundaries are chosen to be sufficiently similar to fixed temperature conditions) it is clear that increasing $\Delta\tilde{T}$ and d increases the Ra value.

Regarding the determination of the Γ value, there is plenty of analytical, numerical, and experimental research on the stability of non-rotating Rayleigh–Bénard convection (RBC). Results on the stability of RBC with physically relevant no-slip velocity boundary conditions and conductive thermal boundary conditions at the vertical boundaries are compiled in Clever and Busse (1974), which considers a plane-layer with $Pr = 0.71$, which is appropriate for air. In Clever and Busse (1974), it is shown cellular convection occurs when the wavenumber is within the range $3 < a < 5$ and $3 \times 10^3 < Ra < 2 \times 10^4$. Note that the geometry used in Clever and Busse (1974) is not relevant to the proposed experiment. However, the ranges of a and Ra provided are useful as approximations for our experimental design.

We relate a to Γ via an approximation applied in Gao and Behringer (1984) such that,

$$\Gamma = \frac{m\pi}{2a}, \tag{6.1}$$

recalling that m is the number of convection rolls. We choose $m = 2$ for ease of observation in the experiment and $3 < a < 5$ from the stability diagram in Clever and Busse (1974). From these specifications, we determine a range of appropriate aspect ratios: $0.89 < \Gamma < 0.52$. To further limit this range, we observe from Clever and Busse (1974) that for $a < 4$, an oscillatory instability onsets at $Ra < 10^4$ and for $a > 5$, the cross-roll and Ekhaus instabilities are dominant for low $Ra < 10^4$. We conclude that $a = 4.5$ is optimal, which, from Eq (6.1), concludes that $\Gamma = 0.7$ is an appropriate value.

When considering RRBC the prominent instability is the Küppers-Lortz instability which is characterised by rolls which bend toward the boundary and oscillate and occurs near onset (Küppers & Lortz, 1969). The onset of the Küppers-Lortz instability is dependent on the rotation rate, Ω, and Pr. The rotating stability relationship between Pr and Ek is described in Clune and Knobloch (1993) for a plane-layer geometry, from which it is clear that $Ek < 8 \times 10^{-3}$ the onset of convection exhibits Küppers-Lortz instability with $Pr \approx 0.7$. Note that the geometry of the experiment is cylindrical and therefore, the $Ra - Ek$ parameter range at which the Küppers-Lortz instability is likely to deviate from that of the plane-layer. We choose to accept the Küppers-Lortz form of instability at onset as acceptable as it is non-chaotic.

While there is no definitive literature on the stability of rotating convection in cylinders with $\Gamma = 0.7$ for $Pr = 0.7$, the results presented in Buell and Catton (1983b) demonstrate that the critical Ra increases as Γ decreases. Additionally, the stability analysis in Clune and Knobloch (1993) suggests that there are ranges of Ra for which rapidly rotating convection will be non-chaotic in the domain suggested above. Therefore, $\Gamma = 0.7$ is deemed to be a suitable aspect ratio for the experiment considered, with and without rotation.

6.4 Independent variables

Next, we consider the independent variables of the system: pressure $\tilde{p}\,(\mathrm{Pa})$, the height $d\,(\mathrm{m})$, the temperatures at the top $\tilde{T}_1(^{\circ}\mathrm{C})$ and bottom $\tilde{T}_0(^{\circ}\mathrm{C})$ of the system, and the rotation rate $\Omega\,(\mathrm{Hz})$. These variables are constrained by both the existing design parameters and practical measures.

We begin by considering the $\tilde{p}$ in the absence of convection. $\tilde{p}$ is limited by the triple point of Iodine and our practical ability to adjust the pressure away from atmospheric pressure (1.01×10^5Pa). From Table E.1 we know that Iodine sublimates at $\tilde{p} = 1.12 \times 10^4$Pa and $\tilde{T} = 114^{\circ}$C. Therefore, we require $\tilde{p} \leq 10^5$Pa. Note that when $\tilde{p} > 1.12 \times 10^4$Pa, we additionally require a steep temperature gradient in order to limit the presence of a parameter range which would allow for the liquid phase of Iodine. Practically, the pressure can be lowered from atmospheric pressure using a low vacuum which is capable of decreasing $\tilde{p}$ to a minimum of 1×10^3Pa. Therefore, we suggest the range of feasible pressures to be $1 \times 10^3\text{Pa} < \tilde{p} < 1 \times 10^5\text{Pa}$.

Next, the temperature at the top and bottom of the system, $\tilde{T}_{0,1}$ is informed by the triple point of Iodine. From Table E.1, the mean temperature, $\overline{\tilde{T}} = 114^{\circ}\text{C}$, is ideal for the sublimation of Iodine, which we want to occur near the centre of the domain. We also require a negative vertical temperature gradient which is sufficiently robust to withstand a lack of precision in heating at the boundaries. Therefore we limit $\Delta\tilde{T} = \tilde{T}_0 - \tilde{T}_1 \geq 5^{\circ}\text{C}$. Ideally, the temperature at the upper boundary would be $\tilde{T}_1 = 0^{\circ}\text{C}$ such that the temperature can be controlled by ice, for simplicity of the design. This corresponds to $\Delta\tilde{T} = 228^{\text{O}}\text{C}$. However, this is not a requirement.

The rotation rate, Ω, is simply limited by the capabilities of the rotation table. We measured the rotation speeds of the table currently available to us. The maximum rotation rate is $\Omega = 3.4\text{Hz}$. This value will limit our Ekman number.

The height of the rotation table d is limited by $\Gamma = 0.7$ which requires that $d = R/0.7$ where R is the radius. We require our experimental domain to sit on the available rotation table, which has a radius of 0.2m. Therefore, we have a maximum radius of our system just below this because our interior radius will be enclosed by a material of some thickness d_{sw}. Let us assume $d_{sw} \geq 0.005\text{m}$. Consequently, $R \leq 0.19\text{m}$ which corresponds to $d \leq 0.278\text{m}$. Additionally, to enable visual observations, we enforce that the system must be sufficiently large, such that $0.05\text{m} \leq d \leq 0.278\text{m}$.

Given that we have determined the ranges of necessary and feasible $\tilde{p}$, $\tilde{T}_{0,1}$, Ω, and d, we consider how these independent variables contribute to the determination of the non-dimensional parameters which are used to understand the regime of convection and to relate physical systems to numerical models. As in previous chapters, we use the Prandtl number,

$$Pr = \frac{\nu}{\kappa}, \tag{6.2}$$

the Rayleigh number,

$$Ra = \frac{\alpha g \Delta \tilde{T} d^3}{\nu \kappa}, \tag{6.3}$$

and the Ekman number,

$$Ek = \frac{\nu}{2\Omega d^2}. \tag{6.4}$$

Hence, we have introduced several dependent variables: the kinematic viscosity, $\nu\left(\tilde{p}, \overline{\tilde{T}}\right)$, the coefficient of thermal diffusivity, $\kappa\left(\tilde{p}, \overline{\tilde{T}}\right)$, and the coefficient of thermal expansion, $\alpha\left(\overline{\tilde{T}}\right)$. Additionally we have the acceleration due to gravity, $g = 9.8\text{m/s}^2$, which is constant.

We begin the investigation of the relationships between our dependent variables and independent variables with the coefficient of thermal expansion. By definition, α is considered at constant pressure so is only dependent on $\overline{\tilde{T}}$ such that,

$$\alpha = \frac{1}{\overline{\tilde{T}}} \tag{6.5}$$

(Dixon, 2007). We consider $\overline{\tilde{T}}$ to be the average temperature of the system and therefore should be the triple point of Iodine, 114.1°C (Yolcu, 2016).

We next consider the kinematic viscosity, which is defined as,

$$\nu = \frac{\mu}{\rho}, \tag{6.6}$$

where μ is the dynamic viscosity and ρ is density. Assuming an ideal gas, $\rho = \tilde{p}/(R_g \overline{\tilde{T}})$, where $R_g = 287.05\text{J/kgK}$ is the specific gas constant of air (Dixon, 2007). μ is also a function of pressure and temperature. In Kadoya et al. (1985), experimental data is used to develop a set of equations to define the relationship between μ, ρ, and $\overline{\tilde{T}}$. This relationship is described in Appendix E.

Figure 6.1a visualises the relationships between μ, $\tilde{\rho}$, and ν each as a function of $\tilde{p}$. The density $\tilde{\rho}(\text{kg/m}^3)$, shown in blue, increases as, $\tilde{p}$, increases while $\mu(\text{Ns/m}^2)$, plotted in red, remains constant. Dynamic viscosity ν increases as $\tilde{p}$ increases.

To quantify the values of $\tilde{\rho}$, μ, and ν, shown in Figure 6.1a, we apply the range of achievable pressures, $1 \times 10^3 \leq \tilde{p} \leq 1 \times 10^5\text{Pa}$, to the ideal gas law to find density and to the $\mu - \tilde{p}$ relationship described in Appendix E to find dynamic viscosity for air with $\overline{\tilde{T}} = 144°\text{C}$. We recover a range of density such that, $9 \times 10^{-4} \leq \tilde{\rho} \leq 9 \times 10^{-1}\text{kg/m}^3$. Within the range of $\tilde{p}$ considered, there is minimal

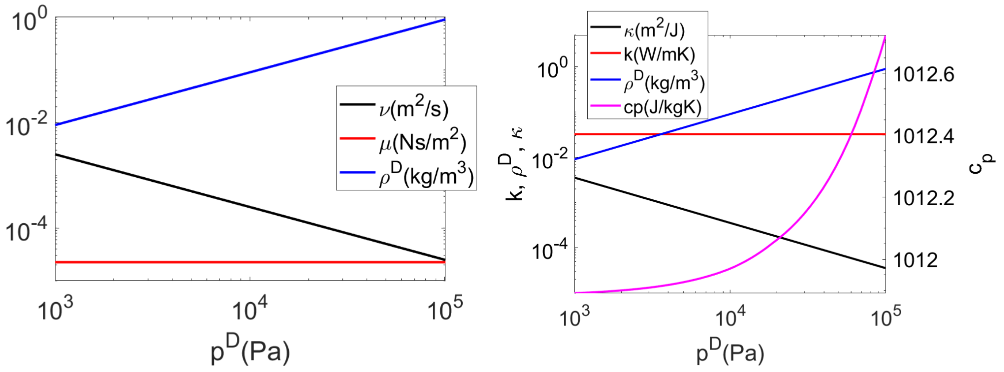

(a) ν, μ, and ρ vs. $\tilde{p}$ (b) κ, k, and ρ vs. $\tilde{p}$

Figure 6.1: Plots showing how, for air, dependent variables vary as pressure varies within the range $1 \times 10^3 \leq \tilde{p} \leq 1 \times 10^5$. (lef) Density $\tilde{\rho}$ (blue), dynamic viscosity μ (red), and kinematic viscosity $\nu = \mu/\tilde{\rho}$ (black) as a function of $\tilde{p}$. (right) Density $\tilde{\rho}$ (blue), thermal conductivity k (red), and the coefficient of thermal diffusivity $\kappa = k/\tilde{\rho}c_p$ (black), on the left vertical axis and– on the right vertical axis– the specific heat c_p is plotted in magenta as a function of $\tilde{p}$. For all values, the average temperature is 114.1°C.

variation in the dynamic viscosity such that, $\mu = 2.2549\times10^{-5}\pm8.2748\times10^{-9}\mathrm{Ns/m^2}$ and the kinematic viscosity is within the range $2.5 \times 10^{-5} \leq \nu \leq 2.5 \times 10^{-3}\mathrm{m^2/s}$.

We use relationships defined in Kadoya et al. (1985) to estimate the coefficient of thermal diffusivity, which is defined as,

$$\kappa = \frac{k}{\tilde{\rho}c_p}, \tag{6.7}$$

where k is the thermal conductivity, and c_p is the specific heat capacity. Appendix E describes the relationship between k and $\tilde{p}$. The definition of density such that $\tilde{\rho} = \tilde{p}/(R_g\bar{\tilde{T}})$ is used to relate k to $\tilde{p}$. Additionally, c_p varies with $\tilde{p}$ and $\bar{\tilde{T}}$. Using data provided in Hilsenrath et al. (1955), an approximate relationship is fitted for air with $\bar{\tilde{T}} = 387.5\mathrm{K} = 114^{\circ}\mathrm{C}$,

$$c_p = p\left(8.35 \times 10^{-6}\ \mathrm{J/kgKPa}\right) + 1011.9144\ \mathrm{J/kgK}. \tag{6.8}$$

Figure 6.1b visualises the relationships between $\tilde{p}$, and κ, k, $\tilde{\rho}$, and c_p, with average temperature $\bar{\tilde{T}} = 114.1^{\circ}\mathrm{C}$. On the left vertical axis, the values of κ, k, and $\tilde{\rho}$ are shown. The right vertical axis shows the values of c_p. In black it is clear

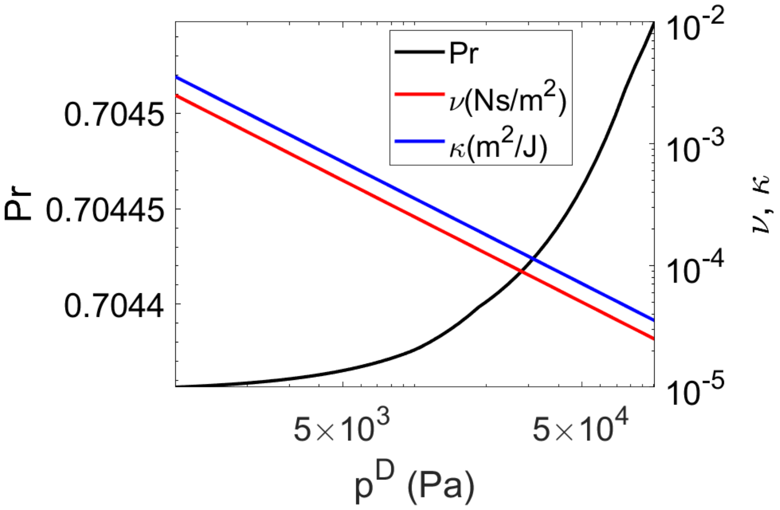

Figure 6.2: Plots of ν, κ, and Pr, for air as a function of $\tilde{p}$. On the right vertical axis, $\nu(Ns/m^2)$ and $\kappa(m^2/J)$ are calculated from Eq (6.6) and Eq (6.7) and plotted in red and blue, respectively. Pr is plotted in black on the left vertical axis and calculated with Eq(6.2).

that, $\kappa(\mathrm{m}^2/\mathrm{J})$, decreases as $\tilde{p}$ increases, while the red line shows that $k(\mathrm{W/mK})$ remains steady. The magenta line shows that $c_p(\mathrm{J/kgK})$ increases as $\tilde{p}$ increases, though the increment of increase is on the order of $10^{-5}\%$ of the average value.

Quantifying the results from Figure 6.1b, we find that the thermal conductivity of the domain has small variations with the range of considered $\tilde{p}$ such that, $k = 3.2 \times 10^{-2} \pm 2.8 \times 10^{-5}\mathrm{W/mK}$. Applying the range of available pressures, $1 \times 10^3 \leq \tilde{p} \leq 1 \times 10^5\mathrm{Pa}$ to Eq (6.8), we find the specific heat capacity is with the values $c_p = 1.0 \times 10^3 \pm 8.4 \times 10^{-1}\mathrm{J/kgK}$. From these values of c_p, k, and $\tilde{\rho}$, we determine the range of values for the coefficient of thermal diffusivity as such, $3.5 \times 10^{-5} \leq \kappa \leq 3.6 \times 10^{-3}\mathrm{m}^2/\mathrm{J}$.

Thus, we can relate Pr, Ek, and Ra to the independent variables $\tilde{p}$, $\tilde{T}$, and d. This enables us to determine the regimes of convection we are able to model within the limits of our experimental design. Recall that we aim to model non-chaotic convection in both rotating and non-rotating domains. In Chapters 3 and 4 we the determine the Ra values at which non-chaotic convection occurs for fixed temperature, fixed flux, and Robin thermal boundary condition configurations, with and without rotation, for $Pr = 0.7$.

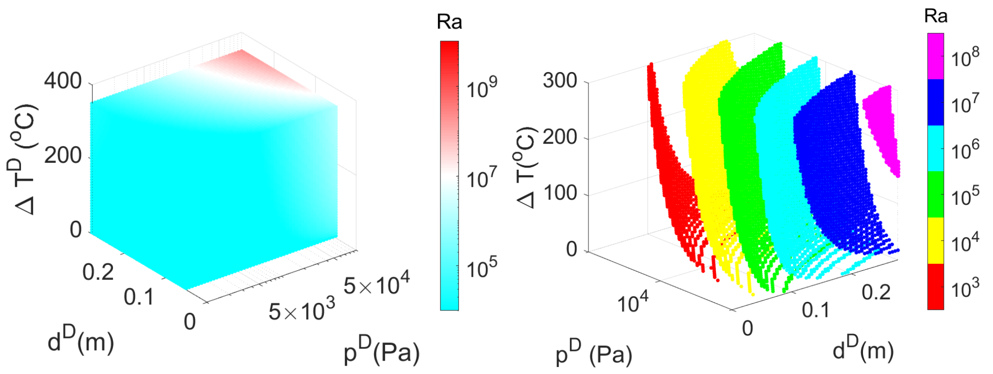

(a) 3D plot (b) Contours

Figure 6.3: Plots of Ra as a function of pressure, domain height, and temperature difference. The latter are limited to: $10^3\text{Pa} \leq \tilde{p} \leq 10^5\text{Pa}$, $0.05\text{m} \leq d \leq 0.287\text{m}$, and $\Delta\tilde{T} \geq 5^{\circ}\text{C}$. In the left-hand plot, for $Ra < 5 \times 10^7$, it is blue and for $Ra > 5 \times 10^7$, it is red. In the right-hand plot, values of Ra are contoured.

We first confirm that $Pr = 0.7$ is achievable within our experimental restrictions. To do so, we calculate Pr with Eq (6.2) as $\tilde{p}$ varies within our predetermined range of $10^3\text{Pa} \leq \tilde{p} \leq 10^5\text{Pa}$, applying our relationships between both ν and κ and $\tilde{p}$. Figure 6.2 shows the resultant calculations of Pr for air as pressure increases from atmospheric pressure. It is evident that as pressure increases, the Pr also increases. However, the changes in Pr are on the order of 10^{-4}. Therefore, we conclude that any pressure within our previously determined ranges sufficiently enables a convecting system where $Pr = 0.7$.

Next, we explore the range of Ra which satisfy the experimental constraints. Figure 6.3 shows the Ra values calculated with Eq (6.3), indicated by colour, for values of $\Delta\tilde{T}$, d, and $\tilde{p}$. As Ra is increased toward 2×10^7, the colour transitions from shades of blue to white, and as Ra increases from 2×10^7 the colour transitions from white to shades of red. The range of possible Ra is $7 \times 10^2 < Ra < 2 \times 10^8$.

The range Ek values is calculated with Eq (6.4) as a function of $\tilde{p}$, d, and Ω, as shown in Figure 6.4. The colours in Figure 6.4 illustrate the Ek values such that the red spectrum indicates weakly rotating systems, $Ek > 10^{-3}$, and the blue spectrum indicates rapidly rotating systems, $Ek < 10^{-3}$. From Figure 6.4, we see that only $Ek \geq 4 \times 10^{-5}$ is possible for the ranges used. Note that we have not included the case for non-rotating convection and $\Omega = 0$ because that corresponds

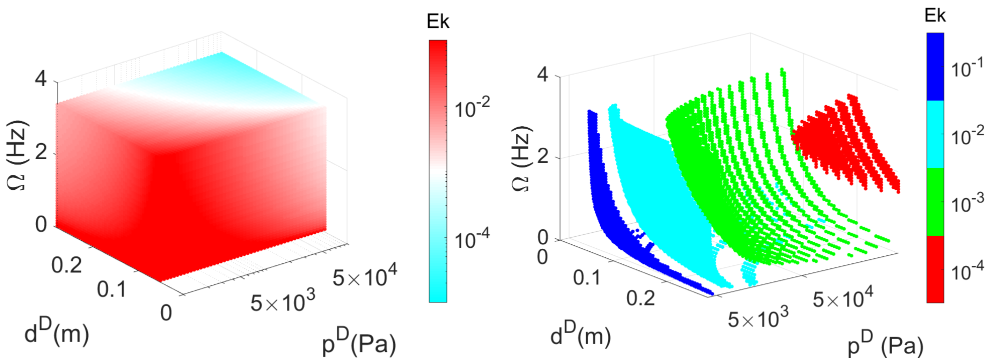

(a) 3D plot (b) Contours

Figure 6.4: Plot of Ek as a function of pressure, domain height, and rotation rate. The latter are limited to: $10^3\text{Pa} \leq \tilde{p} \leq 10^5\text{Pa}$, $0.05\text{m} \leq d \leq 0.287\text{m}$, and $\Omega < 3.4\text{Hz}$. In the left-hand plot, for $Ek > 10^{-3}$ the colour is red and for $Ek < 10^{-3}$ it is blue. In the right-hand plot the contours of Ek are shown.

Ek	Ra_c	Ra_{chaos}
∞	2×10^3	2×10^5
10^{-4}	2×10^5	1×10^6
10^{-5}	2×10^6	2×10^7

Table 6.1: The values of Ra at which convecting systems with either fixed temperature, fixed flux, or Robin thermal boundary conditions transition to chaotic temporal behaviour. Ra_{chaos} for non-rotating, and rapidly rotating convection with the indicated Ek. These results are taken from Chapter 3, Figure 3.11 for fixed temperature and flux conditions and from Chapter 4, Figure 4.8 for the Robin condition.

to $Ek = \infty$.

Referring to Chapter 3 and Chapter 4, we identify the range of Ra values in which sub-chaotic convection is exhibited with and without rotation. From comparison of temporal behaviour between fixed temperature and fixed flux thermal boundary conditions in Chapter 3, we concluded both with and without rotation, the transition to chaos occurred at similar values of Ra for both thermal boundary conditions. This trend continues for Robin thermal boundary conditions, for which, as shown in Figure 4.8 in Chapter 4, when $Bi \leq 10^{-2}$ and $Bi \geq 10^2$, systems transition to chaos at similar values of Ra as the fixed flux and fixed temperature

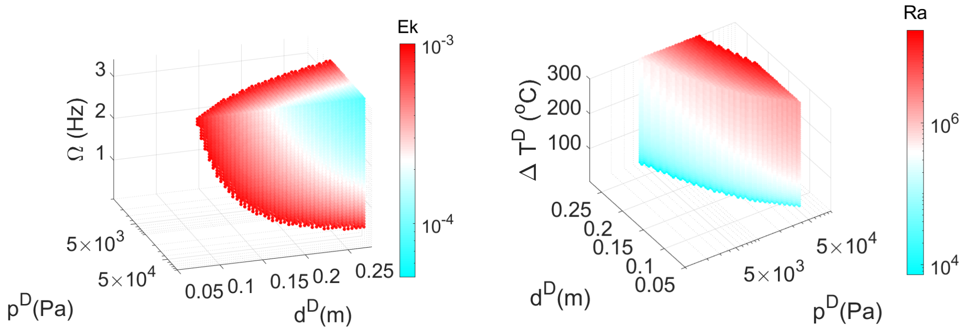

(a) $Ek\,(\tilde{p}, d, \Omega)$ (b) $Ra\left(\tilde{p}, d, \Delta\tilde{T}\right)$

Figure 6.5: Values of Ek and Ra possible and their corresponding $\tilde{p}$, d, Ω, and $\Delta\tilde{T}$. Each range is limited such that $3 \times 10^3 \leq Ra \leq 2 \times 10^7$, $Ek \leq 10^{-3}$, and $5 \times 10^3 \leq \tilde{p} \leq 5 \times 10^4$Pa. In both plots, the colour changes from red to blue as the respective value decreases. Note that each plot is shown from a different perspective.

systems. Table 6.1 lists the values of Ra at which convection onsets Ra_c, and transitions to temporally chaotic behaviour Ra_{chaos} for $Ek = \infty$, 10^{-4}, and 10^{-5}.

Therefore, we know that the range of Ra values in our system for a given Ek must be within the corresponding Ra noted in Table 6.1. Without rotation, only limitations on temperature, pressure, and domain height are relevant. However, in the rotating system, the pressure and domain height also influence the Ekman number. Therefore, we first consider the rotating systems.

In order to reach the rapidly rotating regime which is most appropriate to model atmospheric systems, we set a maximum Ekman number such that $Ek \leq 10^{-3}$ and ideally, $Ek \leq 10^{-4}$. Our experimental constraints limit $Ek \geq 4 \times 10^{-5}$. The range of Ek requires that for a non-chaotic flow, we require $Ra < 2 \times 10^7$, at which flow becomes chaotic for $Ek = 10^{-5}$.

Additionally, the triple point of Iodine occurs at $\tilde{p} = 1.2 \times 10^4$Pa, and thus having a significantly higher pressure within the domain risks Iodine occurring in liquid phase. Therefore, we further limit pressure such that $5\times10^3 \leq \tilde{p} \leq 5\times10^4$Pa.

Figure 6.5 shows the values of Ek and Ra attainable when we limit $Ra \leq 2\times10^7$, $Ek \leq 10^{-3}$, and $5 \times 10^3 \leq \tilde{p} \leq 5 \times 10^4$Pa. The left-hand panel, Figure 6.5a, shows best how changes in d and Ω affect Ek. The right-hand panel, Figure 6.5b, shows

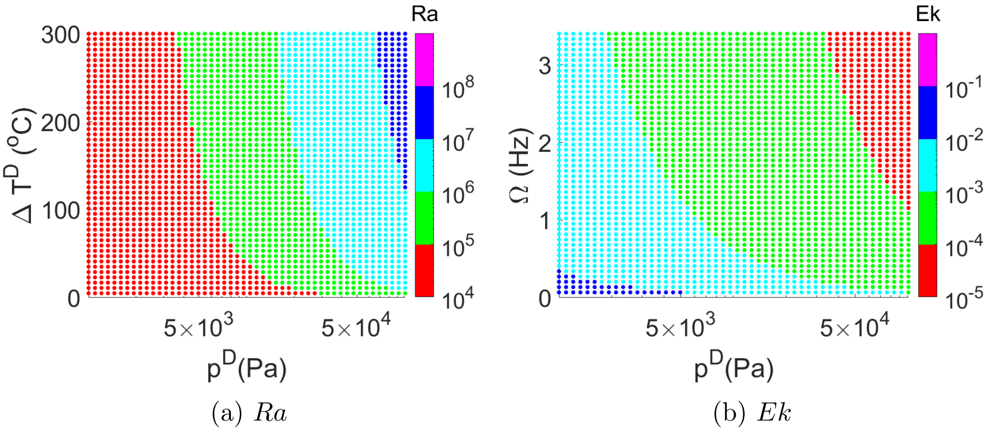

(a) *Ra* (b) *Ek*

Figure 6.6: Plots of *Ra* and *Ek* as functions of pressure and temperature and pressure and rotation rate, respectively. The height is fixed as $d = 0.25$m.

Ra as d, $\tilde{p}$, and $\Delta\tilde{T}$ vary, indicating that for fixed d and $\tilde{p}$, varying $\Delta\tilde{T}$ strongly affects *Ra*.

For the experiment, we must fix d and $\tilde{p}$ while Ω and $\Delta\tilde{T}$ can be altered. However, both $\tilde{p}$ and $\Delta\tilde{T}$ may not be practically constant, rather within a range of precision dependent on the experimental methods. Therefore, we choose a fixed height, and supply ranges of $\tilde{p}$ and $\Delta\tilde{T}$ which would exhibit sub-chaotic convective flows. We choose to maximise d for visibility and to minimise *Ek*, thus $d = 0.25$m. We may generally note that for higher $\tilde{p}$, the *Ek* is lower and *Ra* is higher.

The values of *Ra* and *Ek* possible when $d = 0.25$m and $\tilde{p}$, $\Delta\tilde{T}$, and Ω are varied are plotted in Figure 6.6. The Rayleigh number is below 10^7, our experimentally preferred range, when $\tilde{p} \leq 7 \times 10^4$Pa. However, the Ekman number is larger than 10^{-4} in a similar pressure range such that $p \geq 3.5 \times 10^4$Pa.

We require a system for which $\Delta\tilde{T}$ can be modified to establish *Ra* values within the range $10^3 \leq Ra \leq 10^7$ such that both rotating and non-rotating systems may exhibit sub-chaotic flows. From Figure 6.6a, we observe that for $\tilde{p} \geq 3.5 \times 10^4$Pa, where *Ek* is minimised, $Ra > 10^5$. However, sub-chaotic non-rotating convection does not occur within this range of *Ra* values. Therefore, we recommend two different set-ups for non-rotating and rotating convection.

Without rotation we can ignore the rotation rate as $Ek = \infty$, and we prefer $10^3 < Ra < 2 \times 10^5$. The red region and nearby green points in Figure 6.6a illustrate the $\tilde{p} - \overline{\tilde{T}}$ parameter space which cause appropriate Ra values. Recalling that we prefer $\Delta\tilde{T} = 288^{\circ}\mathrm{C}$, we see that $\tilde{p} < 5 \times 10^3\mathrm{Pa}$ causes $Ra \leq 2 \times 10^7$. This is true for a range of temperature differences such that, $\Delta\tilde{T} \leq 250^{\circ}\mathrm{C}$.

With rotation, we seek to maximise $\tilde{p}$ to minimise Ek while retaining $Ra \leq 2 \times 10^7$. To moderate the Ra value and achieve $Ek \leq 10^{-4}$, we require $3.2 \times 10^4 < \tilde{p} \leq 7 \times 10^4\mathrm{Pa}$. The minimised Ek also requires maximising Ω such that $2\mathrm{Hz} < \Omega$. Figure 6.6a shows that the determined region of pressure allows for appropriate Ra values for any $\Delta\tilde{T}$. Recalling our preference for $\Delta\tilde{T} = 228^{\circ}\mathrm{C}$, let us limit the temperature range such that $150 < \Delta\tilde{T} < 250^{\circ}\mathrm{C}$.

6.5 Materials

Having determined appropriate values of d, R, $\tilde{p}$, and $\Delta\tilde{T}$, our focus turns to the materials of the domain itself. We must choose the type of material and its thickness for both the vertical and horizontal boundaries.

A brief literature review shows that commonly used materials in cylindrical RRBC experiments are Plexiglas, Copper, Aluminium, and Sapphire (Vorobieff & Ecke, 2002; Kunnen et al., 2010). Plexiglas is consistently used as a sidewall material, with $d_{sw} \geq 5\mathrm{mm}$, and numerically modelled using insulating boundary conditions (Vorobieff & Ecke, 1998; Kunnen et al., 2010). Following suit, we suggest Plexiglas sidewalls with $d_{sw} = 5\mathrm{mm}$ as a sufficiently insulating sidewall. Additionally, Plexiglas is transparent and allows for visual observation of the contained system.

Recall that systems with fixed temperature, fixed flux, and Robin thermal boundary conditions on the top and bottom boundaries each exhibit chaotic time-dependence which onsets at similar values of Ra. Note that this is true for the Robin condition when the Biot number sufficiently extreme such that $|\log(Bi)| \geq 2$. Therefore, the upper and lower boundaries should meet the requirements of $Bi \geq 10^2$, recalling that Bi is defined as such

$$Bi = \frac{dk_M}{d_M k}, \tag{6.9}$$

where the M sub-script indicates that the value is related to the boundary.

Table 6.2 lists the thermal conductivity of each material in W/mK. Given the choice of $d = 0.25$ and $\tilde{p} = 1.2 \times 10^4$Pa for the fluid, the thermal conductivity becomes $k = 0.032$W/mK. Thus, Table 6.2 shows the required maximum thickness of each type of bounding material to have $Bi \geq 10^2$.

material	k (W/mK)	max(d_M)(m)
Copper	402 (at 300K)	31
Aluminium	237 (at 273K)	18
Plexiglas	0.17	0.013
air	0.02	0.25

Table 6.2: The thermal conductivities for Copper (Lide, 2003), Aluminium (Touloukian et al., 1970), Plexiglas (Morimune-Moriya & Nishino, 2021), and air (Lide, 2003) are listed along with the maximum thickness, d_M necessary to make the system have Biot number, $Bi \geq 10^2$. The d value is as previously determined.

It is clear from Table 6.2 that both Copper and Aluminium are sufficiently conductive at any reasonable thickness to be used. However, for visibility, Plexiglas is preferable. we therefore advise that the lower boundary be Aluminium with thickness of 0.05m with sidewalls and top boundary of Plexiglas with thickness 0.005m.

6.6 Design summary

Motivated by the simplified precipitation FARE model presented in Hernadez-Duenas et al. (2012), we propose an experiment to physically model two-phase precipitation in a rotating system. The experiment provides a basis for validation of a corresponding numerical model and an opportunity to apply data assimilation by supplying observations from the experiment to the numerical model to predict the physical behaviour.

We have chosen a fluid which sublimates to avoid changes in thermal conductivity at the lower boundary caused by a liquid layer. Iodine is chosen to be sufficiently safe and visible. It sublimates at a triple point where $\tilde{T} = 1141^o$C and

$p = 1.2 \times 10^4$Pa. These parameter values are used to determine the temperatures at the upper and lower boundaries as well as the pressure inside the domain.

The shape of the domain is chosen to be cylindrical in order to avoid trapping flows in the corners of a cubical domain. An ideal aspect ratio, $\Gamma = R/d$, is chosen through a literature review which suggests that to maintain non-chaotic behaviour with two convection rolls in non-rotating systems, $\Gamma = 0.7$ is optimal (Clever & Busse, 1974; Gao & Behringer, 1984). This aspect ratio cause an additional instability to occur at convection onset with rotation, however the onset instability is not chaotic. Therefore, we choose $\Gamma = 0.7$ for our experiment.

The remaining independent variables are temperature $\tilde{T}$, pressure $\tilde{p}$, height d, and rotation rate Ω. We first apply limitations to these values based on the triple point of Iodine and physical feasibility. Additionally, d is limited by Γ and radius of the rotation table which enforces a maximum radius of $R = 0.18$m. We are able to further constrain the variables by requiring certain Ra and Ek values to be possible within the domain. We require $Ra_c < Ra < Ra_{chaos}$. Table 6.1 lists these Ra values for different Ek, which are true for fixed temperature, fixed flux and Robin boundary conditions when $Bi \geq 10^2$. By choosing to minimise Ek to achieve the most rapid rotation, we arrive at optimal values of $d = 0.25$m, $3.2 \times 10^4 < \tilde{p} < 7 \times 10^4$Pa, $\Omega > 2$Hz, and $150 < \Delta\tilde{T} < 250$°C for the rotating configuration. Without rotation, lower Ra values are preferred and therefore lower pressures. Thus, we recommend a set-up where $d = 0.25$m, $\tilde{p} < 5 \times 10^3$Pa, and $\Delta\tilde{T} \leq 250$°C.

We finally chose the materials bounding the domain such that they are conductive and thick enough to have fixed temperature-like conditions, indicated by Biot number, $Bi \geq 10^2$. Due to its transparent nature, we choose Plexiglas on the sidewalls and the upper boundary to allow for improved visual observation. The thickness must be ≤ 0.013m to remain fixed temperature, so we choose a thickness, $d_M = 0.005$m for the Plexiglas. The lower boundary is chosen to be Aluminium of thickness $d_M = 0.05$m.

The design parameters discussed above are summarised in Figure 6.7. The left panel, Figure 6.7a, shows the specifications for the boundary materials, indicating the material and thickness of the upper boundary, sidewalls, and lower boundary.

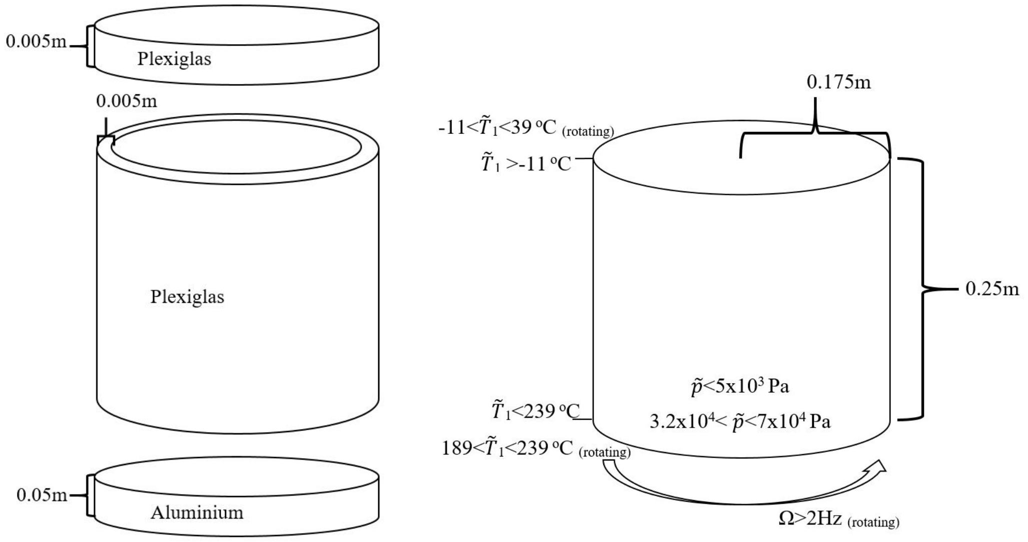

(a) Boundaries (b) Independent Variables

Figure 6.7: Experimental diagrams of the boundaries and interior domain of the proposed experiment. The materials and thicknesses of each boundary is displayed. The pressure, height and radius of the domain are indicated. The pressure, temperature, and rotation rate values are for non-rotating case unless indicated by the subscript $_{(rotating)}$. The height and radius are fixed with and without rotation.

The right panel, Figure 6.7b, shows the interior specifications including the $\tilde{p} = 1.2 \times 10$Pa, $d = 0.25$m, and $R = 0.175$m. The temperature at the upper and lower boundaries is noted for the rotating case and the non-rotating case, from top to bottom, to achieve $\Delta\tilde{T} = 300^o$C when $\Omega = 3.4$Hz and $\Delta\tilde{T} = 25^o$C without rotation. In both cases, the temperatures are set to ensure the average temperature, $\overline{\tilde{T}} = 144.1^o$C, the temperature at which Iodine sublimes from solid to gas.

The next steps for this experiment are to identify a manufacturer for this design and discuss how technical aspects such as applying the vacuum and heating/cooling as well as measurement methods. The heating on the lower boundary and upper boundary, for the non-rotating case, could be achieved using a heating coil, such as those used in electric stove tops. To cool the upper boundary, ice or liquid nitrogen could be used for the rotating case. However, these issues are better determined with aid from a technical expert. As for measurement, temperature probes can be placed at the upper and lower boundaries to monitor how closely they resemble fixed temperature boundaries. Image tracking could be used to observe the movement of the solid Iodine particles. However, the most interesting route of observation is Lagrangian Particle Tracking (LPT). In Godbersen et al. (2021), LPT is used to track air flow in a non-rotating experiment. It is an interesting avenue of research to apply LPT to a rotating experiment with precipitation.

Chapter 7

Conclusion

The ubiquity of rotating Rayleigh–Bénard convection (RRBC) in astrophysical and geophysical fluids has inspired numerical and experimental studies since 1900 (Bénard, 1900). However, neither experimental nor numerical models are currently able to fully emulate the conditions which affect large-scale systems. The idealisations made in fluid models include domain geometry and thermal boundary conditions. Though geophysical and astrophysical systems often occur in roughly spherical geometries, cylindrical geometries are preferred for experimental models. Therefore, applying the boundary conditions of large-scale systems to numerical models in cylindrical domains allows us to link fluid behaviours between astrophysical and geophysical systems with experimental observations. Of the conditions applied to numerical models, the thermal boundary conditions are particularly important due to the essential role temperature gradients play in RRBC. This thesis is concerned with improving our understanding of the role of thermal boundary conditions at the intersection of large-scale, experimental, and numerical systems of RRBC. Section 7.1 provides a summary of the work presented in this thesis followed by section 7.2 which describes directions for future work.

7.1 Summary

The role of thermal boundary conditions in RRBC has previously been studied in a variety of ways. The analytic work presented in Jeffreys (1926) first suggested the more physical fixed flux boundary condition in contrast to the fixed temperature condition used in Rayleigh (1916). These early studies of thermal boundary conditions motivated the derivation of the Robin condition which fills the gap between fixed flux and fixed temperature conditions dependent upon the properties of the fluid and the boundary (Sparrow et al., 1964). Further consideration is neccessary regarding the non-uniformity of heating and cooling in astrophysical and geophysical systems such as the Earth's outer core (Cox & Doell, 1964). Recent studies have sought to integrate these ideas into numerical and experimental models of rotating and non-rotating Rayleigh–Bénard convection to better understand the underlying dynamics of astrophysical and geophysical flows (i.e. Mound and Davies, 2017; Anders et al., 2020; Sahoo and Sreenivasan, 2020; Clarté et al., 2021). However, there remains a gap – which, in this thesis, we have endeavoured to resolve – in understanding the role thermal boundary conditions play in our interpretation of numerical RRBC with respect to experimental models and large-scale flows.

In Chapter 2, we introduced the governing equations for an incompressible fluid which describe the dynamics of RRBC. Rewriting these equations in dimensionless form yielded three non-dimensional parameters: the Prandtl number Pr, Ekman number Ek, and Rayleigh number Ra. A linear system of equations and the no-slip velocity condition (which we used ubiquitously) were also introduced. The linear system was solved using the Dedalus solver (Burns et al., 2016) and the non-linear system was solved with the Nek5000 framework (Nek5000, 2019). The mean kinetic energy balance was described to validate the non-linear numerical setup.

The investigation of thermal boundary conditions began in Chapter 3, by introducing common thermal boundary conditions: fixed temperature, fixed flux, and a mixed condition defined in section 3.2. A linear stability analysis of the 2D system notably confirmed that as rotation becomes more rapid, convection onset behaviour becomes independent of thermal boundary condition, which agrees with results from Calkins et al. (2015) and Clarté et al. (2021) which considered only a stress-free plane layer and spherical shell, respectively.

Next, we described the tools used to quantify and categorise the nonlinear results including a novel method of quantifying the transition from 2D to 3D flow. We related results across boundary conditions by applying the relationship, $Ra_{FF} = NuRa_{FT}$, where $\cdot_{FF}$ relates to the fixed flux and mixed boundary conditions and $\cdot_{FT}$ relates to the fixed temperature boundary condition. We ubiquitously found that the transition to 3D flow and behaviour of zonal flows are not dependent on the thermal boundary condition. Without rotation, our results are similar to results presented in Anders et al. (2020) which considered RBC in a cuboidal domain, finding that fixed temperature and mixed configurations behave similarly near onset. We additionally, found that the fixed flux condition has similar onset behaviour. With rotation, onset behaviour and chaotic, bulk flows are not dependent on thermal boundary condition. However, the boundary condition plays a role in the transition to chaos such that the mixed condition is non-chaotic to higher Ra_{FT} than the fixed flux and fixed temperature systems. Thus, we suggested that the choice of thermal boundary condition between fixed temperature, fixed flux, or mixed condition is not the dominant influence on global flow behaviours of RRBC near onset and at high Ra_{FT} regimes.

However, the true thermal conditions of large-scale and experimental flows are not likely to be purely fixed temperature or fixed flux. Therefore, in Chapter 4, the Robin condition was investigated as an experimentally appropriate thermal boundary condition which interpolates between fixed temperature and fixed flux conditions via the Biot number Bi – a ratio between the properties of the fluid and that of the boundary. At the limits of Robin condition it becomes fixed temperature (as Bi approaches ∞) and fixed flux (as Bi approaches 0). Applying this theory and the $\overline{Nu}$ measurements from numerical results, an original relationship was defined between Ra_{FT} and an effective Rayleigh number $Ra(Bi)$, such that results can be compared across boundary conditions. A linear stability analysis extended our previous results, showing that, as expected from Clarté et al. (2021), as Ek decreases, onset behaviour becomes independent of thermal boundary condition.

The non-linear solutions demonstrated that for $Bi \geq 10^2$ and $Bi \leq 10^{-2}$, the Robin condition was sufficiently close to fixed temperature and fixed flux conditions, respectively. This range agrees closely with the results reported in Clarté et al. (2021). Near fixed temperature and fixed flux limits, the Robin condition behaves very similarly away from onset, as expected from results in Chapter 3. However, in the moderate Bi range – $10^{-1} \leq Bi \leq 10^1$ – wall-localised convection, time-independence, and 2D flows persists to higher Ra_{FT} values than extreme Bi

configurations. For numerically modelling experimental systems, such as those described in Kunnen, Clercx, and Geurts (2008), the difference between using the fixed temperature and Robin condition would be negligible. However, for astrophysical systems, such as the CMB of the Earth, where Bi is on the order of 10^1, the Robin condition may be more appropriate for moderate Ra value studies.

Motivated by variations in heat flux at the Earth's core-mantle boundary (CMB), Chapter 5 described two lateral boundary conditions with inhomogeneous insulation: Positive/Negative and Positive/Zero. Both conditions apply a sinusoidal pattern of heat flux boundary condition along the vertical and azimuthal directions of the cylinder sidewall. The Positive/Negative has both positive and negative heat flux while the Positive/Zero case has a minimum heat flux of zero and is more appropriate for modelling the Earth's core (Mound & Davies, 2017) and experimental setups (Sahoo & Sreenivasan, 2020). The number of peaks in the azimuthal direction m_θ were varied along with the amplitude A_n of the heat flux. We chose m_θ in reference to the dominant number of convection rolls in the uniformly insulated case, m_{UI}, in three ways: $m_\theta = 1 < m_{UI}$, such that the applied length-scale is larger than the scale of convection; $m_\theta = m_{UI}$, such that the variation is of convective length-scale; and $m_\theta = bm_{UI}$, where $b = 0.5$ or 2 and the variation has the length-scale of a secondary convective length-scale. Numerical methods for the Positive/Negative condition were tested for accuracy against the solid steady state, where there is no velocity or time dependence. The Positive/Zero numerical setup was tested using global heat flux calculation. We defined another Nusselt number Nu_k which was appropriate for the inhomogeneous conditions.

Contrary to previous results, we found that both large length-scale and convective length-scale variations caused the γ value (of the form $\overline{Nu} \propto Ra^\gamma$) to decrease from the uniform case (Mound & Davies, 2017). The discrepancy between our result and previous studies is likely due to higher Ek values and lower Ra_{FT} values considered in our study. Investigating the large length-scale Positive/Negative configuration revealed that regions of positive heat flux cause stronger pinning than regions of negative heat flux. The convective-length scale oscillations caused wall-localised pinning of convection rolls within regions of $\theta = 2\pi/m_\theta$. However, in weakly and non-rotating flows, the imposition of wall-localised convection led to time-dependent flow in the bulk. However, the number of convection rolls was not altered by either large nor convective length-scale heat flux in either the Positive/Negative or Positive/Zero case. The exception to this result is a moderately rotating case where the applied heat flux caused the number of convection rolls to decrease as the $Nu(t)$ time series indicated that a secondary solution was excited by the heat flux variation. The number of convection rolls did change when the boundary condition had secondary convective length-scale oscillations. Sufficiently large A_n values led to the applied m_θ becoming dominant along the wall. With rotation, this transition took significant A_n values and without rotation, this led to time-dependent bulk behaviours.

Hence, it is evident that inhomogeneous thermal conditions have a significant effect on RRBC. The effects ought to be taken into consideration when investigating geophysical and astrophysical flows because the variations cause significant changes in wall-localised flow which can lead to irregularities in bulk flow.

Finally, in Chapter 6 we applied numerical results regarding time-dependence and solution forms generated with fixed temperature and Robin conditions presented in Chapter 3 and Chapter 4 to the design of a RRBC experiment with phase change. The experiment was motivated by the study of atmospheric moist convection, and was intended to emulate the FARE model (Hernadez-Duenas et al., 2012), a simplified model of two-phase, precipitating convection. The fluids were chosen to be air with Iodine (which is purple in gaseous and solid form), such that the precipitation may be observed visually. The domain was a cylinder with aspect ratio, $\Gamma = 0.7$ was determined based on a literature review of stability in cylindrically bounded RRBC for $Pr = 0.7$, which is appropriate for air. Numerical results from Chapters 3 and 4 were applied to determine the ranges of the temperature applied at the top and bottom, the pressure, the domain height, and rotation rate for which the flow is non-chaotic. Additionally, the Robin condition results from Chapter 4 informed the specifications of the Plexiglas and aluminium boundaries. The design leaves room for expert advice regarding observation and measurement techniques along with the technicalities of achieving the suggested temperature and pressure ranges.

Thus, we have demonstrated how novel numerical results regarding physically appropriate thermal boundary conditions may be used to strengthen the link between experimental and numerical models.

7.2 Future work

It is natural to consider extensions to and improvements on the ideas presented in this thesis. There are two subsets of future avenues of exploration: numerical and experimental.

7.2.1 Numerical advancements

As can be said of many numerical studies of RRBC, the expansion of the parameter ranges of Ra and Ek that can be calculated would improve our ability to relate results to large-scale systems (Plumley et al., 2016). We used a maximum Ra on the order of 10^8 and a minimum Ek of 10^{-5} which are each insufficient to model astrophysical and geophysical systems such as the Earth's core which is parameterised with $Ra = 10^{20}$, $Ek = 10^{-15}$ (Plumley et al., 2016). While there is evidence of Nek5000 modelling rotating RBC systems with $Ek \geq 10^{-6}$ and $Ra \leq 10^{10}$ for stress-free velocity conditions (i.e. Barker et al. (2014)), the computational expense was decided to be too great for this thesis. In combination with the consideration of lower Pr which are more appropriate for the molten metals of the Earth's outer core, exploration of Ek and Ra ranges which are increasingly appropriate for geophysical and astrophysical flows would improve the relationship between the role of thermal boundary conditions in numerical rotating convection and large-scale flows.

Within the parameter ranges considered in this thesis, the transition to turbulence could be more thoroughly investigated. In our classification of temporal behaviour, variations in flow behaviour when approaching temporal chaos were identified by different attractor forms. These differences suggest that the preferred form of the solution is not uniform across all thermal boundary conditions and that different states of convection are chosen. This could be complemented by an investigation into the energy behaviour at transitions to time dependence. Further investigation into the causes of different transitions and forms of turbulence can illuminate more effects of thermal boundary conditions.

Considering the Robin condition, we observed differences in flow behaviour for $10^{-1} \leq Bi \leq 10^{1}$ compared to more extreme Bi. Future studies may be interested in studying the Robin condition in this moderate regime. There are a plethora of studies with fixed flux or fixed temperature thermal boundary conditions. The behaviours associated to each respective condition may be able to be unified through further investigation into the Robin condition with Bi ranges which are only moderately fixed temperature or fixed flux. Additionally, it would be useful to compare the flows for moderate Bi configurations to experimental observations as a possible reason for deviations in physical and numerical results.

The theory of the Robin conditions could also be extended to the sidewall. This would improve the ability of numerical models to inform experimental design by determining the range of Bi which cause sufficiently conducting or insulating conditions. An extension of this idea would be to apply an inhomogeneous Robin condition to the sidewalls, building on the work presented in Chapter 5. The ability of the Robin condition to provide experiment context to thermal boundary conditions could be applied to inform an experimental study of inhomogeneous thermal boundary conditions on lateral boundaries.

7.2.2 Experimental advancements

An obvious extension of the heterogeneously insulated system numerically modelled in Chapter 5 is to develop an experimental model of the same system. In Sahoo and Sreenivasan (2020), an experimental study of a cylindrical annulus with azimuthally varying heat flux is reported. However, the heating mechanism causes piece-wise insulation rather than smoothly transitioned heat flux. By applying a smoother transition in heat flux to the thermal condition and removing the inner boundary, an experiment of inhomogeneous thermal boundary conditions might better relate to the numerical model presented in this thesis.

Considering the experimental design presented in Chapter 6, the next course of action for the experimental design is to present it to a professional who could offer advice on technical issues such as: how to safely seal the system and keep pressure at the ideal range, and non-stick materials to keep Iodine from crystallising on the cool upper boundary. Further, it would be useful to use the numerical results from Chapter 3 to identify isotherms near to the triple point of Iodine. The isotherms would indicate where in the system phase-change could be expected to occur. By predicting the location of phase change, we may better develop a plan of observation and measurement.

Once conducted, the experimental data could be applied to advancing the understanding of moist convection and more broadly to the improvement of Numerical Weather Prediction. Comparison between experimental measurements and similar numerical models, such as Hernadez-Duenas et al. (2012) for non-rotating systems or T. K. Edwards et al. (2019) for rotating systems, could help improve numerical methods by identifying areas of digital twinning. It may be additionally of interest to develop a rotationally-constrained numerical model of simplified precipitation to improve the connection between the polar region of the atmosphere to the numerical model (Julien et al., 2006). The observations from the experiment may be paired with the numerical model to improve data assimilation, which is the process by which measurements of weather are applied to numerical models to improve forecasts.

Understanding the connection between thermal boundary conditions and numerical models is key to understanding the underlying dynamics of many astrophysical and geophysical flows. It is clear that there is more work to be done in strengthening the links between physical conditions and numerical boundary conditions.

Appendix A

Perturbed Governing Equations

In this appendix, we provide a derivation of the perturbed governing equations of RRBC. In order to derive a linear system of equations, as required for section 2.1, we find a basic state which is determined both static and steady. Therefore, $\boldsymbol{u}_B = 0$ and $\partial/\partial t = 0$ where $\boldsymbol{u}_B$ is the basic state of velocity. We apply these conditions to the dimensionless momentum equation Eq (2.11a), incompressibility equation Eq (2.11b), and the temperature equation Eq (2.11c), and considering only the vertical direction. Denoting the basic state with a $\cdot_B$ subscript, we find

$$\frac{\partial P_B}{\partial z} = RaPrT_B \tag{A.1a}$$

and

$$\frac{\partial^2 T_B}{\partial z^2} = 0. \tag{A.1b}$$

Note that the incompressibility condition has become trivial.

From Eq(A.1b), temperature may take the form,

$$T_B = A_0 z + A_1 \tag{A.2}$$

and A_0 and A_1 may be determined by the application of boundary conditions.

Considering a fixed temperature boundary such that $T(z = -0.5) = 0$ and $T(z = 0.5) = 1$, the basic state of temperature is

$$T_B = -z + 0.5. \tag{A.3}$$

Note that if a fixed flux condition is applied where $\frac{\partial T}{\partial z} = -1$ at each boundary, then $A_0 = -1$ and we may choose $A_1 = 0.5$ arbitrarily to achieve the same thermal basic state.

The pressure basic state is derived by applying the Boussinesq equation of state Eq (2.5) and the temperature basic state Eq (A.3) to Eq (A.1a) such that,

$$\frac{\partial P_B}{\partial z} = RaPr(-z + 0.5). \tag{A.4}$$

Thus, the basic state of pressure is

$$P_B = P_1 - \frac{RaPr}{2}\left(z^2 - z\right) \tag{A.5}$$

where P_1 is the value at $z = z_1$.

We now apply a perturbation to the basic states of velocity, pressure and temperature such that

$$\boldsymbol{u} = \boldsymbol{u}_B + \boldsymbol{u}_p, \qquad P = P_B + P_p, \qquad T = T_B + T_p. \tag{A.6}$$

Note that because $\boldsymbol{u_B} = 0$, $\boldsymbol{u}_P$ necessarily must satisfy any velocity boundary condition. Alternatively, T_B already satisfies the vertical thermal boundary conditions so the perturbation must vanish on the boundaries such that

$$T_p = 0 \qquad \text{at} \quad z = -0.5 \quad \text{and} \quad z = 0.5. \tag{A.7}$$

We re-write the governing equations Eq (2.6), (2.9), and Eq (2.10) for the perturbed variables such that

$$\frac{D\boldsymbol{u}_p}{Dt} + \frac{Pr}{Ek}\hat{z} \times \boldsymbol{u}_p = -\nabla P_p + RaPrT_p\hat{\boldsymbol{z}} + Pr\nabla^2\boldsymbol{u}_p, \tag{A.8a}$$

$$\nabla \cdot \boldsymbol{u}_p = 0, \tag{A.8b}$$

$$\frac{DT_p}{Dt} - w = \nabla^2 T_p. \tag{A.8c}$$

Appendix B

Mean Kinetic Energy Balance Derivation

In this appendix, we follow Hepworth (2014) to derive the mean kinetic energy balance in order to test the accuracy of our non-linear numerical set-up as discussed in section 2.2.2.1.

We begin with the dimensionless momentum equation Eq (2.11a),

$$\frac{\partial \boldsymbol{u}}{\partial t} + (\boldsymbol{u} \cdot \nabla)\boldsymbol{u} + \frac{Pr}{Ek}\hat{z} \times \boldsymbol{u} = RaPrT\hat{z} - \nabla P + Pr\nabla^2\boldsymbol{u}. \tag{B.1}$$

The following vector identity

$$\frac{1}{2}\nabla(\boldsymbol{b} \cdot \boldsymbol{b}) = \nabla(\frac{1}{2}|\boldsymbol{b}|^2) = \boldsymbol{b} \times (\nabla \times \boldsymbol{b}) + (\boldsymbol{b} \cdot \nabla)\boldsymbol{b} \tag{B.2}$$

is applied to the second term on the left-hand side (LHS) of Eq (B.1) and the scalar term is absorbed into the modified pressure. Thus,

$$\frac{\partial \boldsymbol{u}}{\partial t} + (\boldsymbol{u} \times \nabla \times \boldsymbol{u}) + \frac{Pr}{Ek}\hat{z} \times \boldsymbol{u} = RaPrT\hat{z} - \nabla P + Pr\nabla^2\boldsymbol{u}. \tag{B.3}$$

Taking the scalar product of Eq (B.3) with $\boldsymbol{u}$ and integrating over the domain $V(r, \theta, z) = [0, 0.7] \times [0, 2\pi] \times [-0.5, 0.5]$,

$$\frac{1}{\pi 0.7^2}\int_V \frac{1}{2}\frac{\partial|\boldsymbol{u}|^2}{\partial t}\mathrm{d}V = \frac{1}{\pi 0.7^2}\int_V RaPrT\boldsymbol{u} \cdot \hat{z} - \boldsymbol{u} \cdot \nabla P + Pr\boldsymbol{u} \cdot \nabla^2\boldsymbol{u}\mathrm{d}V. \tag{B.4}$$

Note that $\boldsymbol{u}$ is perpendicular to the cross product terms in Eq (B.3). Consequently those terms do not contribute to the integral.

The first term of Eq(B.4) is the time derivative of the global kinetic energy KE, which is defined as

$$KE = \frac{1}{V}\int_V \frac{1}{2}|\boldsymbol{u}|^2 \mathrm{d}V. \tag{B.5}$$

Applying vector identity

$$\nabla \cdot (\boldsymbol{a}f) = f\,(\nabla \cdot \boldsymbol{u}) + (\boldsymbol{a} \cdot \nabla)f \tag{B.6}$$

and assuming a statistically steady state, Eq(B.4) becomes,

$$0 = \frac{1}{\pi 0.7^2}\int_V RaPrTw + Pr\boldsymbol{u} \cdot \nabla^2 \boldsymbol{u} - \nabla \cdot (\boldsymbol{u}P)\mathrm{d}V. \tag{B.7}$$

To make the pressure term vanish, we apply the 3D divergence theorem to the last term of Eq (B.7) such that,

$$\frac{1}{\pi 0.7^2}\int_V \nabla \cdot (\boldsymbol{u}P)\mathrm{d}V = \frac{1}{\pi 0.7^2}\int_S (\boldsymbol{u}P) \cdot \hat{\boldsymbol{n}}\mathrm{d}s. \tag{B.8}$$

Due to the no-slip velocity condition, the surface integral is zero and consequently, the pressure term is also zero.

Thus, Eq (B.7) becomes,

$$\frac{RaPr}{\pi 0.7^2}\int_V Tw\mathrm{d}V = -\frac{Pr}{\pi 0.7^2}\int_V \boldsymbol{u} \cdot \nabla^2 \boldsymbol{u}\mathrm{d}V. \tag{B.9}$$

To simplify the right-hand side (RHS), we adopt index notation such that,

$$\int_V \boldsymbol{u} \cdot \nabla^2 \boldsymbol{u}\mathrm{d}V = \int_V u_i \frac{\partial^2 u_i}{\partial x_j^2}\mathrm{d}V = \int_V \frac{\partial}{\partial x_j}(u_i \frac{\partial u_i}{\partial x_j}) - \frac{\partial u_i}{\partial x_j}\frac{\partial u_i}{\partial x_j}\mathrm{d}V. \tag{B.10}$$

Applying the 3D divergence theorem to the first term,

$$\int_V \frac{\partial}{\partial x_j}(u_i \frac{\partial u_i}{\partial x_j})\mathrm{d}V = \int_S u_i \frac{\partial u_i}{\partial x_j}\hat{n}_j ds, \tag{B.11}$$

the term vanishes due to no-slip velocity conditions on all surfaces.

Returning to vector notation, the mean kinetic energy balance is written as

$$0 = \int_V RaTw + (\nabla \times \boldsymbol{u})^2 \mathrm{d}V. \tag{B.12}$$

Appendix C

Fixed Temperature Parameter List

Summary of parameters numerically simulated in Chapter 3.

Ek	Ra	Δt	N_p	N_e
∞	10^3	2×10^{-4}	6	588
	3×10^3	2×10^{-4}	6	588
	6×10^3	2×10^{-4}	6	588
	1.2×10^4	2×10^{-4}	6	588
	2.4×10^4	2×10^{-4}	6	588
	4.8×10^4	2×10^{-4}	6	588
	10^5	2×10^{-4}	6	588
	3×10^5	2×10^{-4}	6	588
	5×10^5	2×10^{-4}	8	588
	8×10^5	2×10^{-4}	8	588
	10^6	2×10^{-4}	6	4704
	5×10^6	2×10^{-4}	6	4704
	10^7	2×10^{-4}	6	4704

Table C.1: A summary of the parameters for the fixed temperature simulations conducted. A subset of these values are also modelled with fixed flux and mixed boundary conditions. The Ekman number Ek, Rayleigh number Ra, time step ΔT, polynomial order N_p, and number of elements N_e are listed for each simulation.

Ek	Ra	Ro	Δt	N_p	N_e
10^{-2}	3×10^3	0.65	2×10^{-4}	6	588
	8×10^3	1.1	2×10^{-4}	6	588
	1.6×10^4	1.5	2×10^{-4}	6	588
	3.2×10^4	2.1	2×10^{-4}	6	588
	10^5	3.8	2×10^{-4}	8	588
	10^6	12	2×10^{-4}	8	588
	5×10^6	27	2×10^{-4}	8	588
10^{-3}	6×10^3	0.09	2×10^{-4}	6	588
	1.2×10^4	0.13	2×10^{-4}	6	588
	2.4×10^4	0.18	2×10^{-4}	6	588
	4.8×10^4	0.26	2×10^{-4}	6	588
	9.6×10^4	0.37	2×10^{-4}	8	588
10^{-4}	4×10^3	7×10^{-3}	5×10^{-6}	8	588
	1.6×10^5	0.05	5×10^{-6}	8	588
	3.2×10^5	0.08	5×10^{-6}	10	588
	6.4×10^5	0.09	5×10^{-6}	10	588
	1.8×10^6	0.16	5×10^{-6}	10	588
	3.6×10^6	0.23	5×10^{-6}	6	4704
	7.2×10^6	0.32	5×10^{-6}	6	4704
	1.44×10^7	0.45	5×10^{-6}	6	4704
10^{-5}	6.4×10^5	9×10^{-3}	5×10^{-6}	6	4704
	1.8×10^6	0.01	5×10^{-6}	6	4704
	3.6×10^6	0.02	5×10^{-6}	6	4704
	7.2×10^6	0.03	5×10^{-6}	6	4704
	1.44×10^7	0.04	5×10^{-6}	6	4704
	2.88×10^7	0.06	5×10^{-6}	6	4704
	5.67×10^7	0.09	5×10^{-6}	8	4704
	1.2×10^8	0.13	5×10^{-6}	8	4704

Table C.1: A summary of the parameters for the fixed temperature simulations conducted. A subset of these values are also modelled with fixed flux and mixed boundary conditions. The Ekman number Ek, Rayleigh number Ra, Rossby number Ro, time step ΔT, polynomial order N_p, and number of elements N_e are listed for each simulation. The system is dealiased with the 3/2 rule and the time step is adaptive.

Appendix D

Inhomogeneous Sidewall Insulation Additional Lists, Derivations, and Figures

Additional details are provided regarding the investigation of inhomogeneous insulation discussed in Chapter 5.

D.1 Parameter Lists

Table D.1 and Table D.2 list the parameter ranges numerically modelled with the Positive/Negative and Positive/Zero boundary conditions, respectively, as discussed in Chapter 5. The number of convection rolls in the uniformly insulated system m_{UI} is also reported.

Ek	Ra	m_{UI}	m_θ	A_n
∞	10^3	1	1	0.2, 0.5, 1
∞	1×10^3	1	2	0.2, 0.5,1
∞	6×10^3	1	1	1
∞	6×10^3	1	3	4
∞	3×10^5	1	1	1
∞	3×10^5	1	3	1
∞	5×10^5	1	1	1
∞	5×10^5	1	3	1
∞	8×10^5	1	1	1
∞	8×10^5	1	3	1
∞	1×10^6	1	1	1
∞	1×10^6	1	3	1
∞	5×10^6	1	1	1
∞	1×10^7	1	1	1
10^{-3}	2.4×10^4		1	0.5, 1, 2
10^{-3}	2.4×10^4		3	0.5, 1, 2
10^{-3}	4.8×10^4	3	1	0.5, 1, 2
10^{-3}	4.8×10^4	3	3	0.5, 1, 2
10^{-3}	9.6×10^4	4	1	0.5, 1, 2
10^{-3}	9.6×10^4	4	4	0.5, 1, 2
10^{-3}	2×10^5		1	0.5, 1, 2
10^{-3}	2×10^5		3	0.5, 1, 2
10^{-3}	1×10^6		1	0.5, 1, 2
10^{-3}	1×10^6		2	0.5, 1, 2

(a) $Ek = \infty$ and $Ek = 10^{-3}$

Ek	Ra	m_{UI}	m_θ	A_n
10^{-4}	1.6×10^5		1	0.5, 1, 2
10^{-4}	1.6×10^5		4	0.5, 1, 2
10^{-4}	3.2×10^5	3	1	0.5, 1, 2
10^{-4}	3.2×10^5	3	3	0.5, 1, 2
10^{-4}	3.2×10^5	3	4	0.5, 1, 2
10^{-4}	6.4×10^5	8	1	0.5, 1, 2
10^{-4}	6.4×10^5	8	4	0.5, 1, 2
10^{-4}	6.4×10^5	8	8	0.5, 1, 2
10^{-4}	1.8×10^6	2	2	0.5, 1, 2
10^{-4}	3.6×10^6	3	1	0.5, 1, 2
10^{-4}	3.6×10^6	3	3	0.5, 1, 2
10^{-4}	7.2×10^6	3	1	1
10^{-4}	1.44×10^7	2	1	0.5, 1, 2
10^{-4}	1.44×10^7	2	2	0.5, 1, 2
10^{-5}	1.8×10^6		1	0.5, 1, 2
10^{-5}	1.8×10^6		4	0.5, 1, 2
10^{-5}	3.6×10^6	4	1	0.5, 1, 2
10^{-5}	3.6×10^6	4	4	0.5, 1, 2
10^{-5}	7.2×10^6	4	1	0.5, 1, 2
10^{-5}	7.2×10^6	4	4	0.5, 1, 2
10^{-5}	1.44×10^7	3	1	0.5, 1, 2
10^{-5}	1.44×10^7	3	3	0.5, 1, 2
10^{-5}	5.67×10^7	5	1	0.5, 1, 2
10^{-5}	5.67×10^7	5	5	0.5, 1, 2

(b) $Ek = 10^{-4}$ and $Ek = 10^{-5}$

Table D.1: Parameter list of simulations conducted with heterogeneous sidewall insulation prescribed in Eq (5.1), where UI indicates the dominant mode of the uniformly insulated case m_{UI}, and θ indicates the azimuthal mode applied, m_θ.

Ek	Ra	m_{UI}	m_θ	A_n
∞	1×10^3		1, 2	0.2, 0.5, 1
∞	3×10^3	1	1, 2	0.25, 0.5, 1
∞	1×10^5	1	1, 2	0.1, 0.25, 0.5, 1
∞	1×10^6	1	1, 2	0.1, 0.25, 0.5, 1
10^{-3}	2.4×10^4		1, 3	0.1, 0.25, 0.5, 2
10^{-3}	4.8×10^4	3	1, 3	0.1, 0.25, 0.5, 1
10^{-3}	9.6×10^4	4	1, 2, 4	0.1, 0.25, 0.5, 1
10^{-3}	2×10^5		1, 3	0.1, 0.25, 0.5, 1
10^{-3}	1×10^6		1, 2	0.25, 0.5, 1
10^{-4}	1.6×10^5		1, 4	0.2, 0.5, 2
10^{-4}	3.2×10^5	3	1, 4	0.1, 0.25, 0.5, 1
10^{-4}	6.4×10^5	4	1, 8	0.1, 0.25, 0.5, 1
10^{-4}	3.6×10^6	3	1, 3	0.25, 0.5, 1
10^{-4}	1.44×10^7	2	1, 2	0.25, 0.5, 1
10^{-5}	1.8×10^6		1, 4	0.2, 0.5, 1
10^{-5}	3.6×10^6	4	1, 4	0.1 , 0.25, 0.5, 1
10^{-5}	7.2×10^6	4	1, 3	0.1, 0.25, 0.5, 1
10^{-5}	1.44×10^7	3	1, 3	0.25, 0.5, 1
10^{-5}	5.67×10^7	5	1, 5	0.25, 0.5, 1

Table D.2: Parameter list of simulations conducted with heterogeneous sidewall insulation prescribed in Eq (5.2).

D.2 Positive/Negative Solid Steady State

In section 5.3.1, we chose to find a solid steady state solution for RRBC with Positive/Negative boundary conditions. Here, we provide a thorough derivation and of discussion of the results.

A solid steady state solution is a flow which is both time-independent and has no velocity. These conditions simplify the governing equations and allow us to derive an analytical solution. This solution can be compared with the results of numerical simulations conducted in parameter ranges when time-independence and no flow is expected. The comparison is used to validate our numerical system.

In section 5.3.1, we consider a solid steady state which is characterised by time-independence and no fluid motion such that, $\frac{dT}{dt} = 0$ and $\boldsymbol{u} = 0$, in the absence of a thermal wind. By applying these conditions to the non-dimensionalised energy equation, $\frac{DT}{Dt} = \nabla^2 T$, we recover the Laplace equation Eq (5.3). Thus, the temperature must satisfy the fixed temperature boundary condition and the inhomogeneous sidewall condition, Eq (5.1), as well as the Laplace equation.

Thus, the system of equations governing the thermal behaviour is written in cylindrical coordinates, such that,

$$T\left(z = z_0\right) - T\left(z = z_1\right) = 1, \tag{D.1a}$$

$$\frac{\partial T\left(r = R\right)}{\partial r} = \sum_{n=1}^{\infty} A_n \sin\left(f_n z\right) \sin\left(m_\theta \theta\right), \qquad \text{and} \tag{D.1b}$$

$$\frac{\partial^2 T}{\partial r^2} + \frac{1}{r}\frac{\partial T}{\partial r} + \frac{1}{r^2}\frac{\partial^2 T}{\partial \theta^2} + \frac{\partial^2 T}{\partial z^2} = 0. \tag{D.1c}$$

Note that $R = 0.7$ is the radius of the domain wall.

The fixed temperature boundary condition necessitates that at the top and bottom of the cylinder there is no θ or r dependence, while Eq (D.1b) requires θ, r, and z dependencies throughout the rest of the domain. In general, this suggests an ansatz solution of the form,

$$T = \tau\left(z\right) + \tau'\left(z, \theta, r\right), \tag{D.2}$$

where,

$$\tau\left(z\right) = \frac{z}{z_0 - z_1} - \frac{z_1}{z_0 - z_1}, \tag{D.3}$$

which satisfies Eq (D.1a), and

$$\tau'(z, \theta, r) = Z(z)H(\theta)C(r), \tag{D.4}$$

where,

$$Z(z = z_0, \quad z_1) = 0, \tag{D.5}$$

and $H(\theta)$ and $C(r)$ are functions which will satisfy the θ and r components of Eq (D.1b). Thus, τ' also satisfies Eq (D.1b).

Applying this solution to Eq (D.1c), it is clear that τ satisfies the Laplace equation and only the τ' component remains to be solved. Therefore, substituting

Eq (D.2) into Eq (D.1c), with some simplification and shifting all z terms to the right-hand side (RHS), yields:

$$\frac{1}{C}\frac{\mathrm{d}^2 C}{\mathrm{d}r^2} + \frac{1}{rC}\frac{\mathrm{d}C}{\mathrm{d}r} + \frac{1}{r^2 H}\frac{\mathrm{d}^2 H}{\mathrm{d}\theta^2} = -\frac{1}{Z}\frac{\mathrm{d}^2 Z}{\mathrm{d}z^2}. \tag{D.6}$$

It is clear in Eq (D.6) that the left-hand side (LHS) depends only on r and θ while the RHS depends only on z. Consequently, both sides are equal to a constant, here called, f^2. Applying this condition to the RHS obtains:

$$\frac{\mathrm{d}^2 Z}{\mathrm{d}z^2} + f^2 Z = 0. \tag{D.7}$$

Thus, the general solution for the z component of T' is

$$Z(z) = j_{z1}\sin(fz) + j_{z2}\cos(fz). \tag{D.8}$$

Here, j_{z1} and j_{z2} are coefficients. By applying Eq (D.5), it follows that $j_{z2} = 0$, and

$$\sin(z_0 f) = 0,$$

which requires that $z_0 f = n\pi$, where n is an integer greater than zero. Therefore the z dependency becomes,

$$Z\left(z\right) = \sin\left(f_n z\right), \tag{D.9}$$

where f is now defined as $f_n = \frac{n\pi}{z_0}$ with $z_1 = -z_0$.

Now considering the LHS of Eq (D.6), we seek the solutions for the r and θ dependencies. With some simplification, the LHS of Equation (D.6) becomes,

$$\frac{r^2}{C}\frac{\mathrm{d}^2 C}{\mathrm{d}r^2} + \frac{r}{C}\frac{\mathrm{d}C}{\mathrm{d}r} - f_n^2 r^2 = -\frac{1}{H}\frac{\mathrm{d}^2 H}{\mathrm{d}\theta^2}. \tag{D.10}$$

The LHS and RHS of Eq (D.10) are independent of one another, and thus are equal to a constant, chosen to be m_θ^2. Thus, the θ dependence becomes,

$$\frac{\mathrm{d}^2 H}{\mathrm{d}\theta^2} + m_\theta^2 H = 0, \tag{D.11}$$

with general solution,

$$H(\theta) = j_{m1}\mathrm{sin}(m_\theta \theta) + j_{m2}\mathrm{cos}(m_\theta \theta), \tag{D.12}$$

recalling that m_θ is a chosen integer. The constants j_{m1} and j_{m2} are found by applying the boundary conditions, Eq (D.1a) and Eq (D.1b) for each mode m_θ.

Finally, we consider the r dependency. Examining the LHS of Eq (D.10), only the following remains,

$$r^2\frac{\mathrm{d}^2C}{\mathrm{d}r^2}+r\frac{\mathrm{d}C}{\mathrm{d}r}-C\left(f_n^2r^2+m_\theta^2\right)=0. \tag{D.13}$$

Eq (D.13) is the parametric Bessel's equation, which can be re-written as a Bessel's equation by defining $\Pi_n = f_n r$, such that,

$$\Pi_n^2C''+\Pi_nC'-C\left(\Pi_n^2+m_\theta^2\right)=0, \tag{D.14}$$

where the prime denotes derivatives with respect to Π_n.

It is sufficient here to say that, following the work of Lamb (1945), the standard solution to a modified Bessel's equation takes the form,

$$I_m(\Pi_n)=\int_0^\pi e^{\Pi_n\cos(\theta)}\cos\left(m_\theta\theta\right)d\theta. \tag{D.15}$$

Thus, the solution for the radial dependency becomes,

$$C(r)=j_5I_m(\Pi_n), \tag{D.16}$$

where j_5 is a constant coefficient. It is useful to note that, at small Π_n, the modified Bessel function has power law behaviour while, at large Π_n, it behaves exponentially (Fitzpatrick, 2014).

Thus the general solution of the Laplace equation for τ' in cylindrical coordinates is,

$$\tau'\left(z,\theta,r\right)=\sum_{n=1}^{\infty}\sin\left(f_nz\right)\left(\tilde{c}\sin\left(m_\theta\theta\right)+\tilde{d}\cos\left(m_\theta\theta\right)\right)I_m\left(f_nr\right), \tag{D.17}$$

where the coefficient j_5 has been absorbed into coefficients $\tilde{c}$ and $\tilde{d}$.

In order to find the exact solution, the boundary condition described in Eq (D.1b) must be applied, recalling that the conditions in Eq (D.5) have already been applied, and therefore the solution satisfies the fixed temperature boundary condition at the top and bottom. It is first useful to rewrite the boundary condition in terms of the separate dependencies, such that Eq (D.1b) becomes,

$$\frac{\partial\tau'\left(z,\theta,R\right)}{\partial r}=\sum_{n=1}^{\infty}A_n\sin\left(f_nz\right)\sin\left(m_\theta\theta\right). \tag{D.18}$$

Then, substituting in the full general solution, Eq (D.18) becomes,

$$\sum_{n=1}^{\infty} \sin\left(f_n z\right)\left(\tilde{c}\sin\left(m_\theta \theta\right)+\tilde{d}\cos\left(m_\theta \theta\right)\right)\frac{\mathrm{d}I_m\left(Rf_n\right)}{\mathrm{d}r}=\sum_{n=1}^{\infty} A_n \sin\left(f_n z\right)\sin\left(m_\theta \theta\right). \tag{D.19}$$

It is clear that $\tilde{d}=0$, because there is no $\cos\left(m_\theta \theta\right)$ component on the RHS. The remaining z and θ components cancel out, so Eq (D.19) becomes,

$$\tilde{c}\frac{\mathrm{d}I_m\left(Rf_n\right)}{\mathrm{d}r}=A_n, \tag{D.20}$$

which leads to the solution for $\tilde{c_n}$,

$$\tilde{c}=\frac{A_n}{\frac{\mathrm{d}I_m\left(Rf_n\right)}{\mathrm{d}r}}. \tag{D.21}$$

Now the final solution for τ' can be written as,

$$\tau'\left(z,\theta,r\right)=\sum_{n=1}^{\infty}\frac{A_n}{\frac{\mathrm{d}I_m\left(Rf_n\right)}{\mathrm{d}r}}\sin\left(f_n z\right)\sin\left(m_\theta \theta\right)I_m\left(f_n r\right), \tag{D.22}$$

recalling that $f_n=\frac{n\pi}{z_0}$, and that n and m_θ are integers of choice. Note m_θ could be treated the same as n and summed across multiple modes. Thus, the solution form is a superposition of a linear background profile, τ and a product of sines in z and θ, as such,

$$T\left(z,\theta,r\right)=\frac{z}{z_0-z_1}-\frac{z_1}{z_0-z_1}+\sum_{n=1}^{\infty}\frac{A_n}{\frac{\mathrm{d}I_m\left(Rf_n\right)}{\mathrm{d}r}}\sin\left(f_n z\right)\sin\left(m_\theta \theta\right)I_m\left(f_n r\right). \tag{D.23}$$

The linear component of the temperature profile is familiar for conductive systems. However, the τ' component of T, as in Eq (D.22), is not intuitively understood. Figure D.1 visualises the τ' component of the temperature in a solid steady state where $A_n=1$, $n=1$, and $m_\theta=1$. The cyan indicates negative τ' and red indicates positive τ', as shown in the colour-bars. It is clear that $m_\theta=1$ and $n=1$ correspond to a single sine wave in the θ and z directions, respectively, as anticipated. Additionally, the lower plots in Figure D.1 shows how the applied heat flux, illustrated by magenta (positive) to blue (negative) colouring at the domain boundaries, affects the temperature perturbation. It is evident that toward the centre of the domain the temperature perturbation reaches zero as the colour becomes more purple.

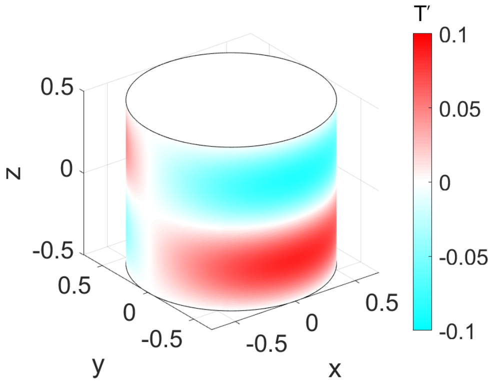

(a) T for full domain

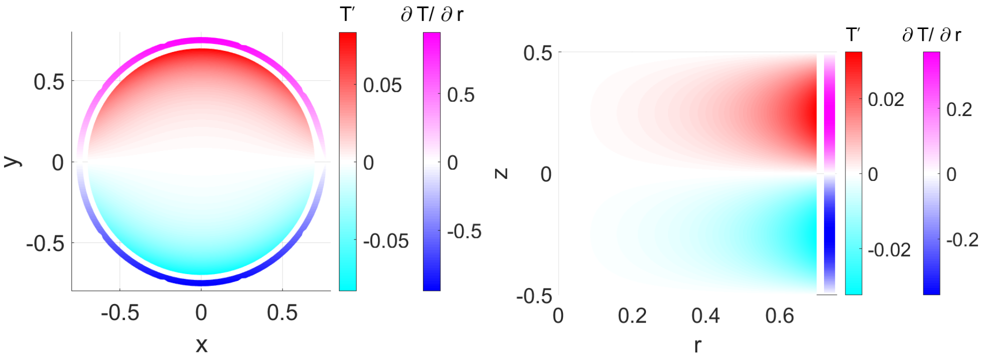

(b) $z = 0.3$

(c) $\theta = \pi/8$

Figure D.1: Temperature plots of the steady state solution Eq (D.22) with azimuthal mode, $m_\theta = 1$, vertical mode, $n = 1$, and amplitude, $A_n = 1$. In the two lower plots, the applied heat flux is indicated on a scale from magenta (positive) to blue (negative) at the domain boundaries.

Figure D.2 illuminates the relationships between the prescribed constants, A_n, n, and m_θ, and the maximum amplitude of τ'. m_θ and n are also varied as shown by the marker shapes and colours, respectively. Markers are circles, squares, diamonds,and triangles as m_θ increases incrementally from 1 to 4. The colours are red, yellow, green, and cyan as n increases incrementally from 1 to 4. Note that n is only varied when $m_\theta = 1$ in order to keep from crowding the plot.

From Figure, D.2, it is clear that as A_n increases, the amplitude of τ' increase. Indeed, if Figure D.2 had been plotted with logarithmic scales on both axes, it would indicate that the maximum amplitude of τ' is proportional to A_n^j, where j is a constant. Increasing n, decreases the maximum τ', though as n increases, the difference between τ's decreases. When m_θ increases, maximum τ' decreases, though less significantly than when n increases. Further, changes in m_θ have a linear relationship with changes in maximum τ'. This suggests that the effects of inhomogeneity in the thermal boundary condition may vary with m_θ.

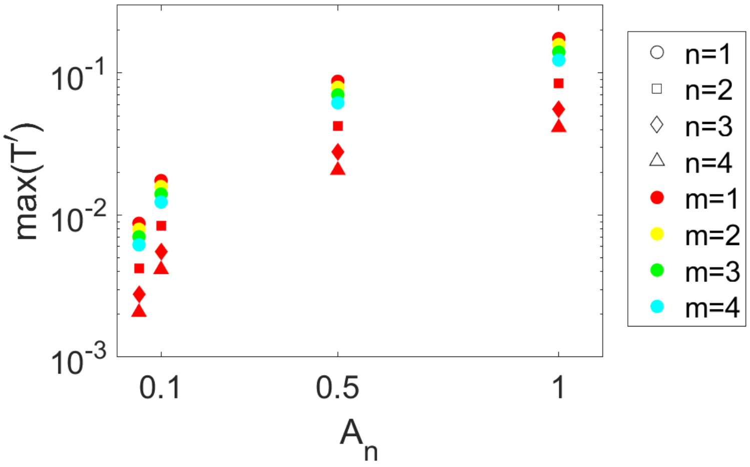

Figure D.2: The maximum deviation from the linear temperature profile, max(τ') as amplitude of the applied heat flux, A_n, varies. The azimuthal mode, m_θ, and vertical mode, n, are also varied as shown by the marker shapes and colours, respectively. Markers are circles, squares, diamonds,and triangles as m_θ increases incrementally from 1 to 4. The colours are red, yellow, green, and cyan as n increases incrementally from 1 to 4.

In summary, we have derived a solid steady state solution for a cylindrical system with boundary conditions, defined in Eq (D.1b) on the side wall and fixed temperatures on the top and bottom. The solution, Eq (D.23) is composed of a linear background profile, τ, and a superposition of sine modes in θ and z, τ'. τ', defined in Eq (D.22), depends on the amplitude, A_n, vertical mode, n, and azimuthal mode, m_θ. τ' is visualised for $A_n, n, m_\theta = 1$ in Figure D.1. The relationship between these variables and τ' is visualised in Figure D.2. We conclude that as A_n increases, so does the maximum amplitude of τ'. However, as n and m_θ increase, τ' decreases, exponentially in n, and linearly in m_θ. The solid steady state solution enables validation of the numerical set-up and the relationships between the solution and A_n, n, and m_θ will inform how we prescribe these constants for each case of Ek and Ra.

D.3 Positive/Zero Heat Flux Accounting

In section 5.3.2, we sought to measure the heat flux through the domain of a system with Positive/Zero boundary conditions. Here, we provide the derivation of the total heat flux.

Following the derivation of Nu in Hepworth (2014), we consider the non-dimensional heat equation, $\frac{DT}{Dt} = \nabla^2 T$. A cylindrical partial domain is defined such that, $V'(r,\theta,z) = [0,R] \times [0,2\pi] \times [-Z,Z']$ where R is the maximum radius, and $Z' < Z$. Now integrating Eq (2.11c) over the volume of the partial domain,

$$\int_{V'} \left(\frac{\partial T}{\partial t} + (\boldsymbol{u} \cdot \nabla) T \right) \mathrm{d}V' = \int_{V'} \left(\nabla^2 T \right) \mathrm{d}V'. \tag{D.24}$$

To define heat flux for a statistically steady state, we assume either a time-independent solution or a time-averaged solution. Hence,

$$\int_{V'} \left((\boldsymbol{u} \cdot \nabla) T \right) \mathrm{d}V' = \int_{V'} \left(\nabla^2 T \right) \mathrm{d}V'. \tag{D.25}$$

Using vector identities,

$$\nabla \cdot (\boldsymbol{a} f) = f (\nabla \cdot \boldsymbol{a}) + (\boldsymbol{a} s \cdot \nabla), \qquad \text{and} \tag{D.26}$$

$$\nabla^2 f = \nabla \cdot (\nabla f), \tag{D.27}$$

where a is a vector function and f is a field, and incompressibility (Eq (2.11b)), Eq (D.25) is simplified. Thus,

$$\int_{V'} \left(\nabla \cdot (\boldsymbol{u} T) \right) \mathrm{d}V' = \int_{V'} \left(\nabla \cdot (\nabla T) \right) \mathrm{d}V'. \tag{D.28}$$

Eq (D.28) is now in a form such that the 3D divergence theorem,

$$\int_V \nabla \cdot \boldsymbol{F} \mathrm{d}V = \int_S \boldsymbol{F} \cdot \hat{\boldsymbol{n}} \mathrm{d}s, \tag{D.29}$$

where S is the surface enclosing V with outward normal vector $\hat{\boldsymbol{n}}$, can be usefully applied as such,

$$\int_{S'} \left(\boldsymbol{u} T \cdot \hat{\boldsymbol{n}} \right) \mathrm{d}s = \int_{S'} \left(\nabla T \cdot \hat{\boldsymbol{n}} \right) \mathrm{d}s. \tag{D.30}$$

Defining $\hat{\boldsymbol{n}}$ in cylindrical coordinates as $(r, 0, 0)$, Eq (D.30) is expanded to a series of surface integrals on the sidewall, denoted $|_{r=R}$, on the lower boundary, denoted, $|_{z=-Z}$, or at the upper bound of partial volume V', denoted, $|_{z=Z'}$. Thus, Eq (D.30) becomes,

$$\int_{-Z'}^{Z'}\int_0^{2\pi} u_r T r\mathrm{d}\theta\mathrm{d}z|_{r=R} + \int_0^R\int_0^{2\pi} u_z T r\mathrm{d}\theta\mathrm{d}r|_{z=Z'} + \int_0^R\int_0^{2\pi} -u_z T r\mathrm{d}\theta\mathrm{d}r|_{z=-Z} = \\ \int_{-Z'}^{Z'}\int_0^{2\pi} \frac{\partial T}{\partial r} r\mathrm{d}\theta\mathrm{d}z|_{r=R} + \int_0^R\int_0^{2\pi} \frac{\partial T}{\partial z} r\mathrm{d}\theta\mathrm{d}r|_{z=Z'} + \int_0^R\int_0^{2\pi} -\frac{\partial T}{\partial z} r\mathrm{d}\theta\mathrm{d}r|_{z=-Z}. \tag{D.31}$$

No-slip velocity conditions require $\boldsymbol{u} = 0$ on $r = R$, and $z = -Z$, causing the first and third term on the left-hand side (LHS) to vanish. Recall, that we are not yet considering the full domain, rather partial domain, V', which has upper bound $-Z < Z' \leq Z$, and therefore we do not apply the no-slip condition on $z = Z'$. Thus,

$$\int_0^R\int_0^{2\pi} u_z T r\mathrm{d}\theta\mathrm{d}r|_{z=Z'} = \\ \int_{-Z'}^{Z'}\int_0^{2\pi} \frac{\partial T}{\partial r} r\mathrm{d}\theta\mathrm{d}z|_{r=R} + \int_0^R\int_0^{2\pi} \frac{\partial T}{\partial z} r\mathrm{d}\theta\mathrm{d}r|_{z=Z'} + \int_0^R\int_0^{2\pi} -\frac{\partial T}{\partial z} r\mathrm{d}\theta\mathrm{d}r|_{z=-Z}. \tag{D.32}$$

The first term on the right-hand side (RHS) is controlled by the sidewall boundary condition. An insulating condition ($\frac{\partial T}{\partial r} = 0$) or specific instances of inhomogeneous insulation such as Eq (5.1) would cause the term to vanish. In such instances,

$$\int_0^R\int_0^{2\pi} \frac{\partial T}{\partial z} r\mathrm{d}\theta\mathrm{d}r|_{z=-Z} = \int_0^R\int_0^{2\pi} \frac{\partial T}{\partial z} r - u_z T r\mathrm{d}\theta\mathrm{d}r|_{z=Z'}. \tag{D.33}$$

It is therefore clear that as long as the heat flux condition along the sidewall has a 0 surface integral, the heat flux at any horizontal plane, should be equal, which is a traditional understanding of Nu (Siggia, 1994; Grossmann & Lohse, 2000). Considering the Positive/Zero case, where the sidewalls have heterogeneous heat flux applied. The heat flux variation defined in Eq (5.2) would not cause the RHS term of Eq (D.33) to vanish. Therefore, it is of interest to consider a more general relationship which accommodates any sidewall thermal boundary conditions. Hence, Eq (D.32) becomes,

$$\int_0^R\int_0^{2\pi} \frac{\partial T}{\partial z} r\mathrm{d}\theta\mathrm{d}r|_{z=-Z} = \\ \int_0^R\int_0^{2\pi} \frac{\partial T}{\partial z} r - u_z T r\mathrm{d}\theta\mathrm{d}r|_{z=Z'} + \int_{-Z}^{Z'}\int_0^{2\pi} \frac{\partial T}{\partial r} r\mathrm{d}\theta\mathrm{d}z|_{r=R}. \tag{D.34}$$

This relationship implies that the heat flux at the bottom is the same heat flux at any horizontal plane summed with the heat flux gained or lost from the sidewall between the bottom and the plane.

Now let $Z' = Z$, to cover the full domain,

$$\int_0^R \int_0^{2\pi} \frac{\partial T}{\partial z} r \mathrm{d}\theta \mathrm{d}r|_{z=-Z} = \int_0^R \int_0^{2\pi} \frac{\partial T}{\partial z} r \mathrm{d}\theta \mathrm{d}r|_{z=Z} + r \int_{-Z}^{Z} \int_0^{2\pi} \frac{\partial T}{\partial r} \mathrm{d}\theta \mathrm{d}z|_{r=R}, \tag{D.35}$$

note that the velocity term on the LHS has vanished due to no-slip velocity conditions on the top of the domain. It is now clear that the heat flux at top and bottom vary dependant on the heat flux removed or added at the sidewalls.

D.4 Additional Figures

We provide several supporting figures for the analysis of results in Chapter 5. Generally, these results are restatements of an effect already seen in a different system.

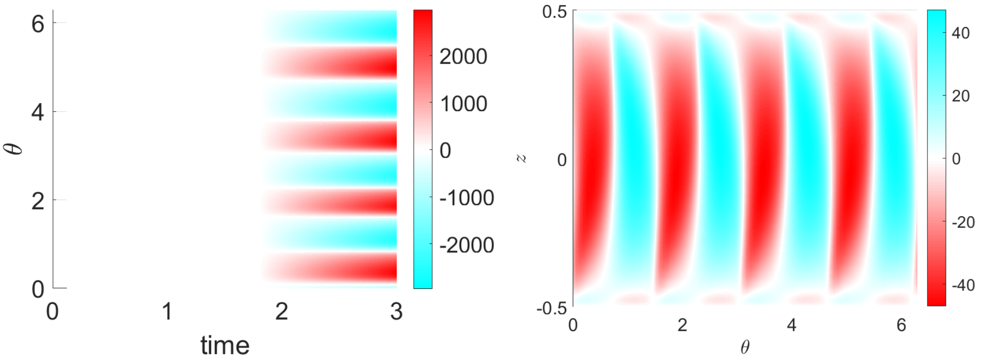

(a) Homogeneous, $A_n = 0$

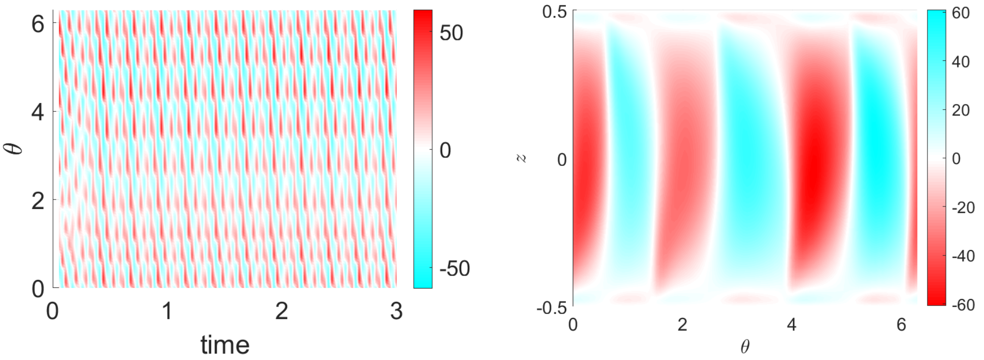

(b) Positive/Negative, $A_n = 1$

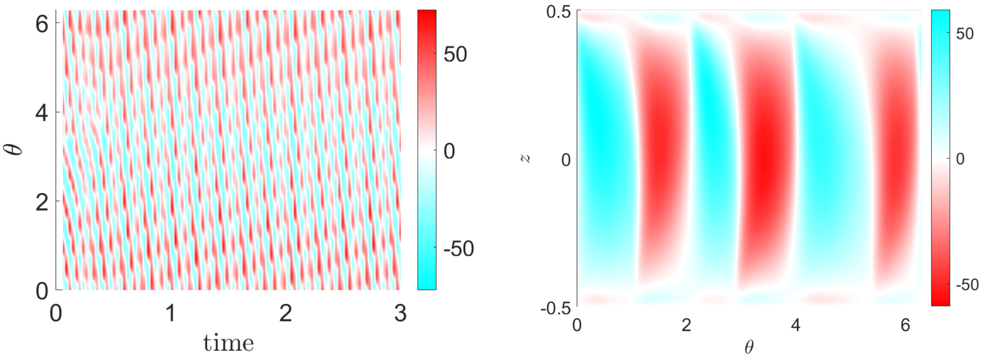

(c) Positive/Zero, $A_n = 1$

Figure D.3: Vertical velocity w for the rotating RBC system with $Ek = 10^{-4}$ and $Ra = 6.4 \times 10^5$. Positive/Negative boundary condition defined in Eq (5.1) and Positive/Zero condition defined in Eq (5.2). Inhomogeneous systems have $m_\theta = 1$ and $A_n = 1$. Left-hand plots are Hövmoller diagrams at $z = 0.3$ and $r = 0.68$. Right-hand plots are taken at time $t = 3$ and $r = 0.685$.

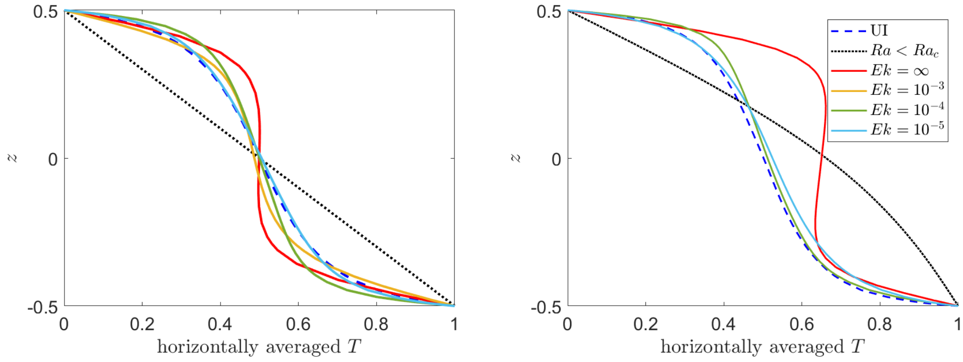

(a) Positive/Negative (b) Positive/Zero

Figure D.4: Plots of horizontally averaged temperature T vs. height z for RBC with either Positive/Negative or Positive/Zero inhomogeneous sidewall condition. The blue dashed line indicates the uniformly insulated case of the same Ra/Ra_c. The black dotted line shows the conducting case where $Ra = 1 < Ra_c$ with $m_\theta = 1$ and $A_n = 0.5$. The colour of each solid line indicates an Ekman number Ek system with inhomogeneous sidewall boundary conditions with $m_\theta = m_{UI}$ and $A_n = 1$.

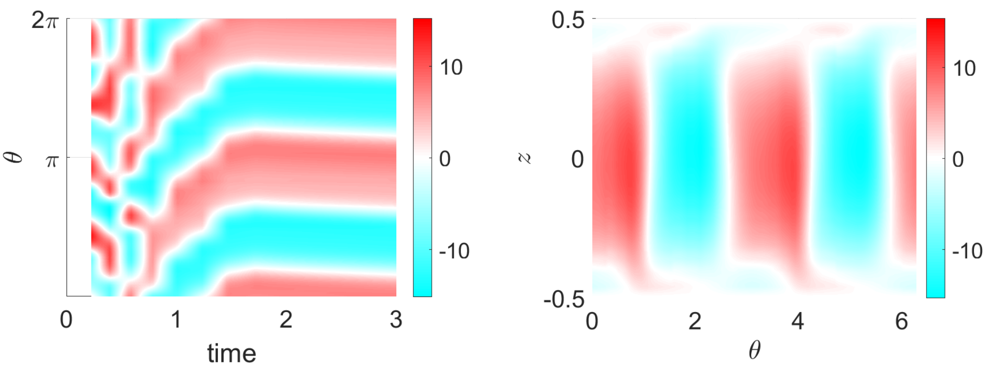

(a) Homogeneous, $A_n = 0$

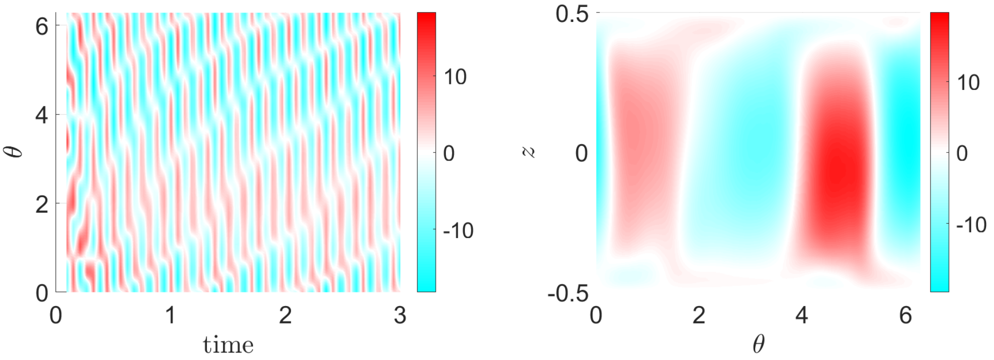

(b) Positive/Negative, $A_n = 1$

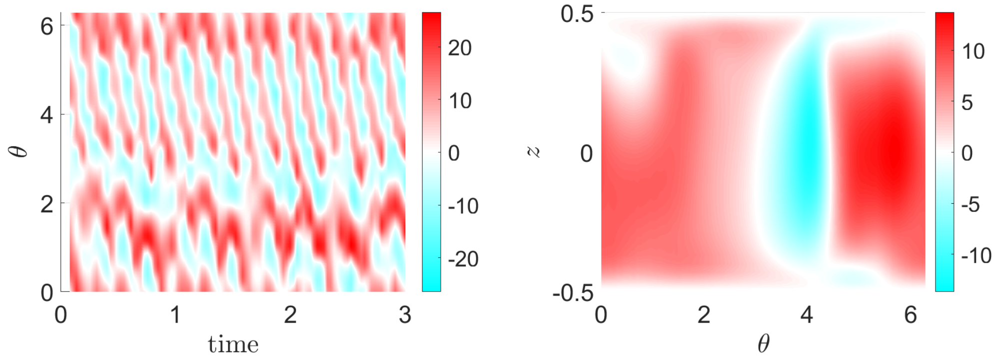

(c) Positive/Zero, $A_n = 1$

Figure D.5: Plots of vertical velocity in a weakly rotating RBC system with $Ek = 10^{-3}$ and $Ra = 9.6 \times 10^4$. On the left (right) are Hövmoller diagrams at $r = 0.685$ and $z = 0.3$ (plots at $t = 3$ and $r = 0.685$. The top plot has homogeneously insulated sidewalls. The lower plots have inhomogeneous insulation as in Eq (5.1) and Eq (5.2), respectively. Both inhomogeneous cases have azimuthal mode $m_\theta = 1$.

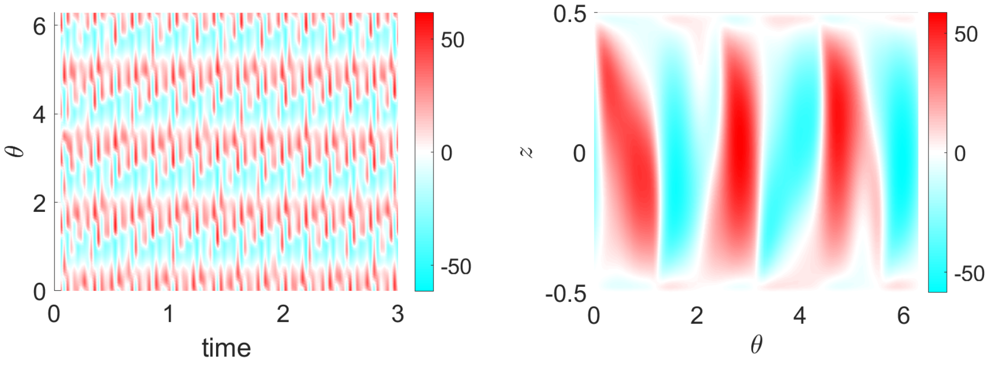

(a) Positive/Negative, $A_n = 2$

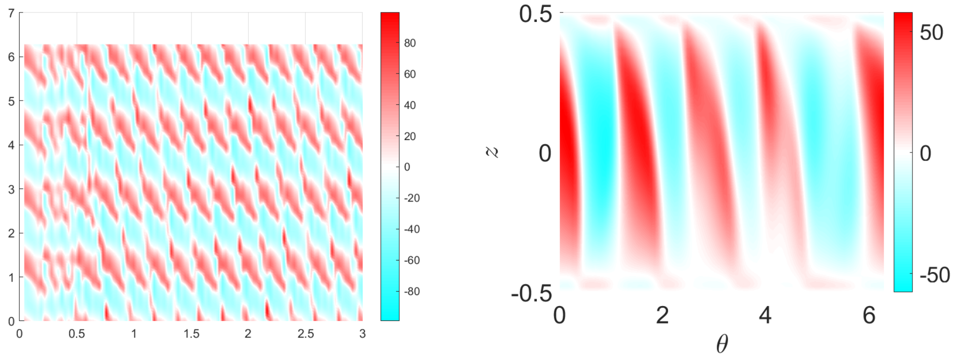

(b) Positive/Zero, $A_n = 2$

Figure D.6: Plots of vertical velocity in an RRBC system with $Ek = 10^{-4}$ and $Ra = 6.4 \times 10^5$. On the left (right) are Hövmoller diagrams at $r = 0.685$ and $z = 0.3$ (plots at $t = 3$ and $r = 0.685$. The top plot has homogeneously insulated sidewalls. For both plots, $m_\theta = 4 = m_{UI}$

Appendix E

Experimental Design Additional Lists and Relationship

This Appendix contain additional information with importance to our experimental design which is described in Chapter 6.

The list of fluids which sublimate and may be visible in solid and gaseous form. We considered these fluids for use in a two-phase experiment in Chapter 6.

Material	TP $\tilde{p}$(Pa)	TP $\tilde{T}$(^{o}C)	Visibility	Hazards [5]
Perfluorocyclohexane [1]	1.27×10^5	59	no info	irritant, not deadly
Hexachloroethane [1]	1.04×10^5	186	visible	irritant, health & environmental hazard
Camphor [1]	4.93×10^4	179	possibly	flamable, irritant, health hazard
Ferrocene [2,3]	1.34×10^4	173	possibly	flammable, irritant, environmental hazard
Iodine [1,4]	1.12×10^4	114	visible	irritant, environmental hazard
Naphthalene [1]	9.33×10^2	80	not likely	irritant, health & environmental hazard

Table E.1: Sublimating substances and their triple point (TP), the pressure, $\tilde{p}$, and temperature, $\tilde{T}$, at which solid, liquid, and gaseous phases can coexist. The visibility of the solid and liquid phases is noted along with hazards of the fluid.

[1] Pavia et al. (2015)

[2] Ullmann et al. (1985)

[3] Fulem et al. (2013)

[4] Yolcu (2016)

[5] The National Library of Medicine (2021)

E.1 Kinematic viscosity

In order to observe how changes in temperature and pressure affect the Prandtl number in section 6.4, we use the relationship defined in Kadoya et al. (1985) between the kinematic viscosity, μ, average temperature, $\bar{\tilde{T}}$, and density, $\tilde{\rho}$.

$$\mu\left(T_R, \rho_R\right) = H \cdot \left[\mu_0\left(T_R\right) + \Delta\mu\left(\rho_R\right)\right], \tag{E.1}$$

where

$$\mu_0\left(T_R\right) = A_1 T_R + A_{0.5} T_R^{0.5} + \Sigma_{i=0}^{-4} A_i T_R^i, \tag{E.2a}$$

$$\Delta\mu\left(\tilde{\rho}_R\right) = \Sigma_{i=1}^{4} B_i \rho_R^i, \tag{E.2b}$$

$$T_R = \frac{\bar{\tilde{T}}}{T^*}, \tag{E.2c}$$

$$\rho_R = \frac{\tilde{\rho}}{\rho^*}. \tag{E.2d}$$

See Table E.2 for the values of the constants.

E.2 Thermal conductivity

In order to observe how changes in temperature and pressure affect the Prandtl number in section 6.4, we use the the relationship developed in Kadoya et al. (1985) between the thermal conductivity, k, average temperature, $\bar{\tilde{T}}$, and density, $\tilde{\rho}$.

$$k\left(T_R, \rho_R\right) = V\left[k_0\left(T_R\right)\right) + \Delta k\left(\rho_R\right)\right], \tag{E.3}$$

where

$$k_0\left(T_K\right) = C_1 T_R + C_{0.5} T_R^{0.5} + \Sigma_{i=0}^{-4} C_i T_R^i, \tag{E.4a}$$

$$\Delta k\left(\rho_R\right) = \Sigma_{i=1}^{5} D_i \rho_R^i, \tag{E.4b}$$

upon recalling equations E.2c and E.2d. See Table E.3 for the values of the constants.

Constant	Value
$T*$	132.5K
$\rho*$	$314.3\mathrm{kg/m}^3$
H	$[6.1609, 0] \times 10^{-6}\mathrm{Pa}\dot{s}$
A_1	$[0.1285, 17]$
$A_{0.5}$	$[2.60066, 1]$
A_0	$[-1.0000, 0]$
A_{-1}	$[-0.7096, 61]$
A_{-2}	$[0.6625, 34]$
A_{-3}	$[-0.1978, 46]$
A_{-4}	$[-0.0077, 0147]$
B_1	$[0.4656, 01]$
B_2	$[1.2646, 9]$
B_3	$[-0.5114, 25]$
B_4	$[0.2746, 00]$

Table E.2: Constants and ranges of constants for Eq E.1 from Kadoya et al. (1985).

Constant	Value
T^*	132.5K
ρ^*	314.3kg/m^3
V	$25.9778 \times 10^3\text{W/mK}$
C_1	$[0.2395, 03]$
$C_{0.5}$	$[0.0064, 9768]$
C_0	$[1.0000, 0]$
C_{-1}	$[-1.9262, 5]$
C_{-2}	$[2.0038, 3]$
C_{-3}	$[-1.0755, 3]$
C_{-4}	$[0.2294, 14]$
D_1	$[0.4022, 87]$
D_2	$[0.3566, 03]$
D_3	$[-0.1631, 59]$
D_4	$[0.1380, 59]$
D_5	$[-0.0201, 725]$

Table E.3: Constants or ranges of constants for Eq E.3 from Kadoya et al. (1985).

References

Ahlers, G., & Behringer, R. P. (1978). Evolution of turbulence from the Rayleigh-Bénard instability. *Phys. Rev. Lett.*, *40*(11), 712–716.

Anders, E., Vasil, G., Brown, B., & Korre, L. (2020). Convective dynamics with mixed temperature boundary conditions: Why thermal relaxation matters and how to accelerate it. *Phys. Rev. Fluids.*

Aujogue, K., Pothérat, A., Sreenivasan, B., & Debray, F. (2018). Experimental study of the convection in a rotating tangent cylinder. *Journal of Fluid Mechanics*, *843*, 355–381.

Aurnou, J., Calkins, M., Cheng, J., Julien, K., King, E., Nieves, D., Soderlund, K. M., & Stellmach, S. (2015). Rotating convective turbulence in Earth and planetary cores. *Phys. Earth Planet Inter.*, *246*, 52–71.

Barker, A. J., Dempsey, A. M., & Lithwick, Y. (2014). Theory and simulations of rotating convection. *Astrophys. J.*, *791*(1), 13.

Batchelor, G. (2000). *An introduction to fluid dynamics.* Cambridge University Press.

Bauer, P., Thorpe, A., & Brunet, G. (2015). The quiet revolution of numerical weather prediction. *Nature*, *525*, 47–55.

Behringer, R. P., Agosta, C., Jan, J. S., & Shaumeyer, J. N. (1980). Time-dependent Rayleigh-Bénard convection and instrumental attenuation. *Phys. Lett.*, *80A*(4), 273–276.

Behringer, R. P., & Ahlers, G. (1982). Heat transport and temporal evolution of fluid flow near the Rayleigh-Bénard instability in cylindrical containers. *J. Fluid Mech.*, *1982*, 219–258.

Bénard, H. (1900). Étude expérimentale des courants de convection dans une nappe liquide. - régime permanent : Tourbillons cellulaires. *J. Theo. App. Phys.*, *9*(1), 513–524.

Bénard, H. (1901). Les tourbillons cellulaires dans une nappe liquide transportant de la chaleur par convection en rgime permanent. *Annales de chimie et de physique*, *23*, 62–144.

Bloxham, J. (2000). Sensitivity of the geomagnetic axial dipole to thermal core–mantle interactions. *Nature*, *405*(6782), 63–65.

Bloxham, J., & Gubbins, D. (1987). Thermal core–mantle interactions. *Nature*, *325*(6104), 511–513.

Brangeon, B., Joubert, P., & Bastide, A. (2015). Influence of the dynamic boundary conditions on natural convection in an asymmetrically heated channel. *Int. J. Therm. Sci.*, *95*, 64–72. https://doi.org/https://doi.org/10.1016/j.ijthermalsci.2015.04.006

Brummell, N. H., Clune, T. L., & Toomre, J. (2002). Penetration and overshooting in turbulent compressible convection. *The Astrophysical Journal*, *570*(2), 825.

Buell, J., & Catton, I. (1983a). Effect of rotation on the stability of a bounded cylindrical layer of fluid heated from below. *Phys. of Fluids*, *28*(4).

Buell, J., & Catton, I. (1983b). The effect of wall conduction on the stability of a fluid in a right circular cylinder heated from below. *J. Heat Trans.*, *105*, 255–260.

Burns, K. J., Vasil, G. M., Oishi, J. S., Lecoanet, D., & Brown, B. (2016). Dedalus: Flexible framework for spectrally solving differential equations. *Astrophysics Source Code Library*, ascl–1603.

Busse, F. H. (1975). Patterns of convection in spherical shells. *J. Fluid Mech.*, *72*(1), 67–85. https://doi.org/10.1017/S0022112075002947

Busse, F. H., & Cuong, P. (1977). Convection in rapidly rotating spherical fluid shells. *Geo. Astro. Fluid Dyn.*, *8*(1), 17–41.

Calkins, M., Hale, K., Julien, K., Nieves, D., Driggs, D., & Marti, P. (2015). The asymptotic equivalence of fixed heat flux and fixed temperature thermal boundary conditions for rapidly rotating convection. *J. Fluid Mech.*

Cardin, P., & Olson, P. (1994). Chaotic thermal convection in a rapidly rotating spherical shell: Consequences for flow in the outer core. *Phys. Earth Planet Inter.*, *82*(3-4), 235–259.

Chandrasekhar, S. (1953). The instability of a layer of fluid heated below and subject to coriolis forces. *Proc. R. Soc. London. Ser. A*, *217*(1130), 306–327.

Chandrasekhar, S. (1961). *Hydrodynamic and hydromagnetic stability*. Dover Publications, Inc.

Chapman, C., & Proctor, M. (1980). Nonlinear Rayleigh–Bénard convection between poorly conducting boundaries. *J. Fluid Mech.*, *101*(4), 759–782.

Charlson, G. S., & Sani, R. L. (1970). Thermoconvective instability in a bounded cylindrical fluid layer. *Int. J. Heat Mass Trans.*, *13*, 1479–1496.

Charney, J. (1948). On the scale of atmospheric processes. *Geofys. Publ*, *17*, 1–17.

Cheng, J., Stellmach, S., Riberio, A., Grannan, A., King, E., & Aurnou, J. (2015). Laboratory-numerical models of rapidly rotating convection in planetary cores. *Geophys. J. Int.*

Cheng, J. S., Aurnou, J. M., Julien, K., & Kunnen, R. P. (2018). A heuristic framework for next-generation models of geostrophic convective turbulence. *Geo. Astro. Fluid Dyn.*, *112*(4), 277–300.

Chong, K. L., & Xia, K.-Q. (2016). Exploring the severely confined regime in Rayleigh–Bénard convection. *J. Fluid Mech.*, *805*.

Chung, K. H., & Hyun, J. M. (2001). Effect of circumferential variation of sidewall temperature on buoyant convection in a vertical cylinder. *Int. J. Heat Mass Trans.*, *44*(13), 2583–2587.

Chung, K. H., Hyun, J. M., & Ozoe, H. (2000). Buoyant convection in a vertical cylinder with azimuthally-varying sidewall temperature. *Int. J. Heat Mass Trans.*, *43*(13), 2289–2301.

Clarté, T. T., Schaeffer, N., Labrosse, S., & Vidal, J. (2021). The effects of a robin boundary condition on thermal convection in a rotating spherical shell. *J. Fluid Mech.*, *918*.

Clever, R. M., & Busse, F. H. (1974). Transition to time-dependant convection. *J. Fluid Mech.*, *65*(4), 625–645.

Clever, R., & Busse, F. H. (1979). Nonlinear properties of convection rolls in a horizontal layer rotating about a vertical axis. *J. Fluid Mech.*, *94*(4), 609–627.

Clune, T., & Knobloch, E. (1993). Pattern selection in rotating convection with experimental boundary conditions. *Phys. Rev. E*, *47*(4), 2536–2550.

Cox, A., & Doell, R. R. (1964). Long period variations of the geomagnetic field. *B. Seis. Soc. Am.*, *54*(6B), 2243–2270. https://doi.org/10.1785/BSSA05406B2243

Croquette, V. (1989). Convective pattern dynamics at low Prandtl number: Part i. *Cont. Phys.*, *30*(2), 113–133.

Currie, L. K., Barker, A. J., Lithwick, Y., & Browning, M. K. (2020). Convection with misaligned gravity and rotation: simulations and rotating mixing length theory. *Monthly Notices of the Royal Astronomical Society*, *493*(4), 5233–5256.

Davies, C. J., Gubbins, D., & Jimack, P. K. (2009). Convection in a rapidly rotating spherical shell with an imposed laterally varying thermal boundary condition. *J. Fluid Mech.*, *641*, 335–358.

Davies, C. J., Gubbins, D., Willis, A. P., & Jimack, P. K. (2008). Time-averaged paleomagnetic field and secular variation: Predictions from dynamo solutions based on lower mantle seismic tomography. *Phys. Earth Planet Inter.*, *169*(1-4), 194–203.

Davies, G. F., & Richards, M. A. (1992). Mantle convection. *J. Geol.*, *100*(2), 151–206.

Daya, Z., & Ecke, R. (2001). Does turbulent convection feel the shape of the container? *Phys. Rev. Lett.*, *87*(18), 184501.

de Wit, X., Guzmán, A. A., Madonia, M., Cheng, J., Clercx, H., & Kunnen, R. (2020). Turbulent rotating convection confined in a slender cylinder: The sidewall circulation. *Phys. Rev.*, *5*.

Dixon, J. C. (2007). The shock absorber handbook. John Wiley, Sons.

Dormy, E., & Soward, A. M. (2007). *Mathematical aspects of natural dynamos*. Chapman; Hall/CRC.

Dowling, T. (1988). Rotating Rayleigh-Bénard convection with fixed flux boundaries. *Sum. Study Prog. in Geophys. Fluids*.

Ecke, R. E., & Niemela, J. J. (2014). Heat transport in the geostrophic regime of rotating Rayleigh-Bénard convection. *Phys. Rev. Lett.*, *113*, 114301. https://doi.org/10.1103/PhysRevLett.113.114301

Ecke, R. E., Zhang, X., & Shishkina, O. (2022). Connecting wall modes and boundary zonal flows in rotating Rayleigh-Bénard convection. *Phys. Rev. Fluids*, *7*(1), L011501.

Edwards, D. K. (1969). Suppression of cellular convection by lateral walls. *J. Heat Trans.*

Edwards, T. K., Smith, L. M., & Stechmann, S. N. (2019). Spectra of atmospheric water in precipitating quasi-geostrophic turbulence. *Geo. Astro. Fluid Dyn.*

Emran, M., & Schumacher, J. (2008). Fine-scale statistics of temperature and its derivatives in convective turbulence. *J. Fluid Mech.*, *611*, 13–34.

Fauve, S. (2017). Henri Bénard and pattern-forming instabilities. *Comptes Rendus Physique*, *18*, 531–543.

Favier, B., & Knobloch, E. (2020). Robust wall states in rapidly rotating Rayleigh–Bénard convection. *J. Fluid Mech.*, *895*.

Fiedler, B. H. (1989). Scale selection in nonlinear thermal convection between poorly conducting boundaries. *Geo. Astro. Fluid Dyn.*, *46*(3), 191–201.

Fitzpatrick, R. (2014). Laplace's equation in cylindrical coordinates.

Friedrich, J., Lee, Y.-S., Fischer, B., Kupfer, C., Vizman, D., & Müller, G. (1999). Experimental and numerical study of rayleigh-bénard convection affected by a rotating magnetic field. *Physics of Fluids*, *11*(4), 853–861.

Fulem, M., Růžička, K., Červinka, C., Rocha, M. A., Santos, L. M., & Berg, R. F. (2013). Recommended vapor pressure and thermophysical data for ferrocene. *J. Chem. Therm.*, *57*, 530–540.

Fultz, D., & Nakagawa, Y. (1955). Experiments on over-stable thermal convection in mercury. *Proc. R. Soc. London. Ser. A*, *231*(1).

Fultz, D., Nakagawa, Y., & Frenzen, P. (1954). An instance in thermal convection of Eddington's 'overstability'. *Phys. Rev.*, *64*(6).

Funfschilling, D., Brown, E., Nikolaenko, A., & Ahlers, G. (2005). Heat transport by turbulent Rayleigh–Bénard convection in cylindrical samples with aspect ratio one and larger. *J. Fluid Mech.*, *536*, 145–154.

Gao, H., & Behringer, R. P. (1984). Onset of convective time dependence in cylindrical containers. *Phys. Rev. A*, *30*(5), 2837–2839.

Gastine, T., Wicht, J., & Aubert, J. (2016). Scaling regimes in spherical shell rotating convection. *J. Fluid Mech.*, *808*, 690–732.

Gibbons, S., Gubbins, D., & Zhang, K. (2007). Convection in rotating spherical fluid shells with inhomogeneous heat flux at the outer boundary. *Geo. Astro. Fluid Dyn.*, *101*(5-6), 347–370.

Glatzmaier, G. A., & Gilman, P. A. (1982). Compressible convection in a rotating spherical shell. v-induced differential rotation and meridional circulation. *Astrophys. J.*, *256*, 316–330.

Godbersen, P., Bosbach, J., Schanz, D., & Schröder, A. (2021). Beauty of turbulent convection: A particle tracking endeavor. *Phys. Rev. Fluids*, *6*, 110509. https://doi.org/10.1103/PhysRevFluids.6.110509

Goldstein, H., Knobloch, E., Mercader, I., & Net, M. (1994). Convection in a rotating cylinder. part 2. linear theory for low Prandtl numbers. *J. Fluid Mech.*, *262*, 293–324.

Goldstein, H. F., Knobloc, E., Mercaderz, I., & Net, M. (1993). Convection in a rotating cylinder. part 1 linear theory for moderate Prandtl numbers. *J. Fluid Mech.*, *248*, 583–604.

Gringé, C., Labrosse, S., & Tackley, P. (2007). Convection under a lid of finite conductivity: Heat flux scaling and application to continents. *J. Geophsy. Rea.*

Grooms, I., Julien, K., Weiss, J. B., & Knobloch, E. (2010). Model of convective Taylor columns in rotating Rayleigh-Bénard convection. *Physical review letters*, *104*(22), 224501.

Grossmann, S., & Lohse, D. (2002). Prandtl and Rayleigh number dependence of the Reynolds number in turbulent thermal convection. *Phys. Rev. E*, *66*.

Grossmann, S., & Lohse, D. (2000). Scaling in thermal convection: A unifying theory. *J. Fluid Mech.*, *407*, 27–56.

Gubbins, D., & Herrero-Bervera, E. (2007). *Encyclopedia of geomagnetism and paleomagnetism*. Springer Science & Business Media.

Guzmán, A. J. A., Madonia, M., Cheng, J. S., Ostilla-Mónico, R., Clercx, H. J., & Kunnen, R. P. (2021). Force balance in rapidly rotating Rayleigh–Bénard convection. *J. Fluid Mech.*, *928*.

Hartmann, R., Chong, K. L., Stevens, R. J., Verzicco, R., & Lohse, D. (2021). Heat transport enhancement in confined Rayleigh-Bénard convection feels the shape of the container (a). *EPL (EuroPhys. Lett.)*, *135*(2), 24004.

Hepworth, B. J. (2014). *Nonlinear two-dimensional Rayleigh-Bénard convection* (Doctoral dissertation). University of Leeds. University of Leeds.

Hernadez-Duenas, G., Majda, A. J., Smith, L. M., & Stechmann, S. N. (2012). Minimal models for precipitating organized convection. *J. Fluid Mech.*

Hernandez-Duenas, G., Smith, L. M., & Stechmann, S. N. (2015). Stability and instability criteria for idealized precipitating hydrodynamics. *J. Atmo. Sci.*

Hernlund, J. W., & Tackley, P. J. (2008). Modeling mantle convection in the spherical annulus. *Phys. Earth Planet Inter.*, *171*(1-4), 48–54.

Herrmann, J., & Busse, F. (1993). Asymptotic theory of wall-attached convection in a rotating fluid layer. *J. Fluid Mech.*, *255*, 183–194.

Hilsenrath, J., Beckett, C., W.-Benedict, Fano, L., Hoge, H., Masi, J., Nuttal, R., Touloukian, Y., & Woolley, H. (1955). *Tables of thermal properties of gases.* NBS Circular 564.

Hoard, C. Q., Robertson, C. R., & Acrivos, A. (1970). Experiments on the cellular structure in Bénard convection. *Int. J. Heat Mass Trans.*, *13*(5), 849–852.

Horn, S., & Aurnou, J. (2017). Rotating convection with centrifugal buoyancy: Numerical predictions for laboratory experiments. *Phys. Rev. Fluids*, *4*(7).

Hu, R., Edwards, T. K., Smith, L. M., & Stechmann, S. N. (2021). Initial investigations of precipitating quasi-geostrophic turbulence with phase changes. *Res. Math. Sci.*, *8*(1), 1–25.

Huang, S., Wang, F., Xi, H., & Xia, K. (2015). Comparative experimental study of fixed temperature and fixed heat flux boundary conditions in turbulent thermal convection. *Phys. Rev. Lts.*

Huang, S.-D., Kaczorowski, M., Ni, R., Xia, K.-Q., et al. (2013). Confinement-induced heat-transport enhancement in turbulent thermal convection. *Phys. Rev. Lett.*, *111*(10), 104501.

Hurle, D., Jakeman, E., & Pike, E. R. (1967). On the solution of the Bénard problem with boundaries of finite conductivity. *Proc. R. Soc. London. Ser. A.*, *296*(1447), 469–475.

Ishiwatari, M., Takehiro, S.-I., & Hayashi, Y.-Y. (1994). The effects of thermal conditions on the cell sizes of two-dimensional convection. *J. Fluid Mech.*, *281*, 33–50.

Jeffreys, H. (1926). Lxxvi. the stability of a layer of fluid heated below. *The London, Edinburgh, and Dublin Philosophical Magazine and Journal of Science*, *2*(10), 833–844.

Jeffreys, H. (1928). Some cases of instability in fluid motion. *Proc. R. Soc. London. Ser. A*, *118*(779), 195–208.

Johnston, H., & Doering, C. R. (2009). Comparison of turbulent thermal convection between conditions of constant temperature and constant flux. *Phys. Rev. Lett.*, *102*(6), 064501.

Jones, C., & Schubert, G. (2015). Thermal and compositional convection in the outer core. *Treatise in Geophysics, Core Dynamics*, *8*, 131–185.

Julien, K., Knobloch, E., Miliff, R., & Werne, J. (2006). Generalized quasi-geostrophy for spatially anisotropic rotationally constrained flows. *J. Fluid Mech.*, *555*, 233–274.

Julien, K., Legg, S., McWilliams, J., & Werne, J. (1996). Rapidly rotating turbulent Rayleigh-Bénard convection. *J. Fluid Mech.*, *322*, 243–273.

Kadoya, K., Matsunaga, N., & Nagashmia, A. (1985). Viscosity and thermal conductivity of dry air in the gaseous phase. *J. Phys. Chem. Ref. Data*, *14*(4).

Khodadadi, J., & Zhang, Y. (2001). Effects of buoyancy-driven convection on melting within spherical containers. *Int. J. Heat Mass Trans.*, *44*(8), 1605–1618.

King, E., Stellmach, S., & Aurnou, J. (2012). Heat transfer by rapidly rotating Rayleigh-Bénard convection. *J. Fluid Mech.*, *691*, 568–582.

King, E., Stellmach, S., Noir, J., Hansen, U., & Aurnou, J. (2009). Boundary layer control of rotating convection systems. *Nature*, *457*.

King, E. M., Soderlund, K. M., Christensen, U. R., Wicht, J., & Aurnou, J. M. (2010). Convective heat transfer in planetary dynamo models. *Geochem. Geophys., Geosys.*, *11*(6).

Koshmeider. (1966). On convection of a uniformly heated plane. *Beitrage zur Physik der Atmosphare*.

Kraichnan, R. H. (1962). Turbulent thermal convection at arbitrary Prandtl number. *Phys. of Fluids*, *5*(11), 1374–1389.

Krettenauer, K., & Schumann, U. (1989). Direct numerical simulation of thermal convection over a wavy surface. *Met. Atmos. Phys.*, *41*(3), 165–179.

Ku, H. H., et al. (1966). Notes on the use of propagation of error formulas. *J. Res. Nat. Bur. Stand.*, *70*(4), 263–273.

Kunnen, R. P. J., Geurts, B. J., & Clercx, H. J. H. (2010). Experimental and numerical investigation of turbulent convection in a rotating cylinder. *J. Fluid Mech.*, *642*, 445–476.

Kunnen, R. P. J., Ostilla-Mónico, R., van der Poel, E. P., Verzicco, R., & Lohse, D. (2016). Transition to geostrophic convection: The role of the boundary conditions. *J. Fluid Mech.*, *799*.

Kunnen, R., Clercx, H., & Geurts, B. J. (2008). Breakdown of large-scale circulation in turbulent rotating convection. *EPL (EuroPhys. Lett.)*, *84*(2), 24001.

Kunnen, R., Clercx, H., Geurts, B., Van Bokhoven, L., Akkermans, R., & Verzicco, R. (2008). Numerical and experimental investigation of structure-function scaling in turbulent Rayleigh-Bénard convection. *Phys. Rev. E*, *77*(1), 016302.

Küppers, G., & Lortz, D. (1969). Transition from laminar convection to thermal turbulence in a rotating fluid layer. *J. Fluid Mech.*, *35*(3), 609–620.

Lamb, H. (1945). *Hydrodynamics*. Dover Publications.

Laube, T., Dietrich, B., Marocco, L., & Wetzel, T. (2022). Turbulent heat transfer in a liquid metal tube flow with azimuthally inhomogeneous heat flux. *Int. J. Heat Mass Trans.*, *189*, 122734. https://doi.org/https://doi.org/10.1016/j.ijheatmasstransfer.2022.122734

Lehmacher, G., & Lübken, F.-J. (1995). Simultaneous observation of convective adjustment and turbulence generation in the mesosphere. *Geophys. Res. Lett.*, *22*(18), 2477–2480.

Liao, X., Zhang, K., & Chang, Y. (2006). On boundary-layer convection in a rotating fluid layer. *J. Fluid Mech.*, *549*, 375–384.

Lide, D. R. (Ed.). (2003). *Crc handbook of chemistry and physics* (84th ed.). CRC Press LLC.

Long, R., Mound, J., Davies, C., & Tobias, S. (2020). Scaling behaviour in spherical shell rotating convection with fixed-flux thermal boundary conditions. *J. Fluid Mech.*, *889*.

Long, R. S. (2020). *Regimes and scaling laws for convection with and without rotation* (Doctoral dissertation). University of Leeds.

Malkus, W. V. (1954a). Discrete transitions in turbulent convection. *Proc. R. Soc. London. Ser. A*, *225*(1161), 185–195.

Malkus, W. V. (1954b). The heat transport and spectrum of thermal turbulence. *Proc. R. Soc. London. Ser. A.*, *225*(1161), 196–212.

Malkus, W., & Veronis, G. (1958). Finite amplitude cellular convection. *J. Fluid Mech.*, *4*(3), 225–260.

Manning, W. D. (2013). *Reactive nitrogen in the tropical troposphere* (Doctoral dissertation). University of York.

Masters, T. G., Johnson, S., Laske, G., & Bolton, H. (1996). A shear-velocity model of the mantle. *Proc. R. Soc. London Ser. A.*, *354*(1711), 1385–1411.

Matthews, P. C. (2003). Pattern formation on a sphere. *Phys. Rev. E*, *67*, 036206. https://doi.org/10.1103/PhysRevE.67.036206

Morimune-Moriya, S., & Nishino, T. (2021). Strong, tough, transparent and highly heat-resistant acrylic glass based on nanodiamond. *Polymer*, *222*, 123661. https://doi.org/https://doi.org/10.1016/j.polymer.2021.123661

Mound, J. E., & Davies, C. J. (2017). Heat transfer in rapidly rotating convection with heterogeneous thermal boundary conditions. *J. Fluid Mech.*, *828*, 601–629.

Nakagawa, T., & Tackley, P. J. (2008). Lateral variations in cmb heat flux and deep mantle seismic velocity caused by a thermal–chemical-phase boundary layer in 3D spherical convection. *Earth Planet. Sci. Lett.*, *271*(1-4), 348–358.

Nakagawa, Y., & Frenzen, P. (1954). A theoretical and experimental study of cellular convection in rotating fluids. *Tellus*, *7*(1), 2–21.

Nek5000. (2019). *Version 19.0* (tech. rep.) [https://nek5000.mcs.anl.gov]. Argonne National Laboratory. Illinois.

Ohta, K., & Hirose, K. (2020). The thermal conductivity of the Earth's core and implications for its thermal and compositional evolution. *Nat. Sci. Rev.*, *8*(4). https://doi.org/10.1093/nsr/nwaa303

Oliveira, J. S., & Wieczorek, M. A. (2017). Testing the axial dipole hypothesis for the Moon by modeling the direction of crustal magnetization. *J. Geophys. Res. Planets*, *122*(2), 383–399.

Oresta, P., Verzicco, R., Lohse, D., & Prosperetti, A. (2009). Heat transfer mechanisms in bubbly Rayleigh-Bénard convection. *Phys. Rev. E*, *80*.

O'Sullivan, C. T. (1990). Newton's law of cooling—a critical assessment. *Am. J. Phys.*, *58*(10), 956–960.

Otero, J., Wittenberg, R. W., Worthing, R. A., & Doering, C. R. (2002). Bounds on Rayleigh–Bénard convection with an imposed heat flux. *J. Fluid Mech.*, *473*, 191–199.

Ouertatani, N., Cheikh, N. B., Beya, B. B., & Lili, T. (2008). Numerical simulation of two-dimensional Rayleigh–Bénard convection in an enclosure. *Comptes Rendus Mécanique*, *336*(5), 464–470.

Pachauri, R., & Meyer, L. (Eds.). (2014). *Climate change 2014: Synthesis report. contribution of working groups i, ii and iii to the fifth assessment report of the intergovernmental panel on climate change.* IPCC.

Parsons, B., & Daly, S. (1983). The relationship between surface topography, gravity anomalies, and temperature structure of convection. *J. Geophys. Res. Solid Earth*, *88*(B2), 1129–1144.

Pauluis, O., & Schumacher, J. (2010). Idealized moist Rayleigh-Bénard convection with piecewise linear equation of state. *Comm. Math. Sci.*, *8*(1).

Pavia, D. L., Kriz, G. S., Lampman, G. M., & Engel, R. G. (2015). *A small scale approach to organic laboratory techniques.* Cengage Learning.

Pellow, A., & Southwell, S. V. (1940). On maintained convective motion in a fluid heated from below. *Proc. R. Soc. London. Ser. A*, *176*(966), 312–343.

Plumley, M., & Julien, K. (2019). Scaling laws in Rayleigh-Bénard convection. *Earth and Spc. Sci.*

Plumley, M., Julien, K., Marti, P., & Stellmach, S. (2016). The effects of Ekman pumping on quasi-geostrophic Rayleigh–Bénard convection. *J. Fluid Mech.*, *803*, 51–71.

Prosperetti, A. (2012). The effect of rotation on the Rayleigh-Bénard stability threshold. *Phys. of Fluids*, *24*, 114101-1 - 114101–16.

Proudman, J. (1916). On the motion of solids in a liquid possessing vorticity. *Proc. R. Soc. London. Ser. A*, *92*(642), 408–424.

Rayleigh, L. (1916). On the convective currents in a horizontal layer of fluid when the higher temperature is on the under side. *Philosophical Magazine*, *32*(192), 529–546.

Reiter, P., Zhang, X., & Shishkina, O. (2022). Flow states and heat transport in Rayleigh–Bénard convection with different sidewall boundary conditions. *J. Fluid Mech.*, *936*.

Riahi, N. (1982). Convection in a rotating layer with nearly insulating boundaries. *Zeit. Mathe. Phys. ZAMP.*

Rossby, H. T. (1969). A study of Bénard convection with and without rotation. *J. Fluid Mech.*, *36*(2), 309–3335.

Sahoo, S., & Sreenivasan, B. (2017). On the effect of laterally varying boundary heat flux on rapidly rotating spherical shell convection. *Phys. of Fluids*, *29*(8), 086602.

Sahoo, S., & Sreenivasan, B. (2020). Convection in a rapidly rotating cylindrical annulus with laterally varying boundary heat flux. *J. Fluid Mech.*, *883*.

Sakuraba, A., & Roberts, P. H. (2009). Generation of a strong magnetic field using uniform heat flux at the surface of the core. *Nat. Geosci.*, *2*(11), 802–805.

Sasaki, Y. (1970). Influences of thermal boundary layer on atmospheric cellular convection. *J. Meteoro. Soc. Japan Ser. II*, *48*(6), 492–502.

Schmalzl, J., Breuer, M., & Hansen, U. (2002). The influence of the Prandtl number on the style of vigorous thermal convection. *Geo. Astro. Fluid Dyn.*, *96*(5), 381–403.

Schmidt, L. E., Oresta, P., Toschi, F., Verzicco, P., Lohse, D., & Prosperetti, A. (2011). Modification of turbulence in Rayleigh Bénard convection by phase change. *New J. Phys.*, *13*.

Schmidt, R. J., & Milverton, S. W. (1935). On the instability of a fluid when heated from below. *Proc. R. Soc. London. Ser. A*, *152*(877), 586–594.

Schubert, G., & Soderlund, K. M. (2011). Planetary magnetic fields: Observations and models. *Phys. Earth Planet Inter.*, *187*(3-4), 92–108.

Schubert, G., Turcotte, D. L., & Olson, P. (2001). *Mantle convection in the Earth and planets.* Cambridge University Press.

Siggia, E. D. (1994). High Rayleigh number convection. *Ann. Rev. Fluid Mech.*, *26*(1), 137–168.

Smith, L. M., & Stechmann, S. N. (2017). Precipititating quasigeostrophic equations and potential vorticity inversion with phase changes. *J. Atmo. Sci.*

Sparrow, E., Goldstein, R., & Jonsson, V. (1964). Thermal instability in a horizontal fluid layer: Effect of boundary conditions and non-linear temperature profile. *J. Fluid Mech.*

Spiegel, E. A., & Veronis, G. (1960). On the Boussinesq approximation for a compressible fluid. *Astrophys. J.*, *131*, 442.

Sprague, M., Julien, K., Knobloch, E., & Werne, J. (2006). Numerical simulation of an asymptotically reduced system for rotationally constrained convection. *J. Fluid Mech.*, *551*, 141–174.

Šrámek, O., & Zhong, S. (2010). Long-wavelength stagnant lid convection with hemispheric variation in lithospheric thickness: Link between Martian crustal dichotomy and Tharsis? *J. Geophys. Res. Planets*, *115*(E9).

Stellmach, S., Lischper, M., Julien, K., Vasil, G., Cheng, J. S., Ribeiro, A., King, E. M., & Aurnou, J. M. (2014). Approaching the asymptotic regime of rapidly rotating convection: Boundary layers versus interior dynamics. *Phys. Rev. Lett.*, *113*(25), 254501.

Stevens, R., Clercx, H., & Lohse, D. (2010). Boundary layers in rotating weakly turbulent Rayleigh–Bénard convection. *Phys. of Fluids*, *22*.

Sumita, I., & Olson, P. (2002). Rotating thermal convection experiments in a hemispherical shell with heterogeneous boundary heat flux: Implications for the Earth's core. *J. Geophys. Res. Solid Earth*, *107*(B8), ETG–5.

Sun, C., Xi, H.-D., & Xia, K.-Q. (2005). Azimuthal symmetry, flow dynamics, and heat transport in turbulent thermal convection in a cylinder with an aspect ratio of 0.5. *Phys. Rev. Lett.*, *95*(7), 074502.

Takahashi, F., & Tsunakawa, H. (2009). Thermal core-mantle coupling in an early lunar dynamo: Implications for a global magnetic field and magnetosphere of the early Moon. *Geophys. Res. Lett.*, *36*(24).

Tang, X., Ntam, M. C., Dong, J., Rainey, E. S., & Kavner, A. (2014). The thermal conductivity of Earth's lower mantle. *Geophys. Res. Lett.*, *41*(8), 2746–2752.

Taylor, G. I. (1923). Experiments on the motion of solid bodies in rotating fluids. *Proc. R. Soc. London. Ser. A*, 213–218.

Taylor, G. I. (1936). Fluid friction between rotating cylinders: Part i—torque measurements. *Proc. R. Soc. London. Ser. A*, *157*(892), 546–564.

Terra-Nova, F., Amit, H., Choblet, G., Tobie, G., Bouffard, M., & Čadek, O. (2022). The influence of heterogeneous seafloor heat flux on the cooling patterns of Ganymede's and Titan's subsurface oceans. *Icarus*, 115232.

The National Library of Medicine. (2021). Pubchem [data retrieved from PubChem, https://pubchem.ncbi.nlm.nih.gov/].

Tobias, S. (2021). The turbulent dynamo. *J. Fluid Mech.*, *912*.

Touloukian, Y. S., Powell, R. W., Ho, C. Y., & Klemens, P. G. (1970). *Thermophysical properties of matter* (Vol. 1). Purdue University.

Trapp, R. (2018). Formation and development of convective storms. *Oxford Research Encyclopedia of Climate Science*.

Tremblin, P., Padioleau, T., Phillips, M., Chabrier, G., Baraffe, I., Fromang, S., Audit, E., Bloch, H., Burgasser, A. J., Drummond, B., González, M., Kestener, P., Kokh, S., Lagage, P.-O., & Stauffert, M. (2019). Thermo-compositional diabatic convection in the atmospheres of brown dwarfs and in Earth's atmosphere and oceans. *Astrophys. J.*, *876*(2).

Ullmann, F., Gerhartz, W., Yamamoto, Y. S., Campbell, F. T., Pfefferkorn, R., Rounsaville, J. F., et al. (1985). *Ullmann's encyclopedia of industrial chemistry*. VCH publishers.

Vallis, G., Parker, D., & Tobias, S. (2019). A simple system for moist convection: The Rainy-Bénard model. *Journal of Fluic Mechanics*, *862*, 162–190.

Veronis, G. (1959). Cellular convection with finite amplitude in a rotating fluid. *J. Fluid Mech.*, *5*(3), 401–435.

Veronis, G. (1966). Large-amplitude Bénard convection. *J. Fluid Mech.*, *26*(1), 49–68.

Veronis, G. (1968). Large-amplitude Bénard convection in a rotating fluid. *J. Fluid Mech.*, *31*(1), 113–139.

Verzicco, R., & Sreenivasan, K. (2008). A comparison of turbulent thermal convection between conditions of constant temperature and constant heat flux. *J. Fluid Mech.*

Verzicco, R., & Camussi, R. (2003). Numerical experiments on strongly turbulent thermal convection in a slender cylindrical cell. *J. Fluid Mech.*, *477*, 19–49.

Vieweg, P. P., Scheel, J. D., & Schumacher, J. (2021). Supergranule aggregation for constant heat flux-driven turbulent convection. *Physical Review Research*, *3*(1), 013231.

Vorobieff, P., & Ecke, R. (1998). Transient states during spin-up of a Rayleigh–Bénard cell. *Phys. of Fluids*, *10*(10), 2525–2538.

Vorobieff, P., & Ecke, R. E. (2002). Turbulent rotating convection: An experimental study. *J. Fluid Mech.*, *458*, 191–218.

Wong, J., Davies, C., & Jones, C. (2018). A Boussinesq slurry model of the F-layer at the base of Earth's outer core. *Geophys. J. Int.*, *214*, 2236–2249.

Yadav, R. K., Gastine, T., Christensen, U. R., Wolk, S. J., & Poppenhaeger, K. (2016). Approaching a realistic force balance in geodynamo simulations. *Proc. Nat. Aca. Sci.*, *113*(43), 12065–12070. https://doi.org/10.1073/pnas.1608998113

Yolcu, H. (2016). A demonstration of the sublimation process and its effect on students' conceptual understanding of the sublimation concept. *J. Turkish Chem. Soc. Sec. C*, *1*.

Zhang, K., & Liao, X. (2009). The onset of convection in rotating circular cylinders with experimental boundary conditions. *J. Fluid Mech.*, *622*, 63–73.

Zhang, X., Ecke, R. E., & Shishkina, O. (2021). Boundary zonal flows in rapidly rotating turbulent thermal convection. *J. Fluid Mech.*, *915*.

Zhong, S. (2009). Migration of tharsis volcanism on mars caused by differential rotation of the lithosphere. *Nature Geoscience*, *2*(1), 19–23.